UNIVERSIDADE D
COIMBRA

Miguel Fernandes Moita

POLARIMETER DEVELOPMENT FOR FUTURE SPACE GAMMA-RAY TELESCOPES

Tese de doutoramento em Engenharia Física, ramo de Instrumentação, orientada pelo Professor Doutor Rui Miguel Curado da Silva e pelo Professor Doutor Jorge Manuel Maia Pereira e apresentada ao Departamento de Física da Faculdade de Ciências e Tecnologia da Universidade de Coimbra.

Dezembro de 2019

UNIVERSIDADE D
COIMBRA

Miguel Fernandes Moita

POLARIMETER DEVELOPMENT FOR FUTURE SPACE GAMMA-RAY TELESCOPES

Tese de doutoramento em Engenharia Física, ramo de Instrumentação, orientada pelo Professor Doutor Rui Miguel Curado da Silva e pelo Professor Doutor Jorge Manuel Maia Pereira e apresentada ao Departamento de Física da Faculdade de Ciências e Tecnologia da Universidade de Coimbra.

Dezembro de 2019

The research reported in this thesis was performed with financial support from the following institutions and programs:

• PhD grant number PD/BD/105922/2014 from Fundação para a Ciência e Tecnologia.

Resumo

Na era da astronomia multi-mensageira, a polarimetria de raios gama pode contribuir para uma compreensão mais ampla dos transientes de raios gama associados à deteção de ondas gravitacionais. Além disso, permite uma compreensão profunda dos processos físicos, geometria e campos magnéticos de fontes como pulsares, explosões solares, núcleos galácticos ativos ou buracos negros. Sendo este o tema científico que beneficia em última análise desta tese, desenvolvemos e analisamos o desempenho de um protótipo de com 2 planos de deteção. Os 2 detetores têm um ânodo segmentado em 8×8 pixels (2×2 mm^2 cada pixel) em cristais de 2 mm de espessura. A configuração do sistema de deteção permitiu-nos avaliar o desempenho polarimétrico de uma câmara e espectrómetro 3D, alterando a distância entre as duas camadas na faixa de energia de 100-600 keV.

Duas versões do protótipo Compton-POLCA foram desenvolvidas no período desta tese e testadas sob um feixe polarizado de ~99% na linha ID15A no ESRF, para energias de 200 a 500 keV (monocromáticas). O fator de modulação polarimétrica foi avaliado em distâncias entre planos que variam de 6 mm a 16 mm em diferentes ângulos de dispersão de Compton. Adicionalmente, foi criado e simulado um modelo de massa no software MEGAlib. Os resultados obtidos confirmam o potencial polarimétrico de detetores CdTe com configuração multicamada e mostraram que a determinação da posição 3D de cada ocorrência em eventos de espalhamento representa uma grande vantagem na medição da polarização, pois permite uma reconstrução mais precisa da cinemática Compton e, portanto, uma seleção mais eficiente dos eventos para otimizar a resposta à modulação da polarização. O protótipo também foi testado nas instalações da LARIX sob um feixe não polarizado (continuo de 20-300 keV), onde os resultados mostraram os erros sistemáticos que podemos obter ao usar geometrias de pixel quadrado e detetor quadrado.

Finalmente, também apresentamos um estudo preliminar da resposta de uma amostra de cristais curvados de GaAs obtidos usando o detetor Compton-POLCA no seu plano focal. Em particular, relatamos a capacidade do detetor apresentar a imagem focada pelas lentes, ou seja: a função de dispersão, energia de passagem e uniformidade. As técnicas de focagem de radiação de altas energias usando lentes de Laue representam a próxima

geração de instrumentação astronómica raios-X de alta energia e raios gama de baixa energia. A sensibilidade sem precedentes alcançável por esses telescópios abrirá definitivamente uma nova janela de conhecimento no domínio da astrofísica das altas energias.

Abstract

In the multi-messenger era, gamma-ray polarimetry may contribute to a wider understanding of gamma-ray transients associated to gravitational waves detection. Furthermore, allows a deep understanding of the physical processes, geometry and magnetic fields of sources such as pulsars, solar flares, active galactic nuclei or galactic black holes. Herein, we developed and analysed the performances of a prototype in a 2 layers Compton configuration based on two CdTe spectro-imagers operated in coincidence. The two CdTe detectors have an anode segmented in 8×8 pixels (2 mm pitch) on 2 mm thick crystals. The detection system configuration allowed us to assess the scattering polarimetric performance of a 3D spectro-imager by changing the distance between the two layers over the 100-600 keV energy range.

Two versions of the Compton-POLCA prototype were developed in the period of these thesis and tested under a ~99% polarized beam in the ID15A beamline at the ESRF, for energies 200-500 keV (monochromatic). The polarimetric modulation factor was evaluated at distances between planes ranging from 6mm up to 16mm at different Compton scattering angles. Along this a mass model was created and simulated in MEGAlib software. The results obtained confirm the fine polarimetric potential of multi-layer configuration CdTe focal planes and showed that the determination of the 3D position of each hit in scattering events represents a great advantage in the measurement of polarization as it allows for a more accurate reconstruction of the Compton kinematics, and therefore, a more efficient selection of the events to optimize the response to the polarization modulation. The prototype was also tested at LARIX facility under a unpolarized beam (20-300 keV continuum) where the results showed the systematics errors that we can obtained when using square pixel and square detector geometries.

Finally, we also present a preliminary study of the response of a sample of GaAs bent crystals obtained using the Compton-POLCA as focal plane detector. In particular, we report on the capability of the CdTe pixel detector to sample the focused image, i.e. the PSF, of GaAs bent crystals, determine its energy pass band and evaluate its uniformity. Such high-energy focusing optics, as broadband Laue lens, represent the next generation

of hard x- and soft gamma-ray astronomy instrumentation. The unprecedented sensitivity achievable by these telescopes will open a new knowledge window in high-energy astrophysics.

Acknowledgements

There are a large number of people who, with their collaboration and/or support, have made this thesis possible.

First of all, I would like to express my sincere gratitude to my supervisors, Rui Silva and Jorge Maia, and from INAF-Bologna, Ezio Caroli, Natalia Auricchio and John Stephen. These were the persons most guide and support me throughout the entire period of this work. Each one tremendously gifted, generous, simple and ready to help. The work of these thesis brought us together and a genuine friendship was built from there. I will never forget some of the moments that I spent with you during the ESRF campaigns: the time spent in the lab; the dinners, harmonized always with a bottle of good wine; the discussions; the valuable suggestions; and even the problematic moments, when your joy kept me going. This work would not be possible without each one of you. I hope the work written here makes you proud, because in a way, represents part of the friendship that I fell for you.

A special thanks to the persons that also participated directly in this thesis, namely: Nuno Carolino, from the LIP workshop team, for his precious help during the electronic development of the detector; Enrico Virgilli, from the University of Ferrara, for his tremendous availability during the Ferrara experiments; Stefano Del Sordo, from INAF-Palermo, for his help during the 2018 ESRF and Ferrara campaigns; Thomas Buslaps, supervisory of the ID15 beamline, always tireless to solve problems; and above all, Marcela Páscoa, you are the most precious gift the department of physics gave me and our lives will get crossed again soon.

To my laboratory colleagues and professors, André Cortez, Prof. Filomena Santos, José Escada, Alexandre Trindade, Prof. Filipa Borges, Prof. Carlos Conde and all the master students that worked in the laboratory during the time frame of this thesis.

Institutionally, I want thank all the elements that constitute the Coimbra pole of LIP and the Physics Department of the University of Coimbra, for providing the necessary conditions and infrastructures which were essential for the accomplishment of my goals.

This work was possible due to the DAEPHYS (Doctorate in Applied and Engineering Physics) and Fundação para a Ciência e Tecnologia for the Ph.D. scholarship PD/BD/105922/2014.

This work is also dedicated to my long-time friends from Figueira da Foz and specially my band mates, Luis and Ivo, this period marks my return to the stages, it has been a pleasure doing it with you both.

To all the friends I made in Coimbra during this period. This period in Coimbra gave me some of the most important friendships of my life, the love, the complicity, the care it was beyond I ever had. I learn so much with each one of you that change me as person. Each one of you has a place in my hearth. It is very difficult to say all your names because there are so many, but three names must be here: Inês Marques, Margarida Sousa and Mariana Santos. You were part of one of the most beautiful moments in my life and you always be my sweet pure love.

To my long-time friends, Sara and Luis. Just by thinking on you a smile appears in my face. I am so proud of you and to be your friend. Thank you for staying at your place so many times, I always returned with my heart fulfilled.

Finally, a specially dedication to my family: my sister Bárbara Moita; my nephew, Vasco Capitão; my grandmother, Maria Fernandes; my father, Joaquim Moita; and above all, to my mother, Graça Fernandes, who always gave me unconditional love, support and belief. You will always be my north star.

.

Contents

Introduction

Astronomy in the medium-energy gamma-ray band (0.1 – 100 MeV) holds a rich promise for elucidating many fundamental questions concerning, e.g., nucleosynthesis in stellar explosions (novae and supernovae), the origin of cosmic rays, the laws of physics on neutron stars and black holes, the active sun or the origin of terrestrial gamma-ray flashes. In addition, this field of astronomy also contributes to the advancement of cosmology and fundamental physics. Over the last decade, the diversity and richness of the gamma-ray sky have been revealed through the joint exploitation of instruments on-board satellites such as International Gamma-Ray Astrophysics Laboratory (INTEGRAL) [1] and the Fermi Gamma-ray Space Telescope [2] in the soft and high-energy gamma-ray domains. Position, spectral and temporal analyses have now been made possible, and hence, confronted to multi-wavelength data in order to probe the underlying physical mechanisms of the observed sources, among them: gamma-ray bursts, novae, supernovae and their remnants, pulsars and their wind nebulae, accreting binary systems and active galactic nuclei, massive stars and stellar formation regions.

Furthermore, in a new era of multimessenger astronomy, joint observations of multi-wavelength electromagnetic emission, gravitational waves, neutrinos and cosmic rays could provide an unprecedent data to understand the physical processes of many astronomical sources. Gamma-ray observations have played a critical role in every multimessenger source identified to date. In fact, the peak power output of electromagnetic counterparts lies in the gamma-ray band for the objects identified so far [3]–[8]. A future

gamma-ray observatory capable of time, spatial, spectral and polarimetric analyses is crucial to understand: the compact objects, gamma ray burst (GRB) and gravitational waves counterparts; the element formation in extreme environments such as kilonovae and supernovae; and the astrophysical jets.

Polarization of high-energy sources is a key observational parameter to understand the emission mechanisms and geometry of a wide number of cosmic objects and events such as GRBs, pulsars, binary black holes (BBH) and active galactic nuclei (AGN), where some degree of polarization is expected [9]–[11]. Even though this has been known for quite some time in the scientific community, only in the last years reliable results were published. The first reliable polarization measurements were by INTEGRAL [12], [13], [22]–[25], [14]–[21], however, the results show significant systemic errors because the instruments onboard were not calibrated on-ground for polarimetric measurements. More recently, the Cadmium Zinc Telluride Imager (CZTI), instrument on-board the Indian astronomy satellite Astrosat, made the most sensitive measurement to date of polarized hard X-ray emission from the Crab pulsar and nebula in the 100-380 keV band [26]; and POLAR, a dedicated to GRB polarimeter made the most sensitive measurements of the polarization of GRBs [27]. These instruments showed the importance of on-ground calibration and a precise mass model for Monte Carlo simulations before the flights [28]–[32].

The Space Instrumentation for Astrophysics (i-Astro) group of the Laboratory of Instrumentation and Experimental Particle Physics (LIP) have been studying, developing and proposing different configuration detection plane prototypes for new high-energy missions that could provide polarimetric observations, contemporaneously with spectroscopy and imaging. These prototypes were semiconductor based (mostly cadmium telluride (CdTe) family) detection planes designed for coded mask or for Laue lens instrument solutions. LIP expertise in this domain motivated several partnership proposals submitted in the European Space Agency (ESA) Cosmic Vision calls: Gamma-Ray Imager (GRI) [33], DUAL [34], ASTROGAM [35], e-ASTROGAM [36] and All-Sky-ASTROGAM [37]. These missions were not selected for launch, however the team continue to improve the techniques and materials for a future high-energy mission. In fact, LIP is currently member of the partnership of the All-sky Medium Energy Gamma-ray Observatory (AMEGO) [38], a National Aeronautics and Space Administration (NASA) probe class mission, to investigate the energy range from 300 keV to >10 GeV. Furthermore, LIP

Coimbra was a partner of the Horizon 2020 project “Activities in the High-Energy Astrophysics Domain” (AHEAD) project that aims the promotion of synergies between the distinct national efforts in high-energy astrophysics in order to provide more coherent and mature future space observatory joint proposals to future European Space Agency (ESA) calls for missions. This project lead to the Advanced Surveyor of Transient Events and Nuclear Astrophysics (ASTENA), a Laue Lens based gamma-ray telescope proposal that is being developed by the University of Ferrara, the Istituto di Astrofisica (INAF-Bologna) and LIP. The focal plane of this instrument will be composed either by segmented or 3D CdTe detectors. Within this scope, the aim of the work herein described is to study the potential performance of a Compton spectro-imager polarimeter (not a mere dedicated polarimeter as previous proposals) in a dual plane configuration and contribute to the development of an optimized design of an ASTENA type CdTe Laue lens focal plane for polarimetric observations.

Objectives

Design, development and test of a dual plane Compton spectro-imager based on 2 CdTe pixelated sensors when used as a scattering polarimeter for high-energy astrophysics. Develop and validate a polarimeter prototype mass model simulation code based in a MEGAlib software tool. Test this new design based on two CdTe pixelated spectro-imagers operated in coincidence at the European Synchrotron Radiation Facility (ESRF) under a ~100% polarized beam. These tests allow the study and the optimisation of parameters such as the distance between the two CdTe pixelated detection layers over the 100-600 keV energy range. Furthermore, the conclusions of these tests allow to assess of the polarimetric performance of a 3D spectro-imager. Test and evaluate the potential of a CdTe pixel detector to operate as a focal plane of Laue lens system based on GaAs bent crystals at the LARge Italian X-ray (LARIX) facility, at the University of Ferrara, Italy. Study and analyse the potential effects on the operational performances of CdTe detector when exposed to the harsh orbital proton environment by testing a prototype under a 14 MeV proton beam at the Instituto de Ciências Nucleares Aplicadas à Saúde (ICNAS) cyclotron facility in Coimbra. Project future high-energy astrophysics mission proposals, based on CdTe multilayer/3D technology, optimized to perform polarimetric observations on the Compton regime.

Thesis Overview

This thesis is divided into 7 chapters:

Chapter 1 – Gamma-ray Polarimetry – introduces the thesis subject, giving an overview of the actual situation of the high-energy photon polarimetry in astronomy. First of all the polarization of gamma-rays is presented (1.1) and a brief description of various physical processes producing polarized hard gamma-ray fluxes is given (1.2). In subchapter (1.3) some of the most significative astronomical sources of polarized high-energy radiation are described. In (1.4) are described polarimetric analysis methods together with examples of the instruments used. The last section (1.5) is dedicated to the future high-energy missions, describing the scientific goals and instrument mission proposal undergoing.

Chapter 2 – Compton-POLCA Detector – describes the Compton-POLCA working principle, its design (electronic system and mechanical setup) and its development. The first part (2.1) is dedicated to the working principle of semi-conductors' detectors, specially CdTe detectors. In (2.2) a brief state of the art of polarimetry with CdTe detectors is presented. Finally, in (2.3) the design and development of the Compton-POLCA Detector is described.

Chapter 3 – Monte Carlo Simulations – is dedicated to a set of simulations using MEGAlib to access the dual polarimeter capabilities, allowing to improve and validate its mechanical design.

Chapter 4 – Experimental Measurements – is dedicated to the series of experiments performed with the Dual Plane Polarimeter. The first experiments were performed at LIP laboratory setup. Then, two campaigns, with different models of the prototype, were performed with a 100% polarized beam in the ID15 beamline of the ESRF. Finally, a series of experiments performed in the X-ray LARIX facility with a non-polarized beam is presented.

Chapter 5 – Proton Radiation Analyses on CdTe Detectors – describes a series of experiments related to proton radiation damage on CdTe Detectors.

Chapter 6 – Laue Lens – is dedicated to a series experiments with the Compton-POLCA using Laue Lens focusing optics in the X-ray LARIX facility.

Chapter 7 – Conclusion – presents the most relevant scientific and technological impacts of this these. The achievements and limitations of the studies and of the detector

developed are discussed together with suggestions of how to explore and correct them. Finally, the prospects of future work are presented.

Author's Contribution

Journal Papers

– N.Simões, J.M.Maia, R.M.Curado da Silva, S.Ghithan, P.Crespo, S.J.C.do Carmo, Francisco Alves , M.Moita, N.Auricchio, E.Caroli, "Inflight proton activation and damage on a CdTe detection plane", Nuclear Instruments and Methods in Physics Research Section A: Accelerators, Spectrometers, Detectors and Associated Equipment, vol. 877, 2018, pp. 183-191.

– M.Moita, E.Carol, J.M.Maia, R.M.Curado da Silva, N.Auricchio, J.B.Stephen, M.Páscoa, A.M.F.Trindade, "Compton polarimetry with a multi-layer CdTe focal plane prototype", Nucl. Instruments Methods Phys. Res. Sect. A Accel. Spectrometers, Detect. Assoc. Equip., vol. 918, no. October 2018, pp. 93–98, 2019.

– Marcela Páscoa, Jorge M Maia, Natalia Auricchio, Rui M Curado da Silva, Paulo Crespo, Sérgio J do Carmo, Miguel Moita, Francisco Alves, Ezio Caroli, "Orbit-like Proton Radiation Damage Analysis on CdTe Detectors," under preparation.

– M. Moita, R. M. Curado da Silva, J. M. Maia, E. Caroli, E. Virgilli, N. Auricchio, J. B. Stephen, F. Frontera, S. Del Sordo, "Polarimetric performance of a Multilayer CdTe Spectro-imager for High-energy Astrophysics," under preparation.

– E. Caroli, N. Auricchio, R. M. Curado da Silva, S. Del Sordo, C. Ferrari, J. M. Maia, M. Moita, J. B. Stephen, E. Virgilli, "Study of Bent Crystals Response for an Hard X-Ray Laue Lens with a Pixel CdTe Detector," under preparation.

International conference proceedings papers

– E. Caroli, G. De Cesare, R. M. Curado da Silva, L. Abbene, N. Auricchio, C. Budtz-Jørgensen, S. Del Sordo, P. Ferrando, J. L. Galvèz, M. Hernanz, J. Isern, I. Kuvvetli, P. Laurent, O. Limousin, J. M. Maia, M. Moita, N. Produit, J. B. Stephen A. Zappettini, "Monte Carlo evaluation of a CZT 3D spectrometer suitable for a Hard X- and soft-γ rays polarimetry balloon borne experiment," in Proceedings of 2015 IEEE NSS/MIC Conference (2016).

– Ezio Caroli, Miguel Moita, Rui M. Curado Da Silva, Stefano Del Sordo, Giovanni De Cesare, Jorge M. Maia, Marcela Páscoa, "Hard X-ray and Soft Gamma Ray Polarimetry with CdTe/CZT Spectro-Imager," Galaxies, vol. 6, no. 3, p. 69, 2018.

Oral Communications in Conferences

– M. Moita, R. M. Curado Da Silva, J. M. Maia, "CdTe Polarimetric Analysis for Future High-Energy Space Missions", *LIP PhD Students Workshop*, 24-25 March 2017, FCTUC, Coimbra, Portugal.

– M. Moita, R. M. Curado Da Silva, J. M. Maia, "Development of a Dual Plane Polarimeter for Future Gamma-ray Space Telescopes", *2nd Doctoral Congress in Engineering – Symposium on Physics Engineering – DCE 2017*, 8-9 June 2017, FEUP, Porto, Portugal.

– M. Moita, R. M. Curado Da Silva, J. M. Maia, "Development of a Dual Plane Polarimeter for Future Gamma-ray Space Telescopes", *ENAA – XXVII National Meeting of Astronomy and Astrophysics*, 20-21 July 2017, FCUL, Lisboa, Portugal.

– E. Caroli, R. M. Curado da Silva, M. Moita, N. Auricchio, S. del Sordo, J. M. Maia, J.B. Stephen, M. Páscoa, "Hard X-ray and Soft Gamma Ray Polarimetry with CdTe/CZT Spectro-imager", *Alsatian Workshop on X-ray Polarimetry*, 13-15 November 2017, University of Strasbourg, Strasbourg, France.

– M. Moita, N. Auricchio, E. Caroli, R. M. Curado da Silva, J. M. Maia, J.B. Stephen, M. Páscoa, "Multilayer Polarimetric Analysis of a CdTe Focal Plane Prototype", *2017 IEEE Nuclear Science Symposium*, 21-28 October 2017, Hyatt Regency, Atlanta, Georgia, USA.

– M. Moita, R. M. Curado Silva, J. Maia, M. Páscoa, A. Cortez, J. Escada, A. Trindade, F. P. Santos, T. Dias, A. De Angelis, "i-Astro Space Instrumentation Development Activities", *Jornadas LIP 2018*, 16-18 February 2018, Évora Hotel, Évora, Portugal.

– M. Moita, R. M. Curado da Silva, J. M. Maia, E. Caroli, E. Virgilli, N. Auricchio, J. B. Stephen, F. Frontera, S. Del Sordo, "Polarimetric performance of a Multilayer CdTe Spectro-imager for High-energy Astrophysics," *2019 IEEE Nuclear Science Symposium and Medical Imaging Conference*, 26 October-2 November 2019, Manchester Central Convention Centre, UK

Poster Communications in Scientific Meetings & Conferences

– M. Moita, R. M. Curado da Silva, J. M. Maia, N. Auricchio, E. Caroli, N. Produit, "Development of a Polarimeter for Future Gamma-Ray Space Telescopes," *XXVI National Meeting of Astronomy and Astrophysics,* 8-9 September 2016, Universiade de Aveiro, Portugal.

– M. Moita, R. M. Curado da Silva, J. M. Maia, E. Caroli, N. Auricchio, "Polarimetric performance of a multilayer CdTe spectro-imager for high-energy astrophysics," *2nd International Workshop on Soft X-ray Single-order Diffraction Grating Technology and Application*, 16-20 October 2019, Universidade de Coimbra, Portugal.

– E. Caroli, N. Auricchio, R. M. Curado da Silva, S. Del Sordo, C. Ferrari, J. M. Maia, M. Moita, J. B. Stephen, E. Virgilli, "Study of Bent Crystals Response for an Hard X-Ray Laue Lens with a Pixel CdTe Detector," *2019 IEE Nuclear Science Symposium and Medical Imaging Conference*, 26 October-2 November 2019, Manchester Central Convention Centre, UK.

1 Gamma-ray Polarimetry

In the gamma-ray domain, most of the instruments built so far provide fine sensitivity in three parameters of celestial emissions: the spectrum, the source location and the time of arrival. Several high-energy missions such as the Compton Gamma-Ray Observatory (CGRO) [39], the INTEGRAL [1] and the Fermi Gamma-ray Space Telescope [2] have already verified the richness of the gamma-ray sky and allowed to enlighten some of the underlying physical mechanisms of the observed sources. However, the polarization angle and degree are two additional parameters of source emissions that remain mostly unknown. A wide number of cosmic objects such as gamma-ray bursts, pulsars and others, are expected to emit polarized radiation [9]–[11]. Thus, these parameters can reveal more information of the emission mechanisms and therefore on the celestial bodies and the environments in which the fluxes were emitted. The measuring principle applied to measure the level of polarization of an observed photon flux depends on the energy region of interest. For instance, in the energy range of relevance of this work, from ~100 keV to ~1 MeV, the standard procedure takes advantage of the polarization dependence of Compton scattering.

1.1 General Description

Polarization is a property of electromagnetic waves that describes the orientation of the electric and magnetic fields, both, oscillating in perpendicular directions. Electromagnetic waves are solutions of Maxwell's equations in a vacuum and to satisfy all four equations, the waves must have the *E* and *B* fields transverse to the propagation direction. The orientation of the fields can be constant in time or it can rotate around a momentum axis. The former case is called linear polarization, the latter circular or elliptical polarization. The polarization of a photon can be parametrised using the Stokes parameters, the four of which form the Stokes vector [40]. The four parameters are defined as follows,

$$S_0 = E_1^2 + E_2^2 \tag{1.1}$$

$$S_1 = E_1^2 - E_2^2 \tag{1.2}$$

$$S_2 = 2\sqrt{E_1 E_2}\cos\delta \tag{1.3}$$

$$S_3 = 2\sqrt{E_1 E_2}\sin\delta \tag{1.4}$$

E_1 and E_2 are the two orthogonal components of the electric field vector and δ is the phase difference between the two. For a 100% linearly polarized photon flux ($\delta = 0$), the polarization angle is then defined by the ratio between E_1 and E_2. When ($\sin\delta = 1$) the flux is circularly polarized and when ($0 < \sin\delta < 1$) the polarization is elliptical. In spite some developments concerning circular polarization detectors for astrophysics have been performed [41], [42], only linear polarization can be measured using current gamma-ray polarimetry techniques. Therefore, circular and elliptical polarization will not be considered in this thesis and linear polarization will from here on simply be referred to as polarization.

The polarization degree as discussed in this thesis refers to the polarization of the photon flux, defined as the relative number of photons polarized in the same direction within a given photon flux. A non-polarized or unpolarized flux consists of a population of photons with a randomly distributed electric field vector orientation, whereas a 100% polarized photon flux refers to a population within which all photons have the same polarization angle. In this section the most important physical processes involved in the production of polarized gamma-rays will be introduced.

1.2 Emission Mechanisms

There are several mechanisms that generate polarized gamma radiation. These mechanisms are mainly non-thermal, and are often associated with extreme events, such as the extreme magnetic field environments present in many astronomical sources. Some of the processes leading to polarized gamma-rays are described in this section, namely: cyclotron emission, synchrotron emission, curvature radiation, bremsstrahlung radiation, Compton scattering, and magnetic photon splitting [9].

1.2.1 Compton Scattering

In the Compton scattering process, an incoming photon is scattered off an electron which can be considered at rest. There are two instances of interest: the first is the general case of Compton scattering, which a high-energy photon collides with an electron; the second case involves the scattering of low-energy photons off relativistic electrons and is known as inverse Compton scattering. For the determination of the polarization properties of Compton and inverse Compton scattering, it is sufficient to consider only Compton scattering, as from the theory of special relativity the interaction can always be transformed into the rest frame of the electron.

The differential cross section for the process is given by the Klein-Nishina formula [43], that in the non-polarized case is,

$$\frac{d\sigma_U}{d\Omega} = \frac{r_0^2}{2}\left(\frac{E'}{E}\right)^2\left[\frac{E'}{E} + \frac{E}{E'} - 2sin^2\theta\right] \tag{1.5}$$

where r_0 is the classical electron radius. E and E', are the energies of the incoming and scattered photons, respectively, and θ is the scattering angle. E, E' and θ are related by the following equation:

$$E' = \frac{E}{1+\varepsilon(\,1-\cos\theta\,)} \tag{1.6}$$

where ε is the energy of the incident photon in units of electron rest energy, $\varepsilon = E / (m_e c^2)$, with $m_e c^2$ being the electron rest energy. For a 100% polarized beam, the differential cross section is no longer isotropic, but depends on the angle of polarization. Section 1.4.1 presents the application of this dependency for measuring gamma-ray polarization. The

degree of linear polarization of the scattered photon, for the non-polarized, U, and polarized case, P, is respectively given by,

$$\Pi_U = \frac{sin^2\,\theta}{\frac{E}{E'} + \frac{E'}{E} - 2\,sin^2\,\theta} \tag{1.7}$$

$$\Pi_P = 2\frac{1 - sin^2\theta\,cos^2\varphi}{\frac{E}{E'} + \frac{E'}{E} - 2\,sin^2\theta\,cos^2\varphi} \tag{1.8}$$

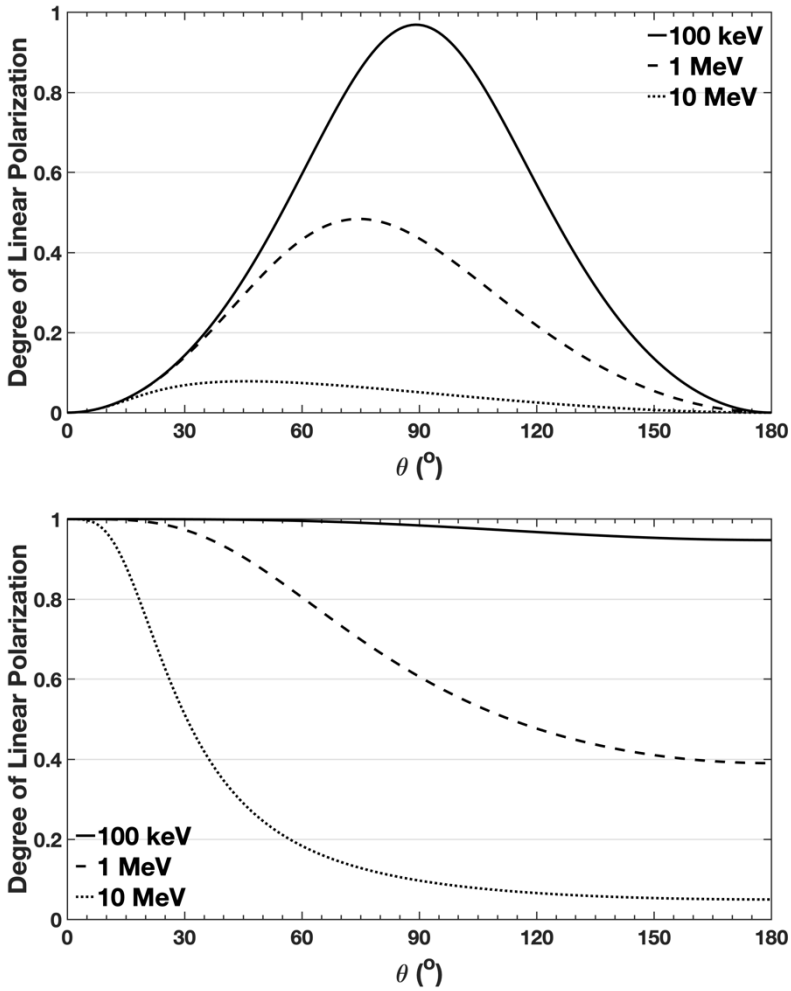

Figure 1.1: Top: the degree of linear polarization of the scattered photons created by a unpolarized incident beam. Bottom: the degree of linear polarization of the scattered photons, at ϕ = 90°, created by a 100% polarized incident beam.

The solutions for equations 1.7 and 1.8 are illustrated in figure 1.1. The figure shows the degree of linear polarization of the scattered photon as function of the scattering angle, θ, for several energies, for the unpolarized and 100% polarized cases. For the unpolarized case, if the incident photons have energies ~100 keV, the degree of linear polarization of the scattered photon can theoretically reach almost 100% for photons scattered at 90°. However, for photons with higher energies, ~1 MeV, the polarization of the scattered photon becomes residual. For the 100% polarized case the degree of polarization of the scattered photon will not suffer much changes for incident photons of ~100 keV. This is no longer true for higher energies, where the degree of polarization decreases drastically with the scattering angle. In summary, Compton scattering can change drastically the polarization signature of the incident photon beam polarization: in the case of polarized beam, the scattered photon can have a lower degree of polarization; or for a unpolarized beam a higher degree of polarization [9].

1.2.2 Bremsstrahlung

Bremsstrahlung is the emission of photons from charged particles accelerated in the electric fields of ions. The emitted energy is inversely proportional to the mass of the particle, most radiation therefore originates from electrons or positrons. However, for certain systems with high densities of protons, like the Sun, the bremsstrahlung component originating from protons can become significant.

The bremsstrahlung process occurs naturally in hot gases and in cosmic ray induced air showers in the Earth's atmosphere. In the presence of a magnetic field or in case of a constant flow direction of the emitting particles the photon flux will be polarized. If the emitting medium is optically transparent in some degree at the photon energy of interest the radiation can be detected by an observer. Polarization degrees as high as 80% are predicted for this process [9].

1.2.3 Cyclotron Emission

Non-relativistic charged particles accelerated in a magnetic field emit cyclotron radiation [9]. As in the case of bremsstrahlung the emitted energy is inversely proportional to the mass of the emitting particle, therefore cyclotron radiation is most significant when

emitted by electrons and positrons. The distribution of the photon emission is characterized by dipole shape with a maximum pointed along the electron momentum vector, this is illustrated in figure 1.2. Most of the photons are therefore emitted in the direction perpendicular to the electron acceleration vector. The polarization vector of the emitted photons will align in the plane spanned by the acceleration and momentum vector of the electrons. The result is that the polarization degree varies with the viewing angle of the observer. The maximum polarization degree will be observed when looking at the source from a direction perpendicular to the magnetic field.

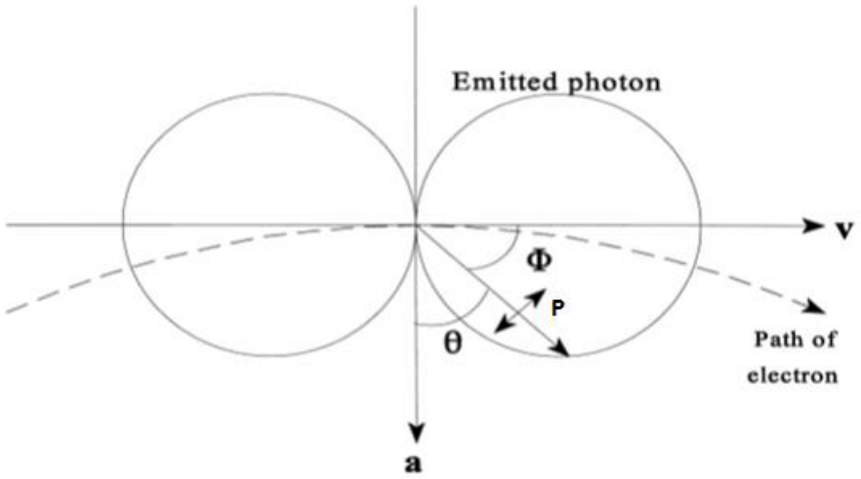

Figure 1.2: Polar diagram showing the dipole radiation emitted by an accelerated electron.

1.2.4 Synchrotron Radiation

The synchrotron emission is the relativistic limit of the magneto-Bremsstrahlung radiation. Due to the relativistic velocities of the emitting particles, the angular distribution of photon emission is beamed in the forward direction for this process, resulting in an emission profile as shown in figure 1.3. The energy of the photon emission here is higher than for cyclotron emission which generally does not exceed 100 keV. The energy spectrum is correlated to that of the electrons which, for many astrophysical sources, can be approximated by a power law, resulting in a power law function for the photons. The polarization degree, Π, of the photons can then be correlated to the electron power law index κ with [9]:

$$\Pi = \frac{\kappa + 1}{\kappa + 7/3} \tag{1.9}$$

For electron power law spectra with $\kappa = 4$, Π can be as high as 80%.

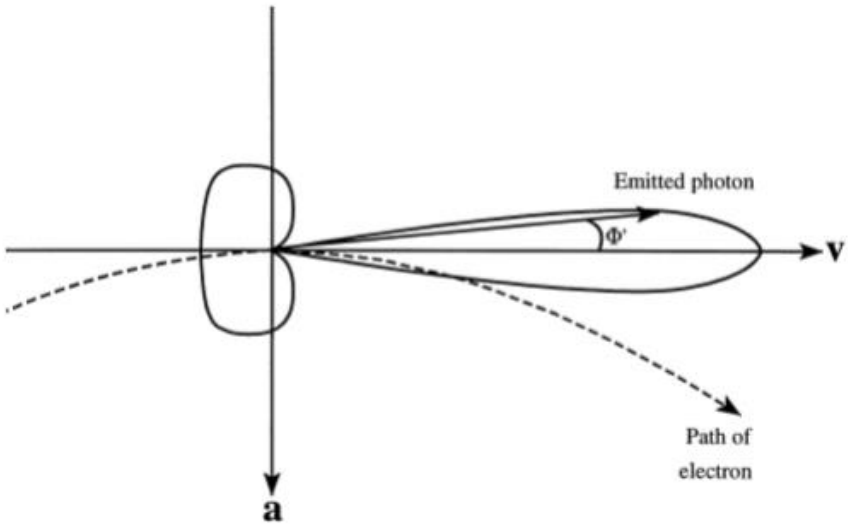

Figure 1.3: Diagram showing the dipole profile emitted by an electron accelerated in the direction a for the case of synchrotron radiation. The emitted photons are polarized in a direction within the plane spanned by the momentum and acceleration vector of the electron.

1.2.5 Curvature Radiation

Curvature radiation is the kind of synchrotron radiation emitted in a curved magnetic field. The power emitted in this case is greater than from standard synchrotron radiation. The polarization characteristics are similar, except that the polarization vector will be now parallel to the local magnetic field, instead of perpendicular as in the case of synchrotron radiation [9].

1.3 Astronomical Polarized Gamma-Ray Sources

Almost all emission mechanisms that lead to the creation of gamma-rays will generate polarized emissions independently of any particular source geometries or physical conditions [9]. Thus, numerous gamma-ray emitting astronomical objects are expected to be sources of polarized emission. Polarimetric observations can provide a unique insight into astronomical objects where several models may fit the observed data equally well. By successfully identifying the correct emission mechanism, many models may be selected and novel information can be obtained about the emission regions. Some of the sources are permanently present in the sky (persistent sources), while others appear only during a short time period suddenly disappearing afterwards (transient sources). We present here a brief description of some examples.

1.3.1 Gamma-Ray Bursts

GRBs are the most extreme explosive events in the Universe. The initial prompt phase lasts typically less than 100 s and may release energy emissions of about $\sim 10^{51}$ ergs. GRBs have spectra that typically peak in the 50-300 keV range, are isotropically distributed on the sky, and have durations from <1 s to 100 s [44]. Long-duration bursts (>2 s) are more likely associated with the death of massive stars [45]–[47], whereas short-duration bursts (<2 s) are more likely associated with the merger of compact star binaries (neutron star-neutron star, neutron star-black hole, etc.) [48] accompanied by a gravitational wave signal [49]. Regardless of the progenitor, a generic fireball shock model [50]–[52] suggests that a relativistic jet is launched from the centre of the explosion. The internal dissipation within the fireball (e.g., via internal shocks or internal magnetic dissipation processes) leads to emission in the X-ray and gamma-ray band, corresponding to the observed GRB prompt emission. Eventually, the outflow is decelerated by the circumburst medium that leads to a long-lasting forward shock, producing well-studied afterglow emissions at longer wavelengths. For reviews on GRBs, see e.g. [45], [53].

It is widely believed that precise measurements of the polarization properties of GRBs should provide crucial information to understand the phenomes beyond these events. Initial measurements derived from gamma-ray missions not specifically designed for polarimetry suggest that prompt GRB emission is polarized at levels between 30 and 100% [13], [17], [54]–[60] and that the polarization angle varies during a burst [60]. More recent

measurements based on Compton events in the CZTI instrument on the ASTROSAT mission [61], [62] and from the POLAR instrument on the Tiangong-2 space laboratory [63][47] have provided additional data. The POLAR data suggest lower polarization levels than some earlier measurements and also provides evidence of variable polarization levels during a GRB. With such a wide range of results, most of limited significance, a consistent picture of GRB polarization [64] remains elusive. High-sensitivity polarization measurements will be required to substantially advance our understanding of GRBs. Furthermore, one of the GRBs detected by POLAR, GRB 70114A, was examined using jointly-observed data from POLAR and Fermi to determine its spectral and polarization properties and seek to understand the associated emission processes [65]. The results hint at a synchrotron origin of the emission but further observations of GRBs are required to verify these evolutionary trends and develop a time-resolved polarization model for the prompt emission of GRBs, as the current models are not predictive enough to enable a full modelling of the observed data.

The recently observation of two simultaneous signatures, a gravitational wave and GRB, emitted by a neutron star merger, has opened a new knowledge window [49]. Joint gravitational-wave and electromagnetic observations are key to obtain a more complete knowledge of these sources and their environments, since they provide complementary information. From one side, gravitational wave signals provide information about the physics of the source such as, e.g., the mass and the distance; on the other hand, the identification of the possible electromagnetic counterpart pinpoints the location of the burst, possibly identifying the host galaxy and properly defining the astro-physical context.

1.3.2 Pulsars

Pulsars radiate a short periodic pulse, and hence are considered to be neutron stars spinning with a high speed. A neutron star has a strong magnetic field of about 10^{12} G. Because, generally, the magnetic axis aligns with the rotation axis, the emission near the magnetic poles sweeps around the rotation axis. Since the emission region of the pulsar rotating around the axis is observed from Earth, we see it like a light house. Among the thousand pulsars observed so far, the emission of MeV gamma-rays were observed only from several of them.

The Crab pulsar, one of the most famous pulsars, has a nebula around it. It is a typical example of a young, rapidly spinning, strongly magnetized neutron star that generates broad-band electromagnetic radiation by accelerating charged particles to near light speeds in its magnetosphere [66]. The hard X-ray and gamma-ray emission is explained by synchrotron radiation and, at higher energies, via inverse Compton scattering. Details of this emission process so far remain poorly understood. Polarization measurements in gamma-rays, particularly as a function of pulse phase, is thought to be a key element necessary to unravel the mystery of pulsar radiation [67]–[69]. The Crab pulsar is the only pulsar to have been detected in polarized gamma-rays [19], [20], [70], [71]. However, the first measurements made by INTEGRAL have not been sensitive enough to adequately reveal the variation of polarization characteristics across the pulse [19]. More recently, the CZTI, made the most sensitive measurement to date of polarized gamma-ray emission from the Crab pulsar and nebula in the 100-380 keV band [26], confirming with high significance the earlier indication [19], [20] of a strongly polarized off-pulse emission. However, it also found a variation in polarization properties within the off-pulse region. In addition, it revealed a swing of the polarization angle across the pulse peaks. This behaviour cannot be fully explained by the existing theoretical models of high-energy emission from pulsars [26].

1.3.3 Binary Black Holes

Binary black hole is a binary system with a black hole and a companion star, where an accretion disk is created because the matter from the companion star flows onto the black hole (figure 1.4). This accretion disk radiates photons in wide band including X-rays and gamma-rays. One of the most well-studied black hole binary is the Cygnus-X1, which is formed by the super-giant 09-B0 with a mass between 20 and 30 solar masses and a black hole candidate measured to be 7-13 solar masses. The spectra from Cygnus-X1 can be distinguished between two spectral states, the hard (low) and soft (high) state. Most of the time is spent in the hard state, transitions to the soft state happen once every several years, when the system typically remains in the soft state for several weeks or months. The standard explanation for the high-energy emission is the inverse Compton scattering of disk photons by hot (∼100 keV) thermal electrons in the inner region of the accretion

flow and its reflection component at the disk, where some degree of polarization is expected.

Two Cygnus-X1 polarimetric measurements were performed: the first with the IBIS instruments [24] with high levels of uncertainties due to the non-optimization of the instrument for polarimetric measurements; more recently the balloon experiment POGO+ made new measurements which allowed to constrain the theorical models, however future observations of other binary black hole are required to generalize the picture and the detailed physics of the accretion that are still under discussion [72].

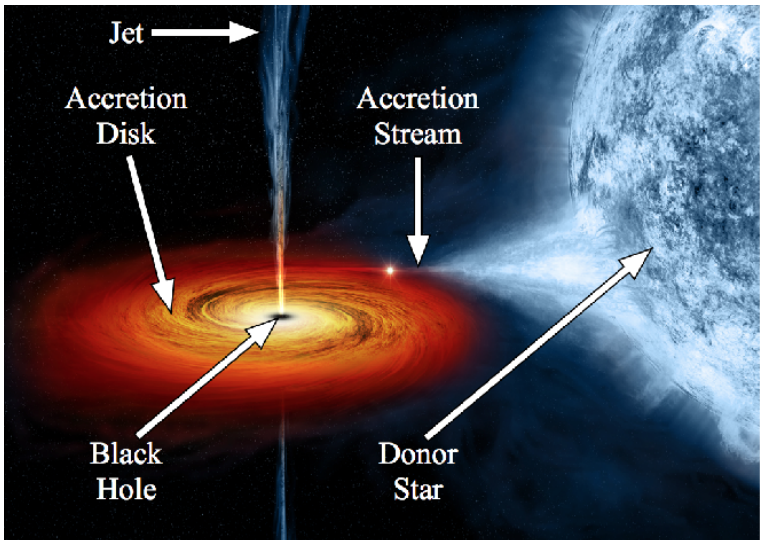

Figure 1.4: Anatomy of a black hole X-ray binary [73].

1.3.4 Solar Flares

Solar flares are explosions in the atmosphere of the Sun, which occur when a large amount of magnetic energy is suddenly released. The largest flares can release up to 10^{32} ergs and last from some minutes to more than 3 hours [9]. The emitted photon energies can go from radio to gamma-rays.

Most of hard X-rays are emitted from the foot points of the flare, as shown in figure 1.5. This region consists of a relatively high-pressure plasma in which bremsstrahlung occurs, thus, some degree of polarization is expected.

The only attempt to measure the polarization of a Solar flare was performed by RHESSI which showed a relatively low level of polarization [74], [75]. Among other reasons the fact that this instrument was not designed as a polarimeter contributed to a

relatively low certainty in the measurement results, leaving room for improvement using a dedicated polarimeter.

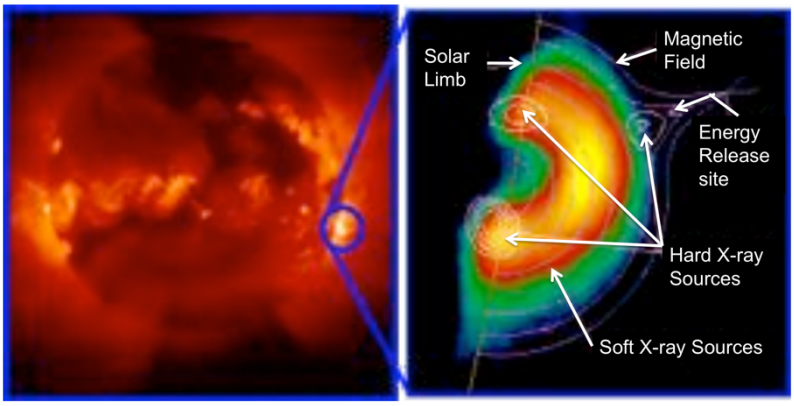

Figure 1.5: On the left an image of the Sun as taken by the Yohkoh Soft X-ray Telescope. On the right a more detailed image of the flare is shown as seen by the Hard X-ray Telescope (HXT). Reproduced from [76].

1.3.5 Active Galactic Nuclei

AGNs are the most luminous persistent sources in the Universe. Located at the centre of active galaxies, AGNs are supermassive black holes that accrete material emitting most of its energy as optical and ultraviolet radiation but emitting as well in the high-energy band. Figure 2.6 shows the schematic view of the unified model of an AGN. Radio and optical band observation indicate that many AGN have relativistic jet outflows. The AGNs dominated by relativistic jets pointing in the observer direction are commonly known as blazars. Blazars are characterized by a non-thermal spectral energy distribution, where two broad components exhibit. The low-energy component ranges from radio to UV, or even X-rays, and the high-energy component starts in X-ray band up to TeV or even higher energies.

It is expected that the low-energy component is due to the synchrotron radiation of the relativistic electrons. Indeed, measurements in the radio and optical bands showed a polarization level of a few percent up to as much as 40%. The high-energy component is construed to be typically associated with inverse-Compton scattering of low-energy photons (leptonic models), although the origin of the seed photons is less well understood. The polarization measurement would be the key to constrain the models.

Furthermore, the recent detection of a neutrino event coincident with a gamma-ray flare in the blazar TXS 0506+056 [77] opens the window of multi-messenger analysis, leading the possibility that relativistic blazar jets be a source of gamma-rays, neutrinos and cosmic rays. Observations across the electromagnetic spectrum are crucial to identify and characterize the sources of neutrinos and cosmic rays. The MeV band is particularly relevant because the MeV flux is the best proxy for the neutrino flux, as GeV-TeV gamma-rays may be opaque within the source and at large distances due to attenuation. Polarization signals in the MeV band can distinguish between blazar emission models [78].

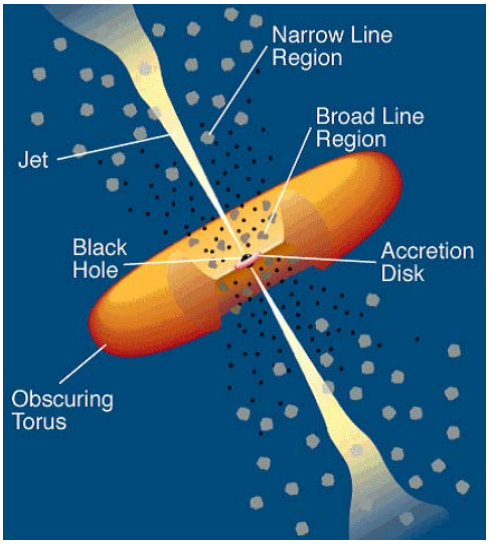

Figure 1.6: The schematic view of AGN [79].

1.4 Polarimetry Techniques

The three different mechanisms responsible for interactions between detector materials and photons in the X-/gamma-ray energy regime are : photoelectric absorption, Compton scattering, and pair production [80], [81]. All these processes lead to the partial or complete transfer of the gamma-ray photon energy to electrons energy. They result in sudden and abrupt changes in the gamma-ray photon history, either the photon either disappears entirely or is scattered through a certain angle. The relevance of such interaction mechanism is a function of the photon energy, depending also on the atomic number

(Z) of the detecting medium, as depicted in figure 1.7. For energies up to ~10 keV (depending on the detector material), the photoelectric effect dominates whereas in the high-energy gamma-ray regime, at energies exceeding twice the electron mass, pair production is the main interaction mechanism. Compton scattering, which below ~10 keV becomes Thomson scattering, dominates between these two regimes.

The physics of these interactions allows to determinate the level and angle of polarization. The selection of the detection techniques applied to determine the polarization parameters is strongly related with the photon energies involved. The spectro-imaging detectors such as the ones i-Astro LIP group are developing in Coimbra, are optimized for energies between 100 keV-1 MeV, thus, relaying mostly on the fundamental physics of the Compton scattering process for linearly polarized photons.

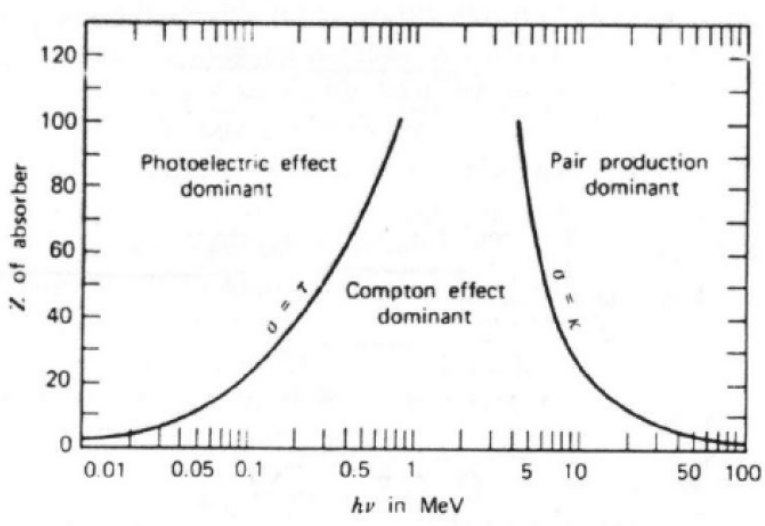

Figure 1.7: Relevance of the different interaction mechanisms as a function of the photon energy and atomic number (Z) of the detecting medium [82].

1.4.1 Compton Scattering Polarimetry

The polarimetric parameters of a high-energy source can be measured by the fundamental concepts that are associated with polarized Compton interactions. As shown in section 1.2.1 the differential cross section for a 100% polarized beam depends on the orientation of the electric vector of the incident photons. In this case, the Klein-Nishina differential cross-section for a free electron at rest becomes [43],

$$\frac{d\sigma_P}{d\Omega} = \frac{r_0^2}{2}\left(\frac{E'}{E}\right)^2\left[\frac{E'}{E}+\frac{E}{E'}-2sin^2\theta\, cos^2\varphi\right] \tag{1.10}$$

Figure 1.8 shows a schematic of the Compton process that will be used as reference for the whole document. We define φ as the azimuthal angle of each individual photon with respect to the photon polarization vector, $\vec{P}$, and ϕ, the azimuthal angle measured with respect to the detector x axis. For both of these angles we use the term *azimuthal angle* during the document. The term *scattering angle* is used to describe the angle θ.

It can be seen from equation 1.10 that the cross-section will be at a maximum for those photons scattered at right angles to the direction of the electric vector of the incident photon. This will lead to an asymmetry in the number of photons scattered in directions parallel and orthogonal to the electric vector of a beam of photons incident on some scattering medium as represented in figure 1.9. The asymmetry of this distribution is dependent on the photon energy, scattering angle and the intrinsic parameters of the polarimeter, such as geometry and energy threshold.

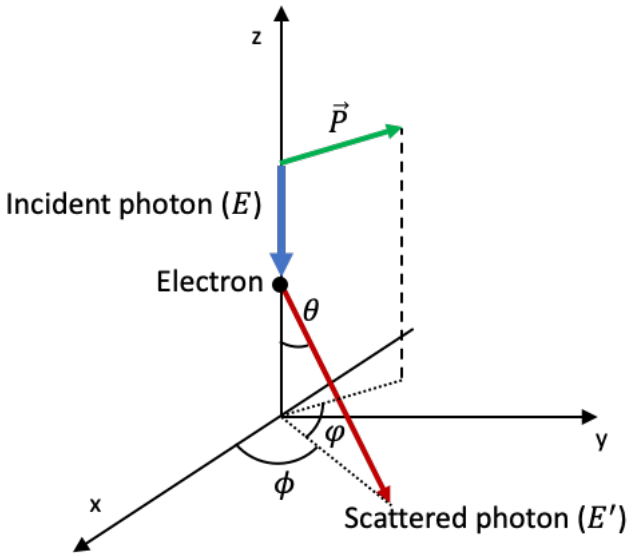

Figure 1.8: Schematic of the Compton Process. The incoming photon (blue; energy E, polarization $\vec{P}$) scatters off a free electron deviating (red; energy E') by a scattering angle θ from its original trajectory. φ is the azimuthal angle of each individual photon with respect to the photon polarization vector. ϕ, is the azimuthal angle measured with respect to the detector x axis.

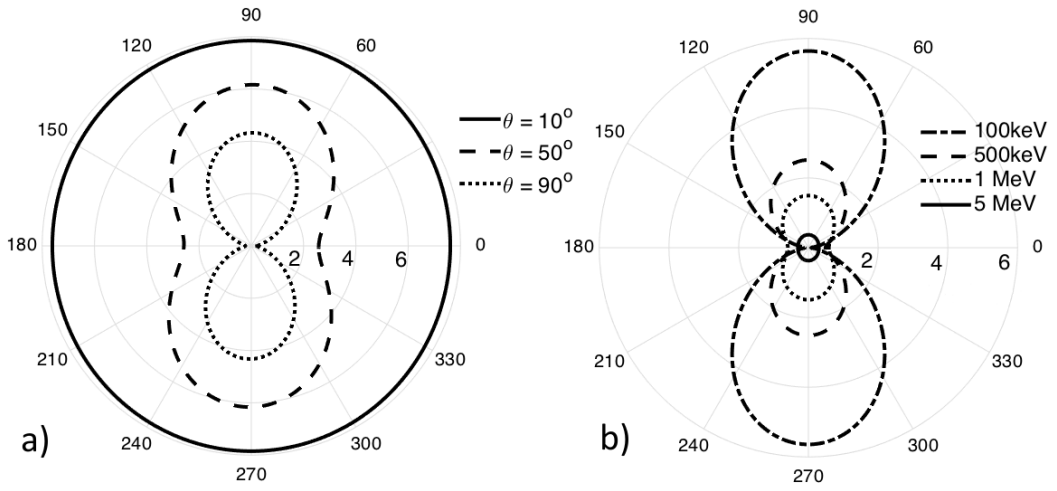

Figure 1.9: Polar plots of the angular distribution in the azimuthal angle for 100% linearly polarized beams undergoing Compton scattering. a) fixed energy at 200 keV; b) fixed scattering angle $\theta = 90°$. The direction of the polarization is parallel to the horizontal axis of the polar plot. The units for both plots are arbitrary.

The polarimetric performance of an instrument is evaluated by calculating the polarimetric modulation factor, Q, that gives an evaluation of the amplitude between the maximum and the minimum of the azimuthal distribution, which comes for $\varphi = 90°$ and $\varphi = 0°$ respectively, and is given by [83],

$$Q(\varepsilon, \theta) = \frac{d\sigma(\varepsilon, \theta, \varphi = 90°) - d\sigma(\varepsilon, \theta, \varphi = 0°)}{d\sigma(\varepsilon, \theta, \varphi = 90°) + d\sigma(\varepsilon, \theta, \varphi = 0°)} = \frac{sin^2\,\theta}{\varepsilon + \varepsilon^{-1} - sin^2\,\theta} \tag{1.11}$$

In this thesis we want to evaluate the performance of a dual plane polarimeter as the one schematized in figure 1.10. Here, the photons are scattered in the top detector, depositing part of their energy there, and then, are absorbed by the bottom detection. The allowed scattering angles are then defined by a hollow cone limited by θ_{min} and θ_{max}. Changing the distance between the two planes different ranges of θ_{min} and θ_{max} can be achieved. For this case equation 1.11 becomes,

$$Q(\varepsilon, \theta_{min}, \theta_{max}) = \frac{d\sigma(\varepsilon, \varphi = 90°, \theta_{min}, \theta_{max}) - d\sigma(\varepsilon, \varphi = 0°, \theta_{min}, \theta_{max})}{d\sigma(\varepsilon, \varphi = 90°, \theta_{min}, \theta_{max}) + d\sigma(\varepsilon, \varphi = 0°, \theta_{min}, \theta_{max})} \tag{1.12}$$

where $d\sigma(\varepsilon, \varphi, \theta_{min}, \theta_{max})$ is the cross sections integrated over the range of θ values that can be derived using equations 1.10 and 1.6,

$$d\sigma(\varepsilon, \varphi, \theta_{min}, \theta_{max}) =$$

$$= \int_{\theta_{min}}^{\theta_{max}} \left(\frac{1}{1+\varepsilon(1-\cos\theta)} + \frac{1}{[1+\varepsilon(1-\cos\theta)]^3} - \frac{2\sin^2\theta\cos^2\varphi}{[1+\varepsilon(1-\cos\theta)]^2} \right) \sin\theta \, d\theta \tag{1.13}$$

In figure 1.11 is represented the modulation factor as a function of θ_{min} and θ_{max} for 300 keV photons calculated using equations 1.12 and 1.13. The modulation factor increases with θ_{min} and θ_{max} and the highest modulation is obtained when θ_{min} and θ_{max} have values ~90°. This is the case of a thin single plane detector. For our prototype, the values of θ_{min} and θ_{max} depends on the size of the detectors and the distance between them. The latest parameter can be adjusted therefore we evaluated the modulation factor for different values of θ_{min} and θ_{max}.

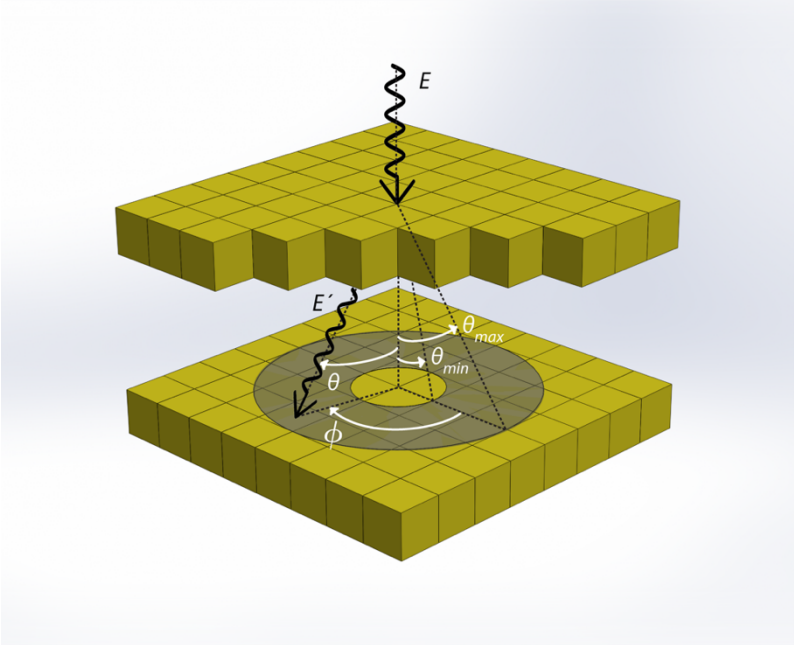

Figure 1.10: Layout of a 2-layer polarimeter. Polarization of photons is measured by selecting those events which are scattered by the top detection plane and subsequently absorbed by the bottom detector. The accepted events have to be scattered in the hollow cone defined by θ_{min} and θ_{max}.

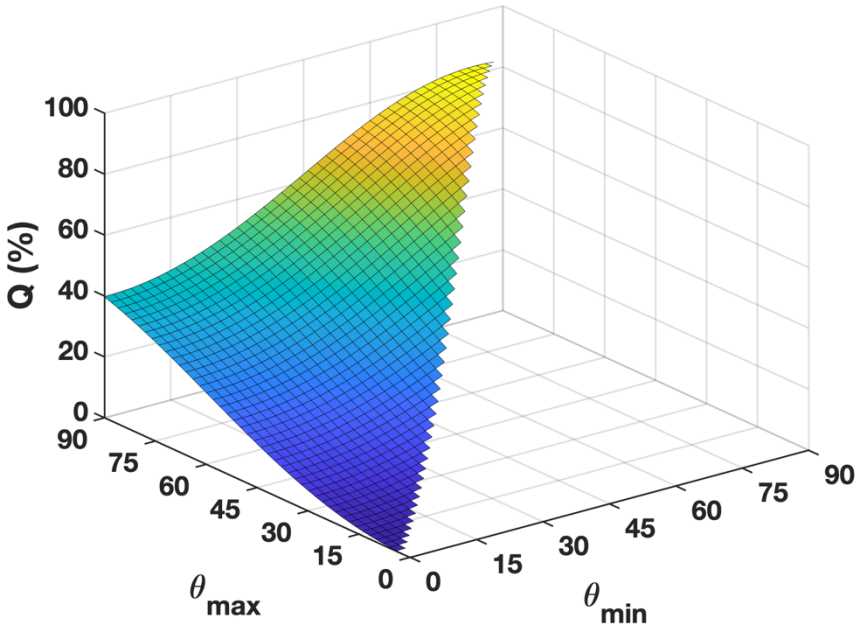

Figure 1.11: Modulation factor as a function of maximum and minimum scattering angles θ_{min} and θ_{max} for a two-layer configuration, as in figure 1.10. The energy of the incident photons is 300 keV.

For the case of a pixelated detector, the modulation factor, Q, can be calculated from the double-event angular distribution around a central irradiated pixel:

$$Q = \frac{N_{//} - N_{\perp}}{N_{//} + N_{\perp}} \tag{1.14}$$

where $N_{//}$ and $N_{\perp}$ are the number of double-events integrated over the two orthogonal directions defined on the detector plane along the maxima and minima of the scattered event distribution [83]. A higher value of Q means that the instrument responds to polarized radiation with a larger modulation and the effect of statistical fluctuations is, in proportion, lower.

In practice, the Q of an $n \times n$ pixels' spectrometer used as polarimeter is calculated by a two-step procedure. The first step is to create the so-called scattering maps of the recorded Compton events. For each Compton event we use the first hit as a reference for the second one, placing it in the centre of an $2n-1 \times 2n-1$ array. The second hit is then placed in the cell that corresponds to the event azimuthal angle, ϕ. At the end, each scattering map cell counts the number of Compton events that have the same azimuthal angle, what-

ever the photon incidence point is. Therefore, the scattering map provides a direct representation of how the detector see the azimuthal dependence of the Compton scattering for polarized photons. In this step an eventually event selection criteria can be performed (e.g., range of scattering angles, θ_{min} and θ_{max}, scattering distance range, energy window, etc.) and the modulation factor is calculated using equation 1.14. The second step is the construction of the modulation curve, i.e., the curve that provides the number of scattered counts as a function of the azimuthal angle. The modulation curve presents the form shown in figure 1.12. Since from a polarized flux the largest number of photons should be scattered at $\varphi \sim 90°$, the minimum of the modulation curve constructed with ϕ corresponds to the most frequent orientation of the photon's polarization vectors, i.e., the polarization angle of the incoming flux, as exemplified in figure 1.12.

The modulation curve is built dividing the scattering map on a fixed number of angular sectors to cover 360° and integrating the counts inside each angular sector. The aperture of the angular sectors should be chosen taking into account the discretization level of the detector (i.e., the pixel dimensions) and the double counts statistics. Because of the segmented nature of the detector, the integration of count inside a defined angular sector should take into account effects due to pixels that lie across their borders. Methods to account for these pixels are, for example, that of distributing the pixel counts proportionally to the area of the pixel intercepted by two adjacent angular sectors. This division can be simply analytic or performed by means of a uniform random distribution of the counts, or still being determined using a Monte Carlo simulation on a realistic model of the detector [9], [84].

At the end, the modulation curve obtained for a given event selection, can be fitted with the following function:

$$N(\phi) = a_0 \left(1 + a_1 \cos\left(2\phi - a_2 + \pi/2\right)\right) \tag{1.15}$$

where a_0, a_1 and a_2 are the fitting parameters. The polarization angle ($P = a_2$) of the incoming flux corresponds to the phase of the modulation curve fit.

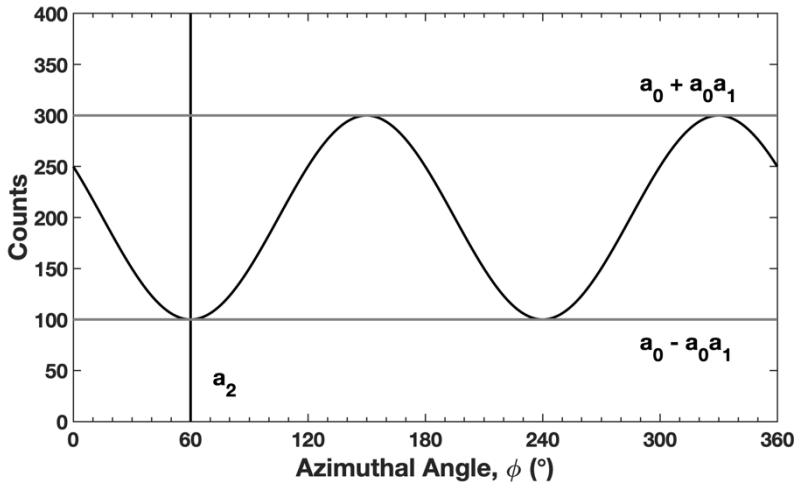

Figure 1.12: The solid line represents the ideal modulation curve pattern from the Compton scattering of polarized photons. a_0, a_1 and a_2 are the fitting parameters of equation 1.15. The modulation curves shown represent those that would be seen by a continuous detector with infinitesimal spatial resolution.

To determine the degree of linear polarization of an incoming flux, whose polarization degree is unknow, it is necessary to perform the analysis with a 100% polarized dataset. This analysis serves as a calibration of the polarimeter and provides the expected Q factor for 100% polarized incident photons, Q_{100}. The degree of linear polarization Π is then given by,

$$\Pi = \frac{Q}{Q_{100}} \tag{1.16}$$

For a given polarimeter, another parameter is of fundamental importance to quantify its final performance, once implemented in a particular instrument: the Minimum Detectable polarization (MDP). MDP gives a measure of the confidence that polarization is detected: if the reconstructed polarization fraction is equal to MDP, then there is only a 1% probability that it is resulting from statistical fluctuations of an unpolarized flux. The expected MDP should be significantly smaller than the degree of polarization to be measured. For a space polarimeter in a background noise environment, the following relation estimates the MDP at the 99% confidence level [85]:

$$\mathrm{MDP} = \frac{4.29}{A \cdot \varepsilon \cdot S_F \cdot Q_{100}} \sqrt{\frac{A \cdot \varepsilon \cdot S_F + B}{\Delta T}} \tag{1.17}$$

where Q_{100} is the modulation factor for a 100% polarized source, ε the double event detection efficiency, A the polarimeter detection area in cm^2, S_F the source flux (photons/s/cm^2), B is the background count rate (counts/s), and ΔT the observation time in seconds.

1.4.2 On-Ground Calibrations

The modulation response of a space polarimeter can be complex since it depends on the energy spectrum and the orientation of the source with respect to the instrument line of sight. A fine method to access the polarimeter measurement potential is the Monte-Carlo simulation of its performances, which need to be benchmarked beforehand with on-ground calibrations. An uncontrolled systematic error in the instrument response can result in polarization signal contaminated by systematic errors, even if the incoming radiation is not polarized. On-ground calibration must therefore be performed with both polarized and non-polarized photon beams.

Compton polarimeters can be calibrated on ground with radioactive sources used in particular setups. A first calibration method is based on the partial linear polarization generated by an unpolarized gamma-ray beam after Compton scattering [9], [86]–[88]. A drawback of this technique is that the efficiency is very low (most of the photons will not scatter in the direction that we want).

Polarized photon beams (up to ~99%) can also be produced as synchrotron radiation, e.g. at the ESRF. This has been the main method that we have been used to evaluate the performance of our detectors. A series of experiments based on a CdTe pixel detector prototypes has been carried out at the ESRF with the main objective to assess the performance of a CdTe focal plane as a spectro-imager polarimeter up to 750 keV [89]–[96]. Two calibration campaigns were also carried out with the POLAR satellite before the flight at the ESRF [28]–[30]. However, an issue with calibrations at accelerator facilities is that they usually deliver very fine pencil beams, whereas the full measurement of a space polarimeter response requires a broad beam source covering a large fraction of (if

not all) the instrument. A way to simulate uniform irradiation is to place the polarimeter on a motorized table designed to provide a scan of the instrument during irradiation [30].

Another method, which was used by the POLAR collaboration [28], [29], is based on the correlated polarization of the two 511 keV photons emitted back-to-back in the annihilation of a positron and an electron. The measurement can be done with a ^{22}Na positron source placed at the centre of the setup. Then, one of the 511 keV photon from the source is detected in the polarimeter to calibrate, while the other is detected in coincidence by a relatively simple Compton polarimeter of known modulation response.

To perform measurements with unpolarized sources the most common technique is using a radioactive source by using a simple laboratory setup and irradiate the detector plane with a radioactive source. This method has the disadvantage that these sources have a limited number of energy lines, conditioning the measurements to those energies. They are also difficult to collimate; thus, only full surface measurements are possible. The POLAR collaboration generated an unpolarized source with the 100% polarized beam at the ESRF by adding offline two data sets of events with orthogonal polarization, uniform illumination of the detector and equal number of events. Those two sets of data present perpendicular directions of polarization, and the sum of both is equivalent to a 0% polarization signal [28]–[30], [97]. In this thesis we irradiate the detector with a hard X-ray generator with an energy pass-band from a few keV to about 300 keV, at the LARIX facility located in the Scientific-Technological Pole of the University of Ferrara. The emission of the hard X-ray generator is fully unpolarized.

1.4.3 Astronomical Compton Polarimeters

Only a limited number of successful polarization measurements have been performed in space, in the gamma-ray energy regime. The main reason is the combined complexity of both the measurement itself and the environment in which the measurements have to be performed. The absorption of gamma-rays by the atmosphere requires measurements to be made either at high altitudes using balloons, or above the atmosphere using satellites. These constrain the mechanics and the mass of the payload which combined with the high background and the low signal detection efficiency make measurements challenging. Nevertheless, several polarimeters based on the Compton scattering process were already capable to perform polarimetric measurement in space context. Typically,

two types of detectors have been used measure the interaction points: scintillator and semiconductor detectors. In the former one, the detection is made indirectly, shifting the wavelength of the incident radiation to visible or ultra-violet photons before the collection with photomultiplier tubes. In the latter, the radiation is measured directly through the collection of the product of interaction arisen in their mediums, i.e. the charge pairs deposited.

High-altitude balloon experiments (~40 km) have long provided an ideal platform for gamma-ray instrument development, sometimes leading to subsequent space missions. In many cases balloon experiments are themselves designed to provide significant scientific capability. Although there are many advantages for balloon payloads (most notably, larger mass and power budgets), there are also many challenges. The most significant of those challenges are the atmospheric absorption and scattering, and the limited exposure that is offered by the short duration of flights (typically up to a few days) of current ballooning technology. There have been several balloon programs dedicated to polarimetry or as one of the primary goals, being the most relevant: the Compton Spectrometer and Imager (COSI) [98]–[101] launched on May 16, 2016 and lasting 46 days, performed polarimetric analyses one intense GRB (GRB 160530A) [102], [103] ; the Polarized Gamma-ray Observer (PoGO) program which conducted two balloon flights, the PoGO-Lite Pathfinder [104]–[106] launched in 2013 and the PoGO+ launched in 2016. Polarization results from the Crab pulsar [107] and the Cygnus X-1 microquasar [72] have been reported.

Satellite experiments have the big advantage of reducing the atmospheric absorption and increase the time exposures, however, it presents greater expenses and risks. The first attempts to measure the polarization from astronomical high-energy sources with satellite experiments were made by: the Burst And Transient Source Experiment (BATSE) [108] instrument onboard CGRO, which detected evidence of polarization in the prompt gamma-ray emission from GRB930131 and GRB960924 [58]; and the Ramaty High-Energy Solar Spectroscopic Imager (RHESSI) [109], measured the polarization of the prompt gamma-ray emission from GRB21206 [54], [56] and from solar flares [74], [75]. These instruments are however primarily designed for spectroscopy, timing and imaging, and were never calibrated before flight with polarized and unpolarized sources. As a result their polarization measurements have large systematic and statistical errors and their results are now considered unreliable by the scientific community [56], [57].

The INTEGRAL Soft Gamma-Ray Imager (IBIS) [110], [111], was the first instrument capable to perform a reliable polarization measurement in space from the Crab pulsar and nebula [19]–[23], from the gamma-ray emission of the black hole binary system Cygnus X-1 [24], [25] and from the prompt emission of three GRBs, GRB140206A, GRB061122 and GRB041219A [12]–[16]; furthermore, the Spectrometer on INTEGRAL (SPI) [112], [113] reported polarization measurements from the prompt emission of GRB 041219 and GRB061122 [15], [17] and from the black hole binary system Cygnus X-1 [18].

Later, two dedicated polarimeters were launched to space: the Gamma-ray bursts Polarimeter (GAP) [114], a dedicated large field of view Compton polarimeter on-board of the small solar power sail demonstrator "IKAROS" flown in 2011 [115], which performed polarization measurements for three bright GRBs [60], [116]; and the POLAR instrument [117], launched on September 2016 and placed on the Chinese space station Tiangong 2, detected a total of 55 GRBs, five of which, were selected perform detailed analysis of their polarization properties [63].

Two more instruments were able to perform polarimetric analyses: the Soft Gamma-ray Detector (SGD) on-board the Japanese satellite Hitomi, placed in a low Earth orbit (LEO) on February 2016 [118], [119], performed polarimetric measurements from the Crab pulsar and nebula [120].; and the CZTI on-board the ASTROSAT, an Indian satellite designed to make multi-waveband observations of astronomical sources launched in September 2015 [121], [122], detected a total of 47 GRBs, among which eleven were bright enough to compute their polarization signature [61], furthermore it measured the polarization signature of the Crab pulsar and nebula [26]. These two instruments are examples of CdTe based spectro-imagers that were able to perform detailed polarimetric measurements after a series of polarimetric calibrations and test on-ground.

The four last missions will be briefly described in the next section due to their importance in the high-energies polarimetry field. They provided an insight of the technological state of the art of the instruments and calibration procedures. Therefore, we will briefly describe the instruments, the mission objectives, the calibration procedures and the results obtained.

1.4.3.1 GAP

The GAP experiment is a Japanese Compton polarimeter aboard the IKAROS solar sail launched in May 21st 2010. The main propose of the IKAROS mission was to evaluate the performance of the solar sails in the interplanetary space. IKAROS has an extremely thin 7.5 µm polyimide membrane with 20 m diameter. Reflecting the photons from the sun, this sail translates solar radiation pressure to the thrust of the spacecraft [123].

The GAP [114], [124], mounted on the bottom panel of IKAROS (pointing in the antisolar direction), is fully designed to measure a degree of linear polarization in the prompt emission of GRBs in the energy range of 70-300 keV. Due to its position, GAP always observed the deep universe during the cruising phase of IKAROS. The instrument is composed of an assembly of two coaxial detectors, one made with a plastic scintillator and the other with caesium iodide (CsI) crystals. The central plastic works as the Compton scatterer, and the angular distribution of scattered photons coinciding with the plastic scintillator is measured by the surrounding CsI scintillators, see figure 1.13.

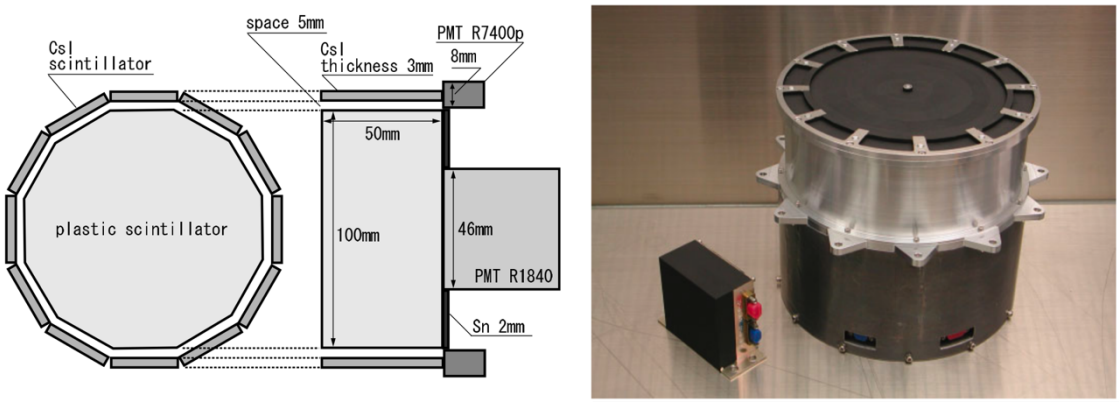

Figure 1.13: Left: A schematic view of the GRB polarimeter. A central dodecagonal plastic scintillator works as gamma-ray scatterer, and the angular distribution of scattered photon is measured by the surrounding 12 CsI scintillators [114]. Right: Photo of GAP-S and its power unit (GAP-P) [124].

To estimate the capability of GAP and verify the model parameters before the flight a series of Monte Carlo simulations were performed with GEANT4 and a ground-based calibration using the GAP proto-flight model (PFM) was carried out at KEK Photon Factory (beam line PF-14A). The experiment used a monochromatic 80 keV pencil beam of

0.8 mm diameter and 82% polarization allowing to calculate the modulation factor and detection efficiency for these conditions. The observed distributions of coincidence photons of the 12 CsI units are shown in figure 1.14 together with the Monte Carlo simulations [124].

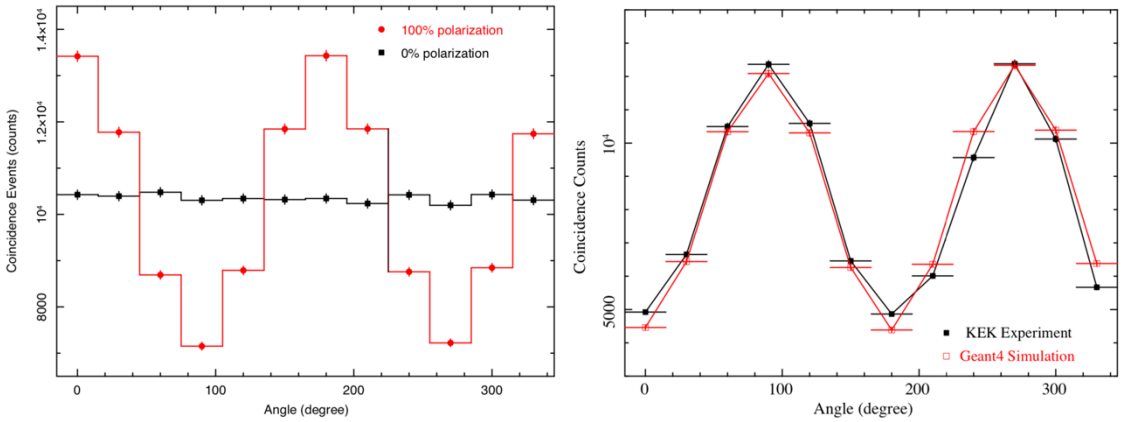

Figure 1.14: Left: Modulation curve for a monochromatic gamma-ray beam of 100 keV, 100% polarization (filled circle) and non-polarization (filled square) obtained from Monte Carlo Simulations. Right: The modulation curves for the monochromatic 80 keV with 82% polarized X-ray beam measured by the experiment at KEK Photon Factory (red points), and the result by Geant-4 simulation in the same condition [124].

The most relevant result of the GAP was the observation of the GRB100826A in 2010 [60]. The data was analysed in the 70-300 keV energy band and divided in two intervals to avoid the weak polarization degree caused by the polarization angle changes during the entire burst duration, figure 1.15. The polarization angle was observed to vary by ~90° during the prompt emission, which can be interpreted as evidence for patchy emission, patchy magnetic field, or as photospheric emission from a variable jet. The combined fit for the two intervals, assuming that the polarization degree is the same for both intervals, reveals a polarization degree of Π = 27±11% with 99.4% (2.9 σ) confidence level [60].

According to the Japan Aerospace Exploration Agency (JAXA), IKAROS finished all planned experiments in December 2010, but the instrument continued to work beyond that date. The mission entered in hibernation in 2012, and the GAP observations stopped, due to lack of power from the solar panels.

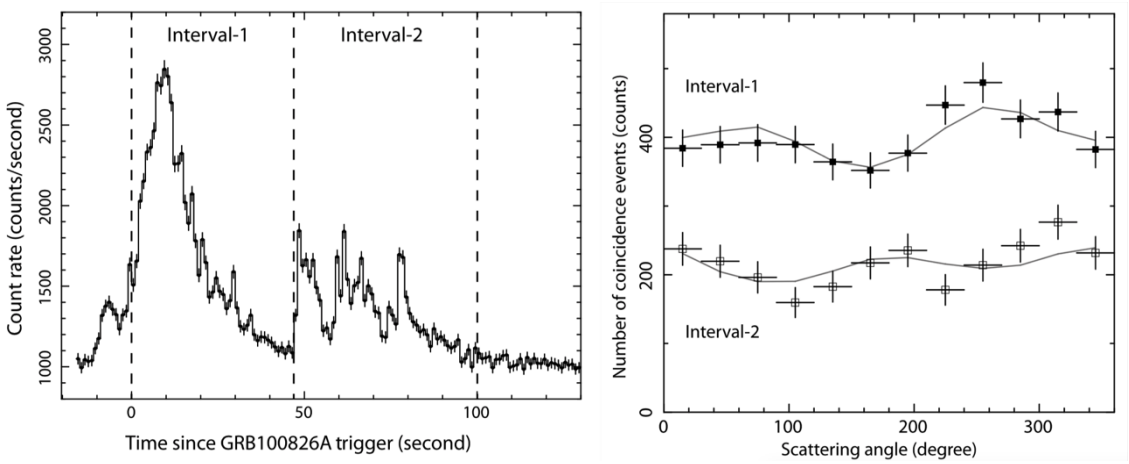

Figure 1.15: Left: Lightcurve of the prompt gamma-ray emission of GRB100826A detected by the GAP. The data was divided into Interval 1 and 2 for the polarization analysis. Right: Polarized signal observed with GAP from GRB100826A in the 70-300 keV energy range [60].

1.4.3.2 POLAR

POLAR is a Swiss/Chinese mission dedicated to GRB polarization measurements. It has been launched on September 15th, 2016 and placed on the Chinese space station Tiangong 2. The POLAR detector design consists in 25 independent modular units, each one with 64 (8×8) plastic scintillator bars with dimensions 6×6×200 mm^3 each (figure 1.16). Each unit is read-out by a flat panel multi-anode photomultiplier tube mechanically coupled to the bottom of the scintillator bars via a thin transparent optical pad, and enclosed in a 1 mm carbon fiber socket. The electrical signals coming from the photomultiplier are first processed by an Application Specific Integrated Circuits (ASIC) and Field Programmable Gate Array (FPGA) at the front-end electronics, then sent to the POLAR central computer, where the trigger decision is taken depending on the outputs of all modular units. This modular design provides a good mechanical stability and enables the interchange of modules during the testing phase of the detector [28]–[30], [97], [117], [125], [126].

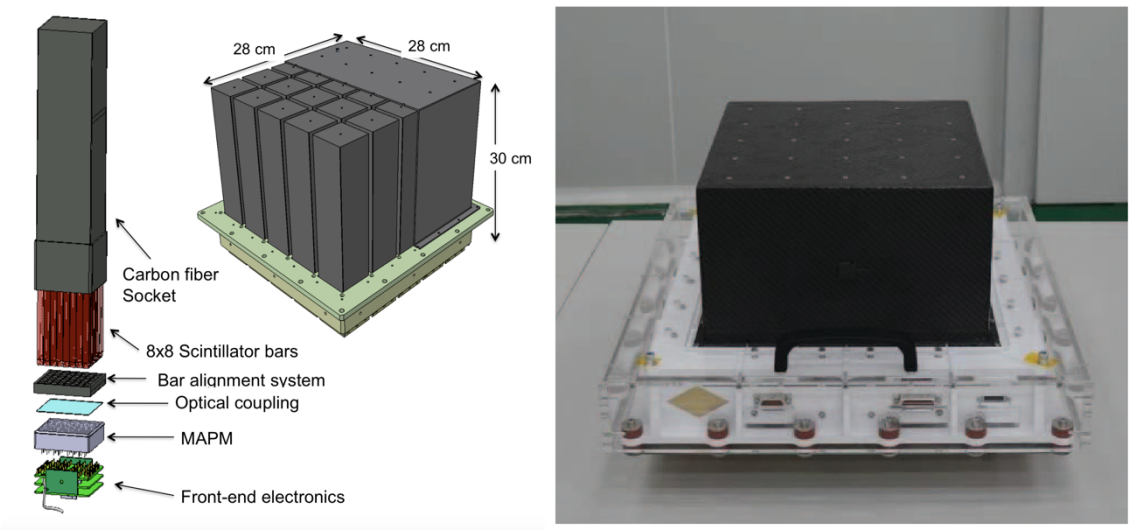

Figure 1.16: Left: Schematic overview of one single POLAR module together with the full 5x5 module instrument [28]. The full flight ready POLAR instrument [125].

An exhaustive series of Monte Carlo simulations and tests with polarized and unpolarized beams were performed before the flight in order to calibrate the polarimeter, leading to several versions of the complete POLAR detector. The firsts polarimetric measurements were made with a qualification model (QM), which consisted in one module of the POLAR instrument. The model was tested in laboratory with partially polarized radioactive sources and at the ESRF beam line ID15A, with a 100% polarized synchrotron radiation source [28], [29]. The flight model (FM) was then fully calibrated again using a 100% polarized beam at the beam line ID11 at ESRF. Unpolarized samples were produced by adding the modulation curves from two orthogonal polarization directions [30]. Using the GEANT4 package, a complete model of the POLAR set-up was also constructed to provide a high reliable simulation of its properties and performance. The fidelity of the model and residual systematic were demonstrated using data from the ESRF calibration of the FM [30]. As an example, figure 1.17 shows the modulation curves obtained for 110 keV both polarized and unpolarized (the last formed using the data from two measured different polarization angles). Figure 1.17 c) presents the corrected modulation obtained by dividing the measured polarized modulation curves for 110 keV by the measured unpolarized modulation curve instrument performance and simulation of the POLAR detector [30].

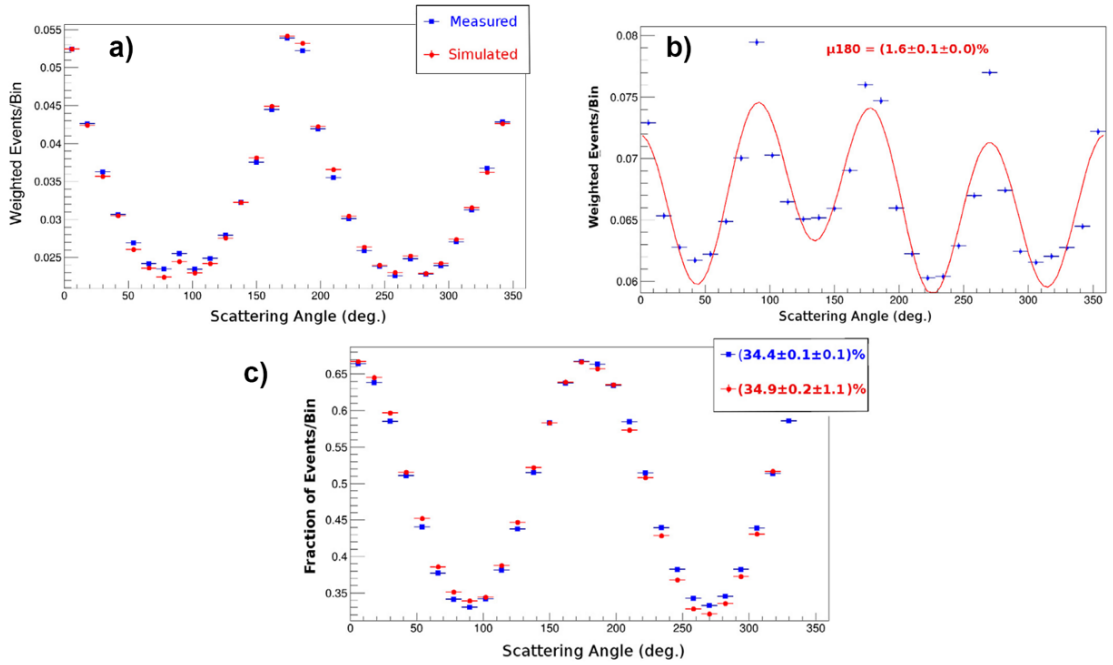

Figure 1.17: a) The measured polarized modulation curves (square) using the full POLAR instrument, together with the simulated results (circles). b) Unpolarized modulation curve formed using the data from two measured different polarization angles. c) The measured polarized modulation curves for 110 keV divided by the measured unpolarized modulation curve (square) and the measured polarization curves divided by the simulated unpolarized sample (circle) for the full instrument [30].

POLAR was able to measure the light curves of 55 GRB's till its shut down in 31 March 2017 due to a failure in its power distribution unit [63]. To make statistically significant GRB polarization measurements with negligible systematic errors, a subsample of five GRBs were selected for detailed analysis of their polarization properties [63]. A summary of the proprieties of the five GRBs analysed is presented in table 1.1, figure 1.18 presents the obtained modulation curves of GRB 170101A and GRB 170114A. Data time resolved analysis were performed because of possible polarization degree changes during the burst period, as suggested by GAP analysis. A detailed mass model was also designed and for each GRB, a range of simulations were performed using information for several instruments. The results indicate with high precision that the prompt gamma-ray emission of GRBs is not highly polarized, as some models have predicted. Furthermore, the results favour a low polarization level and can reject the hypothesis that all GRBs are unpolarized, while several individual GRB polarization levels are still found to be consistent with zero polarization. Further evidence for low but non-zero polarization degree values was found when performing time-dependent analysis.

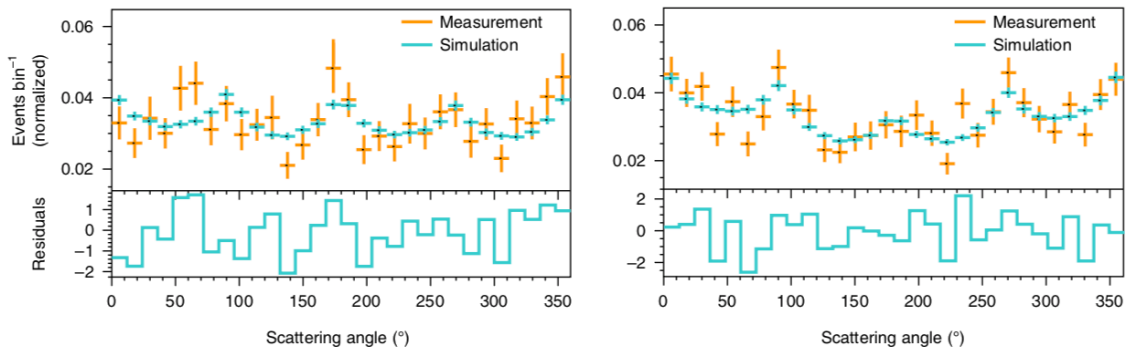

Figure 1.18: Measured and best-fitting simulated modulation curves for GRB 170101A on left and GRB 170114A on the right. Orange crosses are the measured modulation curves normalized to have a total bin content of unity, after subtracting the background. The blue crosses are the Monte Carlo-produced modulation curves best fitting the measured data. The blue histograms below are the fitting residuals [63].

Table 1.1: Summary of the five GRBs analysed by POLAR. The different properties of the five GRBs and two time bins of GRB 170114A are included. In units of erg cm^{-2} in the 10-1000 keV energy range. NA, not applicable; PA, polarization angle; PD, polarization degree [63].

GRB	T_{90} (s)	Fluence	PD	PA (°)	PA change
161218A	6.76	1.25×10^{-5}	9%	40	No
170101A	2.82	1.27×10^{-5}	8%	16.4	No
170127C	0.21	7.4×10^{-6}	11%	38	Unknow
170206A	1.2	1.34×10^{-5}	10%	106	No
170114A	8.0	1.93×10^{-5}	4%	164	Yes
170114Ap1	NA	NA	15%	122	NA
170114Ap2	NA	NA	0.49%	17	NA

1.4.3.3 Hitomi

Hitomi, also known as ASTRO-H, was a Japanese satellite with the objective of observe the sky in the field of X-rays and low energy gamma-rays. It carried four instruments operating in a band of energy ranging from 0.3 keV to 600 keV [118]. One of the instruments was a Compton telescope, which acted as a Compton polarimeter in the 5-600 keV range: the Soft Gamma-ray Detector (SGD). The SGD consist in two identical sets of detectors placed on opposite sides of the spacecraft each one consisting in a 3×1 array of identical Compton cameras (figure 1.19a)). Each Compton camera consists of a

stack of 32 layers of 0.6 mm thick Si pixel sensors followed by 8 layers of 0.75 mm thick CdTe pixel sensors, surrounded by 2 layers of 0.75 mm thick CdTe pixel sensors on the four sides as shown in figure 1.19 b). The hybrid design of the Compton camera module allows to use the Si sensors as scatterer, since Compton scattering is the dominant process in Si above ~50 keV compared with ~300 keV for CdTe. The CdTe sensors are used as the absorber of the gamma-ray following the Compton scattering in the Si sensors [119], [127]–[132].

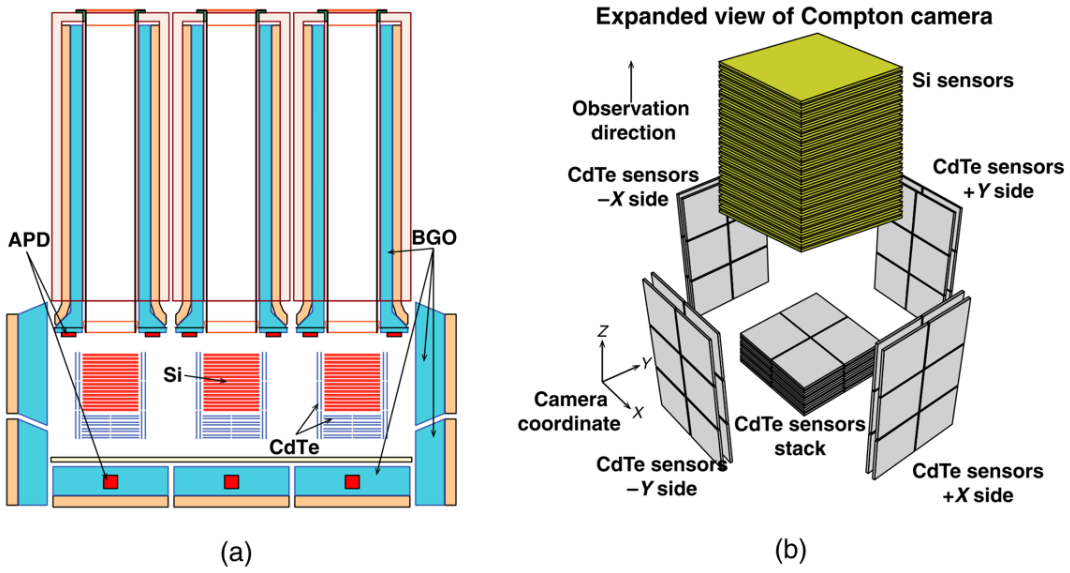

Figure 1.19: Schematic module of a) set of detectors with an array of 3×1 Compton camera modules b) expanded view of sensor configuration of a Compton camera [119].

The SGD Compton camera took 15 years to be developed, being optimized to detect gamma-rays up to 600 keV. Two polarimetric measurements campaigns were performed using highly polarized (≥99%) gamma-rays at the SPring-81 synchrotron radiation facility. In the first campaign it was evaluated the polarimetric performance of an early prototype for the SGD Compton camera [133] . The final model of a SGD Compton camera was then calibrated before the flight, as well as a Monte Carlo simulation with detailed mass model was performed [134]. Figure 1.20 shows the modulation curve obtained from a 122.2 keV beam. The 100% polarized beam data was corrected with simulated unpolarized data.

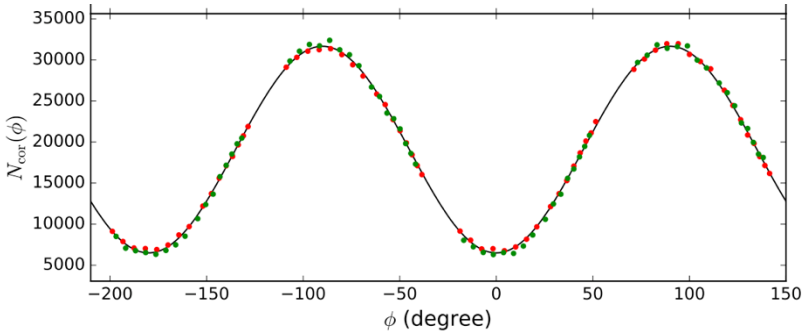

Figure 1.20: Modulation curve obtained from a 122.2 keV beam at the SPring-81 synchrotron radiation facility. The polarized data obtained experimentally was corrected with unpolarized data from Monte Carlo simulations [134].

The satellite was placed in a LEO on February 17th, 2016 and on March 26th an attitude error occurred and the Hitomi switched to survival mode. JAXA ceased efforts to recover satellite in 28th April and declared the mission lost. Just before the satellite failure, it performed 5200 seconds of observations in the Crab nebula and allowed the SGD to detect clearly the Crab polarization between 60 and 160 keV. The analysis has been done through deep analysis of Crab and background data, and comparison with Monte Carlo simulations. The obtained polarization fraction of the phase-integrated Crab emission (sum of pulsar and nebula emissions) is 22.1% ± 10.6%, and the polarization angle is 110.7° ± 13°. The polarization angle measured by SGD is consistent with the projected spin axis of the pulsar (124°) [120].

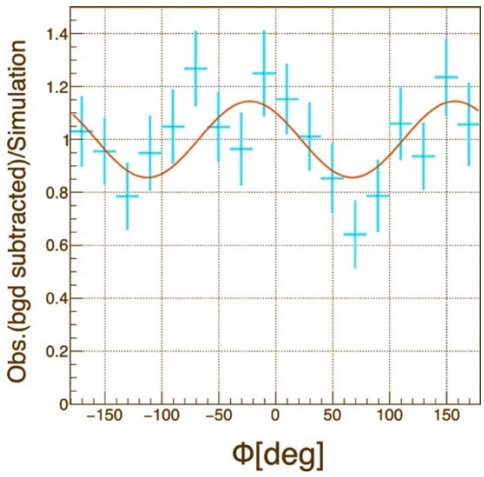

Figure 1.21: Modulation curve obtained with SGD during the Crab observation. The data points show the ratio of the background-subtracted observation data to the unpolarized simulation data [120].

1.4.3.4 ASTROSAT

ASTROSAT is an Indian satellite designed to perform multi-waveband observations of astronomical sources. The five instruments on board cover the visible (320-530 nm), near UV (180-300 nm), far UV (130-180 nm), soft X-ray (0.3-8 keV and 2-10 keV) and hard X-ray (3-80 keV and 10-150 keV) regions of the electromagnetic spectrum [135], [136]. It has been launched on 2015 September 28 on a LEO by a PSLV Indian rocket. All instruments are operating successfully since then [135], [137].

One of its instruments, the Cadmium Zinc Telluride Imager (CZTI) is a coded mask telescope composed with a 1000 cm^2 array of CZT detectors. The CZTI works as a spectroscopic instrument with a coded mask imaging capability in the energy range of 20-150 keV [122], [138]. As shown in figure 1.22 the instrument is divided in four quadrants in a 4×4 matrix, each one consisting in a 16×16 pixel array, of 5 mm thick CZT. In figure 1.22 is shown an exploded view of CZTI to show all the components and a picture of the fully assembled CZTI before being integrated with the spacecraft [121], [122].

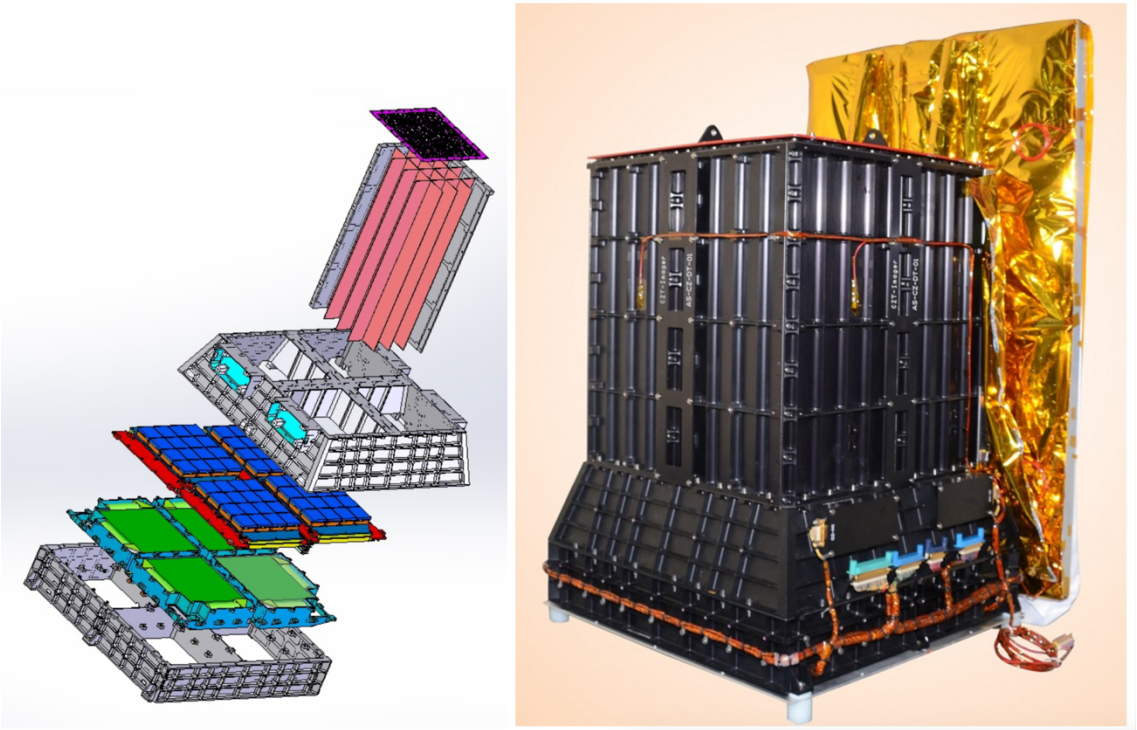

Figure 1.22: Exploded view of CZTI on left and a picture of the fully assembled CZTI before being integrated with the spacecraft.

During its ground calibrations the instrument was calibrated for polarimetric measurements showing to possess significant polarization measurement capability in 100-300 keV. The instrument was calibrated using a partially polarized beam of X-rays, produced by scattering 356 keV gamma-rays from the radioactive source ^{133}Ba at ~90 degrees. Figure 1.23 shows the modulation curves obtained for partially polarized X-rays from ^{133}Ba source at two polarization angles, 0° and 45°. It also shows curve obtained for unpolarized X-rays emitted directly from the ^{133}Ba source and the modulation curves obtained from the GEANT4 simulations [31], [32].

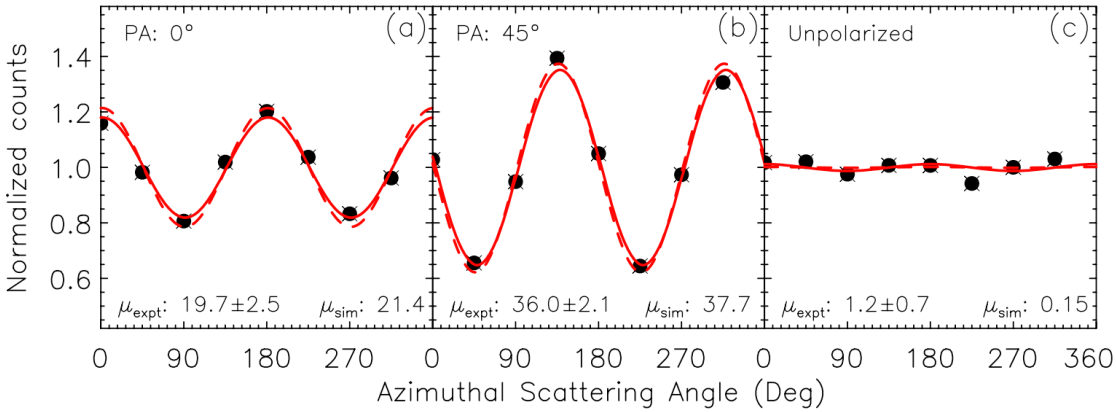

Figure 1.23: a) and b) Experimentally measured modulation curves for partially polarized X-rays from ^{133}Ba source at two polarization angles, 0° and 45° respectively. c) The same curve measured for unpolarized X-rays from ^{133}Ba. The dashed line shows the modulation curves obtained from the GEANT4 simulations of the experimental setup.

In the first one year of operation (2015 October 6 to 2016 October 5), CZTI has detected a total of 47 GRBs, among which eleven were bright enough to compute their polarization signature [61]. One example, GRB160821A, where a strong polarization fraction has been measured and is shown in figure 1.24. Most of the studied GRBs were highly polarized, implying most probably emissions with origin in synchrotron radiation in a uniform magnetic field.

In 2016-2017, the CZTI team also measured the polarization signature of the Crab pulsar and nebula resulting in the most precise determination of the pulsar and nebula polarization properties. Time-resolved analysis revealed a strong polarization fraction in the off-pulse region, associated with a shift of the polarization angle. Also, the polarization angle seems to shift along the rise and the decay of the pulsar's pulses (figure 1.25),

which cannot be fully explained by the current theoretical models of high-energy emission from pulsars [26].

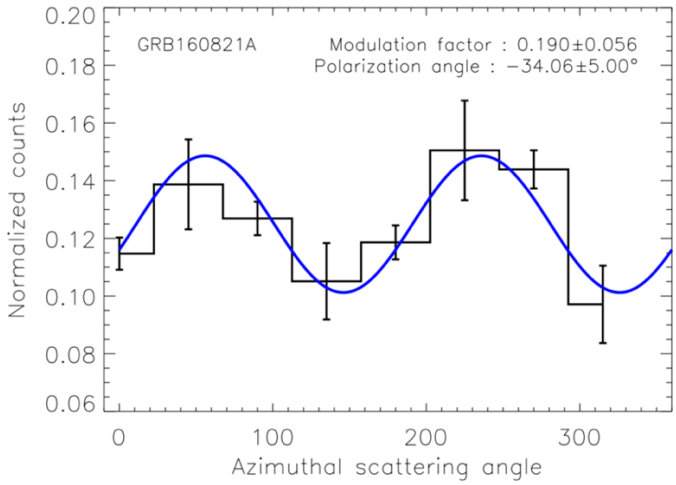

Figure 1.24: Modulation curve for GRB 160821A. The data are corrected from CZTI non-uniformity effects. The blue solid line is the sinusoidal fit to the data. From [61].

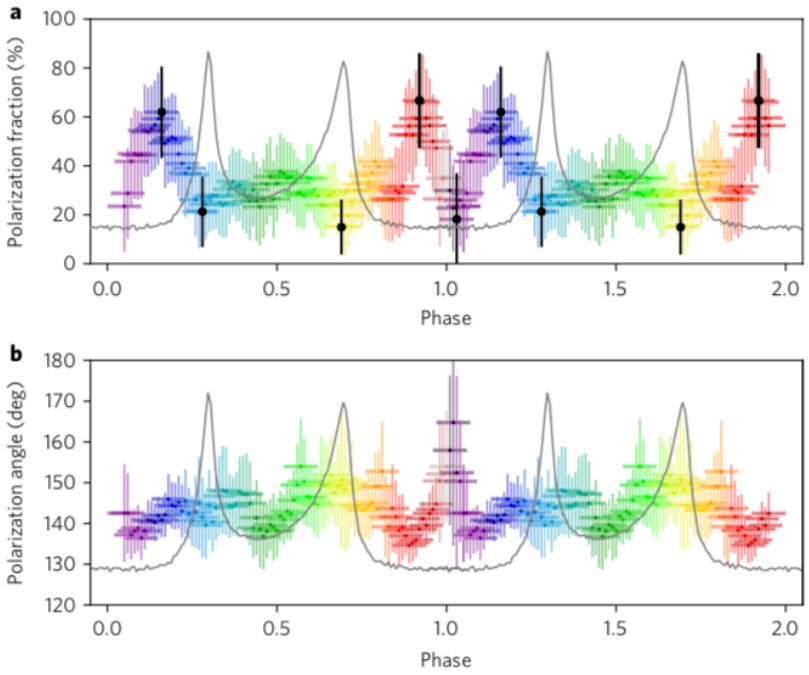

Figure 1.25: Phase resolved polarimetry of the Crab pulsar and nebula. We see the evolution over the pulsar's phase of the polarization angle and fraction (from [26]).

1.5 Future missions

Improvements on the high-energy instruments' performance have differed between energy bands. In the hard X- ray/low-energy gamma-ray (E~10-100 keV) the Nuclear Spectroscopic Telescope Array (NuSTAR) have been covering the sky with good sensitivity since 2012 [139]. In the high-energy gamma-ray (E>100 MeV) bands the pair-creation telescope aboard Fermi [2] is the main responsible for creating an inventory of over 3000 steady sources of high-energy gamma-rays [140]. The low-and medium-energy gamma-ray domains (E~0.1-100 MeV) have so far not experienced a comparable development. This energy band have been covered by instruments such as; the imaging Compton Telescope (COMPTEL) [141], on-board of the CGRO [141]; the IBIS [110]; and the SPI [112]. However, the sensitivity of these instruments is far from the ones achieved in the other energy domains (figure 1.26). This has not resulted from a paucity of interesting science, but from technology constraints that have limited advances in detection sensitivity. New technologies are now under study to build an affordable instrument that goes well beyond the sensitivity of the INTEGRAL satellite or the COMPTEL telescope.

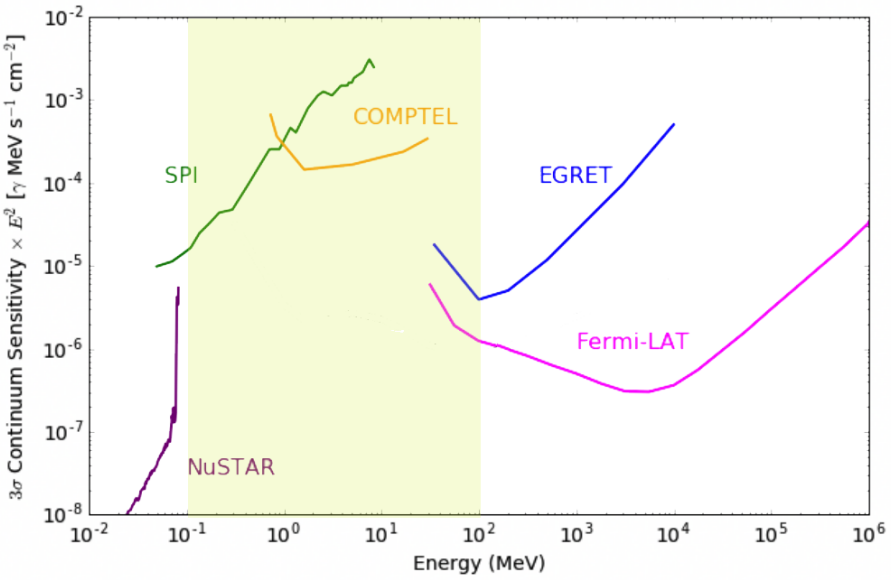

Figure 1.26: Point source continuum differential sensitivity of different X- and gamma-ray instruments. Adapted from [142].

1.5.1 Scientific Goals

A future mission in the high-energy astronomy with a wide field of view and broad energy range can provide break-through capabilities in three areas of MeV astrophysics: capability in time-domain and multimessenger astrophysics with excellent synergies with observations at other wavelengths; polarization capability that can probe conditions and processes in astrophysical jets and in the magnetospheres and winds of compact objects; and nuclear line spectroscopy that brings a new insight into the topical area of element formation in dynamic environments.

There are many scientific goals in the recent high-energy mission proposals. In fact, a series of white papers were submitted in the Decadal Survey on Astronomy and Astrophysics (Astro2020), a partnership between the National Academies and the astronomical community to identify key priorities in astronomy and astrophysics, showing the importance of an mission that covers this energy band with improved time, spatial, spectral and polarimetric capabilities [78], [143], [152]–[156], [144]–[151].

One of the most promising field that could provide unprecedent information to understand the physical processes of many astronomical sources is the multimessenger astronomy. Three historic events in astronomy demonstrated the importance of coordinated multimessenger and multiwavelength follow-ups of multimessenger sources: a core-collapse supernova explosion, SN 1987A which approximately two to three hours before the visible light from SN 1987A reached Earth was observed a burst of neutrinos by three observatories [7]; a gamma-ray burst from the neutron star merger detected by the Fermi Gamma-ray Burst Monitor, coincident with the gravitational wave GW170817A detected by LIGO/Virgo [8]; and a gamma-ray flare from the Blazar TXS 0506+056 detected by Swift in the X-ray band, Fermi-LAT in the GeV range, MAGIC in the TeV band, and the IceCube the correspondent neutrinos [3]–[6]. In response to these events, improvements have been made to follow-up neutrino searches, Fermi-LAT transient reporting, and follow-up procedures by Swift and other observatories [143]. Using a network of astronomical observatories multimessenger observations can now detect four messengers from the Universe: Electromagnetic radiation (from radio to high-energy gamma-rays); Gravitational Waves; Neutrinos; and cosmic rays. Each of the different messengers carries distinct information that can be combined for a better understanding of relevant questions in astrophysics.

Gamma-ray observations have played a critical role in every multimessenger source identified to date. In fact, the peak power output of electromagnetic counterparts lies in the gamma-ray band for the objects identified so far: short GRBs for gravitational wave counterparts and blazars (active galaxies whose jets are aligned to our line of sight) for neutrino counterparts. A future gamma-ray observatory capable of time, spatial, spectral and polarimetric analyses is crucial to understand: the compact objects, GRB and gravitational waves counterparts; the element formation in extreme environments such as kilonovae and supernovae; and the astrophysical jets; among many sources [38].

Nuclear astrophysics is another main scientific goal for a future gamma-ray observatory. Exploding stars inject important amounts of kinetic energy and newly synthesized chemical elements into the interstellar medium in such a way that they completely shape the chemical evolution of galaxies. Thanks to the penetration power of high-energy photons and the association of gamma-ray lines to specific radioisotopes, the observation of supernovae and novae with gamma-rays can provide a privileged diagnostic tool with respect to measurements performed in other wavelengths [38].

1.5.2 Instrument Proposals

Several high-energy missions proposals are currently in preparation. Herein, we briefly describe the missions that are currently part of the ambitions of the i-astro group at LIP. They use the most recent technologies for gamma-ray detection and have polarimetry as one of the primary goals.

1.5.2.1 ASTENA

The ASTENA mission has been proposed within the context of the European project AHEAD. It consists of a Wide Field Monitor-Imaging Spectrometer (WFM-IS) working in the passband 2 keV-20 MeV and a Narrow Field Telescope (NFT) in the passband 50-600 keV (figure 1.27).

The WFM-IS consists of 6 blocks of 3 detection units, accommodated as shown in figure 1.27. Each WFM-IS unit consists of an array of detection elements, each made of a scintillator bar (CsI(TI) or similar) 5 cm long, with an hexagonal cross section of about 75 mm^2, viewed by two Silicon Drift Detectors (SDD) 0.45 mm thick, one on the top (side of entrance of the celestial photons) and other on the bottom. The total expected

effective area of the WFM-IS through the mask is about 4000 cm^2 up to 30 keV, 6000 cm^2 up to 150 keV and about 1.2 m^2 beyond 200 keV. Thanks to its design, the WFM-IS is particularly suitable to be triggered by celestial transient events, like short and long (also low luminosity) GRBs, X-/gamma-ray counterparts of Gravitational Wave events, Tidal Disruption Events, etc, with 1 arcmin accuracy for prompt follow up with the NFT, measuring the prompt emission spectrum and the polarization status at high energies (>80 keV).

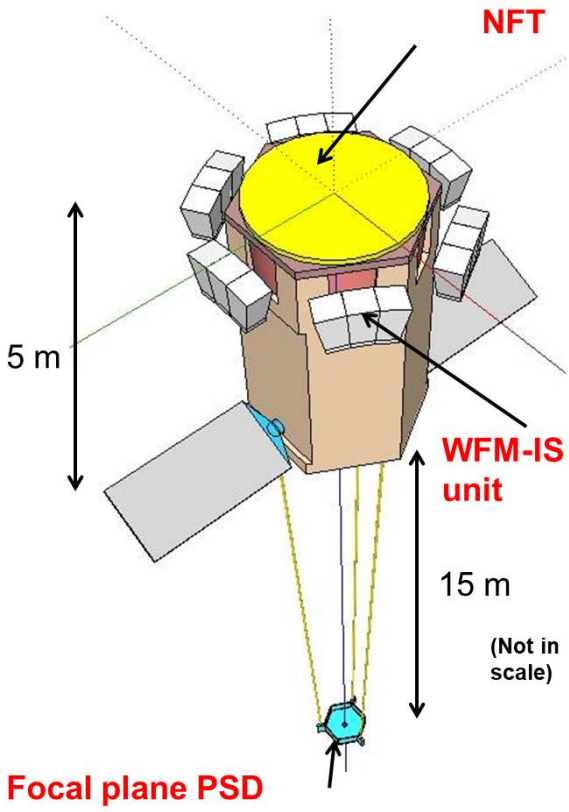

Figure 1.27: Configuration of the ASTENA mission concept in flight.

The NFT is focusing optics telescope based on a spherical Laue lens, that diffracts the hard X-/soft gamma-rays and focus on a detector plane [157]. The diffracting crystals are bent tiles of silicon (Si) and germanium (Ge) with reflecting planes (111), cross section of 30×10 cm^2 and curvature radius of 40 m (focal length = 20 m). The crystals are disposed on rings with the outermost ring radius of 1.5 m. With this size, the projected geometric area is about 7 m^2. Concerning the NFT focal plane detector, the adopted configuration consists of 4 layers of drift strip detectors of CZT [158], each layer with a

cross section a 80×80 mm^2 and a thickness of 20 mm. The goal is to achieve a 3-D position sensitivity of 300 μm and a detection efficiency higher than 80% in the entire operational energy range of the NFT. With these spatial sensitivity properties, the focal plane detector has been demonstrated to be also sensitive to photon polarization for Compton interactions [84], [159], [160].

ASTENA takes advantage of the 15 years of partnership between LIP, INAF-Bologna, INAF-Palermo and University of Ferrara to access the performance of Laue Lens focusing telescopes with CdTe/CZT focal detector planes [84].

1.5.2.2 e-ASTROGAM

The e-ASTROGAM is a gamma-ray mission concept proposed as a response to the ESA Call for the fifth Medium-size mission (M5) of the Cosmic Vision Science Programme. The payload is shown in figure 1.28. It consists in a detector composed by a Silicon tracker, a calorimeter, and an anticoincidence system allowing to study the Universe in the photon energy range from 0.3 MeV to 3 GeV [36].

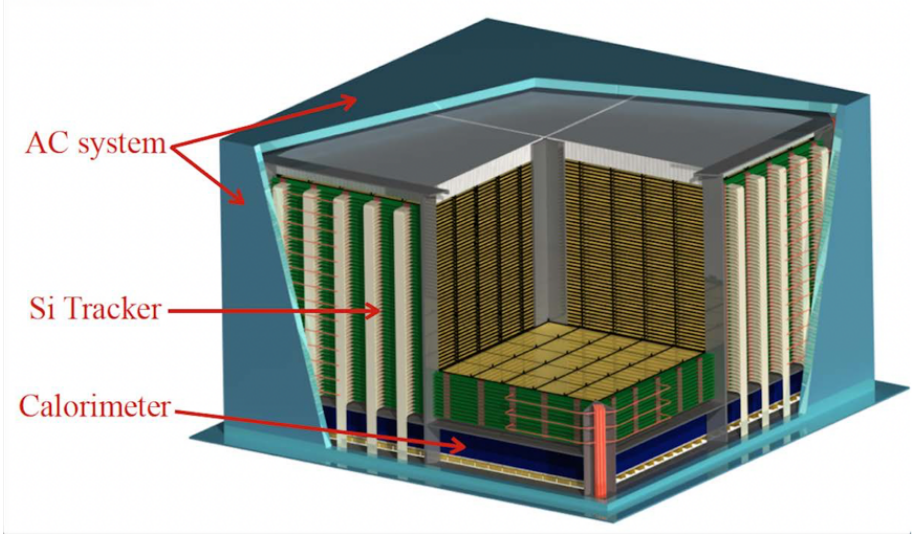

Figure 1.28: Overview of the e-ASTROGAM payload showing the silicon Tracker, the Calorimeter and the Anticoincidence system [36].

The Si Tracker is the heart of the e-ASTROGAM payload. It is based on the silicon strip detector technology widely employed in medical imaging and particle physics experiments (e.g. ATLAS and CMS at LHC), and already applied to the detection of

gamma-rays in space with the AGILE and FERMI missions. The Tracker is divided in four towers, with 56 layers each, spaced 10 mm. Each layer is a 5×5 array of double-sided strip detectors (DSSDs). The DSSDs have 500 μm thickness and 9.5×9.5 cm^2 area. The total detection area is 9025 cm^2 and the total Si thickness is 2.8 cm [36].

The Calorimeter is a pixelated detector made of a high-Z scintillation material (Thallium activated Caesium Iodide, CsI(TI)) for an efficient absorption of Compton scattered gamma-rays and electron-positron pairs. It consists of an array of ~34×10^3 parallelepiped bars of CsI(TI) of 8 cm length and 5×5 mm^2 cross section, read out by silicon drift detectors (SDDs) at both ends, arranged in an array of 23×23 elementary modules containing 64 crystals each [36].

1.5.2.3 AMEGO

With the unsuccessful proposal of e-ASTROGAM to ESA, the core teams of the mission concept move the efforts to the AMEGO mission, a probe class international mission concept under development between NASA and European partners. AMEGO combines high sensitivity in the 200 keV to 10 GeV energy range with a wide field of view, good spectral resolution, and polarization sensitivity. The instrument is similar to the e-ASTROGAM consisting in a tracker, made of Si DSSDs and CsI calorimeter. However, AMEGO includes also a CZT calorimeter (figure 1.29) [38].

The CZT calorimeter consists of an array of 8×8×40 mm^3 bars. One layer sits below the tracker and another extends partially up the outer sides of the tracker. It provides a precise measurement of the location and energy of the scattered gamma-ray. The CZT bars are operated in a drift mode that enables 3D reconstruction of the location of the interaction in the detector, thus providing excellent positional resolution (<1 mm) as well as very good energy resolution (<1% at 662 keV) at room temperature [38].

Recently our team evaluate the polarimetric potential of e-ASTROGRAM and AMEGO missions in the Compton regime by Monte Carlo mass model simulations with MEGAlib toolkit [161]. The performance of e-ASTROGAM was analysed by simulating Si tracker and calorimeter alternative configurations and detection materials, within missions' volume, mass and power margins. The modulation polarimetric factor, and the MDP were calculated for different polarized source types and for variable incidence angle measurement conditions. Finally, the polarimetric performances of both instruments was compared and analysed. Modulation factors obtained ranged between Q ~0.2 and Q ~0.4

in the 0.2-2.0 MeV band and MDP ~0.65% was estimated for a 100% polarized Crab type source, 1 Ms observation time and 3σ significance.

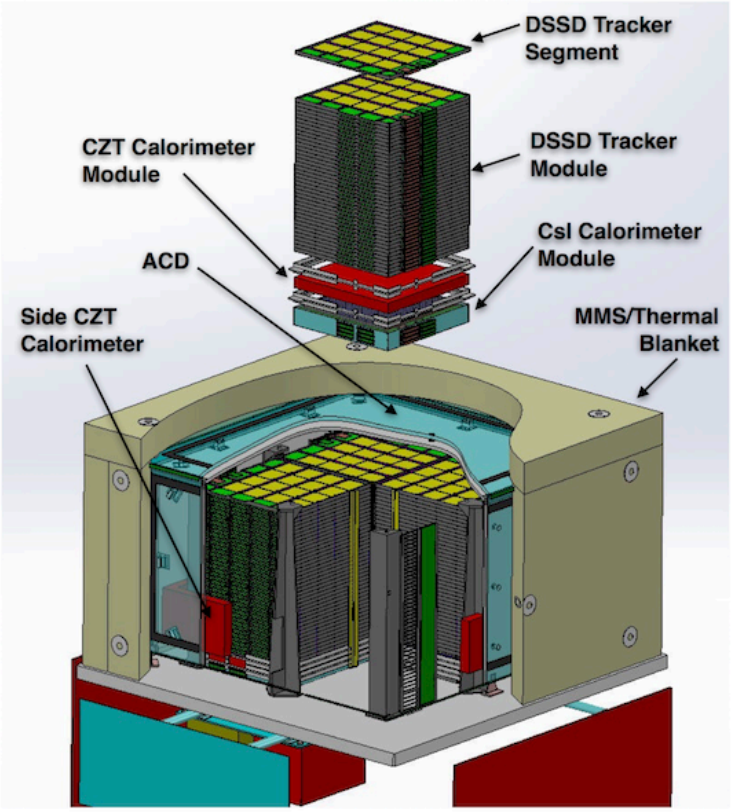

Figure 1.29: Scientific payload overview of AMEGO [38].

The modulation factor obtained for each instrument mass model under 100% polarized monochromatic, far-field point sources in the 0.25-2.5 MeV energy range is represented in figure 1.30. The modulation factor obtained for e-ASTROGAM is slightly better than AMEGO's modulation. This difference can be explained by the superior number of Si elements of the e-ASTROGAM tracker (5×5 DSSD arrays). A larger number of Si elements in the *x* and *y* instrument axis generates more near-90° scattering angles, improving modulation resolution [161].

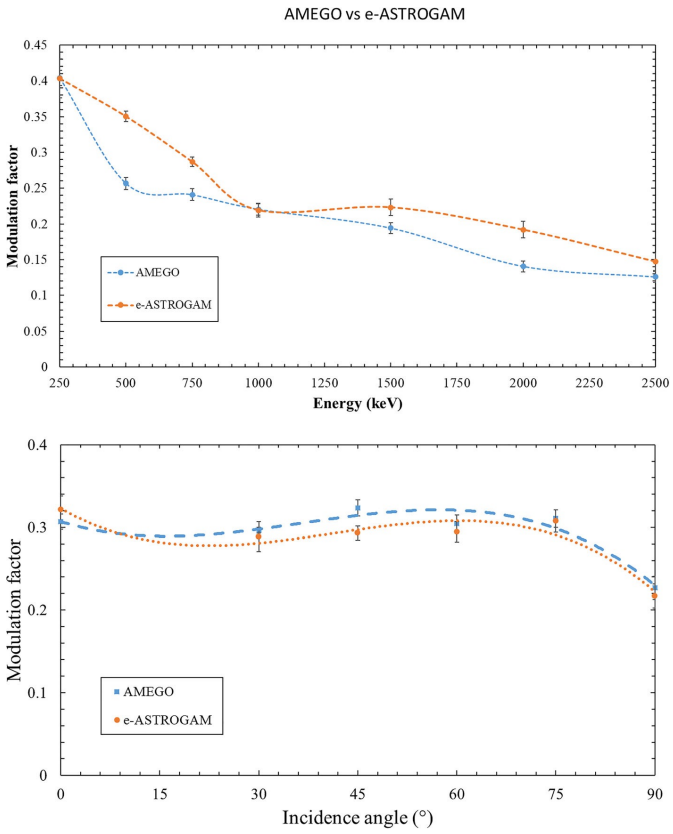

Figure 1.30: AMEGO vs e-ASTROGAM polarization modulation as a function of the energy, for a Crab type source in the 0.2-2.0 MeV energy range [161].

1.5.2.4 POLAR-2

After the success of the dedicated GRBs polarimeter POLAR placed on board the Chinese space laboratory Tiangong-2 in 2016 a new mission is being prepared, the POLAR-2. The project is being implemented by four institutions from four countries: The University of Geneva from Switzerland, the National Centre for Nuclear Research of Poland, the Max Planck Institute for Extraterrestrial Physics of Germany and the Institute of High Energy Physics of the Chinese Academy of Sciences. The mission was already selected to fly on the Chinese space station however, no further reports have been published yet [162]. Our group is currently under negotiation to be a part of the POLAR-2 mission team.

2 Compton-POLCA Detector

2.1 Semiconductor Detectors

As seen the previous chapter for gamma-ray astronomical observations the most used type of detectors has been the semiconductor and scintillator detectors. For polarimetric measurements, where the energy resolution of the interactions is not the priority, the scintillator detectors provides a good solution for astronomical observations. However, if we pretend to design an all-sky gamma-ray instrument with good spectral, spatial, temporal and polarimetric capabilities semiconductor detectors provide better solutions. Amongst the advantages it includes: superior energy resolution when compared with scintillation detector; compact size; relatively fast timing characteristics; and an effective thickness that can varied to match the requirements of the application [80].

2.1.1 Principle of Operation

Generally, the principle of operation of a semiconductor detector is based on the collection of the charges, created by the primary photon interactions, through the application of an external electric field. The simplest configuration possible is schematized in figure 2.1, a planar detector, that is, a slab of a semiconductor material with metal electrodes on

the opposite faces of the semiconductor. Photon interactions produce a number of electron-hole pairs in the semiconductor volume proportional to the energy of the radiation that interacts with the semiconductor. As a result, a number of electrons are transferred from the valence band to the conduction band, and an equal number of holes are created in the valence band. Under the influence of an electric field, electrons and holes travel to the electrodes, where they result in a pulse that can be measured in an outer circuit. The holes travel in the opposite direction and can also be measured.

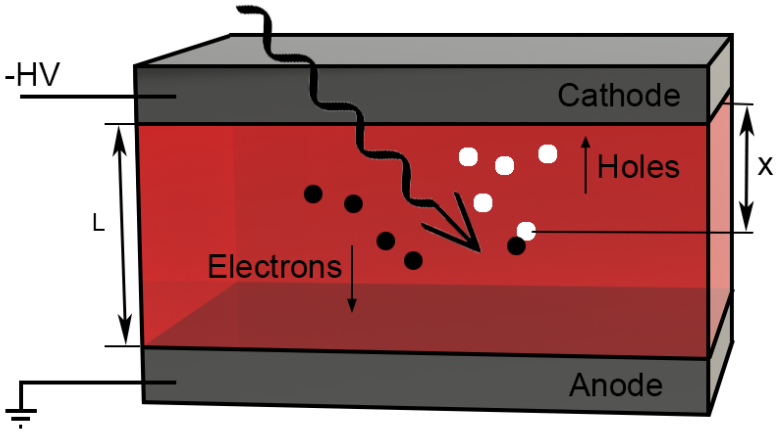

Figure 2.1: Planar configuration of a semiconductor detector. Electron-hole pairs, generated by radiation, in a location *x*, are swept toward the appropriate electrode by the electric field.

Semiconductors are crystalline materials whose outer shell atomic levels exhibit an energy band structure. This band structure arises because of the close, periodic arrangement of the atoms in the crystal which causes an overlapping of the electron wavefunctions. The energy bands are regions of many discrete levels which are so closely spaced that they may be considered as a continuum, while the "forbidden" energy gap is a region in which there are no available energy levels at all. The highest energy band is the conduction band. Electrons in this region are detached from their parent atoms and are free to roam about the entire crystal. The electrons in the valence band levels, however, are more tightly bound and remain associated to their respective lattice atoms. The band gap energy is the minimum energy that is required to excite an electron from the valence to the conduction band. For a nuclear radiation semiconductor detector, the energy band gap

should be small enough that the electron-hole ionization energy (<5 eV), and large enough for high resistivity and low leakage currents. For high resistivity material such as CdTe, the configuration employed is as shown in figure 2.1. However, in the case of Si or Ge detectors this is impractical because the currents generated due to the application of an external bias would often be larger than those created by incident radiation. For these materials a diode configuration is normally used, where a doped n semiconductor is joined with a doped p semiconductor forming a depletion region. The depletion region exhibits some very attractive properties as a medium for the detection of radiation. The electric field that exists causes any electrons created in or near the junction to be swept back toward the n-type material, and any holes are similarly swept toward the p-type side. The region is thus depleted in that the concentration of holes and electrons is greatly suppressed. The only significant charges remaining in the depletion region are the immobile ionized donor sites and filled acceptor sites. Because these latter charges do not contribute to conductivity, the depletion region exhibits a very high resistivity compared with the n- and p-type materials on either side of the junction. Electron-hole pairs that are created within the depletion region by the passage of radiation will be swept out of the depletion region by the electric field. The external potential applied in the electrodes will then produce an electric field strong enough to extract the electron-hole pairs and produce the electrical signal that will be measured [80], [81], [163], [164].

Table 2.1: Principal physical properties of the Si, Ge, CdTe and CZT semiconductors [165].

Material	Si	Ge	CdTe	$Cd_{0.9}Zn_{0.1}Te$
Atomic number	14	32	48, 52	48, 30, 52
Density (g cm^3)	2.33	5.33	6.20	5.78
Band Gap (eV)	1.12	0.67	1.44	1.57
Resistivity (Ω cm)	10^4	50	10^9	10^{10}
$\mu_e\tau_e$ (cm^2 V^{-1})	>1	>1	10^{-3}	10^{-3}-10^{-2}
$\mu_h\tau_h$ (cm^2 V^{-1})	~1	>1	10^{-4}	10^{-5}

In summary, the choice of the proper semiconductor material for a radiation detector depends mostly on the application. So far, the Si detectors are mostly chosen in the soft X-ray band (<15 keV). Si-PIN diode detectors and SDDs operated with moderate cooling

by means of small Peltier cells, show excellent spectroscopic performance and good detection efficiency below 15 keV [166]–[170]. On the other side, Ge detectors are unsurpassed for high resolution spectroscopy in the hard X-ray energy band (>15 keV) and will continue to be the first choice for laboratory-based high-performance spectrometers [171], [172]. However, there has been a continuing interest to development room temperature detectors with compact structure having the portability and convenience of a scintillator but with a significant improvement in energy resolution. To this end, CdTe and CZT have been considered very appealing for gamma-ray detectors and are now widely used for the development of spectrometer prototypes for astrophysical applications [165], [173]–[175]. Table 2.1 presents the principal proprieties of these four semiconductor materials.

2.1.2 Photon Efficiency

The photon must interact with the semiconductor so the charges can be created and collected. The three main interaction mechanisms of gamma-rays with matter are photoelectric absorption, Compton scattering and pair production. In photoelectric absorption the photon transfers all its energy to an atomic electron; in the Compton scattering a photon interacts and transfers only a fraction of its energy to an electron, producing a hot electron and a degraded photon; in pair production a photon with energy above a threshold energy of 1.02 MeV interacts within the Coulomb field of the nucleus producing an electron and positron pair. The interaction cross sections are highly dependent on the atomic number: In photoelectric absorption it varies as $Z^{4.5}$; in Compton scattering as Z and Z^2 for pair production [80].

As a result of the interaction mechanisms, the incident radiation intensity (I_0) will be attenuated and the intensity of the radiation transmitted (I) by a given absorber of thickness L can be found using the law of attenuation.

$$I = I_0 e^{\mu L} \tag{2.1}$$

where μ is the linear attenuation coefficient, expressed in cm^{-1} and given by $\mu = n\sigma$, where n is the number of atoms per unit of volume [80]. Given its dependence with the density of the absorber material, it is usually described as mass attenuation coefficient μ / ρ, which

describes the effective cross-sectional area of atoms per unit mass of absorber and it is expressed in cm^2/g. In figure 2.2 is presented the mass attenuation coefficient for Si, Ge and CdTe. The colours represent the energy range where a give interaction mechanism is dominant: blue for photo absorption; red for Compton scattering; and green for pair production. Figure 2.3 shows the total efficiency (I / I_0) for a 2 mm thick detector of the same three materials calculated with equation 2.1. CdTe is clearly the material that have a better efficiency for energies from 0.1-1 MeV due to its higher atomic number. With a 2 mm thickness detector is possible to have 100% efficiency up to 100 keV. Furthermore, for CdTe the photoelectric absorption is the main process up to about 200 keV. Neglecting the escape of gamma-rays from the detector volume, only the photoelectric effect results in the total absorption of the incident energy and thus gives useful information about the photon energy. An optimum spectroscopic detector must favour photoelectric interactions. However, for polarimetric measurements using the Compton scattering process, this interaction should have a good efficiency in the operational energy ranges, despite of lower photoelectric efficiency and degraded spectral performance. For a correlation with the experiment performed, figure 2.4 shows the photoelectric and Compton scattering efficiencies (I / I_0) for a 2 mm CdTe detector in the energy ranges between 100-500 keV. Despite that the total attenuation presents a drastic drop, the efficiency of the Compton scattering process remains constant. We can expect that the Compton process will have an efficiency around ~10% for the all energy range. Furthermore, the decrease of photo absorption efficiency will lead to a higher ratio between the Compton scattering and the photo absorption efficiencies, e.g. for a ~260 keV incident beam we is expected that the events recorded will be ~50% due to photo absorption and ~50% due to Compton scattering, while for a 100 keV beam, ~80% will be photoabsorption.

Equation 2.1 also shows a dependence of the thickness of the material and the efficiency of the detector. Increasing the thickness, the photon must cross more material volume thus, the probability of interaction increases and consequently the efficiency. However, for a planar detector this presents drawbacks in terms of spectral and polarimetric performance. Regarding the polarimetric performance, the dependence of the polarimetric modulation factor with the Compton scattering angle also results in a performance degradation with the increase of the detector thickness. The modulation factor is maximised for angles near 90°. A thicker detector will increase the collection of Compton events with scattering angles below 90°, decreasing the modulation factor. A

thicker detector also causes the deterioration of the charge collection efficiency and consequently the spectral performance off a detector as we will show further.

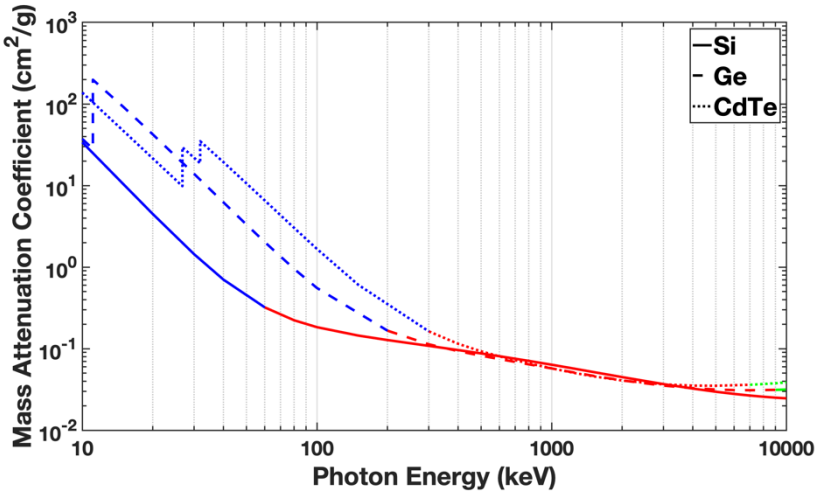

Figure 2.2: The mass attenuation coefficient as a function of the photon energy for Si, Ge and CdTe. The energy range where photoabsorption dominates is shown in blue, the range where Compton scattering dominates in red and the energy range where pair production dominates in green.

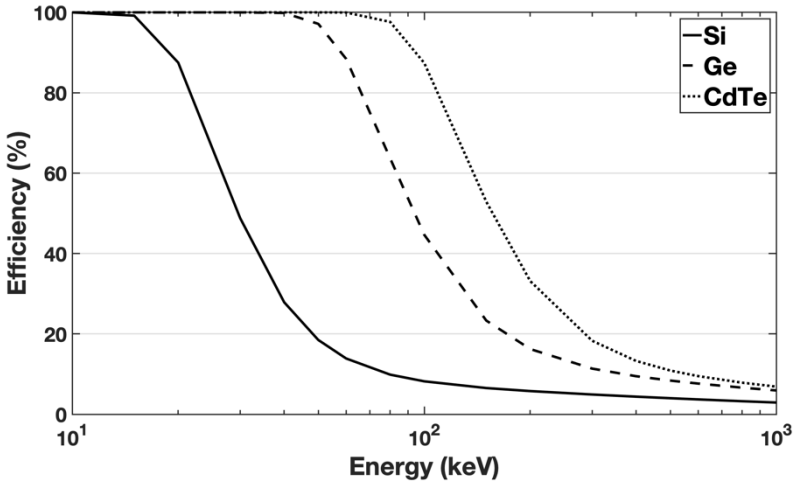

Figure 2.3: Total efficiency comparation of a 2 mm thick detector of Si, Ge and CdTe.

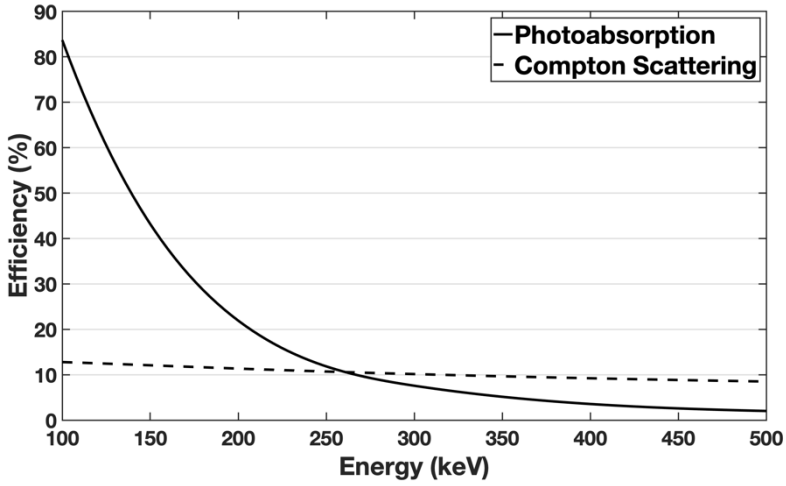

Figure 2.4: Photoelectric and Compton scattering efficiencies for a 2 mm CdTe detector.

2.1.3 Charge Collection Efficiency

The charge collection efficiency and the charge carriers' mobility are crucial properties of a radiation detector because they strongly affect the spectroscopic performance and in particular the energy resolution. In an ideal detector all the charge carriers, electrons and holes, are swept to the contacts, this process is referred to as "full charge collection". Unfortunately, this is generally not the case, especially for most compound semiconductors, as CdTe, where the effect of charge carrier loss from trapping must be taken into account. For a planar detector, having a uniform electric field, as the one represented in figure 2.1, the charge collection efficiency (*CCE*), that is, the induced charge normalized to the generated charge, is given by the Hecht equation [80]:

$$CCE = \frac{Q}{Q_0} = \frac{E}{L}\left[\mu_h\tau_h\left(1-\mathrm{e}^{-\frac{x}{\mu_h\tau_h E}}\right)+\mu_e\tau_e\left(1-\mathrm{e}^{-\frac{L-x}{\mu_e\tau_e E}}\right)\right] \tag{2.2}$$

where L is the detector thickness, x is the distance from the cathode to the point of charge creation, E the electric field intensity given by $E = V/L$ for planar electrode configurations, being V the bias voltage between the cathode and the anode. μ_h and μ_e are the hole and electron mobilities respectively, and τ_h and τ_e the correspondent lifetimes. The product of these last two variable is usually used to describe the carriers' mobility properties and is expressed in cm^2/V. A higher $\mu_h\tau_h$ and $\mu_e\tau_e$ results in a higher charge collection efficiency therefore, a good spectral performance.

As can be seen in table 2.1 the product of the charge mobility and mean free drift time for CdTe and CZT is considerably lower than for Si and Ge, especially for holes. A lower charge mobility and lifetime cause charge trapping and consequent signal charge loss. Trapping centres are mainly caused by structural defects (e.g., vacancies), impurities, and irregularities (e.g., dislocations, inclusions). Moreover, the significant difference between the transport properties of the holes and the electrons, as in CdTe and CZT, produces peak asymmetries and long tails. This difference also creates a dependence of the charge collection efficiency with the interaction depth of the absorbed photon. In figure 2.5 is presented this dependence for the planar configuration of figure 2.1, irradiated from the cathode side. For a 2 mm Si detector the *CCE* is ~100% due to high mobility of the charge carriers. For a bulk CdTe with the same thickness and bias voltage conditions, the *CCE* is considerably lower. Furthermore, it changes along the material thickness: if the interactions occurs near the anode, the holes must travel all the material in order to be collected, increasing the probability of being trapped and consequently decreasing the *CCE* to its minimum. One of the techniques to overcome this effect in a planar detector is irradiating the detector through the cathode side, as illustrated in figure 2.1 [175], [176]. This configuration increases the probability of photon interaction near the cathode, especially for lower energies, causing a quick hole collection.

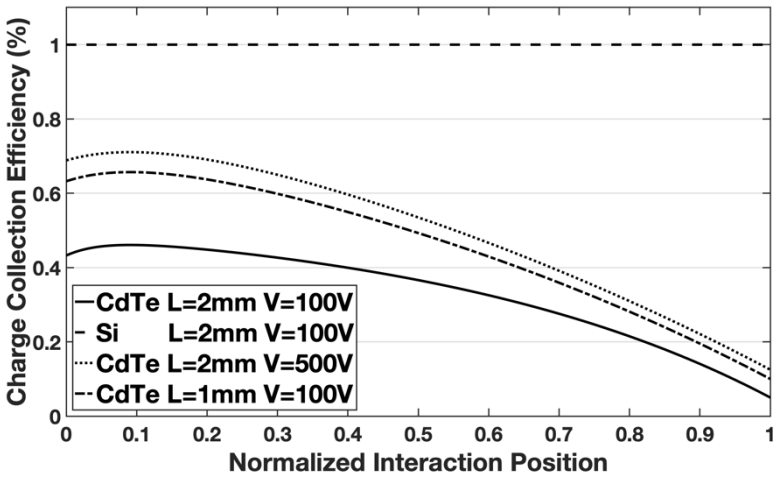

Figure 2.5: Charge collection efficiency (*CCE*) vs. the normalized interaction position (from cathode) of incoming photons.

Unipolar detectors, wherein the signals are mainly influenced by the electrons (single charge carrier sensitive), have also been developed to minimize the influence of holes in the detector signals. A pixel detector is an example of a technique where the signals are mainly influenced by the electron contribution. This important feature is due to the particular shape of the weighting potential generated by the pixel anode layout: it is low near the cathode and rises rapidly close to the anode; according to this characteristic, the charge induced on the collecting pixel, proportional to the weighting potential is mostly contributed from the drift of charge carriers close to the pixel (electrons). The weighting potential and then the detector signals are further unipolar as the pixel size/detector thickness ratio decreases. This is generally referred to as the small pixel or near field effect [177].

As shown in figure 2.5 reducing the detector thickness also improves the charge collection efficiency but, reduces also the photon efficiency of the detector as seen before. The figure also shows an improvement of the charge collection efficiency with the bias voltage. However, in this case, if the detector electrodes form ohmic contacts with the CdTe crystal the detector leakage current is directly proportional to the electric field. The leakage current shot noise eventually becomes the dominant noise source and prohibits higher field strengths. CZT was developed to achieve higher resistivities and lower leakage currents. Changing the Zn concentration, the band gap can be extended up to 1.64 eV and the resistivity risen up to 10^{11} Ω.cm. Despite the drawback of much lower hole life time of CZT compared to CdTe, improved energy resolution has been demonstrated with CZT detectors [178], [179].

2.1.4 Leakage Current

When voltage is applied to a junction detector by reverse bias, a small current of the order of a fraction of a microampere is normally observed. The origins of this leakage current are related both to the bulk volume and surface of the detector. One source of bulk leakage is the thermal generation of electron-hole pairs within the depletion region. If a valence electron acquires enough thermal energy it can cross the bandgap into the conduction band. The intrinsic carrier concentration for a semiconductor is proportional to e^($-E_g/kT$), where E_g is the energy of the band gap, k is Boltzmann's constant and T is the absolute temperature [180]. Semiconductors with small band gap energies, (such as

Ge), must be cooled to reduce the carrier concentrations to acceptably low noise levels. The CdTe in opposition, has a large band gap, allowing it to be used at room temperature. A second source of bulk leakage current is the minority carrier diffusion across the detector junction. Because the minority carriers are generated continuously on both sides of the junction and are free to diffuse, a steady-state current will result that will be roughly proportional to the area of the junction.

There is also leakage associated with surface phenomena. In fact, for CdTe the surface leakage through the side edge dominates over the bulk current [181]. There are several reasons for the surface leakage. The surface impurities created during the crystal manufacture and the proprieties of the surface electrodes are some of them. One technique that has been used to reduce surface leakage is to use a guard ring on the detector surface, surrounding the cathode electrode. Adopting a guard-ring it is possible to reduce the leakage current by more than an order of magnitude [182].

The material of the electronic contacts with the CdTe crystal also play an important role in the leakage current. The most common material is Platinum (Pt), used in a configuration Pt/CdTe/Pt. This configuration forms ohmic contacts with the CdTe crystal producing a detector leakage current which is directly proportional to the electric field. To improve this characteristic, configurations such as In/CdTe/Pt and Al/CdTe/Pt have been developed. These metals form Schottky contacts with the CdTe, reducing the leakage current and operation at much higher electric fields becomes possible, which minimize the charge-trapping distortions, without excessive increasing of the electronic noise [181], [183].

One of the main disadvantages of diode detectors is its time instability, generally termed as polarization phenomena, which is characterized by a progressive loss of detection efficiency, charge collection efficiency and energy resolution with time after applying the bias voltage. The polarization phenomena has been described in several works, [184]–[189]. The physical mechanisms underlying this effect have been well investigated through different approaches: measurement of current-voltage characteristics [185], spectroscopic investigations [184], and measurement of the electric field distribution inside the detectors by using the Pockels effect [187]. All studies agreed that polarization is due to ionization (hole detrapping) of deep acceptors close to the rectifying contact (In/CdTe or Al/CdTe). Under reverse bias operation, the progressive drift of the holes toward the electrodes produces a negative space charge accumulation at the anode resulting in a modification of the electric field with time. CdTe diode detectors biased with electric

fields greater than 5000 V/cm and cooled down 25ºC can operated for several days without significant polarization effects. Switching off the bias voltage at regular time intervals is also one possible solution for the minimization of polarization effects [165].

2.1.5 Electronics

Figure 2.6 shows a typical spectroscopic system based on a semiconductor detector. In summary, the detector signals are amplified by a charge sensitive preamplifier (CSP), shaped by a linear amplifier (shaping amplifier) and finally the energy spectra is obtained by a multichannel analyser (MCA) which samples and records the shaped signals.

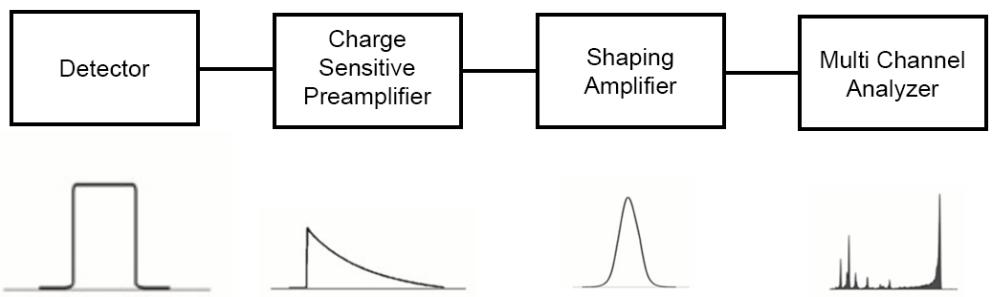

Figure 2.6: Block diagram of a typical spectroscopy system.

The first element is the CSP that provides the interface between the detector and the following pulse-processing electronics (shaping amplifier and MCA). The preamplifier is designed to integrate the induced current induced by the movement of electrons and holes in the detector under the influence of an applied electric field. The signal is characterized by a fast-exponential leading edge followed by a slow exponential decay. The leading edge, generally described by the peaking time (i.e., the time at which the pulse reaches its maximum), depends on the time width of the current pulse, that is, on the collecting time of the charge created in the detector (typical values of few hundreds of nanoseconds). The pulse height is proportional to the generated charge and then to the energy of the detected events. The exponential falling edge decreases with a time constant (few hundreds of microseconds) equal to the product of the capacitance and the resistance of the feedback loop. As stated before, there are events with the same energy but that

generate different charge collection times. To avoid these events that could produce pulses with different heights, the time constant is typically chosen several orders of magnitude greater than the peaking time. On the other side, a time constant too large can produce overlapped pre amplified pulses.

The primary functions of the shaping amplifier (linear amplifier) are to shorten and to amplify the CSP output pulses. The simplest concept for pulse-shaping amplifier is the use of a *CR* filter (high-pass filter in the frequency domain or differentiator in the time domain) to shorten the pulses, followed by an *RC* filter (lowpass filter in the domain of frequencies or integrator in the time domain) to improve the signal-to-noise ratio. The shaping amplifiers are generally analog devices characterized by different pulse shapes (*CR-RC*, Gaussian, triangular, trapezoidal) and few different shaping time constant values. Generally, the shaping time constant of a shaping amplifier is an important parameter for optimum energy resolution and throughput. The choice of the proper value of the shaping time constant (e.g., the time constant of the *CR-RC* filters) should take into account several factors: (i) ballistic deficit, (ii) noise, (iii) pile-up, and (iv) dead time [80].

Finally, the last stage of the processing chain concerns the measurement of the shaped pulse heights (i.e., the energy of the events) and the creation of the pulse height spectra (energy spectra). This process is known as the MCA mode. An MCA is used to sample and to record the shaped pulses and to generate the energy spectrum. Generally, the main task of a pulse processing chain is to give the best energy resolution possible and the true rate of the events.

2.2 POLCA Experiments

This thesis follows a series of experiments named POLCA (POlarimtery with Cadmium Telluride Arrays) [88]–[96]. These experiments have been developed by a partnership between LIP, INAF-Bologna, INAF-Palermo and University of Ferrara with the main objective to assess the performance of a CdTe focal plane as a polarimeter up to 750 keV. In order to aid the optimization of the design of this detector, a series of experiments based on a CdTe pixel detector prototypes was carried out at the ESRF where a ~99% polarized gamma-ray beam is available.

The first experiment of the series was performed with three CdTe monolithic matrices of different thickness (3.4, 5.0 and 7.5 mm). Each detector consisted of 4×4 pixels (2.5

mm×2.5 mm each) [90], [91]. Figure 2.7 shows the box that holds the detector, the 16 preamplifiers, and the bias circuits for the detectors. The system uses coincident circuitry in order to select the Compton events (if two events are acquired in a certain time window, usually in the order of 1 μs, the system sends a flag). Due to the 90° double event distribution symmetry produced by a polarized photon beam was possible to irradiate a corner pixel of 4×4 and consider the obtained distribution as a 90° quadrant of a virtual 360° distribution obtained around the considered pixel as a central pixel of a 7×7 matrix. This experiment was able to verify this method by irradiating a corner pixel and rotating the detector by 90° four times obtaining the full 360° distribution.

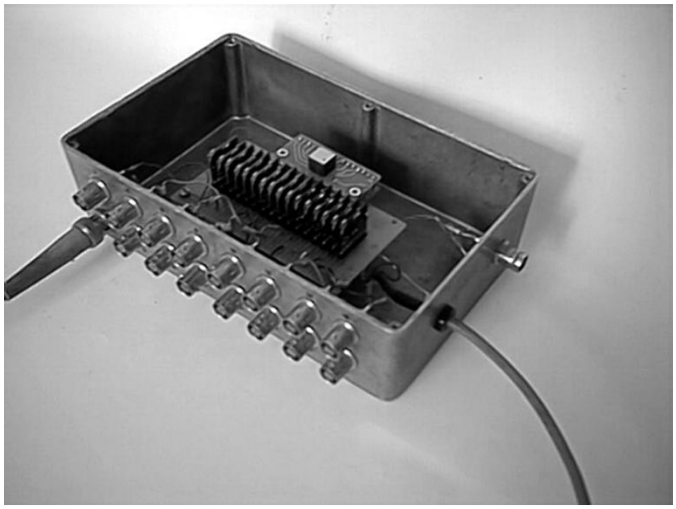

Figure 2.7: The box containing the pixelated CdTe monolithic matrix and the 16 preamplifiers.

The results for the three detectors under test are shown in table 2.2. Three energies were tested: 100 keV, 300 keV and 400 keV. The results showed a higher modulation factor for thinner detectors. This is due to dependence of the modulation factor with the scattering angle θ. In the considered energy range the Q is maximised for angles near 90°. Inside thinner matrices Compton interactions with scattering angles θ that differ from 90° have a higher probability to escape from the detector and therefore, the double events that interact inside the detector are those with θ near 90°, therefore the higher Q was obtained for the thinnest matrix (3.4 mm).

Table 2.2: POLCA I polarimetric Q factors. Based on [90], [91].

Detector Thickness	Experimental Modulation Factor, Q		
	100 keV	300 keV	400 keV
3.4 mm	0.150 ± 0.051	0.460 ± 0.036	0.360 ± 0.091
5.0 mm	-	0.400 ± 0.120	0.330 ± 0.130
7.5 mm	-	0.390 ± 0.060	0.310 ± 0.065

In 2016 a new detecting system was designed and tested. It consisted in a 5 mm thick CZT IMARAD device with 16×16 pixels, each with 2.5×2.5 mm^2 area. Due to limitations in the back-end electronics (only 128 channels available) only 11×11 pixels have been connected for a total sensitive area of ~8.0 cm^2 [92], [93], [96]. As in the case of POLCA I, a corner pixel of the 11×11 CZT matrix was directly irradiated and the obtained distribution was analysed as a 90° quadrant of a virtual 360° planar distribution around the same pixel, allowing to extrapolate the distribution obtained to an equivalent 21×21 matrix, generating distributions up to the 10th order pixels.

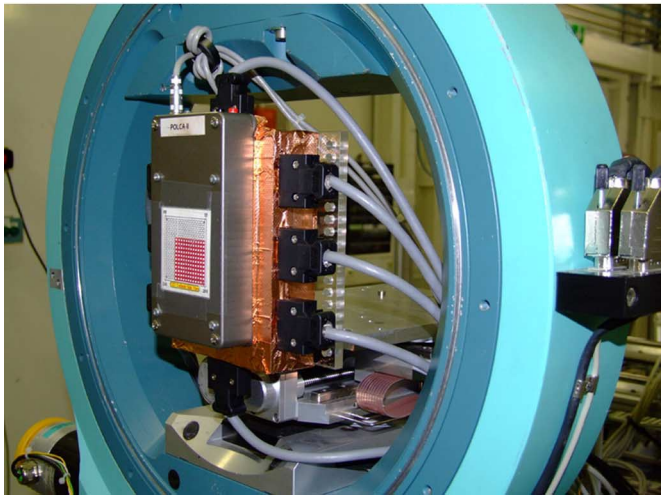

Figure 2.8: POLCA II detecting system inside the experimental hutch of the ID15A beamline at the ESRF. The large ring provides the rotation around directions parallel to the beam axis. In its centre we placed the CZT pixelized prototype detector.

The modulation factor was obtained for energies between 150-650 keV (figure 2.9), and shown an increase up to 250 keV, Q ~0.42, and slowly decreases till reaching ~0.15 for 650 keV. The lower modulation factor for 150 keV is due to the lower efficiency of collecting the double events for this energy; the energy deposited in the first Compton

can be under the minimum energy threshold of the system, and the system is unable to detect it. For higher energies the probability of Compton interactions occurring with a scattering angle θ lower than 90° is higher and the double event efficiency decreases, therefore the modulation measured peaked at ~300 keV.

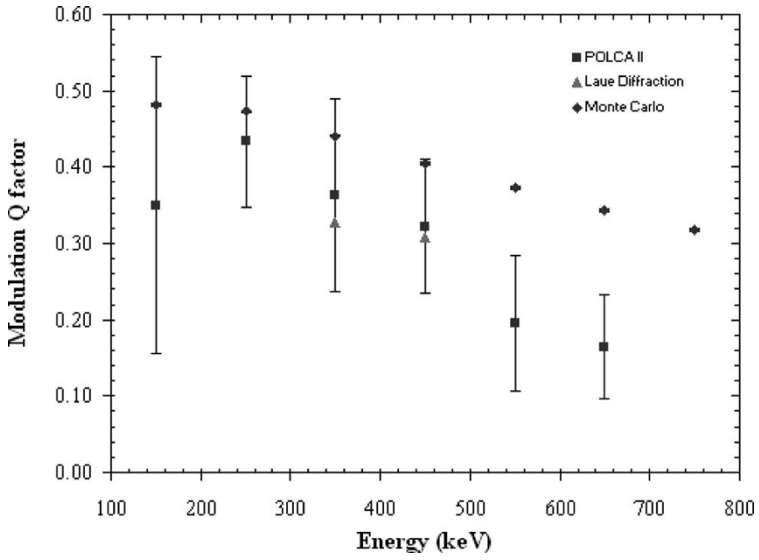

Figure 2.9: The Q factor as function of the energy. The Q factor obtained for 350 and 450 keV Cu Laue monochromator diffracted beams is also shown. Monte Carlo simulation results obtained in similar conditions are shown for comparison [92].

This system also allowed to perform the first polarimetric studies with a copper Laue monochromator crystals [92]. A set of polarimetric measurements were performed by interposing copper crystals (prepared by the University of Ferrara) between the polarized beam and the prototype CZT detector, 75 cm away from the surface of the detector. The three copper samples employed had a face centred cubic crystalline structure with (111) diffraction planes perpendicular to the surface of the crystal, and are similar to the crystals that we intend to employ in a Laue lens system operating in a future gamma-ray telescope. Both the detector system and crystal were mounted on co-aligned computer-controlled 3-axis and rotation positioning systems.

Measurements were performed at 350 keV and 450 keV. At both energies the transmitted beam and one or more diffracted beams by the Cu crystal structure were observed in the CZT matrix. Since the Laue lens system is based on the first order diffracted beam detection, we studied the characteristics of this beam, in particular its intensity, its polarization direction and polarization level and its diameter. So far, as the precision of our

measurements allowed, no changes were observed in the beam diameter, in the polarization level or in the polarization direction of the beam. The projection of the first order diffracted beams in the CZT matrix was about 10 mm from the transmitted beam, for 75 cm distance between the lens and the detector. Therefore, small angle (<1°) Laue diffraction of gamma-rays inside a crystal does not change the polarization state of the original beam. It must be stressed that this result is the experimental evidence of the hypothesis that was postulated by [89] and [90]. In figure 2.9 the *Q* factor obtained for 350 keV and 450 keV diffracted beams show a good agreement with *Q* obtained for a synchrotron beam of the same energy when no diffraction crystals are used.

A more detailed study with Laue lens was performed in [93]. In this experiment the Cu crystal was mounted on a 3-axis linear motion stage coupled with a 2-axis rotation stages to properly align the crystal with respect to the incident beam and to perform the rotation of the crystal itself around the virtual axis of the lens. In this way it was possible to emulate the equivalent of the Laue rings for each available energy line. The detector unit was mounted on a computer controlled 2-axis and micro positioning system at 200 cm from the crystal. For each beam energy, the Laue diffraction condition for the given Cu crystal was found and the crystal was rotated around directions parallel to the axis beam to simulate a Laue ring, composed of 16 elements (one every 22.5º), figure 2.10. For each Cu crystal configuration, the detector was moved in order to intercept the diffracted beam always into the same pixel in the central part of the sensitive surface. The modulation *Q* factor obtained is presented in figure 2.10, and confirmed that the Laue diffraction process does not affect (within few%) the polarization status of the incoming photons.

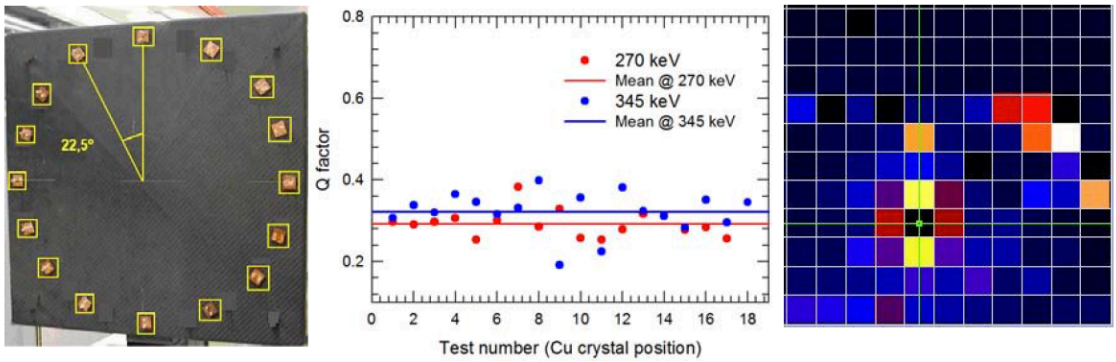

Figure 2.10: Demonstration model simulated 16 elements Laue lens ring (left). The modulation factor obtained for each Cu crystal position in the Laue lens simulation tests (centre). The scattering maps of the diffracted beam at 270 keV impinging on the detector pixel 201 (target pixel is black with a green spot) [191] (right).

One important factor that can influence significantly the polarimetric measurements is the direction of the incoming photons from the polarized radiation source with respect to the focal plane of the polarimeter. In [95] it was evaluated the polarimetric response of the CZT prototype as a function of the inclination of a polarized beam with respect to the optical axis of the detector from 0 to 10° tilt angle. For this experiment, the detector central pixel was irradiated by the polarized beam forming different inclination angles with the optical detector axis: 0°, 0.5°, 1°, 1.5°, 2°, 3°, 4°, 5° and 10°. These measurements at different tilt angles were then repeated for different energies (200 keV, 300 keV, 400 keV and 511 keV) and for initial polarization directions parallel to the detector plane axis: *x* and *y*.

In figure 2.11 is presented the *Q* factors as a function of the tilt angle. It is visible that for tilt angles up to 2° tilt angle the factor is not significantly affected by the beam inclination. However, for a beam whose polarization vector lies orthogonally to the beam projection generated by its inclination, the contributions of polarization modulation and beam inclination are added and the distribution is evidently asymmetric. This generate a dramatically increase of the *Q* factor for angles >2° that could induce some confidence in the results that is not real. For a beam whose polarization vector is parallel to the beam projection the two contributions are opposite and tend to cancel each other and the *Q* factor dramatically decreases. This study shows the importance of a pointing system with accuracy better than 1° for an instrument designed for polarimetry. This accuracy should be enough so that double event distributions can be read directly with no further need of correction methods.

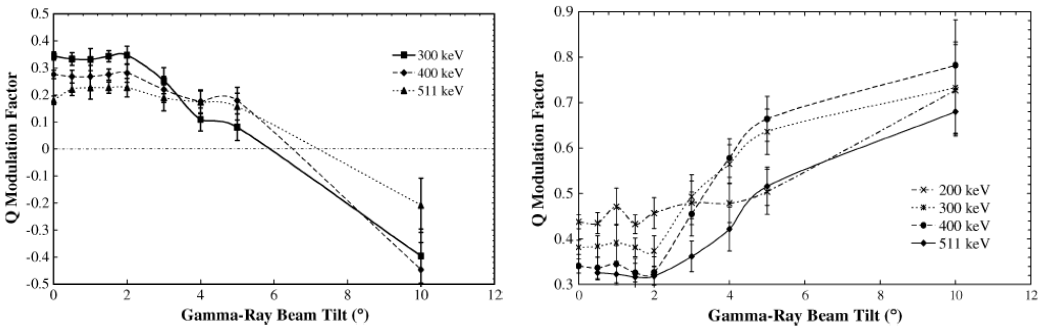

Figure 2.11: Left: The *Q* factor as a function of the tilt angle of the ESRF 100% polarized beam for several energies with the polarization vector parallel to the *x* axis. Right: polarization vector parallel to the *y* axis [95].

Polarization degree and polarization angle orientation are the most important parameters that astronomical polarimetric analysis can provide. A deep study regarding the performance of the CZT detectors by varying these parameters was done in [96]. To analyse the sensitivity to the beam polarization degree, during each measurement, a polarized 400 keV monochromatic beam was used. The polarization angle was fixed in a parallel direction to the detector *x* axis. Measurements were performed for different beam polarization degrees: 100%, 80%, 65% and 50%. The results are presented in figure 2.12 (left) and show a good linear relation between the polarization level of the beam and the measured factor. At least, down to 50% this CZT prototype showed a good sensitivity to the beam polarization degree.

To study the detector potential to determine the polarization angle orientation a detector central pixel was irradiated by a 100% polarized monochromatic beam (200 keV, 300 keV, 400 keV and 511 keV) and the detector was rotated by the azimuthal angle of: 5°, 20°, 30°, 40° and 45°. Figure 2.12 (right) shows a summary of obtained results. The linear fits calculated for each energy are also represented. Overall analysis of these results shows a good agreement between measured polarization angle and the effective beam polarization angle. The best agreement was found for the set of measurements performed at 300 keV. Actually, it is at approximately 300 keV that better polarization sensitivity is obtained (Q ~0.4) as shown in [92].

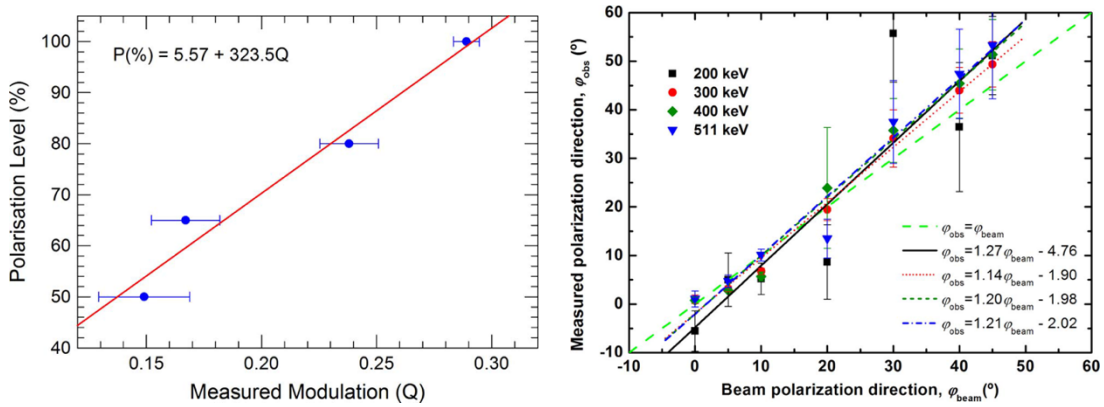

Figure 2.12: Left: Modulation factor for a 400 keV photon for different polarization degrees [96]. Right: measured polarization angle as a function of the effective ESRF beam polarization angle for 200 keV, 300 keV, 400 keV and 511 keV [96].

Other method to generate polarized photons is by irradiating a target with an unpolarized beam. The generated Compton photon beam will be partially polarized, see section

1.2.1. In 2014 this method was employed in a polarimetry dedicated workbench designed at LIP laboratory [88]. A ^{22}Na source was placed a few centimetres from an aluminium target and the detector plane was placed perpendicular to the source in order to detect the scattered photons with scattering angles of ~90°. For this photons was expected a polarization degree of 66.6%. The polarized beam generated in the target is uncollimated, so instead of previously tested irradiation conditions such as central matrix pixel scatterer or scatterer-calorimeter configurations, in this case the detector was irradiated a large active detection surface where all the detection units (pixels) operated simultaneously as a scatterer and as an absorber. The detector was additionally rotated for three different azimuthal angles relatively to the polarization direction: 0°, 45° and 90°. The results are summarized in table 2.3 and exhibited a fairly good agreement with the expected results emphasizing the fine potential of CZT based polarimeters operating under low flux and low polarization levels.

Table 2.3: Measured polarization angle, modulation factor and estimated polarization degree [88].

Detector Angle (°)	Measured Polarization Angle (°)	Modulation Factor, Q	Degree of Polarization (%)
0	12.0 ± 5.8	0.117 ± 0.018	39.0 ± 6.0
45	33.3 ± 9.53	0.118 ± 0.019	39.3 ± 6.3
90	97.5 ± 4.3	0.116 ± 0.009	38.6 ± 3.0

POLCA series experiments showed that CdTe based pixels Arrays could potentially perform fine polarimetric measurements up to 650 keV. Table 2.4 summarizes the results obtained. It reveals the performance of this kind of detectors for different situations that could occur in astronomical context. Different test configurations were also evaluated.

Table 2.4: Performance of CdTe based detectors in different experiments.

Reference	Parameter analysed	Relevant Results
[90]	Detector thickness	Higher *Q* factor for thinner detectors.
[92]	POLCA II performance	The *Q* factor as function of the energy was obtained.
[93]	Performance of Laue lenses	Laue diffraction process does not affect (within few %) the polarization
[95]	Inclination of polarized beam	*Q* factor degradation for tilt angles >2°.
[96]	Polarization Degree	Good results agreement with the expected degree of polarization.
[96]	Polarization Angle Orientation	Good results agreement with the expected angles of polarization.
[88]	Polarized beam obtained through the scattering of an unpolarized beam in aluminium target	POLCA II was able to obtain the polarization parameters of the low level and low fluxes produced.
[88]	Full surface irradiation tests	Full surface analysis in agreement with one pixel irradiation analysis.

2.3 Compton-POLCA Design

Based on the knowledge gained in the previous experiments a new design was developed for this thesis, the Compton-POLCA. The main challenge for this work is to develop the system based in two CdTe ACRORAD detectors that consists in a more realistic approach of a real mission instrument, as the NFT, since these are composed by several layers of detectors. The two detectors planes should be on top of each other and the system must allow the movement between them. With this geometry we can evaluate the performance of the polarimeter as a function of the scattering angles of the interactions. These studies are essential to validate the multi-layer configuration when operating as polarimeters. The system developed is schematized in figure 2.13 and consists in the following subsystems:

– *Detection System*: Two detectors of 64 pixels each.

– *Front-end electronics (*POLCA-FEE*)*: 8×16 channels eV Products ASICs.

– *Read-out electronics (*TAKES*)*: 128 channel capability, coincidence circuitry and digital-to-analog converter.

– *I/F*: Serial to parallel interface box.

– *Acquisition board (*NI DAQ PXI-6533*)*: Data acquisition computer interface.

– *Computer*: data collecting system operating under user written software in LabVIEW® environment.

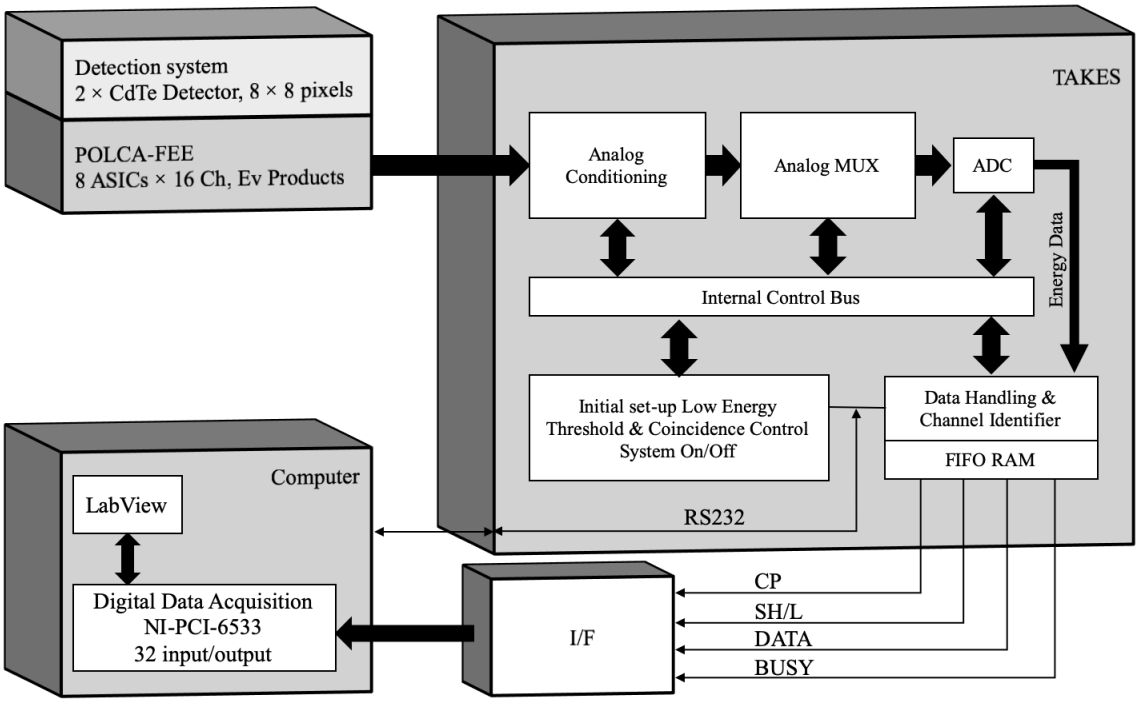

Figure 2.13: Compton-POLCA system diagram.

2.3.1 Detectors

The detector prototypes available for this work were 2.0 mm thick ACRORAD ohmic CdTe matrices with 8×8 pixels, each pixel with 1.9×1.9 mm^2 and 0.1 mm gap between consecutive pixels, for a total 2.56 cm^2 sensitive area. In the segmented side, the electrodes (anodes) were composed by Au/Ni/Au/Pt while on the crystal opposite side the contact electrode was a 300 nm thickness layer of Pt. A diagram of the detectors and a picture of a bare detector seen from anode side are shown in figure 2.14.

The spectral performance of one of these detectors was evaluated during the master thesis of Nelson Simões [192], which also intended to measured and analysed the effects generated by protons on CdTe. The measured operational characteristics are summarized in table 2.5. Notice that for this experiment only a sub-group of 2×2 pixels was evaluated without any pixel discrimination.

Table 2.5: Operational characteristics of the CdTe detector operated at room temperature and -600 V [192].

Active Area	~0.16 cm^2
Leakage current density – $I_{leakage}/A$	0.51 ± 0.08 μA/cm^2
Equivalent noise charge	595 ± 8 e^-
Energy resolution	12.6 ± 0.4% @ 122 keV 4.6 ± 0.2% @ 511 keV 2.3 ± 0.2% @ 1275 keV

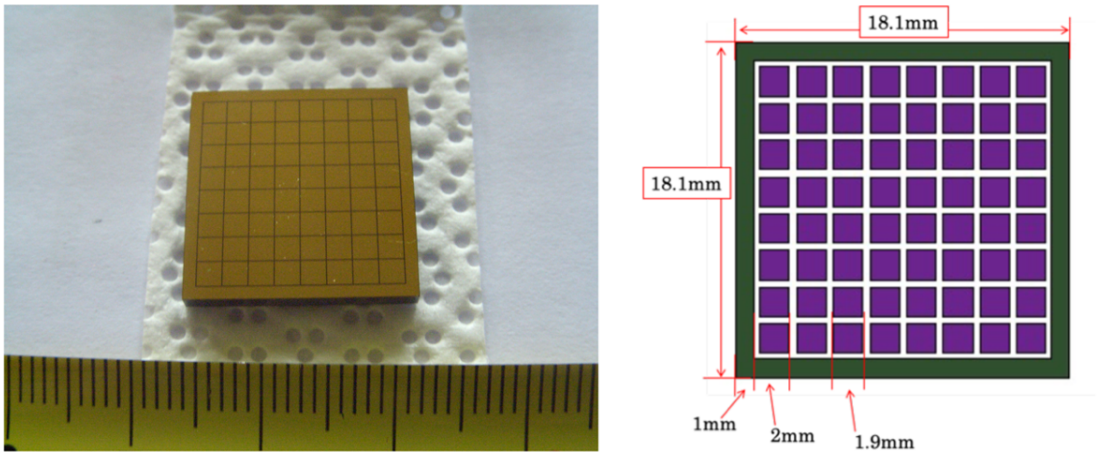

Figure 2.14: Left: picture of an ACRORAD bare detector seen from anode side. Right: dimensions diagram of a detector.

Five of the detectors available were bonded by AUREL in 2013 to custom-made PCBs. The objective was to apply the detectors easily to different experiments. Two configurations were designed: vertical pins configuration (figure 2.15 left); and horizontal pins configuration (figure 2.15 right). In the first design of the Compton-POLCA we used of one detector with vertical pin configuration for the bottom plane detector and one with horizontal pins configuration for the top plane detector. However, during the system assemble phase we come across several problems with the bonding of these detectors. The bonds between the detector and the PCB broke very easily and we lost several units because of this problem. We were able to repair and use two detectors for the 2017 ESRF campaign, however with a modest performance. This mechanical configuration will be presented in detail in section 2.3.3.

In the second version of the Compton-POLCA we contracted the Due2lab to perform bonds on ACRORAD bare detectors. The new boards were made in DiClad laminate, a

reinforced composite for use in high frequency applications, and customized for the Compton-POLCA system. A picture of the new boards is shown in figure 2.16 and a detailed explanation about the mechanical configuration is made in section 2.3.3.

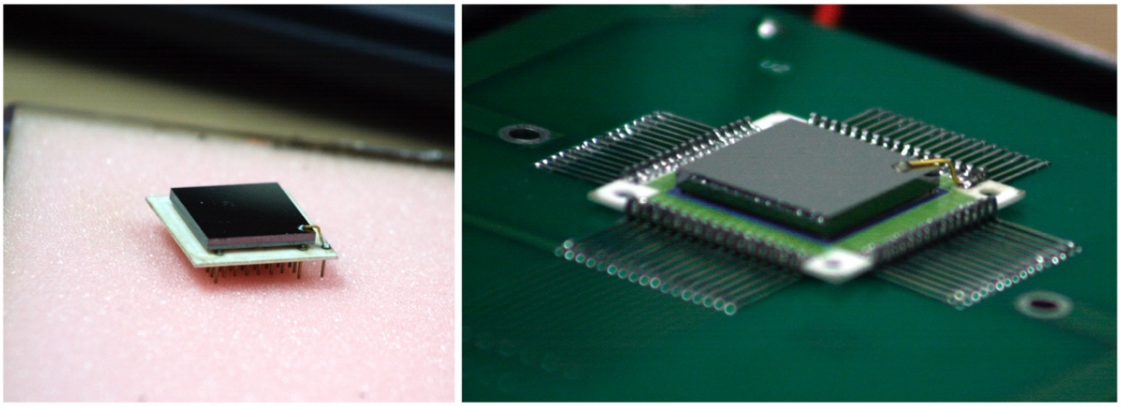

Figure 2.15: ACRORAD detectors bonded by AUREL. Left: vertical pin configuration. Right: horizontal pin configuration.

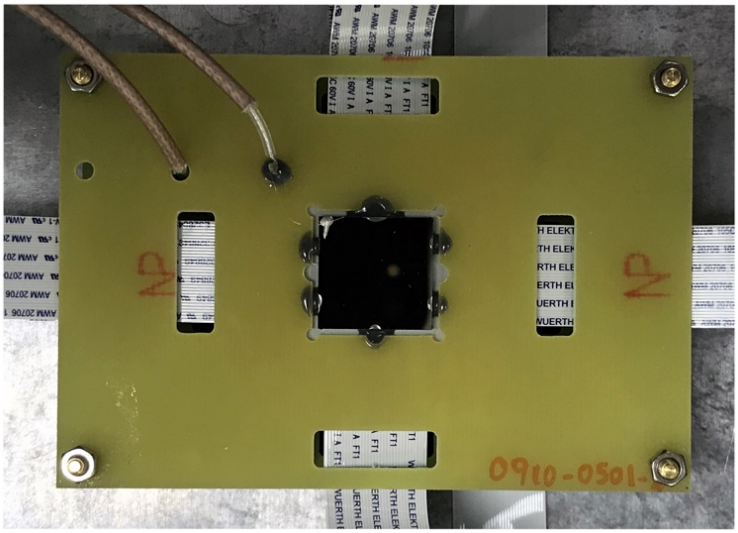

Figure 2.16: ACRORAD detectors bonded to a DiClad laminate by Due2lab. To improve the mechanical resistance the sides of the detector where glued with epoxy to the board.

Each detector needs to be biased with a negative voltage applied to the cathode. To do this we use a DC-DC convertor, an EMCO CA05N-5, which is capable to convert a +5V DC voltage into an adjustable negative high voltage to bias the detector (-500-0V). The circuit implemented is shown in figure 2.17. The high voltage can be adjusted by action

of a potentiometer and a HV monitor can be used to read a low voltage (0-2.048V) that is proportional to the high voltage applied to the detector (-500-0V). To avoid damaging the detector, a *RC* circuit is placed in the regulator output. This will ensure that the voltage is applied gradually to the detector. For the *RC* values used we expect that the detector is fully biased after ~2 min. The power regulation circuit was placed inside the detector box in the first prototype version but, for the second version, we decided to remove all the active components inside the detector box to avoid thermal heating the CdTe, and an external box and a PCB were designed for that propose. For all the experiments the bias voltage was set to -100V.

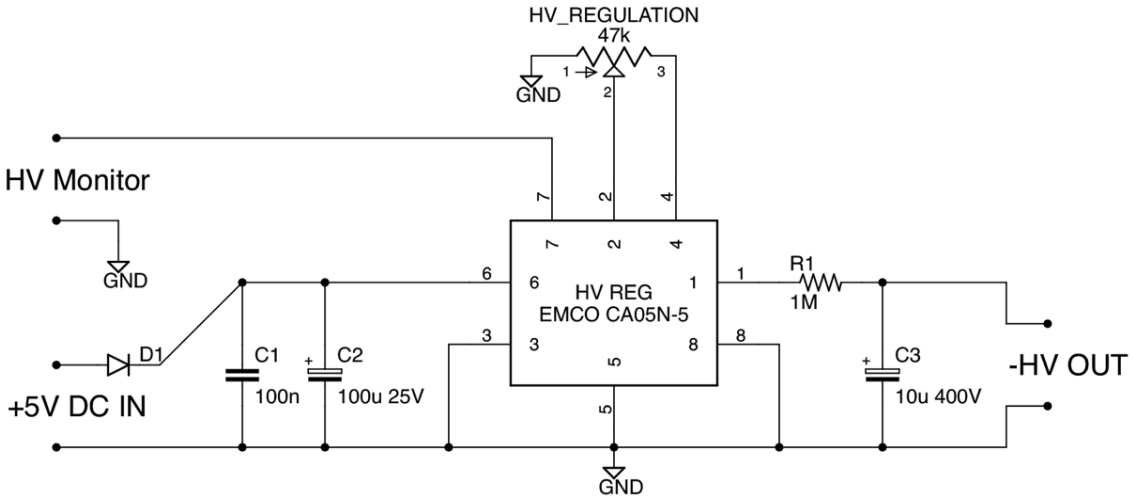

Figure 2.17: Electronic diagram of the DC-DC converter circuit that provides the high-voltage to the detector.

2.3.2 POLCA-FEE

The front-end electronics converts the detector charge into a voltage pulse with amplitude proportional to the charge collected. Each pixel will be independently amplified and shaped. This was commonly implemented using discrete transistors and operational amplifiers. Nowadays, with the big development in the detectors the number of channels/cm^2 increased substantially, conditioning the use of the big discrete electronics used before. Integrated circuits with sub-micron feature size have now been used. Those imaging systems are read out by custom-made ASICs.

The front-end electronics available is a custom-made unit based on 8 ASICs from eV Products, with 16 channels each. This unit has been in use since the POLCA 2 experiments and we name it POLCCA-FEE. In figure 2.18 is shown the electronic schematic of one ASIC which receives the charge of 16 pixels from the detector and converts individually to a voltage pulse through 16 analog outputs. The schematic is them reproduced by 8, allowing to read the 128 pixels signals from the detectors. In figure 2.19 is shown the POLCA-FEE PCB and its enclosure. The input connections from the detectors are made through 2×100 pin Panasonic connectors (figure 2.19 right) and the outputs are made through 8×DB37S Connectors, one for each ASIC, placed in the peripheral side of the box (figure 2.19 left). The power regulation is made with a LT1763, which converts the input voltage (+4V to +20V DC), to the operation voltage of the ASICs (+3.0V).

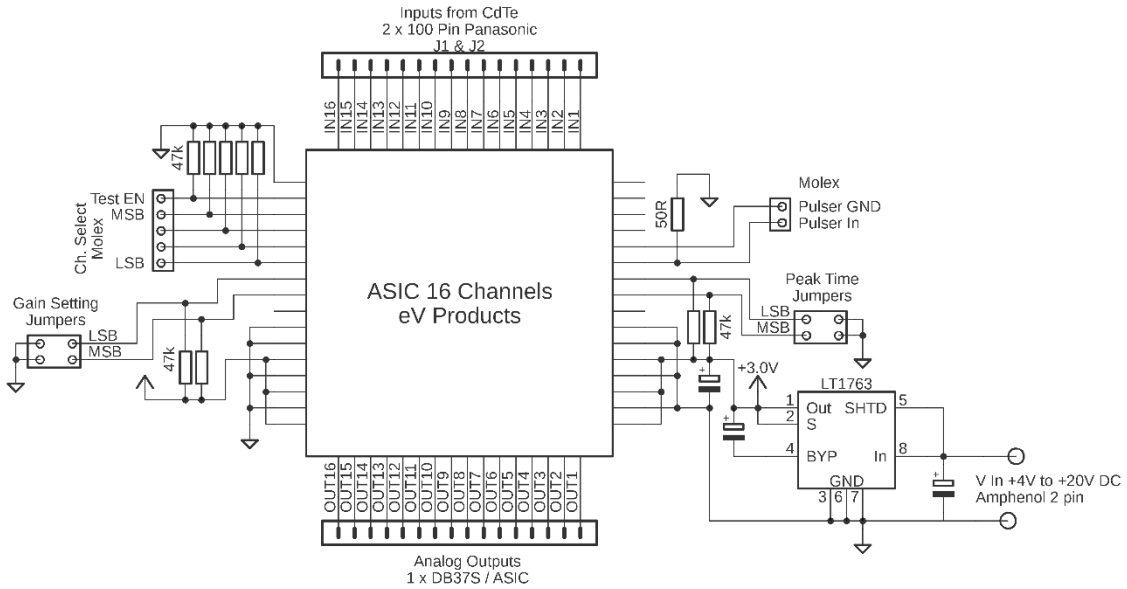

Figure 2.18: Electronic schematic for one ASIC of the POLCA-FEE.

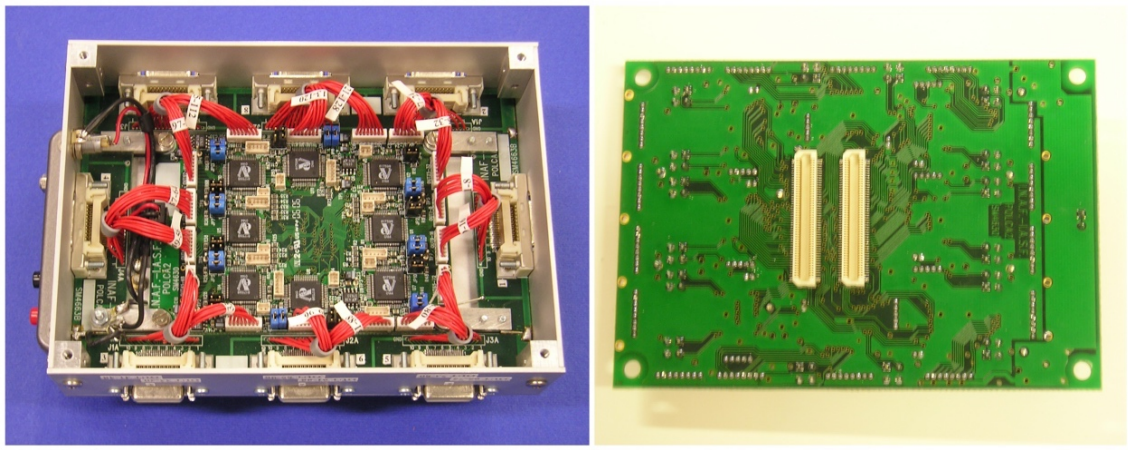

Figure 2.19: Picture of the POLCA-FEE board. Left: bottom side; Right: top side.

Several features are available in the POLCA-FEE. By acting on couples of on-board jumpers, any ASIC's gain and peaking time can be independently regulated. The possible values are listed in table 2.6. The ratio between the ASIC output voltage and the energy was obtained in previous experiments and is presented in figure 2.20. Based on these results we set the gain to 50 mV/fC and a shaping time of 1.2 µs for each ASIC. By using these values, we expect that the system is able to read photon energies up to 1 MeV. This value is further adjusted in the read out system.

Table 2.6: Possible values for the peaking time and gain of the ASICs, settable by two set of micro-switches on the ASIC board.

Gain	JP (i)		Peaking	JP (i+1)	
(mV/fC)	LSB	MSB	Time (µs)	LSB	MSB
200	0	0	0.6	0	0
100	1	0	1.2	1	0
50	0	1	2.4	0	1
33	1	1	4	1	1

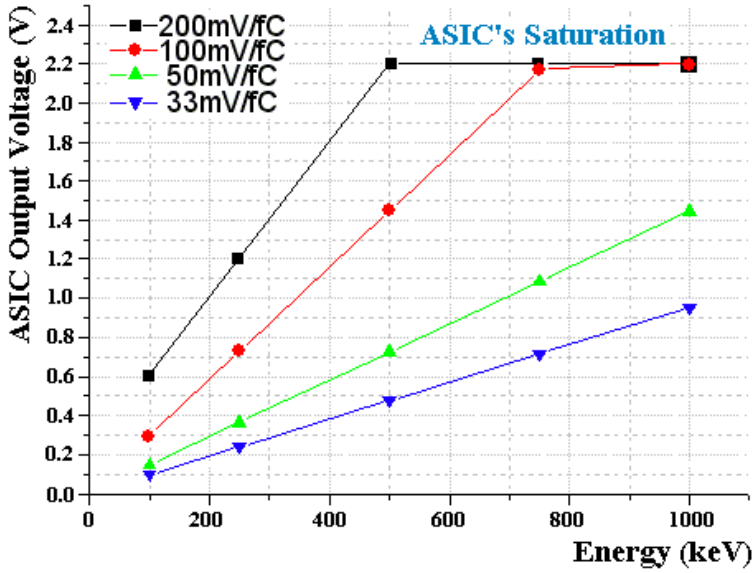

Figure 2.20: The operational range of ASIC vs set gain value.

2.3.3 Detectors and POLCA-FEE Mechanical Arrangement.

One of the main challenges for this work was to develop an electro-mechanical arrangement that could incorporated the two detector planes and the POLCA-FEE. The main requirements for the design were:

– Two detector planes on top of each other.

– Possibility to change the distance between planes.

– The detectors should be aligned to each other.

– The interface with the POLCA-FEE should be through 2×Panasonic 100 pin connectors.

– The electronic path between the pixel and the connector should be as minimum as possible to prevent signal loss and cross talks.

– Both detectors should enclose in one light tight and electrically shielded container.

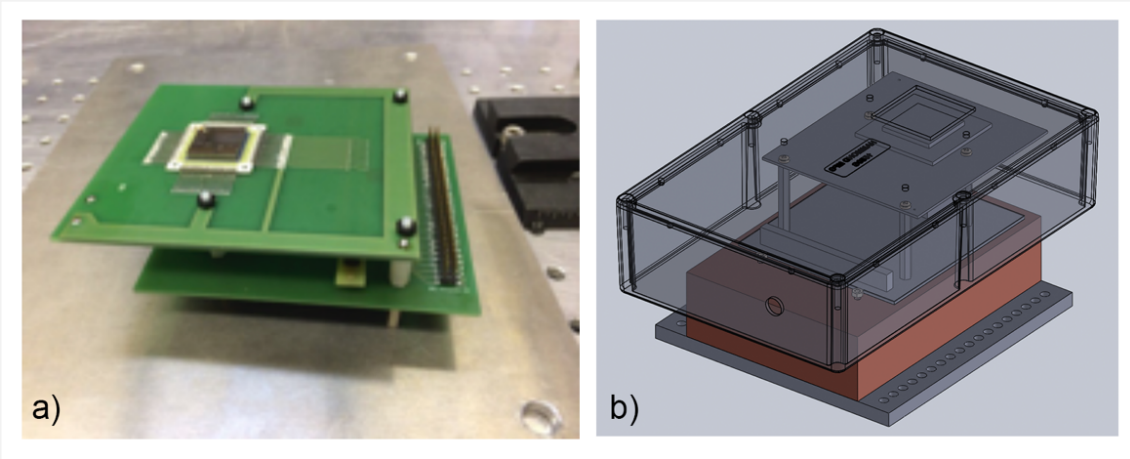

Figure 2.21: a) Picture of the two PCBs developed to place the ACRORAD detectors with the AUREL configurations shown in figure 2.15. b) CAD drawing Compton-POLCA detector and POLCA-FEE mechanical arrangement. The top enclosure is transparent only to show the two detectors PCBs; the red box is the POLCA-FEE.

In figure 2.21 is presented the first version of the electro-mechanical design where each detector is placed in an individual PCB (figure 2.21 a)). The bottom PCB is fixed and is used as interface for the POLCA-FEE, containing the and 2 Panasonic connectors on its bottom side. The connection between the top PCB and the bottom PCB is made through a 64-pin flat cable. To change the distance between planes we use hexagonal aluminium spacers between the two PCBs, which are available in many different sizes. However, this process revealed to be very intrusive and time consuming and, due to the critical conditions of the detector's bonds, this process lead to the loss of several pixels during the experiment. In figure 2.21 b) is shown the Computer-aided Design (CAD) where the POLCA-FEE (red box) and the detectors enclosure (transparent) are visible.

The detector and POLCA-FEE mechanical arrangement was redesigned in 2018. We used two ACRORAD bare detectors and we contracted Due2lab to perform bonds in a new board made in DiClad laminate, a reinforced composite for use in high frequency applications. Based on the experience we had with the previous design, several features were improved on the new design. Each detector was soldered in an individual PCB, and a third PCB was designed to make the interface between the detector boards and the front-end electronics, see CAD drawing in figure 2.22. The bottom side of the interface board includes the two Panasonic connectors (J1, J2) to connect to the front-end electronics and, the top side of the interface PCB, 8 high density connectors to connect the PCB boards via 8 flexy cables (4 for each detector board) (figure 2.23 left). To adjust the distance

between planes a new system was developed. The bottom detector is fixed, and a spring/rod system is placed to move the top detector externally. Four knurled nuts outside the box allows the user to change the distance between planes continuously. The rod has an M3 thread with a 0.5 pitch, thus, by placing a marker in the knurled nuts we are able to precisely know the distance by counting the number of turns. A section view of the CAD drawing, highlighting the new translation system, is presented in figure 2.24.

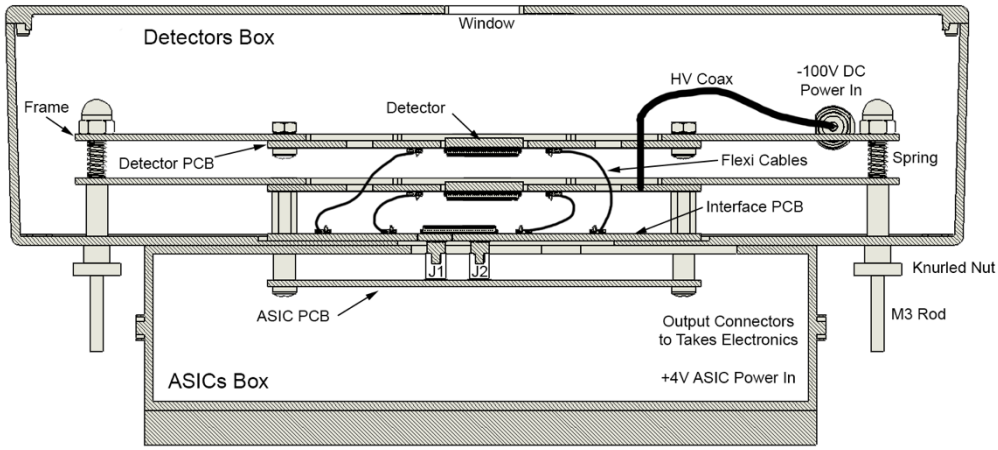

Figure 2.22: Mechanical drawing of the second version of the Compton-POLCA detector and POLCA-FEE mechanical arrangement.

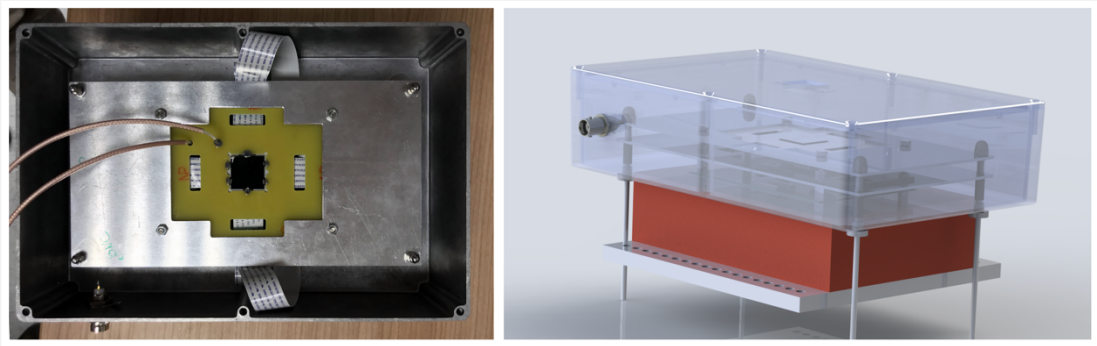

Figure 2.23: Picture and drawing of the second version of the Compton-POLCA detector and POLCA-FEE mechanical arrangement.

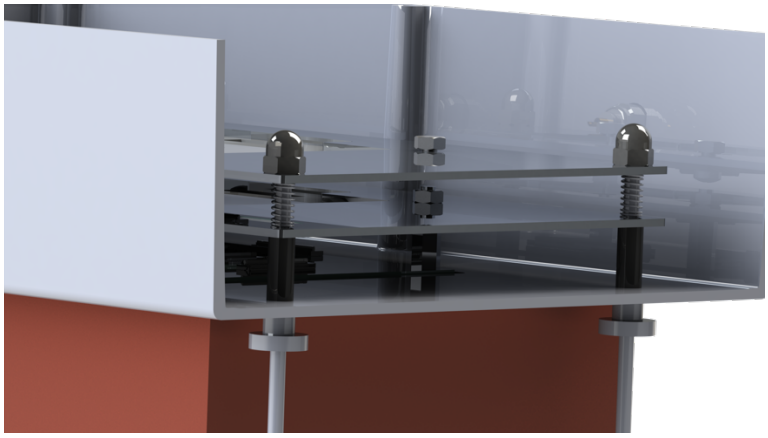

Figure 2.24: Section view of the Compton-POLCA CAD drawing, highlighting the detectors translation system.

2.3.4 Read Out Electronics

To read the analog signals from the FEE and convert to digital we used a custom-made unit that we call the TAKES (figure 2.25). This unit has been in use since the POLCA 2 experiment. It consists in 8 boards, with 16 channels each, that receive the analog signals from each POLCA-FEE ASIC. Any analog signal entering the TAKES is firstly presented to a voltage comparator that exclude the signals below a certain voltage defined by the user. This value will correspond to the minimum energy threshold of the system, E_{min}. If the analogue signal overcomes E_{min}, is then stretched for a time of the order of the input pulse rise-time (~0.7 μsec) and converted in digital by the ADC. Each channel gain can be adjusted individually by using a trimmer inside the TAKES, and to ensure that the signal does not saturate and extend the system operational range we also interface the ASICs and the TAKES board with 12 kΩ resistors. We expect a total operational range between ~40-750 keV.

The digital signals will then pass through a coincidence system that discriminate the single, double and multiple events. The system sends a flag if two signals are detected within the coincidence time, selectable among 1, 2, 4, 8 and 16 μs. The system also comprises a relative time counter gives the temporal gap between two subsequent events with a time resolution of 0.8 μs. The 11bits available allows a maximum gap between two subsequent events up to ~1.6 ms (i.e. ~600 counts⁄s). Above this value the TAKES sends a time-overflow flag. The final output word of the TAKES is composed by 32 bits (table 2.7) coded in serial form. The data is then converted in parallel form, in an external serial-

to-parallel interface box, and read in a NI PXI-6533 data acquisition hardware that is connected to a computer.

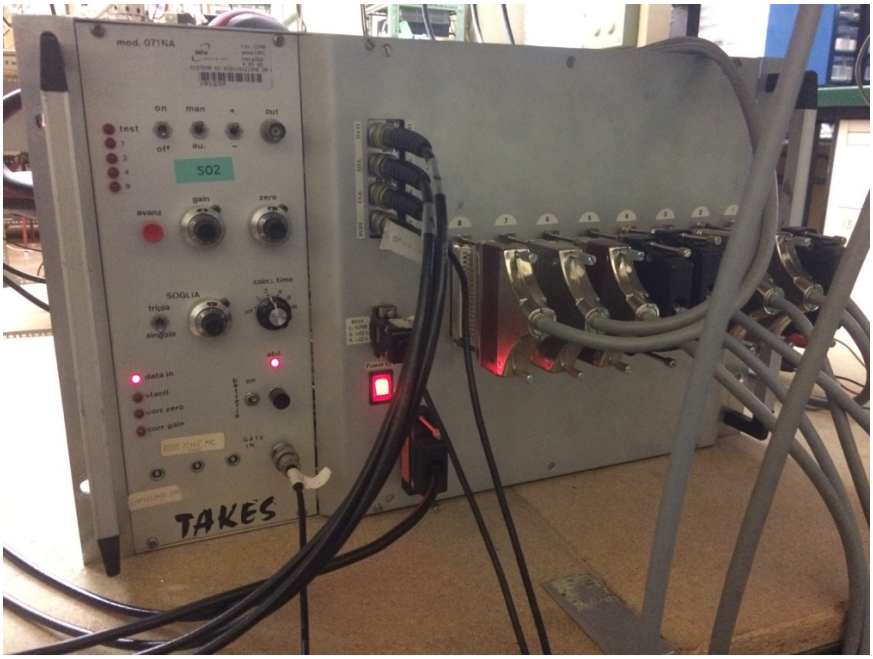

Figure 2.25: TAKES multiparametric back-end.

Table 2.7: TAKES output data format.

Data Field	TAKES Word (Bit)	Length (Bit)	Notes
Energy	0-9	1024	Energy of the hit.
EO	10	2	Energy Overflow: if the signal is higher than the system operational range this flag is set to 1 (energy overflow), while 0, is marked as a "good event".
EE	11	2	End of Event: if the time gap of the subsequent event is lower than a value selected, this flag is set to 1 and the hit belong to a multiple event. If 0, the hit is a single event or the last hit of a multiple event.
Channel #	12-19	256	TAKES Channel given in 8 bits. Only 7 bits are used for the 128 channels.
Time	20-30	2048	Time intervals between two subsequent events. The time in seconds is obtained by multiplying this value by 0.8 μs.
TO	31	2	Time overflow flag: this flag is set to 0 if the time interval is less than 0.8×2048 s, while is 1 (overflow) in the opposite case.

Each channel number presented in the output word corresponds to a specific channel ASIC which in turn corresponds to a real detector pixel. For a correct visualization of the data we need to convert the TAKES channel in a pixel number in the acquisition and analyses software. Firstly, we assign the detector pixels numbers as presented in figure 2.26 and then we associate for each pixel the correspondent TAKES channel presented in figure 2.27. In both maps is shown also the ASIC chip association for each pixel.

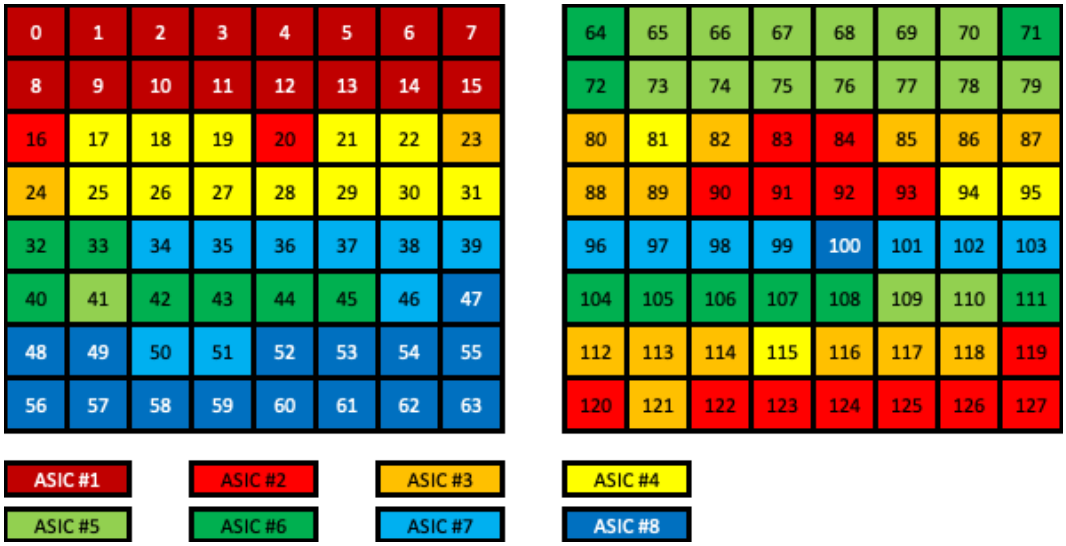

Figure 2.26: Numbers assigned to the detector pixels. Left is the bottom plane detector and right the top plane detector.

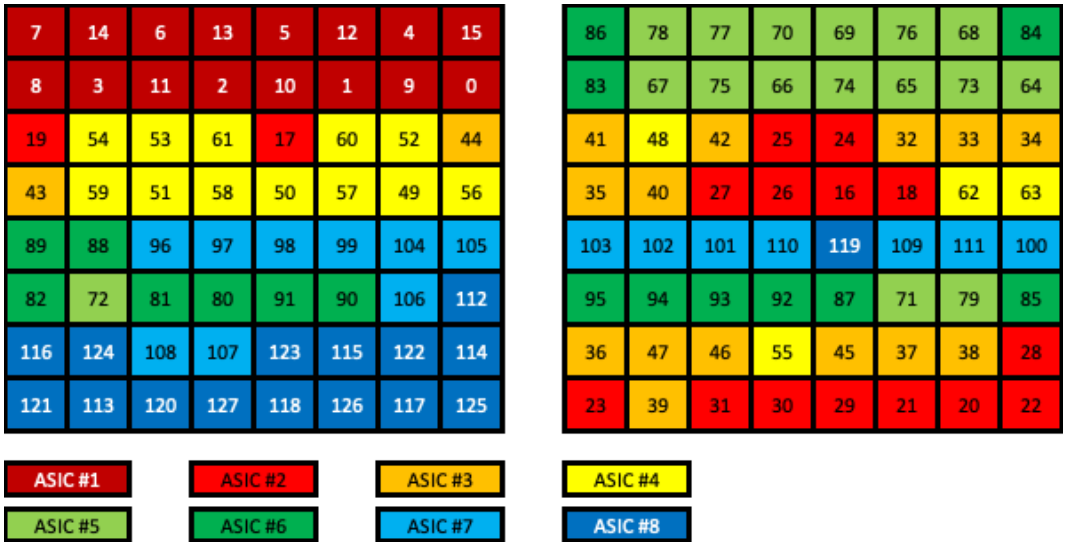

Figure 2.27: TAKES channel association of the pixel number in figure 2.27. Left is the bottom plane detector and right the top plane detector.

2.3.5 Acquisition Software

The acquisition software was developed in LabVIEW® and was designed to read, decode and record the output from the TAKES system. The software was designed to allow real time analyses, such as, real-time spectrograms, intensity maps and pixel histograms. This information will allow to monitor the experiment and obtain the position and energy of the beam, count rate, etc. The software also records the data in an ASCII file so it can

be analysed by an external software to perform the analyses. In figure 2.28 is presented the software flowchart which is divided in three sections: Configuration; Acquisition Control; and Real Time Analyses.

Configuration: These section groups the configurations that must be set by the user before starting the measurement (bottom/left of the user interface in figure 2.29). It features the following controls:

– Acquisition mode: Test – The data will be discarded at the end of the acquisition; Measure – the data will be saved in an ASCII file.

– Acquisition end: it is possible to define the end of acquisition by the total number of counts or total time.

– Measurement file name: name of the file that will be saved. The suffix will increment automatically if it sees the same name in the folder.

– Log file comment: used to record characteristics of the acquisition, e.g. beam energy.

– Look up table: turn on or off the look up table that converts the TAKES channel ID into pixel ID.

Acquisition Control: Groups the acquisition start and stop and the acquisition general parameters that are monitored in real time during the measurement (top/left of the user interface in figure 2.29):

– Start/Stop acquisition.

– Acquisition parameters updated in real time: start date; time elapsed; total number of counts; and total counts per second.

Real time Analyses: The software is designed to provide a set of real-time analyses to monitor the experiment. The following features are available.

– Intensity maps (bottom/right figure 2.29): Each detector has its own intensity map that accumulates the events in the correspondent pixel. A cursor in each map allows to select a pixel. The information of the selected pixel is presented in the boxes below: pixel counts; pixel number; TAKES channel number; ASIC number and ASIC channel. Three switches on bottom allows the user to: switch off the selected pixel; reset all the pixels to zero counts; and switch on all the pixels.

– Energy Spectrum (top/right figure 2.29): energy spectrum of the selected pixel. The four controls on right allows the user to select: between the bottom detector cursor or the top detector cursor; linear scale or logarithmic scale; reset the spectrum to zero counts; and auto reset to zero counts in a defined time interval (especially useful to make the gain equalization). The other control on the right allows to get peak details, using the two vertical cursors on the graph.

– Pixel histogram (top figure 2.30): histogram of the 64 pixels of each detector. The switch on right allows the user to select between detectors

– ASIC histogram (bottom figure 2.30): histogram of the ASIC channels. The knob on right allows to select the ASIC.

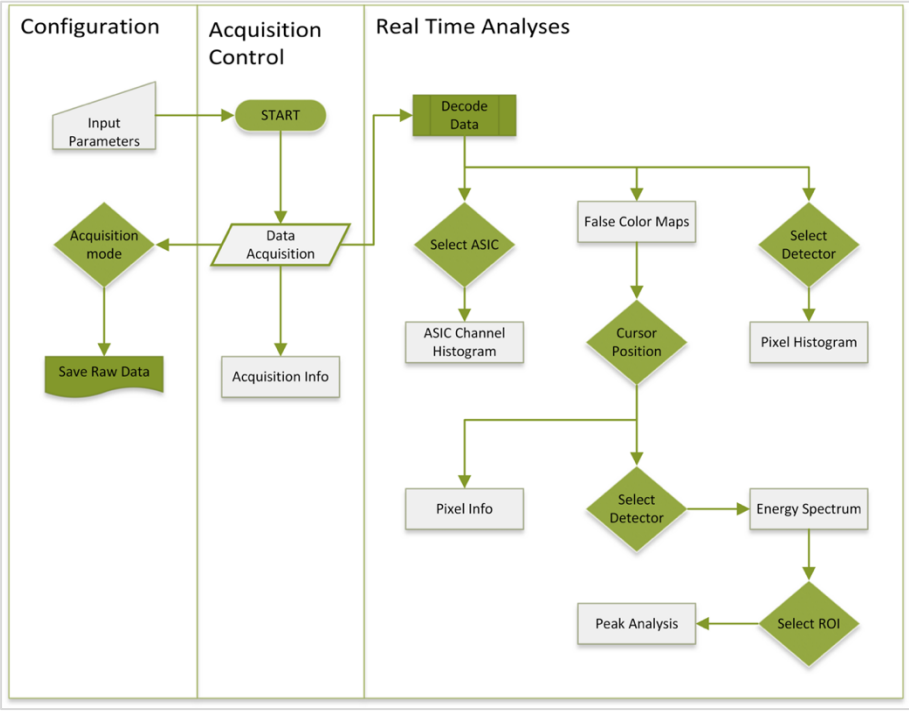

Figure 2.28: Software flowchart.

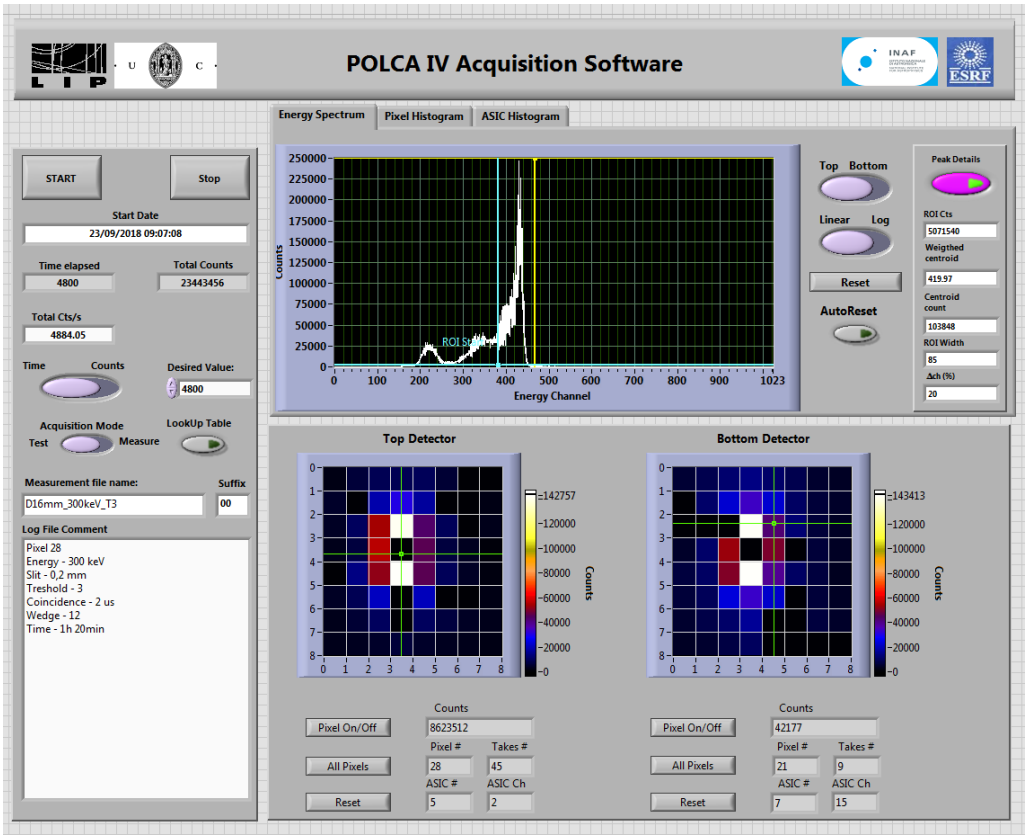

Figure 2.29: Main window of the Compton-POLCA Acquisition Software. Screenshot took during the ESRF 2018 campaign.

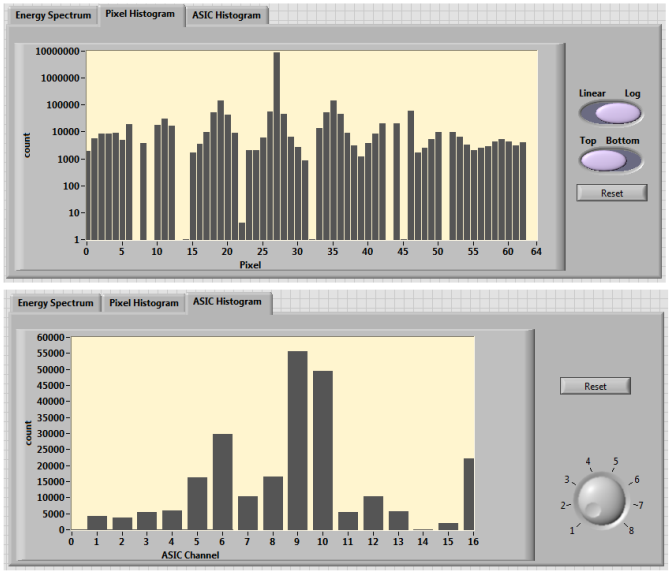

Figure 2.30: Pixel histogram and ASIC Channel histogram. Screenshot took during the ESRF 2018 campaign.

3 Monte Carlo Simulations

In order to analyse the polarimetric performance and plan the tests to be performed at the ESRF with the Compton-POLCA, a series of simulations was performed with Medium-Energy Gamma-ray Astronomy library (MEGAlib). Its objective is to analyse the dependence of the modulation factor in relation of several parameters: energy; distance between planes; beam polarization angle; beam degree of polarization; and minimum energy threshold. The data selection to calculate the polarimetric parameters will be also subject to study. There are two instances of interest in a dual plane detector geometry: single plane interactions, interactions concerning the Compton double events that occur in the same detector; and dual plane interactions, Compton double events that occur in both planes. Both these interactions we will be analysed in order to understand how they influence the polarimetric performance of the instrument. By doing this we will analyse the influence of the scattering angle of the double events selected on the modulation factor Q.

3.1 MEGAlib

MEGAlib is a set of software tools which is designed to simulate and analyse data of gamma-ray detectors, with a special focus on Compton telescopes [193]. While MEGAlib was originally developed for astrophysics, it has been expanded and used for ground-

based applications such as medical imaging and environmental monitoring. The library includes all necessary data analysis steps from simulation/measurements via calibrations and event reconstruction to high-level data analysis such as image reconstruction.

MEGAlib contains a geometry and detector description tool for the detailed modelling of different detector types and characteristics, providing an easy-to-use simulation program based on GEANT4. For different Compton telescope detector types (electron tracking, multiple Compton or time of flight based) specialized Compton event reconstruction algorithms are implemented in different approaches (Chi-square and Bayesian). The high-level data analysis tools allow to calculate response matrices, perform image deconvolution (specialized in list-mode-likelihood-based Compton image reconstruction), determine detector resolutions and sensitivities, retrieve spectra, determine polarization modulations, etc.

In order to start the simulation, the instrument mass model must be created. The Geomega package is included in the MEGAlib software for this propose. In figure 3.1 is presented the mass model created. It is a dual plane detector configuration, each detection plane comprises a 7×7 pixels CdTe matrix, pixel size 1.9×1.9 mm^2, inter pixel gap 0.1 mm and 2 mm thickness. These dimensions are based on the ACRORAD detectors described in 2.3 however, the detector array is an 7×7 matrix instead of a 8×8 because, to avoid asymmetry issues in the analysis, we want that the centre of the matrix is coincident with a pixel centre and that double events distribution could be symmetric. That is only possible in a detector array with an odd number of pixels in each direction. The mass model includes two layers of aluminium on the top and bottom of the detector to simulate the detection system enclosure and a PCB below the detectors. The definition of a trigger is customizable and is defined in the Geomega file. For our proposes we set different triggers depending on the analyses we want to perform. Another important detector parameter defined in the Geomega file in minimum energy threshold of the detector. If the threshold is too high the detector is not able to detect all the photons, specially the Compton events that leave only a small fraction of the original photon energy.

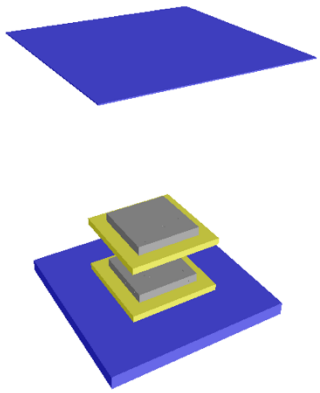

Figure 3.1: MEGAlib CdTe dual-plane Monte Carlo mass model.

A Cosmic Simulator for MEGAlib based on GEANT4 (Cosima) is integrated in the MEGAlib package, and is a universal simulator for low-to-medium energy gamma-ray telescopes. Cosima simulates gamma-rays with specified energies onto the instrument mass model. These gamma-rays interact with the instrument model by means of photo-effect, Compton scattering, and pair creation, as it would in a real environment. These simulation-triggered events are recorded on a “sim” file for further analysis, to be used with tools included in the MEGAlib package. The exposure time of the simulated gamma-rays is user defined by the number of triggered events. Whenever the simulation gives a trigger Cosima stores the hit information in a file. To simulate the ESRF beam we defined a monochromatic, homogeneous beam which simulates a highly controllable environment as the one we will have in the ESRF ID 15A beamline. Figure 3.2 shows the energy spectrum obtained for 100,00 triggered events with beam energies from 100-900 keV in steps of 200 keV.

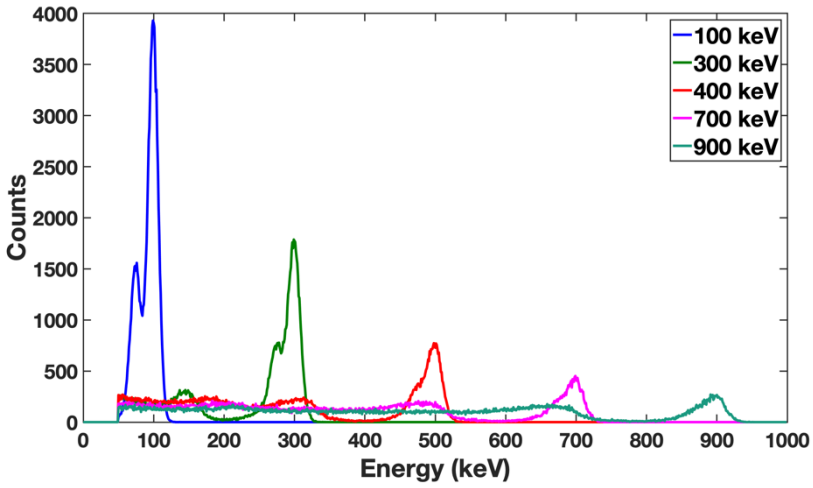

Figure 3.2: Energy spectrum obtained for a 7×7 CdTe dual plane detector configuration for a monochromatic, homogeneous beam of energies from 100-900 keV.

3.2 Event Efficiencies

Since the maximum semiconductor thickness allowed within good detection operational performances is limited, a multi-layer semiconductor detecting system offers the possibility to increase photon detection efficiency by piling several layers of material in a larger sensitive volume. With a higher photon efficiency, we can detect more events which is is an important factor when analysing distant and very often faint astronomical objects. To evaluate the total detection efficiency (i.e. the ratio between the photons that interact in the detector volume and the total number of simulated photons sent in the direction of the detector) of a dual plane detector and compare with a single plane, we irradiate the central pixel of both detector configurations with an homogeneous circular beam with 2 mm radius beam. A systematic study was performed covering energies from 100-900 keV and distances between planes of 4, 8 and 12 mm for the dual plane detector configuration. A total number of 1×10^6 photons were simulated for each case, and the total detection efficiency was calculated by selecting the total number of photons that interact in the detector volume. In order to evaluate the polarimetric performance of the detector we must select the Compton events with two hits in the detector volume (a photon scattering event and a photo-absorption event), thus, the absolute efficiency of these events was also calculated for each simulation.

The results of the total detection efficiency are presented in figure 3.3 and the double event efficiency in figure 3.4. As a result of the increase of the material thickness the total

detection efficiency of the dual plane detector configuration is higher than the total detection efficiency of the single plane configuration For both configurations the total detection efficiency decreases exponentially due to the decrease of the photo-absorption cross section as shown in section 2.1.2. The ratio of Compton interaction rises with the energy resulting in an initial increase of the double event efficiency, as figure 3.4 shows. For this detector thickness, the peak of double event efficiency stands between 200-300 keV and then it smoothly decreases for higher energies, due to the increasing number of photons that cross the material without interacting or that generate a single interaction inside the pixel and then escape from the detector volume. Regarding double events efficiency exclusively interacting with the 2 detection planes as a function of the distance between planes the results show a decrease of the double event efficiency for longer distance between planes. This is consequence of the decrease of the allowed scattering angles: increasing the distance between planes will reduce the hollow cone of Compton events that are scattered on the top detector and absorbed on the bottom detector (figure 1.10). The scattered photons that do not fall within this hollow cone escape from the detector and the position of the second hit is indeterminable. For this 4 mm CdTe total thickness, double event efficiencies of about ~6.5% were obtained: the sum of ~3% (2 × ~1.5%) for the two planes in the single mode plus ~3.5% in the dual mode. The efficiencies presented in figure 3.3 and 3.4 are consistent with previous experimental and simulation results obtained with CdTe detectors by our group, in particular 10%-12% double event efficiencies for 7.5 mm up to 10.0 mm thickness prototypes [91], [194].

The double events' efficiency decrease with the distance is irrelevant for spectral measurements, since the total efficiency is practically identical for all distances (see figure 3.3).

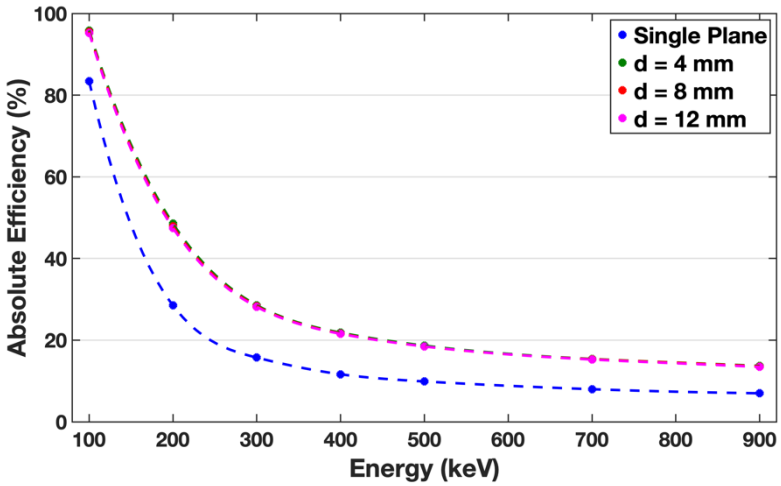

Figure 3.3: Total detection efficiency obtained for the single plane and dual plane configurations in the energy range from 100-900 keV and distance between planes 4, 8 and 12 mm. These latest are practically superposed.

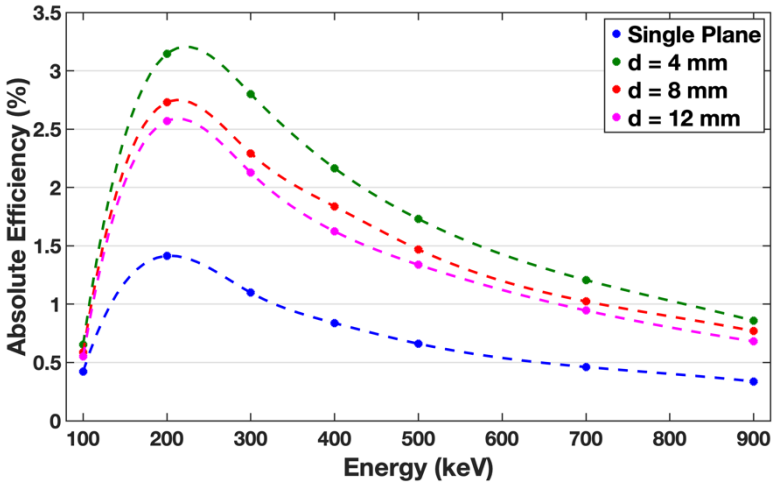

Figure 3.4: Double event efficiency obtained for the single plane and dual plane configurations in the energy range from 100-900 keV and distance between planes 4, 8 and 12 mm.

3.3 Polarimetric Performance

In order to calculate the polarimetric parameters in MEGAlib, two type of simulations must to be performed: a non-polarized beam and a polarized beam. The software uses the nonpolarized data to correct systematic effects due to the detector geometry. Figure 3.5

shows an example for a 300 keV beam presenting the modulation curves for the nonpolarized and the 100% polarized cases. The corrected modulation curve is shown in figure 3.6 along with the fitting curve whose parameters are used to calculate the polarization parameters.

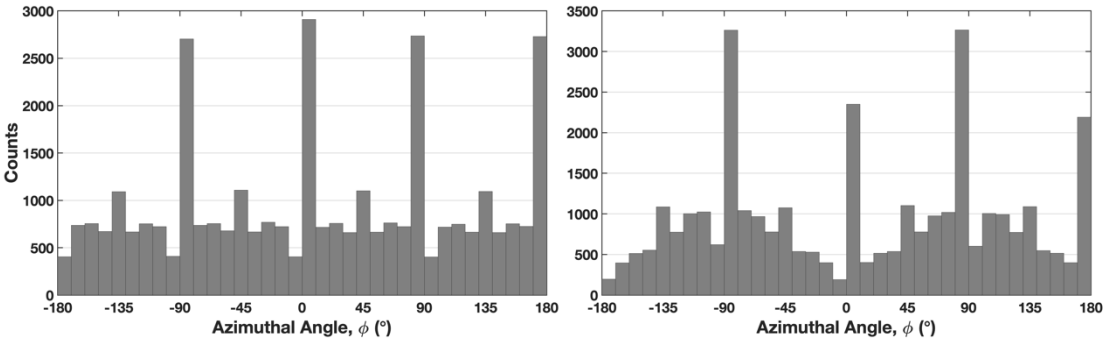

Figure 3.5: Modulation curve obtained from simulations of a nonpolarized (left) and 100% polarized (right) 300 keV beam.

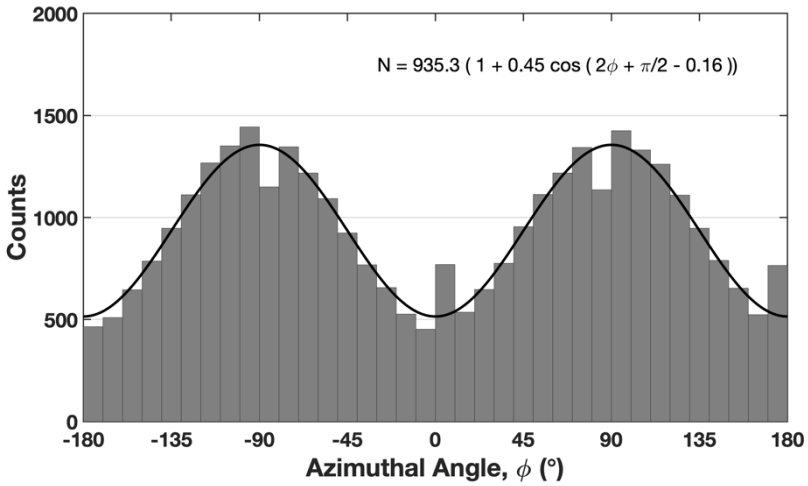

Figure 3.6: Corrected modulation curve obtained when combining the nonpolarized and 100% polarized curves from figure 3.5.

3.3.1 Single Plane Operation Mode

Firstly, we analysed the polarimetric performance of the detector selecting single plane interactions, single plane operation mode. We evaluated it in a single plane configuration and in a dual plane configuration by selection just the double events that occur on the bottom plane. Previous polarimetric studies with single plane CdTe based detectors with

similar characteristics have shown that the best modulation factor is obtained in the energy range between 200 keV and 400 keV (for a Q factor between ~0.3 and ~0.4) [88], [91]–[96], [195].

In figure 3.7, the modulation factor is presented as function of the beam energy for a single plane detector. For this simulation set, a 100% polarized, homogeneous circular beam with 2 mm radius beam was generated, irradiating the central pixel of a single CdTe 7×7 matrix detector. A total of 5×10^5 double events was stored during each measurement by setting the trigger in Geomega to record just the photons that generate two events in the detector. Figure 3.7 also gives an evaluation of the polarimetric performance for two minimum energy thresholds of detector: 30 and 60 keV. As expected, the best modulation factor is obtained in the energy range between ~150 keV and ~400 keV. However, this peak is dependent on the minimum energy threshold of the detector as the figure shows. With a higher minimum energy threshold, the detector is not capable to record all the Compton events due to the small fraction of energy they deposit in the detector, thus reducing the double event efficiency. This effect is presented for energies <200 keV because it is when the energy fraction is lower.

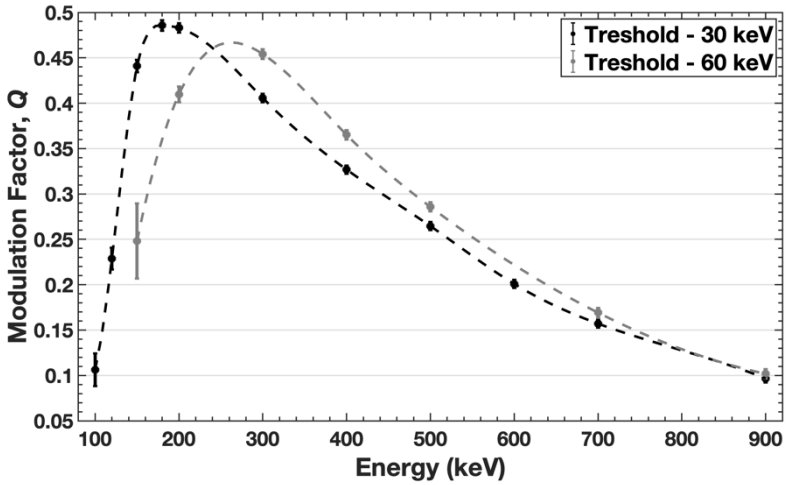

Figure 3.7: Modulation factor as function of the energy for a single plane detector for beam energies from 100 to 900 keV. The black markers are the results for a single plane detector configuration with a minimum energy threshold of 30 keV and the grey markers of 60 keV.

The polarimetric performance of single plane interactions in a dual plane configuration was also evaluated. For this simulation set, a 100% polarized and homogeneous beam

with 2 mm radius was generated, irradiating the central pixel of a dual plane detector configuration. The trigger in Geomega was set to register the Compton double events occurred in the bottom plane thus, for polarimetric evaluation, only the photons that are scattered in the central pixel of the bottom detector and are absorbed also in the bottom detector will be selected. A systematic study of the detector polarimetric performance covering the energy range between 100-900 keV and three distances between plane detectors (4, 8 and 12 mm) was performed. A total of a 1×10^5 double events were stored for each measurement. The results are presented in figure 3.8 where is also shown the single plane case. There are not many differences between the four cases suggesting that the top plane detector do not affect the polarimetric performance of the bottom plane, when operating individually.

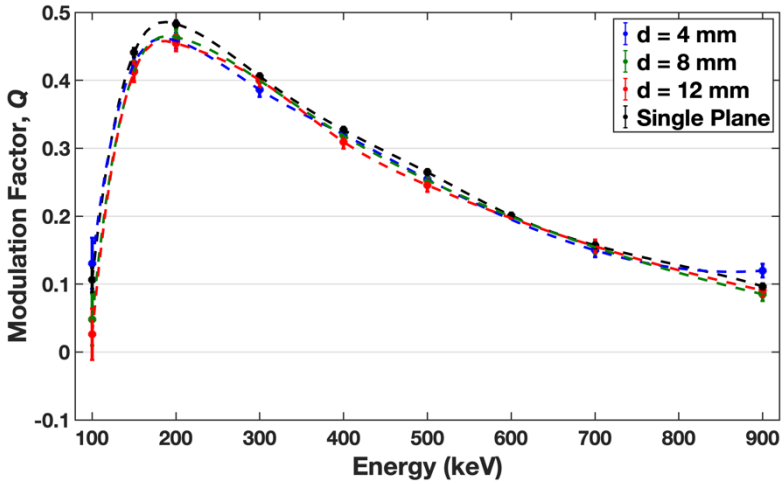

Figure 3.8: Modulation factor as function of the energy for a dual plane detector configuration in a single plane operation mode. The blue, green and red markers are the results for a dual plane detector with distances between planes of 4, 8 and 12 mm respectively. The grey markers are the results for a single plane detector.

3.3.2 Dual Plane Operation Mode

The aim of this simulation set was to evaluate the polarimetric performance of the dual plane detector by selecting only Compton double events that are scattered on the top plane and absorbed on the bottom plane, dual plane operation mode. As seen in section 1.4, in this case the allowed scattering angles forms a hollow cone defined by θ_{min} and θ_{max} Changing the distance between the two planes different θ_{min} and θ_{max} can be achieved. For

this simulation set a 100% polarized, homogeneous beam with 2 mm radius was generated, irradiating the central pixel of the dual plane detector configuration. The simulation trigger was defined to collect the Compton events that tigers both detectors. We simulate these conditions for distances between detectors planes ranging between 4 mm and 12 mm and energies range from 100 keV to 900 keV.

The modulation factor as function of the distance between planes is presented in figure 3.9. As expected, the modulation factor decreases with the increase of distance between layers. Increasing the distance between planes will decrease the values of θ_{min} and θ_{max} and, as seen in section 1.4.1, this will decrease the modulation factor. For this energy range the modulation factor is maximized for scattering angles ~90°. As an example, the θ_{max} for 4 mm is ~75° and for 12 mm ~50°. In figure 3.10 is shown the modulation factor as function of the photon energy, for distances between planes of 4, 8 and 12 mm. The curves are similar to the single plane case, however for higher distances between planes, Q reveals to be approximately constant for energies above ~400 keV.

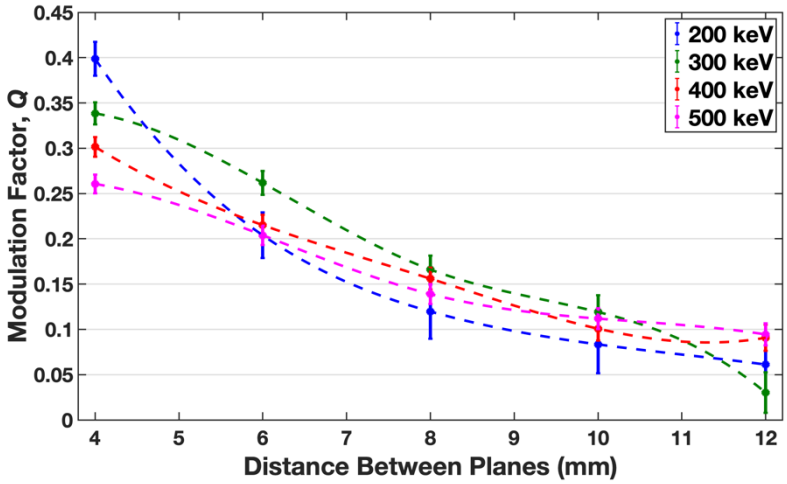

Figure 3.9: Modulation factor as function of the distance between planes for beam energies 200-500 keV for a dual plane detector configuration in a dual plane operation mode.

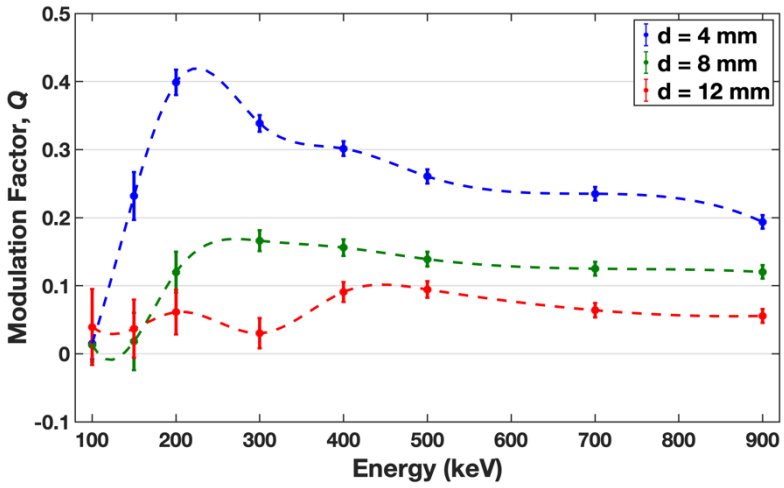

Figure 3.10: Modulation factor as function of the energy for distances between planes of 4, 8 and 12 mm for a dual plane detector configuration in a dual plane operation mode.

The most important parameters when performing astronomical polarimetric analyses are the polarization degree and angle. A higher modulation factor indicates a higher confidence on the measurements of these two parameters. However, is also crucial to test the detecting systems for different polarization levels and angle directions. Thus, the next logical step was to analyse the potential to measure these parameters by selecting dual plane interactions. A systematic study was performed by setting the polarization level from 10% to 100% in steps of 10%, and then changing the polarization direction vector from 0° to 90° in steps of 10°, for the 100% case. For both studies a central pixel of dual plane detector was irradiated by a homogeneous beam with 2 mm radius. We simulated the same conditions for a range of energies from 200-500 keV and inter-plane distances of 4 and 12 mm. The results are shown in figure 3.11 and figure 3.12. The behaviour of both analyses is similar. For an inter-plane distance of 4 mm the results are consistent with the beam parameters. However, for the 12 mm case, where the allowed scattering angles are low, the errors become very significant. This result is in accordance with the low modulation factors obtained when the distance between planes is 12 mm.

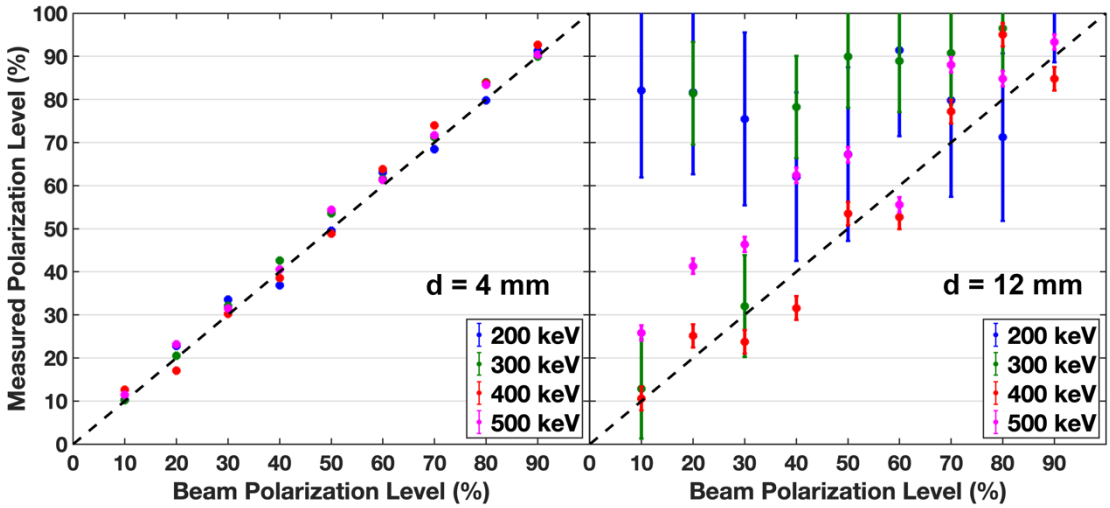

Figure 3.11: Measured polarization level versus beam polarization level for energies 200-500 keV and distances between planes of 4 and 12 mm for a dual plane detector configuration in dual plane operation mode. The dotted line represents the expected result when $\Pi_{obs}=\Pi_{beam}$.

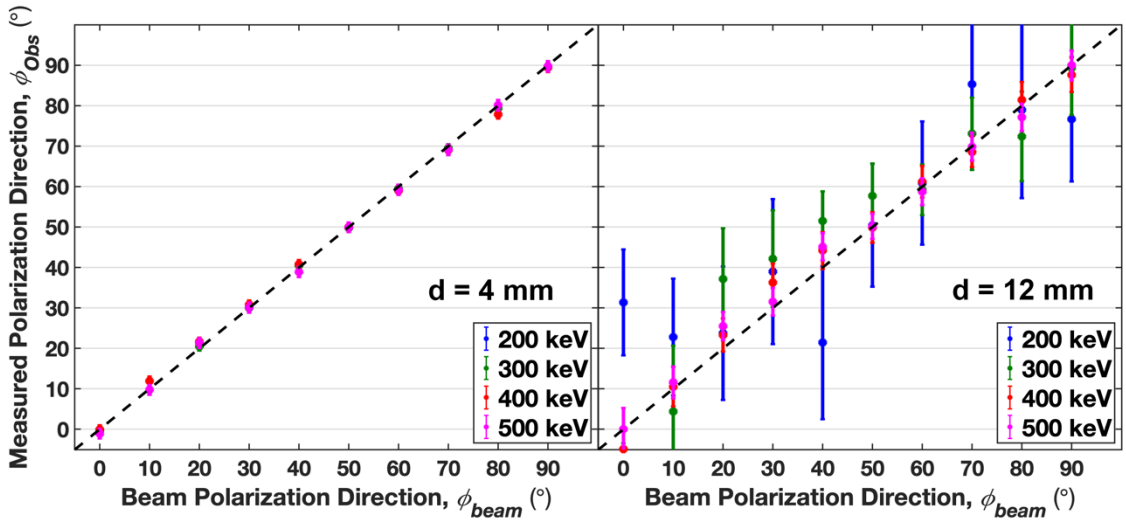

Figure 3.12: Measured polarization direction, ϕ_{obs}, versus beam polarization level, ϕ_{beam}, for energies 200-500 keV and distances between planes of 4 and 12 mm for a dual plane detector configuration in dual plane operation mode. The dotted line represents the expected result when $\phi_{obs}=\phi_{beam}$.

To make a more comprehensive study about the dependence of the modulation factor with the Compton scattering angle in a dual plane detector a series of simulation was

performed with the objective to reduce the range of scattering angles of the events selected for polarimetric analyses as low as the dual plane geometry allow. To achieve this, we irradiated a corner pixel of the 7×7 CdTe arrays and, in each measurement, only the bottom plane double events of one order of pixels are selected. By pixel order we mean the distance from the irradiated pixel, in pixel units. As an example, if we irradiate the pixel number 0: the first order pixels are pixel 1 and 8 and the second order pixels are 3 and 16. As we are interested dual plane operation mode, we refer to pixels on the bottom plane. For a 4 mm inter-plane distance, the first order of pixels will integrate double events with scattering angles from ~14° to ~37°, while for a 7th order case will integrate double events with scattering angles from ~73° to ~75°. In figure 3.13 is presented the modulation factor as a function of the scattering angles for a 300 keV beam. The error on the *x* axis represents the range of scattering angles allowed for each analysis. Three distances between planes are shown: 4, 8 and 12 mm. The results of the different distances align perfectly with each other, showing the increase of the modulation factor with the increase of the scattering angle. The value of *Q* reaches even higher values as the ones in the single plane detector configuration. This suggest that a higher pixel order can provides best polarimetric performances. This effect could be explained by the longer distance between the two interactions forming a double event. Longer distances between double events' interactions provides higher precision on the azimuthal angle measurement increasing the modulation factor.

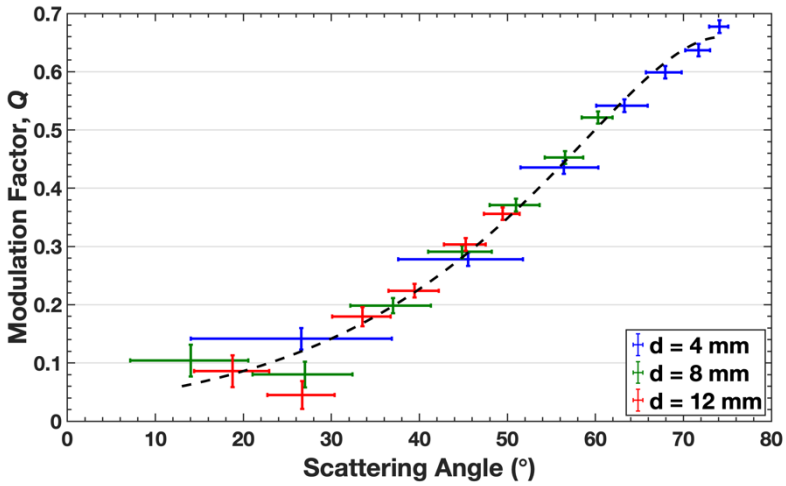

Figure 3.13: Modulation factor as function of the scattering angle for a dual plane detector configuration in a dual plane operation mode irradiating a detector corner pixel by a 300 keV beam, 100% polarized beam.

3.3.3 Full Detector Operation Mode

Finally, we analysed the polarimetric performance of the dual plane detector by combining the previous selections and use every double event that occur in the detector to perform the polarimetric analyses (top plane double events; bottom plane double events; and dual plane double events), full detector operation mode. Therefore, we irradiate the centre of the 7×7 CdTe matrix with a 100% polarized, homogeneous beam with 2 mm radius. We simulate these conditions for distances between planes ranging from 4 mm to 12 mm and energies from 100 keV to 900 keV. A total number of 5×10^5 double events were stored during each simulation.

The results of the modulation factor as function of the detector plane distance are presented in figure 3.14. By combining all the double events, the modulation factor starts by decreasing and then increases marginally with the detector plane distance over 6 mm. The combined modulation starts by decreasing up to 6 mm because the dual plane modulation contribution decreases. Over 6 mm distance, the dual plane mode efficiency shows a decrease that can reach ~25% for 12 mm (see figure 3.4) and therefore this mode contributes with a lower weight for the overall modulation, which, consequently, tends to approach the single layer mode modulation level, increasing marginally with distance (between 2 and 5%). However, the shorter distance configuration between planes is the best option in the full detector mode since best MDP is obtained for the higher detection efficiency case (4 mm), when the modulation varies just marginally with the distance. A 10% better MDP (see equation 1.17) can be estimated for 4 mm, when compared with 12 mm, in the considered simulations' energy band.

In another perspective, figure 3.15 shows the same results, highlighting the modulation factor as a function of the energies for detector plane distances of 4, 8 and 12 mm in the full detector operation mode. The curves follow the same trends of those obtained for a single plane case.

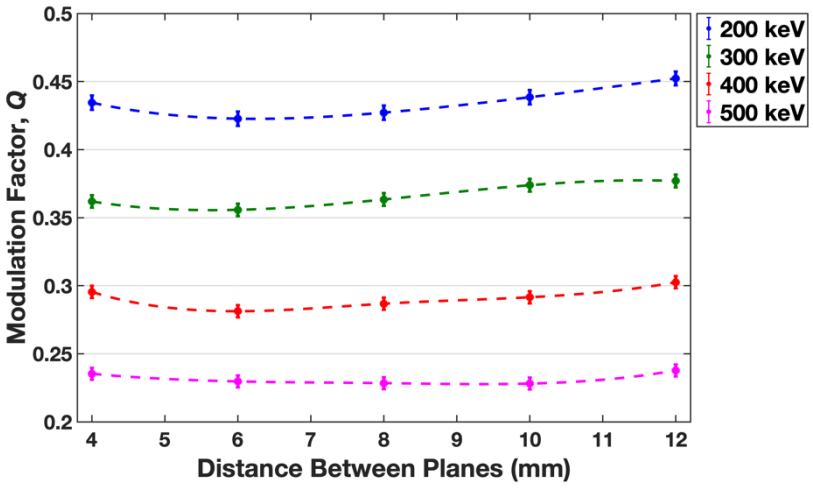

Figure 3.14: Modulation factor as function of the distance between planes for beam energies 200-500 keV for a dual plane detector configuration in a full detector operation mode.

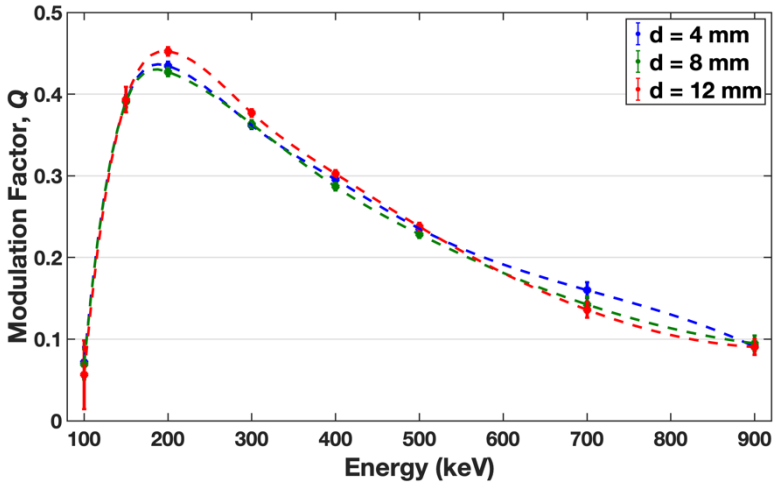

Figure 3.15: Modulation factor as function of the energy for distances between planes of 4, 8 and 12 mm for a dual plane detector configuration in a full detector operation mode.

As we did in the dual plane operation mode, we analysed the potential of the dual plane detector configuration in full detector operation mode detector to determine polarization degree and angle by combining all the double events. A systematic study was performed by setting the polarization level from 10% to 100% in steps of 10%, and then changing the polarization direction vector from 0° to 90° in steps of 10°, for the 100% case. For both studies the central pixel of dual plane detector configuration was irradiated by a

homogeneous 2 mm radius beam. We simulated the same conditions for a range of energies from 200-500 keV and inter-plane distances of 8 and 12 mm. The results are shown in figure 3.16 and figure 3.17. For all distances and energies, this operation mode provides the degree and angle of polarization with great precision. This result is in accordance with the high modulation factors obtained.

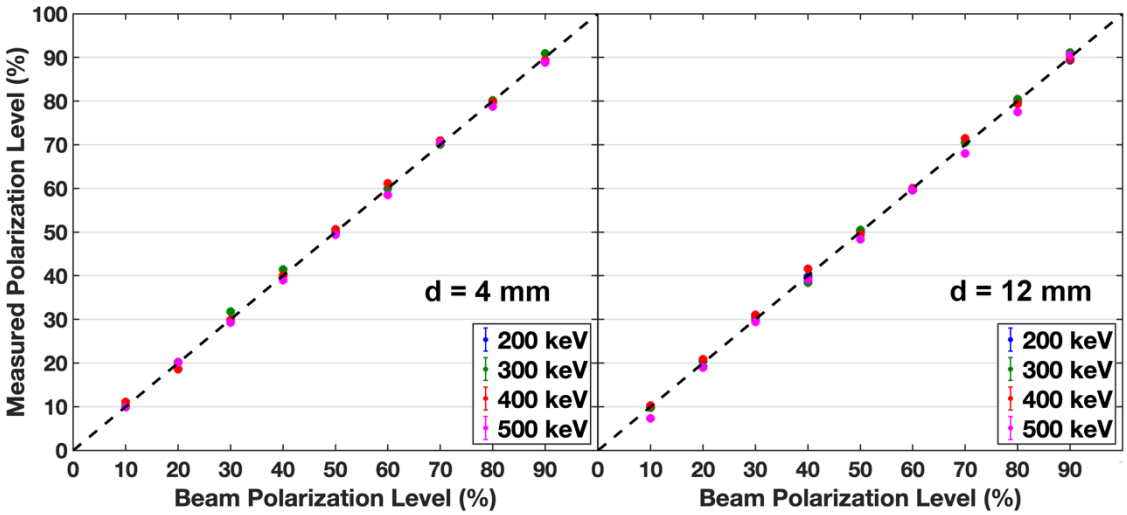

Figure 3.16: Measured polarization level versus beam polarization level for energies 200-500 keV and distances between planes of 4 and 12 mm for a dual plane detector configuration in full detector operation mode. The dotted line represents the expected result when $\Pi_{obs}=\Pi_{beam}$.

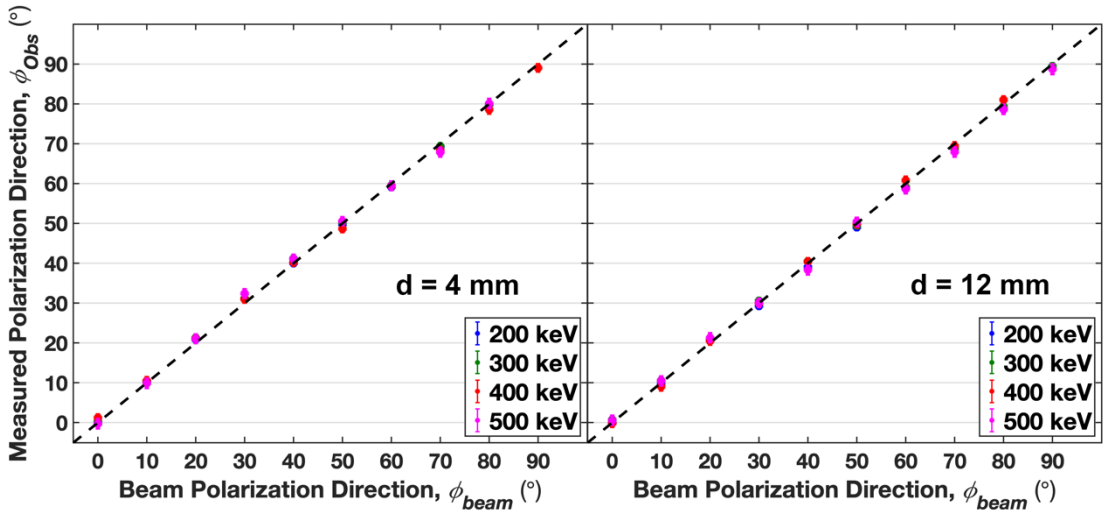

Figure 3.17: Measured polarization direction, ϕ_{obs}, versus beam polarization level, ϕ_{beam}, for energies 200-500 keV and distances between planes of 4 and 12 mm for a dual plane detector configuration in full detector operation mode. The dotted line represents the expected result when ϕ_{obs}=ϕ_{beam}.

So far, all the simulation runs were performed by irradiating the detector in the centre of one pixel to mimic the irradiation conditions at the ESRF beamlines. However, in a real astronomical environment, the detector will be irradiated in the full active surface and every pixel will act as a scattered and as an absorber. The objective of the next simulation presented is to evaluate the polarimetric performance of the dual plane detector when irradiated by a 100% polarized, homogeneous 2 cm radius beam, thus the full active surface of the detector. A systematic study covering the energy range between 200 keV and 500 keV and plane detector distances from 4 to 12 mm was performed. The results of figure 3.18 show that by combining all the double events and irradiating the full active surface, the modulation factor starts by decreasing and then increases marginally with the detector plane distance over 6 mm. The combined modulation starts by decreasing up to 6 mm because the dual plane modulation contribution also decreases. As explained before, for the single pixel irradiation case, over 6 mm the dual plane mode efficiency shows a decrease that can reach ~ 25% for 12 mm (figure 3.4) and therefore this mode contributes with a lower weight for the overall modulation, which, consequently, tends to approach the single layer mode modulation level.

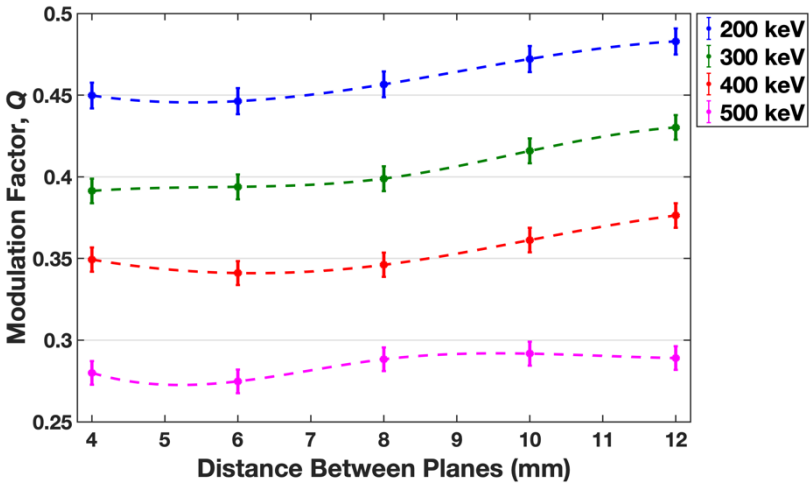

Figure 3.18: Modulation factor as function of the distance between planes for beam energies from 200 to 500 keV when irradiating the full surface of the detector.

3.4 Discussion

One of the obvious advantages of a multi-layer configuration detecting system, when comparing to single layer configuration, is its high efficiency potential due to the possibility to stack a large volume of sensitive material layers. Due to limitations in CdTe material growing, the thickness of a single layer is limited to 10 mm. Multilayer solution is a major advantage for astronomical proposes since most of the sources present low fluxes and fast transients require high efficiency. For polarimetry, detection efficiency is even more relevant since double Compton interactions must be recorded additionally to single event detection.

By performing this simulation analysis, we observed that there are multiple factors that impact the polarimetric performance of a pixelated dual plane configuration prototype. Comparing the results obtained for the different operation modes at 300 keV, we achieved a modulation factor $Q = 0.405 \pm 0.005$ for the single plane operation mode; $Q = 0.34 \pm 0.01$ for the dual plane operation mode (inter-plane distance 4 mm); and $Q = 0.362 \pm 0.005$ for the full detector operation mode (inter-plane distance 4 mm). Therefore, the double events generated in the dual plane mode present shallower scattering angles than 90° resulting in a lower modulation factor Q. However, by evaluating the modulation factor versus the scattering angle we can realize that for higher pixel orders there is an increase of the modulation factor reaching values of 0.68 for scattering angles from 73.1° to 75.1°. This shows that there is another factor related to the distance between double

events' interactions that has the effect to increase the modulation factor due to better resolution of the double events' trajectories. However, if we select only high order double events, despite having a better modulation we will work with lower statistics. Therefore, this selection can be useful just in case the celestial source flux is very strong, which is not the case of almost non-transient gamma-ray sources. The results obtained also revealed that by combining all the double events, by irradiating the full active surface, the modulation factor starts by decreasing and then increases marginally with the detector plane distance over 6mm. However, since the dual plane mode efficiency decreases with the planes distance by up to ~25% for 12 mm distance, the best MDP is obtained for the higher detection efficiency case (4mm), since the modulation varies just marginally with the distance. A 10% better MDP can be estimated for 4 mm distance, when compared with 12 mm, in the simulations' energy band.

In the next chapter, we present a set of experiments performed with a dual plane CdTe protype, the Compton-POLCA, in order to validate the simulation code and to explore the operational potential of such kind of instruments as polarimeters. The simulated results were used as input to the design detector geometry and to elaborate the test plan for the prototype.

In the dual plane operation mode, the highest modulation factor is obtained for scattering angles of ~90°, thus, the planes should be as close as mechanically possible. This way we are able to collect the Compton events at scattering angles near 90° and achieve the higher polarimetric performances of the instrument. In our case, the thickness of the detector is 2 mm, so, it will be desirable to reach to distances between the two planes as low as 4 mm (considering that the PCB that supports each detector has a thickness ~1.5 mm). The maximum detector plane distance is set to ~12 mm, in order to remain at an inter-plane distance that allow a relatively compact instrument for space missions' limited volumes. In order to study the potential to measure the polarization direction, we present a set of measurements when changing the polarization angle direction (0°- 45°).

4 Experimental Measurements

To evaluate the performance of the Compton-POLCA detector we must test it under unpolarized and polarized X-/gamma-rays. There are several ways to generate polarized X-/gamma-rays. Naturally radioactive sources emit isotropically non-polarized gamma-rays. However, it is possible to generate partially polarized gamma-rays from photons emitted by the radioactive source, by Compton scattering metal (Al for example) or plastic scintillator [88]. A drawback of this technique is that the efficiency is very low and the it is not possible to generate a 100% polarized beam. To obtain a near 100% polarized photon beam the only alternative is to use the radiation generated by a synchrotron. Several synchrotron facilities are available around the world, providing a limited amount of beam-time under request and approval of a scientific proposal by a scientific council. Considering the Compton-POLCA operational energy range cannot be generated by most of middle and small-size synchrotron facilities, the high-energy beam-line ID15A at the ESRF located in Grenoble, was the best choice to perform of a beam-test. The past POLCA experiments were also performed at beam-line ID15A, thus the team experience on the facility was an asset.

Before the ESRF experiments a series of tests were performed at the LIP-Coimbra laboratory where an experimental setup was mounted. The objective of these experiments was to evaluate all systems individually and optimize the pixel channels' gain parameters for the experiments. Using a ^{133}Ba and a ^{57}Co radioactive sources, a preliminary evaluation tests of the spectral performance and calibration was performed. However, to test the

Compton-POLCA detector under a collimated and uniform unpolarized beam source in a wider energy band we made a proposal within the context of the AHEAD project to access the LARIX facility, located in the Scientific-Technological Pole of the University of Ferrara. This facility provides an unpolarized hard X-ray source, capable of generate a beam with an energy pass-band from a few keV to about 300 keV.

The setups developed at the LIP laboratory, ESRF and LARIX, the results obtained with them are presented in this chapter by chronological order.

4.1 LIP-Coimbra Experiments

These experiments were performed between March to September 2017 and took place in the i-Astro LIP laboratory located in Coimbra, Portugal. The objective was to prepare the system for the upcoming ESRF experiments.

4.1.1 Single Plane Detector – POLCA 2

At first the system available was the POLCA 2, mounted during the master thesis of Marco Pinto [88] and described in section 2.2 (figure 4.1). For his work the POLCA-FEE was used as front-end electronics however, the read-out system was just a part of the TAKES system described in 2.3.4, capable of reading only 16 channels. To read the 128 channels from the Compton-POLCA the INAF-Bologna kindly sent us the complete TAKES system used POLCA 2 and Laue-POLCA experiments. The first challenge was to put the system as it was before and get used to all the system capabilities. This was done while the Compton-POLCA detector system was being developed in our workshops.

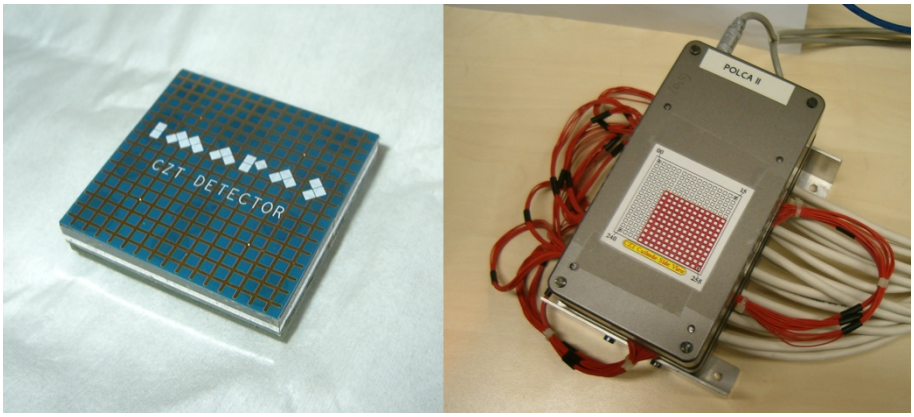

Figure 4.1: Picture of the 16×16 IMARAD detector array (left) and its enclosure (right).

After the full assemble of the system, we tested it by placing a ^{133}Ba and a ^{57}Co radioactive sources on top of the detector and measured their spectrum. In figure 4.2 is presented the intensity maps obtained with the application software based on LabVIEW®. Note that besides the 16×16 detector array, the system is only capable of reading 128 channels, thus, the system was designed to read a 11×11 array on the corner of the detector active surface. Figure 4.3 presents the respective spectrums obtained from both radioactive sources. The results obtained are in accordance with the previous experiments ensuring that all systems work correctly [88], [92], [93], [96].

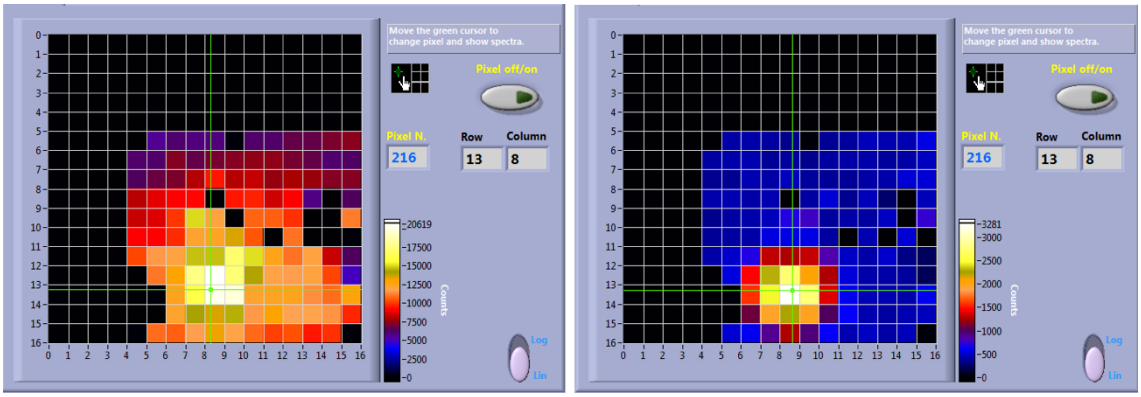

Figure 4.2: Intensity maps obtained from emissions of a ^{133}Ba (left) and a ^{57}Co (right) radioactive sources with the POLCA 2 detecting system.

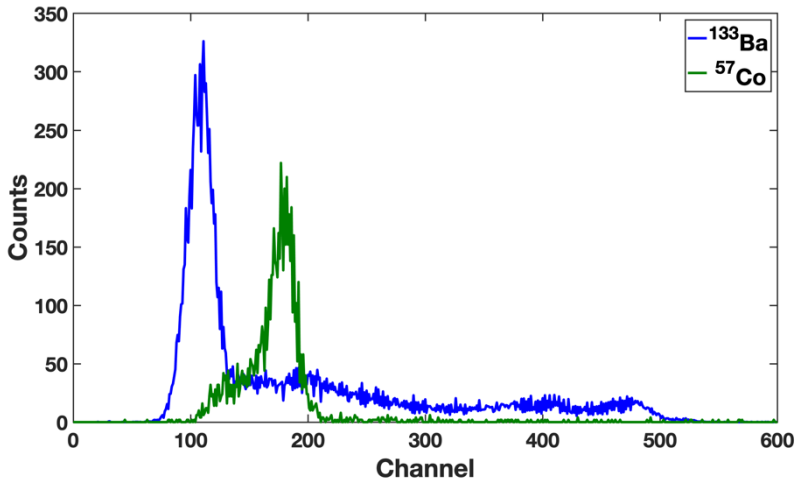

Figure 4.3: Energy spectrums obtained from emissions of a ^{133}Ba and a ^{57}Co radioactive sources with POLCA 2 detecting system.

4.1.2 Compton-POLCA

After the full assemble of the first version of the Compton-POLCA described in 2.3 a setup was mounted in order to evaluate the system performance with radioactive sources. A CAD drawing of the setup is shown in figure 4.4. The Compton-POLCA detector and POLCA-FEE mechanical arrangement is attached to two linear translation stages allowing to move the detection in the *x*-*y* plane. The translation stages are operated manually, and allow a maximum translation of 50 mm in each direction with position readings of 10 µm. A manual rotation stage that allows rotations of 360°, with position readings of 5° is as coupled the detector arrangment, and an optical rail that increases the translation in *x* direction by 100 mm. To hold the radioactive source, four long rods are screwed to the optical table and to a stainless-steel support. By moving the translation stages, we will move the detector relatively to the radioactive source. In the centre of the stainless-steel support is drilled a 1 cm hole to place the radioactive source. For a better source collimation, a series of Pb discs were placed between the support and the radioactive source.

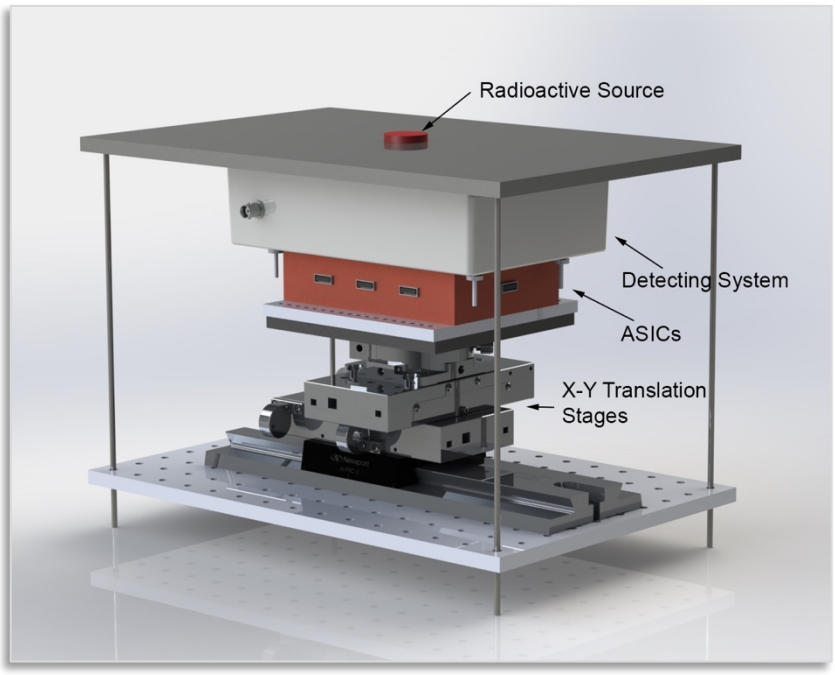

Figure 4.4: Drawing of the experimental setup mounted in the LIP-Coimbra laboratory.

During this phase, we come across several problems with the bonding of detectors and we lost several pixel units (see chapter 2.3.1). Before the ESRF campaign only one detector presented an acceptable performance for the beam line tests. Herein is presented the measurements performed on September 2017 by using the detector in the top plane detector position of the Compton-POLCA.

Firstly, we proceed to the multiparametric electronics chain equalization. Each channel chain has a different response that influence the energy spectrum. By adjusting the trimmers available on each analog channel of the TAKES boards we can achieve similar responses for all the pixels simplifying the reconstruction of events for polarimetric measurements. Each TAKES' boards allow a gain adjustment from 0.5 up to 1.5 with respect to the main amplifier gain. By making several scans over the entire active surface of the detector and using as reference line the 356 keV photopeak of the ^{133}Ba source, we were able to equalize the gain of each chain to have the peak centroid on channel ~540 using the acquisition software tool.

For the final measurement we used a ^{133}Ba and a ^{57}Co radioactive sources to perform a scan over to the total active surface of the detector. Because both sources are uncollimated it is challenging to centre them in a single pixel surface. Therefore, for each measurement we placed the radioactive sources in the centre of a subgroup of four pixels and

using the translation stages we move the detector in 4 steps of 4 mm in the *x* and *y* direction, therefore, covering all the detector active surface. Only the events triggered by the system as single events were selected for the fore coming analyses.

The intensity map obtained by selecting the single events is presented in figure 4.5. Analysing the condition of the detector is possible to see that it presents 8 dead channels, however, it has large subgroups of pixels with good performance that allow polarimetric measurements. For a better evaluation of the detector response uniformity figure 4.6 presents the number of single events as function of the pixel number obtained. The mean value for all the pixels was 1.732×10^5 and the standard deviation 3.1976×10^4 (~18%)

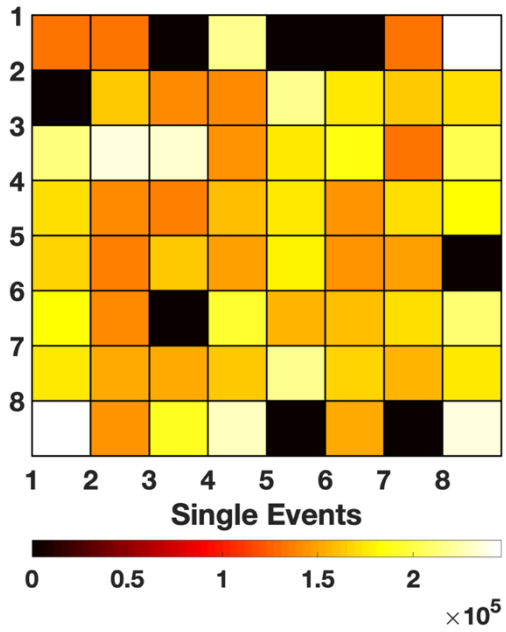

Figure 4.5: Intensity single events maps obtained from the single events measured during the detector scans with the a ^{133}Ba source at the LIP laboratory.

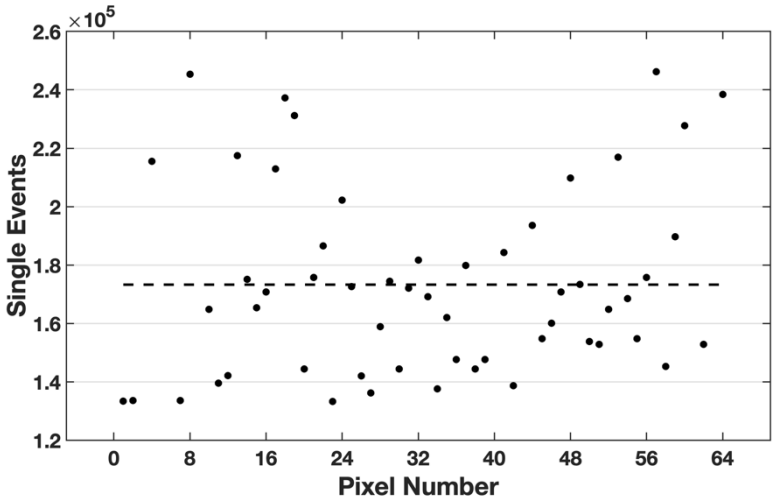

Figure 4.6: Single events as function of the pixel number obtained from the detector scans with the a ^{133}Ba source in LIP laboratory. The dotted line is the average: 1.732×10^5 single events.

From the selected single events, we draw an energy spectrum for each pixel and each energy. In figure 4.7 is presented an example for pixel 37 for emissions of both radioactive sources (^{133}Ba and a ^{57}Co). Fitting a gaussian function for each peak, we were able to calculate the peak centroids for each pixel and obtain the calibration line (channel vs energy). Three emission lines were used: 81 keV and 326 keV from the ^{133}Ba source and 122 keV form ^{57}Co source. In figure 4.8 is presented the peak centroids for the 326 keV line of ^{133}Ba versus the pixel number, revealing also the pixel response uniformity for this energy. The data analysis showed that for this energy the standard deviation from the mean value is ~0.1%.

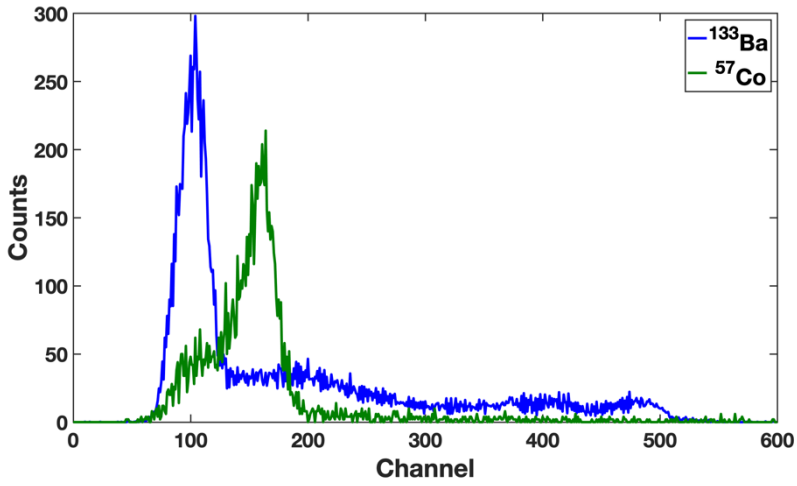

Figure 4.7: Sample of a normalized spectra of the radioactive sources used to calibrate the detector in the laboratory.

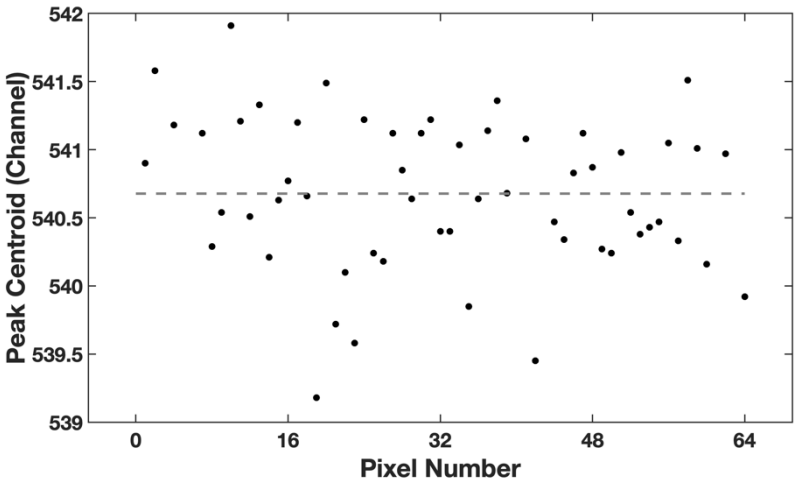

Figure 4.8: Gain pixel equalization of the ^{133}Ba 356 keV photopeak. The horizontal line represents the peak channel average, 540.67keV.

Another important parameter to consider is the minimum energy threshold of the system. In the previous laboratorial measurements presented, we were only interested in single events. Most of these events are photoelectric absorptions which are fine to perform spectral analysis. Therefore, we were able to set the minimum energy threshold as high as ~70 keV. However, this threshold is quite high for polarimetric measurements where the Compton events can deposit only a small fraction of the total energy of the incident photon. At the ESRF measurements this threshold was lowered. Note that the value presented for the energy threshold is a mean value for all the pixels. The TAKES read-out

electronics allows to set this parameter by eliminating all the events below a defined voltage value, by setting it manually with a potentiometer. Since each channel have its own response, a different energy threshold was set for each one the pixels' matrix. A good channel uniformity also leads to a good uniformity in minimum energy threshold.

4.2 ESRF ID-15 Beamline Test Setup

The ESRF open competitive calls every semester in order to apply for beam time at the ESRF beam lines. During the period of this thesis two proposals were submitted to apply for time at the ID15A beamline with the objective to evaluate the performance of the Compton-POLCA. The first in October 2016 and the second in April 2018. Both proposals were awarded 12 shifts (8 hours each shift) of beam time.

ID15A is dedicated to applications of high-energy X-ray radiation to materials chemistry and engineering, providing a ~99% polarized beam with photon energies from ~20 keV up to ~500 keV. The beam line is composed of two in-line experimental hutches for high-energy X-ray experiments. The first, EH2, was conceived for materials engineering experiments, and the second, EH3, was designed for materials chemistry experiments. The insertion device available is a U22 undulator with 2 m of length, a period of 22 mm and an undulator strength parameter, K_{max}, of 1.78 [196]. The flux of the U22 undulator in function of photon energy is shown in figure 4.9. The polarization orientation of the beam is always horizontal. The beam flux decreases exponentially with time due to gradual losses in the main electron storage ring. The electron beam intensity is proportional to the photon intensity in our beam line, which is monitored centrally by ESRF detectors.

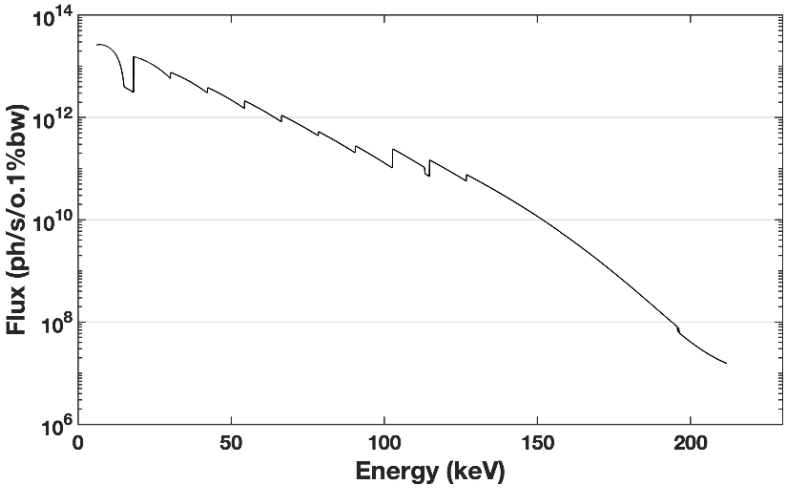

Figure 4.9: ID15A U22 undulator flux as function of the photon energy.

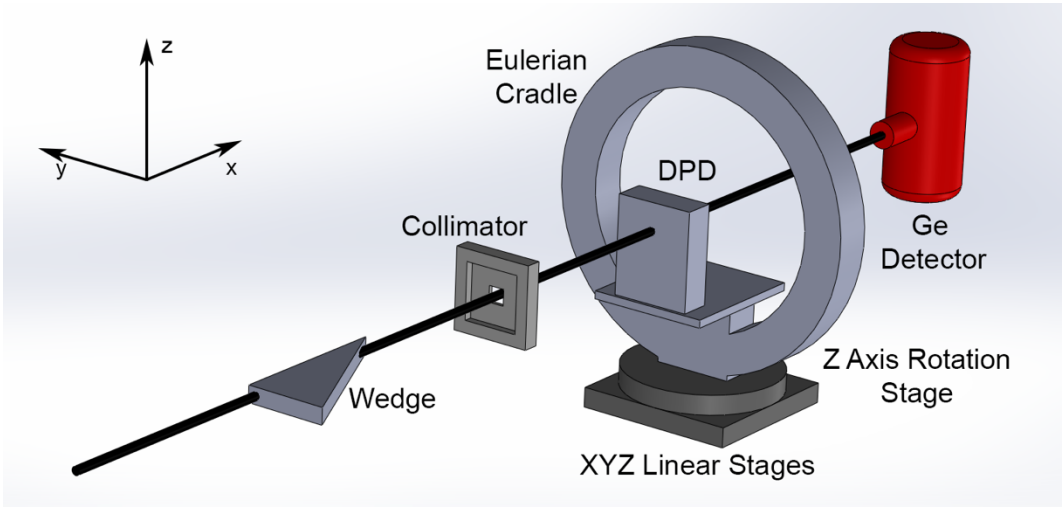

Figure 4.10: Beam line schematic inside the experimental hutch.

A schematic of beam line inside the experimental hutch is presented in figure 4.10. Before the beam irradiates the Compton-POLCA it crosses a wedge and a collimator (figure 4.11). The wedge is an aluminium absorber with a shape of a triangular prism which is used to reduce the photon intensity to levels compatible with our data acquisition system. The triangular shape of the wedge associated with an automized linear stage allows to reduce continuously the beam flux from 0 to 10 orders of magnitude. After the wedge a tungsten collimator with a variable square aperture is placed to adjust the beam size from 0.1 mm to 2 mm. The collimated beam then reaches the Compton-POLCA which is mounted perpendicular to the beam to a 5-axis motorized system: 3 linear stages allows

to move along the *x*, *y* and *z* directions; a rotation stage set the movement around the *z* axis; and a Eurelian cradler the rotation around the *x* axis (figure 4.13). Finally, a high precision Ge (HPGe) detector is positioned at the end of the beam line (figure 4.13) to monitor the energy of the beam and room background (e.g. lines form scattering material around our detector).

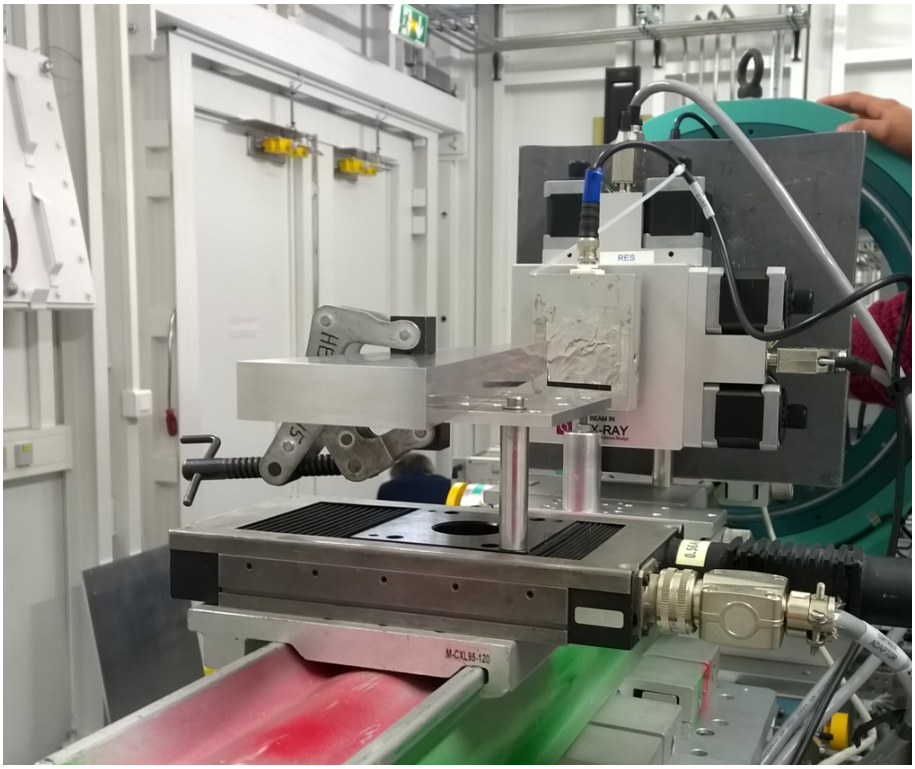

Figure 4.11: View from the beam pointing direction. It visible the wedge and the square aperture collimator.

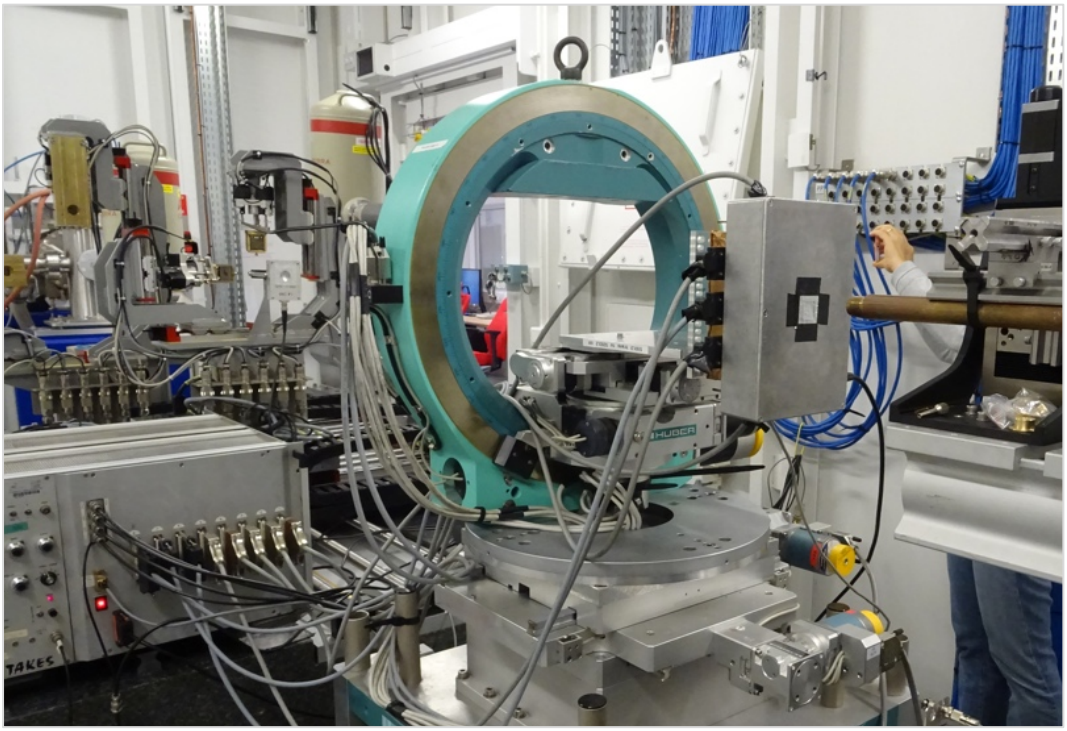

Figure 4.12: The Compton-POLCA mounted on 5-axis motorized stage and TAKES.

Figure 4.13: Opposite view of the beam pointing direction. It shows the beam entrance, the Compton-POLCA mounted to the 5-axis motorized stage and the Ge detector in the end of the line.

All the detector subsystems (detector, power supply, multiparametric electronics) have been mounted inside the experimental hutch, leaving in the control room only the serial to parallel interface box and the computer with the NI6533 data acquisition board and the application computer. Through the ESRF control console was possible to manage all the positioning of the linear and rotation stages, the optics hutch shutter, the wedge positioning and the beam slit size. The acquisition computer was placed next to the console line so, for each measurement, we move the detector to the initial position and start the run in the acquisition computer. The acquisition software allows real-time analysis in order to monitor the data quality during the acquisitions. To increase the efficiency of the available beam time for measurements a series of macros were written to perform a series of runs in which all the necessary movements of the setup motors were define. Then, the data acquired by the Compton-POLCA was recorded in just one file that was cropped during the data analysis based on the TAKES time stamp.

4.3 The ESRF 2017 Campaign

The first campaign at the ESRF ID15A beamline was performed from September 27th until October 1st, 2017. The objective of this campaign was to access the polarimetric performance of the Compton-POLCA both as single plane and as dual plane detector configuration. The top detector was the same as the one used in the LIP laboratorial experiments. The bottom detector was one of the units whose electric contacts broke during the LIP experiments, however we were able to repair by asking a rebounding to Due2Lab just before the ESRF campaign. The beam energy was set to 278 keV for all the all campaign and we were able to perform measurements with two distances between planes (6 mm and 10 mm) and three polarization angles (0°, 20° and 45°). The recorded data was analysed off-line by a Matlab® software custom tool which allows the selection of single, double and multiple events (photons undergoing at least three interactions in the detection plane). These selections of events were then used for different analysis. A detailed description of the data selection methods will be presented before each analysis.

4.3.1 Non-Uniformity Correction Procedure

There are several effects that under certain conditions might introduce different kinds of errors in the modulation factor measurement. However, for CdTe pixelized matrices the dominant source of error is the non-uniformity in pixel response due to material imperfections throughout the matrix bloc. It may vary by more than 25% for a significant fraction of the pixels. Another important source of systematic errors is related to our experiment, in particular the alignment accuracy of the beam with respect to the irradiated pixel centre and the alignment between detectors. In order to minimize these sources of error before each measurement we performed a complete beam scan of all detector pixels. The scan was performed with ESRF polarized beam at 278keV for both detectors at the same time. The matrix of each detector obtained from the single events recorded in each pixel was then used to correct the inherent non-uniformities in the response of the detector pixels. We estimate the true double event counts for each pixel by:

$$N_{true} = \frac{N_{pol}}{N_{non}} N_{max} \tag{4.1}$$

where $N_{pol}$is the number of double events detected (that depend on the beam polarization), N_{non} is the number of single events of the response map obtained when the pixel is directly irradiated and N_{max} the is maximum value among all the matrix pixels single events. By applying this method to the pixels surrounding the irradiated pixel, the error introduced by the non-uniformity of the detector matrix response is minimized, thereby improving the precision of the calculated modulation factor.

In order to correct any possible misalignment of the detectors with respect to the beam axis, each pixel was divided in 16 sub-pixels that were scanned with a 0.5×0.5 mm^2 beam for 10 s each, carrying out 1024 steps in total. Figure 4.14 shows a diagram of the detector matrix scan for two pixels. The *mesh* command on the terminal allowed us to automate the *x*-*y* motors and record the complete scan in one acquisition file. Using the time information in the TAKES output data word we are able to reconstruct with precision the number of events accumulated when the beam is in each pixel and discard the time interval when the beam is moving across one pixel and the subsequent. Figure 4.15 presents the intensity pixel maps obtained by selecting the single events for both detectors.

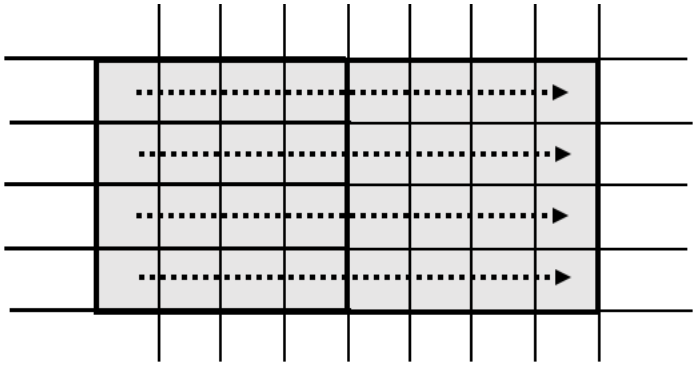

Figure 4.14: Diagram of the detector matrix scan for two pixels. Each square is a sub-pixel, the bold line the pixels limits. The arrows are the direction of the pixel scan. When a line scan ends It returns to the beginning of the next line.

By performing the detector matrix scan over the entire detector surface, we were also able to evaluate the condition of the detector pixels. Almost half of the top detector pixels were dead or noisy. By comparing to the intensity map obtained during the LIP experiments (figure 4.2) performed a week before, is obvious that some of the contacts of the pixels broke during the trip to the ESRF. However, the rebounded detector at the bottom plane revealed an acceptable condition to perform the measurements planed. As we are mainly interested in the Compton interactions that are scattered in top plane and absorbed in the bottom, we can use one pixel in the top detector as the scattered unit and have a subgroup of pixels in the bottom plane to obtain the azimuthal distributions of the scattered photons. A detailed explanation of the pixel selection is made before the polarimetric analyses presentation. For a better evaluation of the detector response uniformity figure 4.16 presents the number of single events as function of the pixel number obtained for both detectors. The mean value was 1.6013×10^5 single events for the bottom detector and 4.1668×10^5 for the top detector. The standard deviations are 2.9455×10^4 (~18%) and 6.5786×10^4 (~16%) respectively.

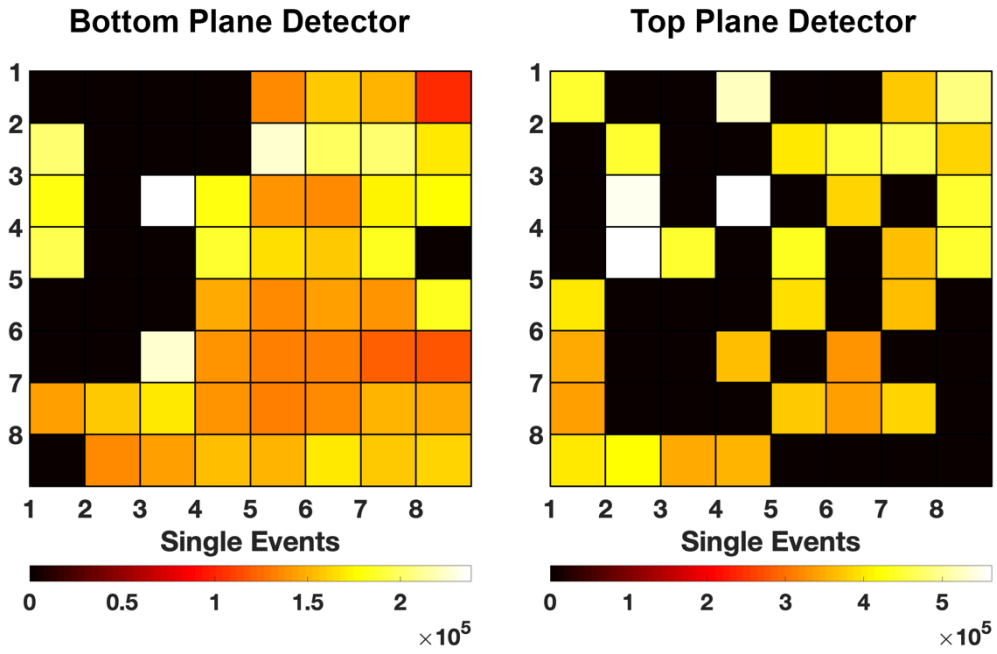

Figure 4.15: Intensity maps obtained from the single events measured during the detector matrix scan with a 278 keV beam at the ESRF.

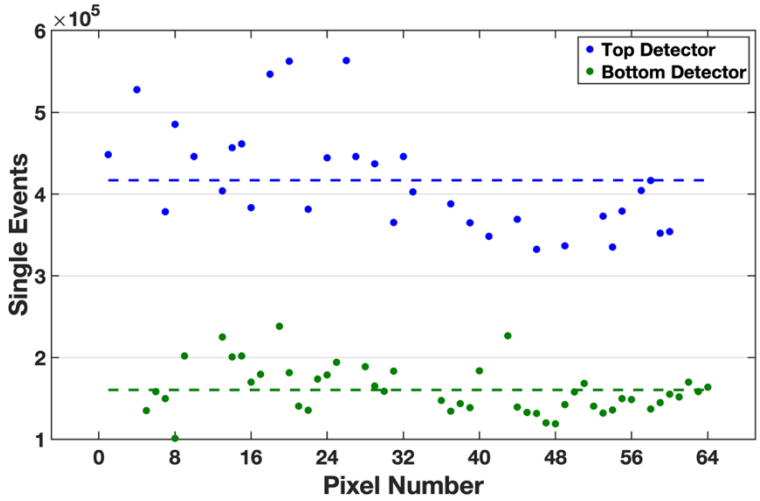

Figure 4.16: Single events as function of the pixel number obtained from the detector pixel scans with a 278 keV beam at the ESRF for both detectors. The dotted lines are the average: bottom – 1.6013×10^5 single events; top – 4.1668×10^5 single events.

4.3.2 Spectroscopic performance

From the selected single events we draw an energy spectrum for each pixel. In figure 4.17 is presented an example for pixel 20 of both detector planes. By using a sum of

gaussian functions for each peak, we were able to fit the data and calculate the peak centroids. In figure 4.18 shows the full energy peak centroid obtained for each pixel. The data analysis demonstrated that the top detector is quite uniform, the standard deviation from the mean value being about 1.8%, while the bottom detector exhibits a gain dispersion up to 25%. The reason for this is that the top detector was previous equalized in the laboratory before ESRF campaign, but the bottom was only tested during the campaign and there was no opportunity to equalize it. In figure 4.19 is presented the energy resolution (FWHM/E) calculated for each pixel of each detector. The results show that the bottom has a slightly better performance with an average resolution of 7.5% while the top detector shows an average of 9.4%. The standard deviation from the mean value is around 21% for both detectors.

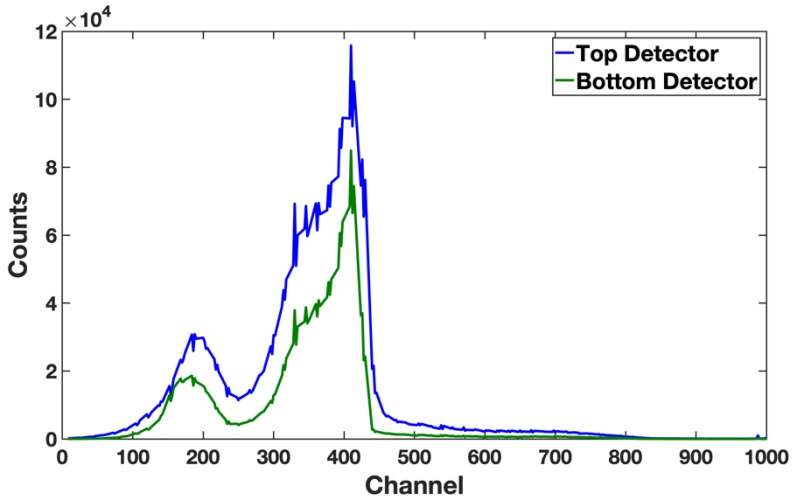

Figure 4.17: Energy spectrum obtained by the Compton-POLCA detector for the ID15A monochromatic beam at 278 keV.

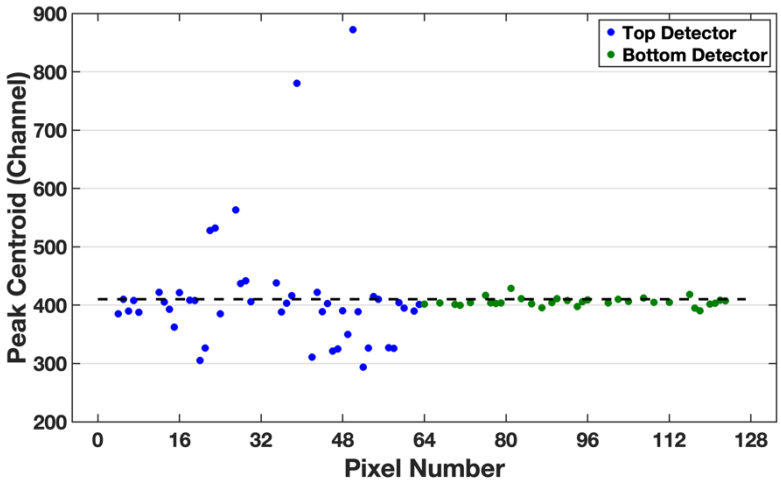

Figure 4.18: Uniformity of pixel gain (full energy peak centroid) of the two detector planes. The horizontal line represents the average peak channel: 410.1 Channel.

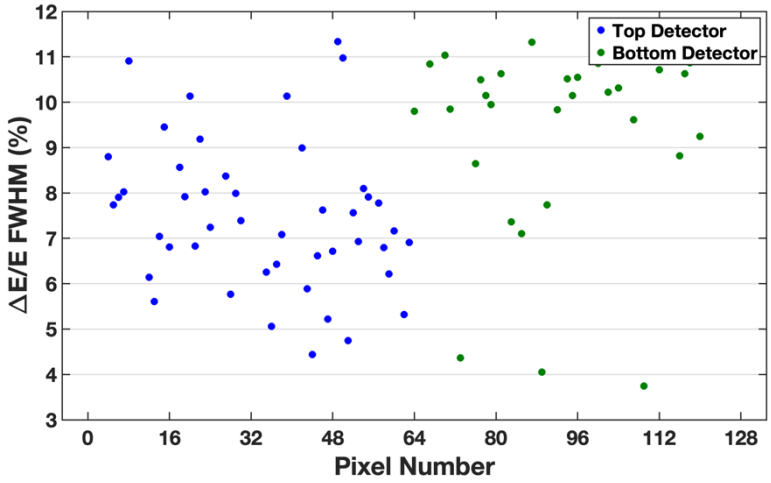

Figure 4.19: Energy resolution of the two detector planes. The horizontal line represents the average resolution: 8.3%.

4.3.3 Polarimetric Performance Evaluation

4.3.3.1 Data Selection and Corrections

Due to measurement limitations because of the noisy and dead pixels, we selected the best places to irradiate the detector in order to achieve the maximum range of scattering and azimuthal angles on the analyses. As we are mainly interested in the dual plane in-

teractions, we need just one pixel from the top detector to be used as a scattered. In opposite, for the bottom, we need the maximum pixels as possible in order to collect the maximum scattered photons. The bottom detector presented a region from column 4 to 8 in good condition that can be used for that (figure 4.20). Furthermore, due to the 90º symmetry in the azimuthal distribution demonstrated by the Klein-Nishina equation, we are able to calculate the modulation factor by selecting double events in a 90º quadrant in the azimuthal plane. Therefore, four corner detector pixels were irradiated in order to obtain double events with higher scattering angles. As presented in figure 4.20 the position selected to irradiate the detector provide a pixel in good condition on the top detector and 4×4 matrix in the bottom detector. The pixels were selected so we could generate double events with azimuthal angles in a 360º range, a 90º quadrant for each pixel measurement. By doing this we were able to collect azimuthal angles of a 7×7 virtual matrix. For each measurement, the modulation factor was calculated and the final modulation factor presented is the average of the 4 measurements and the error the correspond standard deviation. The pixels chosen were pixel 19, 38, 54 and 59. For each pixel, we recorded the interactions obtained for inter-plane distances of 6 and 10 mm. For the polarization angle measurements, we positioned the beam in pixel 45. In this pixel, we could simulate a 5×5 matrix irradiated at the central pixel. Table 4.1 presents by chronological order the measurements performed. For all the measurements the energy beam was set to 278 keV, the slit size set to 1×1 mm^2 and the minimum energy threshold to ~40 keV. The wedge was set so we could achieve a count rate ~1×10^5 counts/s.

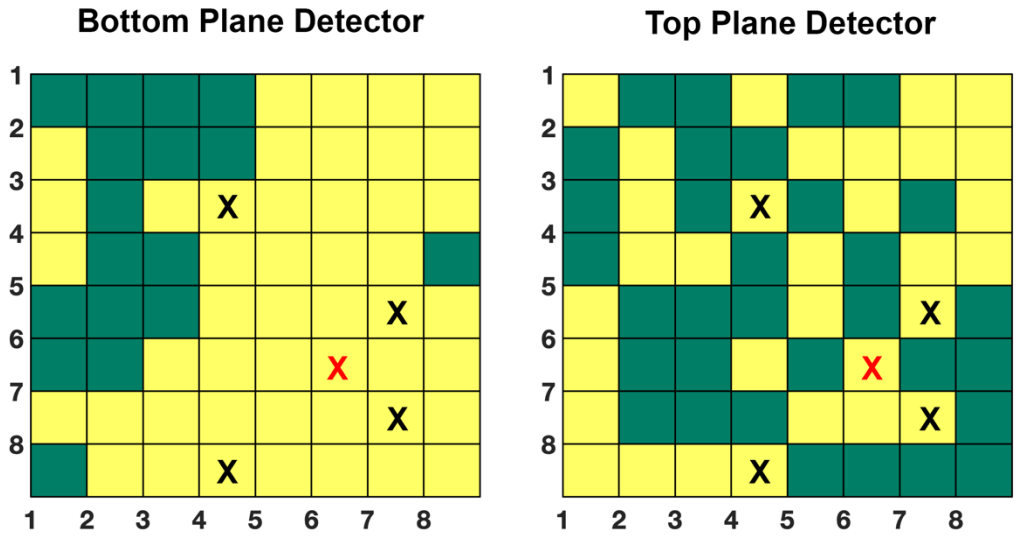

Figure 4.20: Detector maps diagrams: yellow – good pixels; green – bad pixels The black markers are the pixels irradiated for the modulation factor versus the distance between planes measurements (pixel 19, 38, 54 and 59). The red marked is the pixel irradiated for the polarization angle rotation measurements (pixel 45).

Table 4.1: ESRF 2017 measurements performed by chronological order.

#	Irradiated Pixel	Detector Rotation (º)	Distance Between Planes (mm)	Acquisition Time (s)
1	19	0	6	4500
2	38	0	6	4500
3	54	0	6	4500
4	59	0	6	4500
5	59	0	10	4500
6	54	0	10	4500
7	38	0	10	4500
8	19	0	10	4500
9	45	0	6	3600
10	45	20	6	3600
11	45	45	6	3600

For the polarimetric analyses only the double events triggered by the system were selected. Multiple events are excluded from the analyses since we cannot determine the order of each hit. For double events, we know which is the first interaction because this is coincident with the position of the pixel irradiated by the collimated beam and therefore

during the analysis we exclude double events that do not have at least one interaction in the target pixel, e.g., chance coincidence events due to noise and flaring pixels and/or triple events in which the first interaction in the target pixel was under the low energy threshold. Since the ID15A beam was monochromatic, we also applied a further simple selection of double events using the energy deposited in each hit. Knowing the beam energy, we have selected as good double events only those for which the sum of the two interactions is within a window centred at the selected beam energy. Furthermore, considering the Compton kinematics and the detector geometry we also evaluate the energy of each hit. Since the incoming beam has an energy of 278 keV, for the single plane operation mode (scattering angles ~90º), we expect that the first hit has an energy ~100 keV and the second ~180 keV. For the double layer interactions, the energy of the events depends on the scattering angles we are looking for, so we select an energy range accordingly.

4.3.3.2 Single Layer Polarimetric Performance

We started by analysing the specific polarimetric performance of the bottom detector in the dual plane configuration. As seen in the simulations performed in section 3 we expect that the modulation factor does not change for a dual plane detector configuration in single plane operation mode in comparison to a single plane configuration. Unfortunately in the top plane detector, due to described pixel conditions, we were not able to measure the modulation factor within an acceptable associated error. Even though, ID15A beamline energy was limited to a 278 keV monochromatic beam, previous polarimetric studies with single plane CdTe based detectors with similar characteristics have shown that the best modulation factor is obtained in the energy range between 200 keV and 400 keV (for a Q factors between ~0.3 and ~0.4) [88], [91]–[96], [195]. This analysis was performed with the data from measurement #9 of table 4.1, where a central pixel of a 5×5 array was irradiated. The number of recorded double-events ranged from ~10^4 up to 10^5 per pixel. The modulation factor obtained was 0.46 ± 0.01 which is in accordance with the past experiences.

4.3.3.3 Modulation factor vs distance between planes

Afterwards, we studied the modulation factor for different distances between detectors. For each measurement (#1-#8, table 4.1) we selected and analysed the double-events in dual plane operation mode. The final modulation factor was calculated be averaging the modulations factor of the 4 pixels irradiated for each inter-plane distance (6 and 10 mm). The error is the correspondent standard deviation.

Observed experimental results presented in figure 4.21 show a decrease of the modulation factor when the distance between planes was increased, as expected and explained in the previous chapter. Furthermore, in figure 4.21 it is also represented the results obtained from simulations for the same beam conditions and distances between planes from 2-14 mm. Results show a good agreement of the trends of both experimental and simulated results however, it presents slight lower modulation level for the 6 mm measurements that can be due to several other effects not included in the simulation code (eventual minor axial or rotational misalignment between the planes, individual pixel response change with time and non-uniformity, etc.). We can conclude that the contribution for the instrument modulation of double-events recorded between different material layers depends significantly from the distance between planes. Then, the distance between layers is an essential parameter to consider when designing and dimension a multi-layer instrument for high-energy polarimetry.

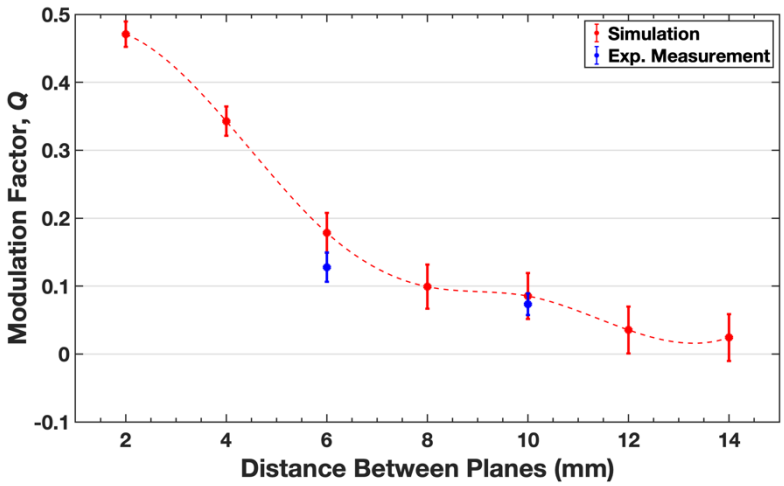

Figure 4.21: The modulation factor measured for 278 keV photons at two different distances between the detector planes compared with the simulations for distances between planes from 2-14 mm.

4.3.3.4 Polarization angle measurements

Finally, we analysed detector potential to determine the polarization angle orientation in dual plane operation mode. For this we analyse the measurements #9-#11 of table 4.1 which corresponds to a centre pixel irradiation of a 5×5 matrix. Figure 4.22 presents the scattering maps obtained for beam polarization direction of 0°, 20°, and 45. These maps provide a direct representation of how the detector see the azimuthal dependence of the Compton scattering for polarized photons. Is visible the differences for the different polarization angle orientations. In order to optimize the double-event histogram readout and obtain the modulation curves, $N(\phi)$, we applied the radial bin technique (RBT) [9], by dividing the matrix into 24 radial bins of 15º each. Pixels partially crossed by angular bin lines contribute only with a fraction of the number of events equal to the fraction of its area that is in the sector. This is an approximation since real hits inside each pixel are not uniformly distributed but have a radial dependence relative to the position of the first Compton interaction of a double event. The modulation curve curves, $N(\phi)$, for the three beam polarization directions are presented in figure 4.22. As expected from theory, for a polarization angle of 0° a maximum number of Compton photons were detected in the perpendicular direction with respect to the polarization direction. Inside the experimental hutch it corresponds to the vertical direction. This matches with the fact that the beam polarization is horizontal inside the hutch since the polarization is always perpendicular to the maximum intensity direction.

The measured angles were 2.0° ± 8.5°, 25.0° ± 6.0° and 46.3° ± 3.2° for the effective ESRF beam polarization angle of 0°, 20° and 45°, respectively. Therefore, polarization angles were determined with a resolution lower than 10°. Figure 4.23 presents the measured polarization angle (φ_{obs}) as a function of the effective ESRF beam polarization angle (φ_{beam}) at 278 keV. The linear fit calculated is also represented. Overall analysis of these results shows a good agreement between measured polarization angle and the effective beam polarization angle, in accordance with the previous studies [96].

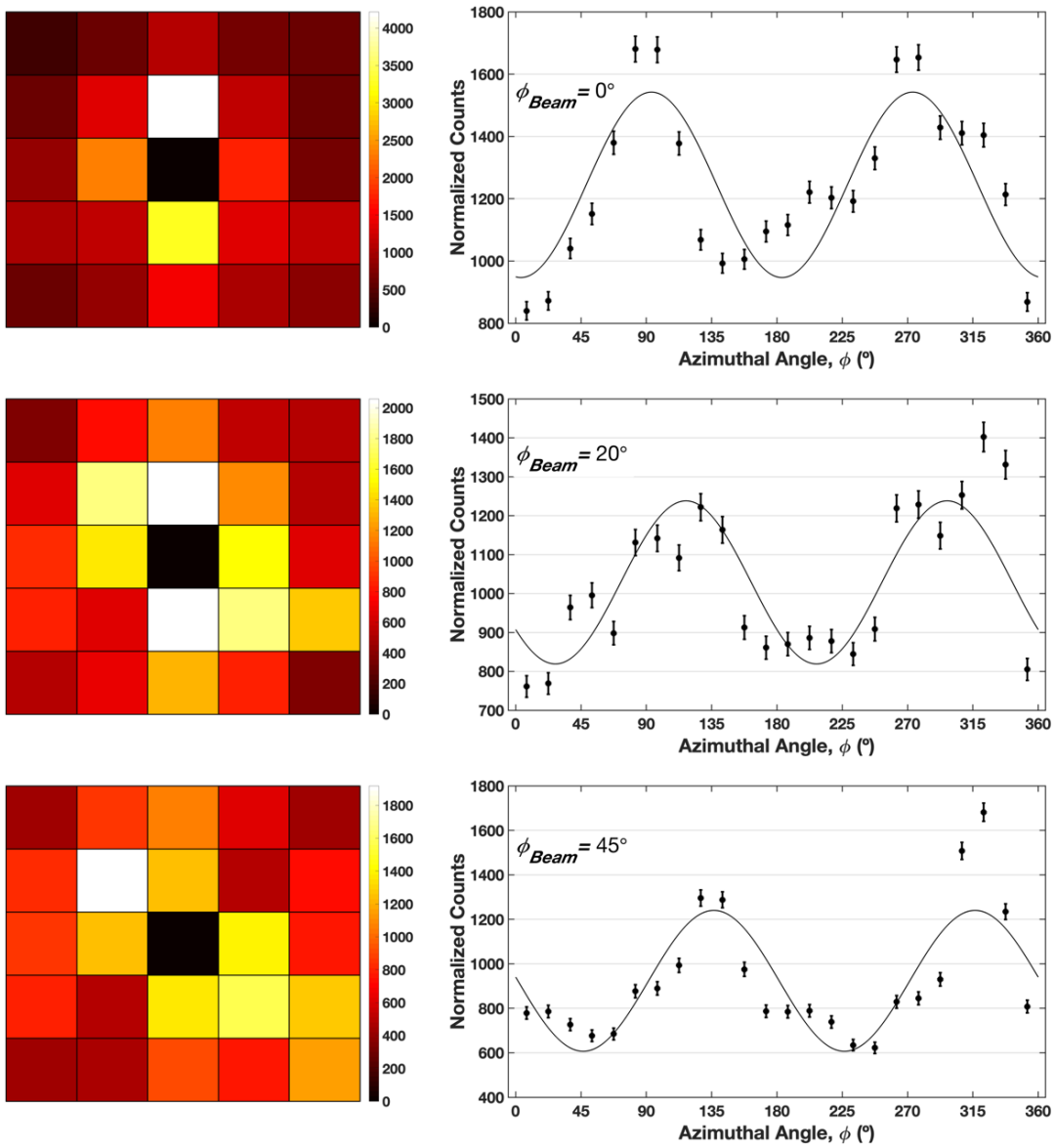

Figure 4.22: Scattering maps and modulation curves obtained inside a 15° radial bin, centred on a 5×5 detector matrix for polarization angles of: 0°, 20° and 45°.

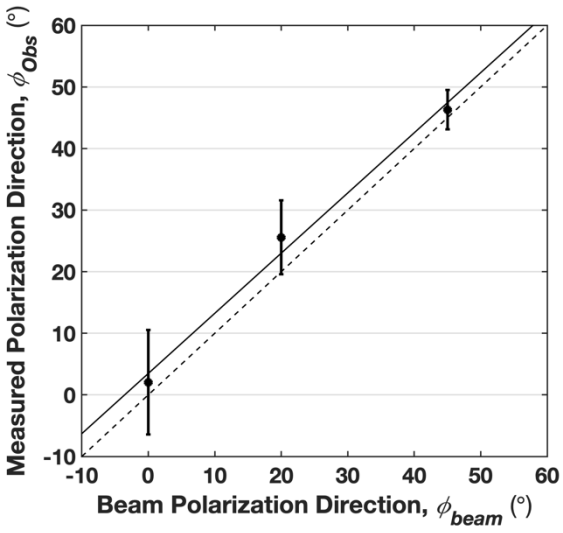

Figure 4.23: The measured polarization angle as a function of the effective ESRF beam polarization angle for 278 keV. The errors associated to each measured polarization angle were obtained by averaging the angle of the two maxima and the two minima of each double-event modulation curve applying a 90° independent partial fitting, since the polarization is 90° symmetric. A linear fitting was applied (ϕ_{obs}=0.95ϕ_{beam}+5.23) and is represented by the solid line. The dotted line represents the expected result were ϕ_{obs}=ϕ_{beam}.

4.3.4 Discussion

Herein, were presented the polarimetric performances of a two-layer CdTe prototype under a polarized gamma-ray beam, obtaining consistent results with the simulations performed in the previous chapter. The modulation factors were measured for single plane operation mode (Q~0.46). When operating the prototype in the dual plane operation mode, we observed that the factor decreased with the increase of the distance between planes as expected, since in this energy range the modulation is maximized for scattering angles ~90◦, decreasing the modulation as the scattering angle decreases to shallow angles. Modulation factors of Q~0.13 and Q~0.08 were obtained respectively for 6 mm and for 10 mm distance between planes. When combining single plane and dual plane operation modes, high polarimetric performances are achieved, close to single plane operation mode, with the advantage of the high detection efficiency provided by the multi-layer solution. Measurements also show that a polarization angular resolution lower than 7° can be achieved in the two-layer mode. These results confirm the fine polarimetric potential of multi-layer configuration CdTe focal planes.

4.4 ESRF 2018 Campaign

Notwithstanding the good results of the ESRF 2017 campaign, in order to validate our MEGAlib simulation model and prototype design for a high-energy space telescope, the prototype should be tested and its performance analysed in a wider energy band and for more distances between planes. This was the objective set for the September 2018 ESRF campaign. During the 4 days campaign we were able to perform experimental sets with four energies (200, 300, 400 and 500 keV) and five distances between planes (8, 10, 12, 14 and 16 mm), irradiating both the detector centre and the detector corner pixels. In table 4.2 is shown the chronological order of the measurements performed and the different parameters that changed. The recorded data was analysed off-line by a Matlab® software custom tool which allows several data selections depending on the analyses we want. A detailed description of data selection is made in the beginning of each section.

Table 4.2: ESRF 2018 measurements performed by chronological order.

Pixel	Energy (keV)	Distance Between Planes (mm)	Slit (mm×mm)	E. Threshold (keV)	Wedge (mm)	Acquisition time
Scan	200	16	0.2×0.2	~100	70	120 s/Pixel
Scan	300	16	0.2×0.2	~100	12	120 s/Pixel
Scan	400	16	0.5×0.5	~100	0	180 s/Pixel
27	200	12	0.2×0.2	~50	70	4800 s
27	300	12	0.2×0.2	~50	12	3600 s
27	400	12	0.5×0.5	~50	0	3600 s
27	500	12	1.8×1.8	~50	0	7200 s
27	500	10	1.8×1.8	~50	0	7200 s
27	400	10	0.5×0.5	~50	0	3200 s
27	300	10	0.2×0.2	~50	12	3600 s
27	300	8	0.2×0.2	~50	12	3600 s
27	400	8	0.5×0.5	~50	0	3600 s
27	500	8	1.8×1.8	~50	0	7200 s
27	200	8	0.2×0.2	~50	70	3600 s
63	300	8	0.2×0.2	~50	12	3600 s
0	300	8	0.2×0.2	~50	12	3600 s
63	300	10	0.2×0.2	~50	12	3600 s
63	300	12	0.2×0.2	~50	12	3600 s
0	300	12	0.2×0.2	~50	12	3600 s
63	300	14	0.2×0.2	~50	12	3600 s
63	300	16	0.2×0.2	~50	12	3600 s
Scan	500	16	1.8×1.8	~100	0	200 s/Pixel
63	400	16	0.5×0.5	~50	0	3600 s

4.4.1 Non-Uniformity Correction Procedure

As we did in the ESRF 2017 campaign we proceed to a detector matrix scan in order to correct the non-uniformity in pixel response and evaluate the spectral performance of each detector pixel (see section 4.31). We centred the beam in one detector corner pixel and proceed to a scan over all the 8×8 matrix detector for each energy. The *mesh* command on the terminal allowed us to automate the *x*-*y* motors and record the 64 steps in one acquisition file. Using the time information in the TAKES output data word we were then able to reconstruct with precision the number of events accumulated when the beam

is centred in the pixel and discard the time interval when the beam is moving across one pixel and the subsequent. The position of the wedge and the slit size was set to keep the count rate $<1\times10^5$ counts/s. As the beam flux changes with the beam energy these two parameters were optimized for each energy used. To decrease the noisy events and because we are only interested in the single events, the minimum energy threshold for these measurements was set to ~100 keV. Table 4.3 summarizes the acquisition conditions for each measurement and the respective count rate.

Table 4.3: Acquisition conditions summary of each pixel scan measurement. The energy presented was measured by the HPGe detector available at the ID15A beamline. The Counts/s is calculated by dividing the total number of acquired events (single, double and multiple) in the correspondent detector, by the total time of the complete *mesh* run. The noisy pixels that we cannot extract any data were excluded in this calculation. However, noisy events from the "good" pixels were not excluded.

Energy (keV)	Acquisition Time (seconds/pixel)	Beam Size (mm×mm)	Wedge (mm)	Counts/s	
				Top Det.	Bottom Det.
198.7	120	0.2×0.2	70	~1000	~680
296.8	120	0.2×0.2	12	~1800	~1470
392.4	180	0.5×0.5	0	~780	~680
491.1	200	1.8×1.8	0	~50	~88

Figure 4.24 presents the intensity maps obtained from the single events measured during the detector matrix scan with a 300 keV beam. Evaluating the detector's response, we find a total of 12 dead/noisy pixels: 8 on the bottom detector and 4 on the top detector. For a better evaluation of the detector response uniformity figure 4.25 presents the number of single events as function of the pixel number obtained for both detectors. The mean value was 1.3310×10^5 single events for the bottom detector and 1.6146×10^5 for the top detector. The standard deviations are 8.5483×10^3 (~6%) and 9.6266×10^3 (~6%) respectively. The uniformity response was considerably better than the one obtained during the previous experiment.

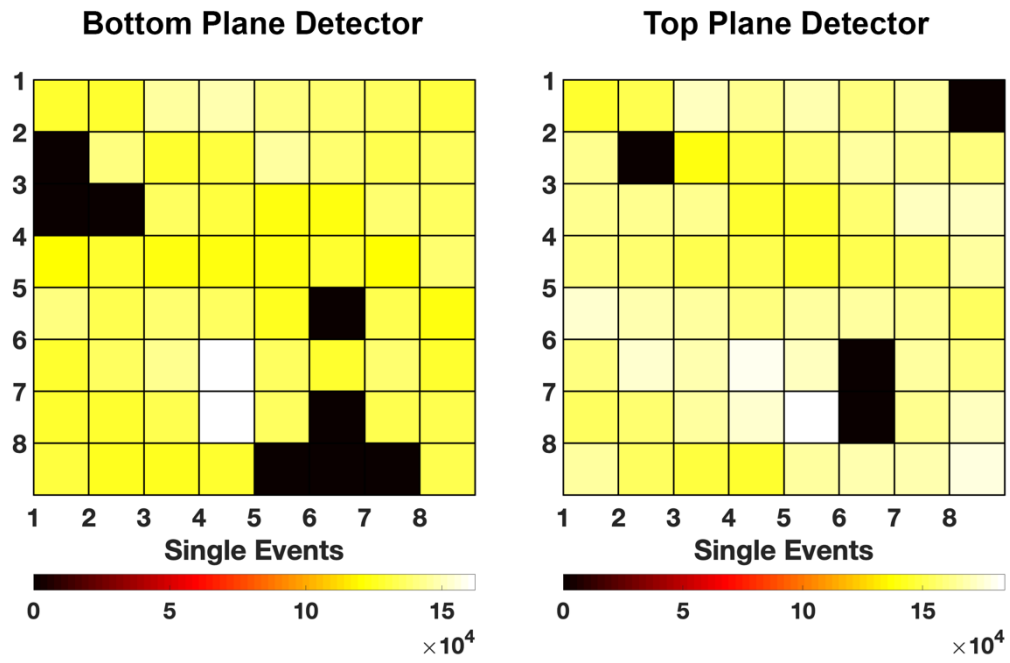

Figure 4.24: Intensity maps obtained from the single events measured during the detector matrix scan with a 300 keV beam at the ESRF.

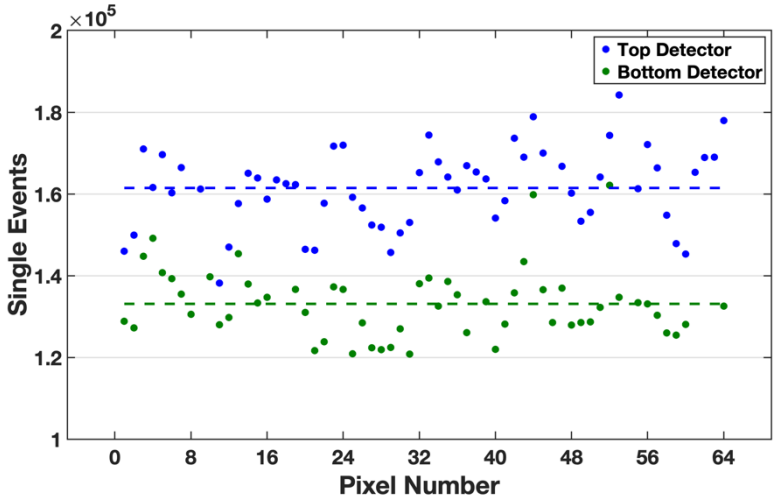

Figure 4.25: Single events as function of the pixel number obtained from the detector pixel scans with a 300 keV beam at the ESRF for both detectors. The dotted lines are the average: bottom – 1.6013×10^5 single events; top – 4.1668×10^5 single events.

4.4.2 Spectroscopic performance

From the selected single events obtained from the detector scans we draw an energy spectrum for each pixel and energy. Using a sum of gaussian functions to fit the data we

were able to calculate the peak centroids for each pixel. Figure 4.26 presents an example of the energy spectrum achieved for 200, 300, 400 and 500 keV photons beam, measured with pixel 27. The peak centroids for each pixel are presented in figure 4.27, and the correspondent energy resolution ($\Delta E/E$) in figure 4.28. Table 4.4 presents the average values obtained for each detector. The results demonstrated that the detectors are quite uniform, in the worst case (200 keV) the standard deviation from the mean value for the bottom detector is ~4.3%, while the top detector exhibits a gain dispersion of ~3.5% for the worst case of 200 keV.

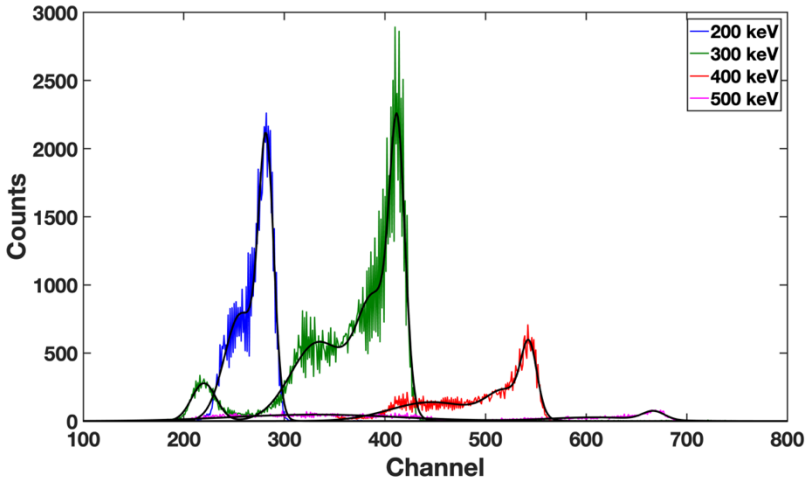

Figure 4.26: Energy spectrum in channels obtained for a 200 keV, 300 keV, 400 keV and 500 keV beam, measured with pixel 27.

Table 4.4: Peak centroid and energy resolution average for both detector planes obtained for the four photon energies used.

Energy (keV)	Bottom Detector		Top Detector	
	Centroid (Ch)	Resolution (%)	Centroid (Ch)	Resolution (%)
198.7	279 ± 12	6.5 ± 2.3	281 ± 10	8.2 ± 3.8
296.8	420 ± 12	3.9 ± 0.5	421 ± 11	5.0 ± 1.8
392.4	556 ± 15	3.3 ± 0.6	558 ± 14	4.2 ± 1.5
491.1	688 ± 19	3.9 ± 0.4	689 ± 17	4.6 ± 1.4

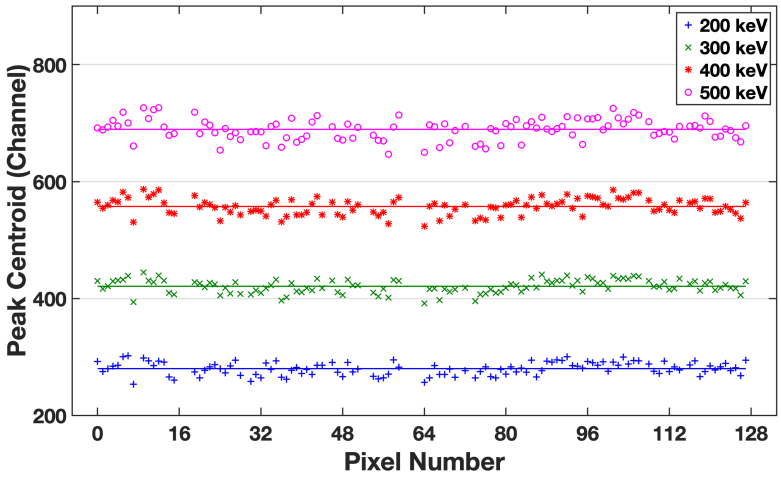

Figure 4.27: Uniformity of pixel gain (full-energy peak centroid) for the four photon energies used. The horizontal lines represent the peak channel average for each energy summarized in Table 4.4.

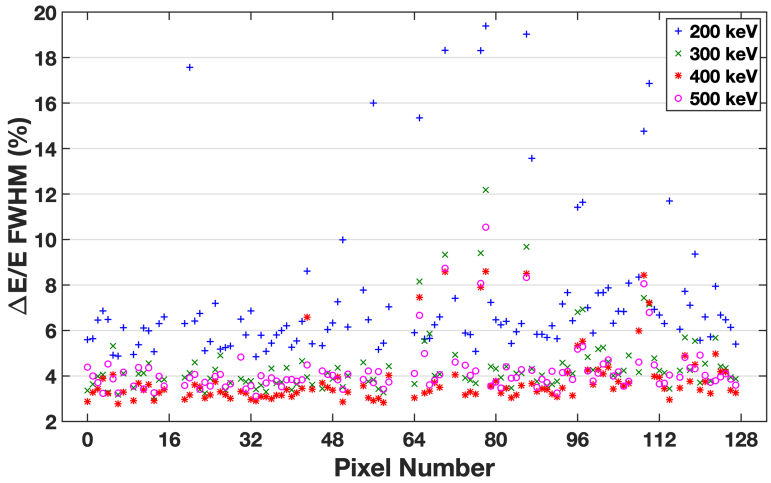

Figure 4.28: Energy resolution in function of the pixel number for the four photon energies used.

During the detector scan we also perform spectral measurements with the HPGe detector available in the hutch, so we can calibrate each pixel of our Compton-POLCA. In figure 4.29 is shown an example for pixel number 27. The four energy points can be fitted using a linear fit of the form (E=*Channel*×m+b) that can be used to convert the channels in keV. In figure 4.30 is presented the spectrum from figure 4.26 with the channel to energy conversion.

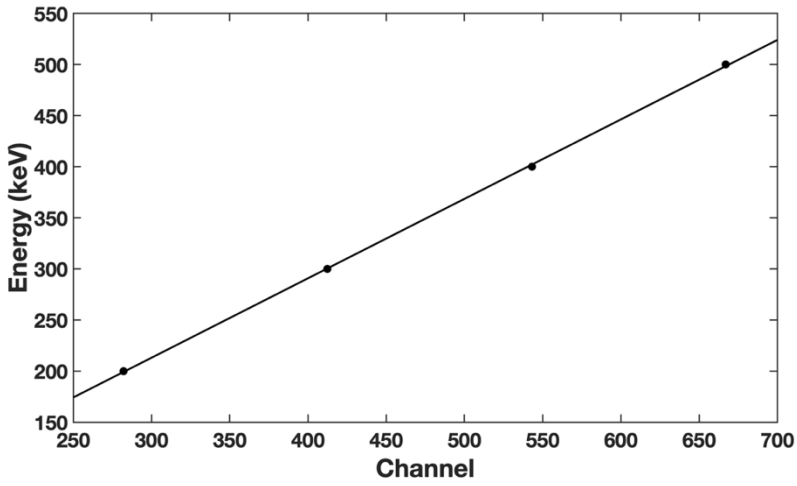

Figure 4.29: Calibration line for pixel number 27.

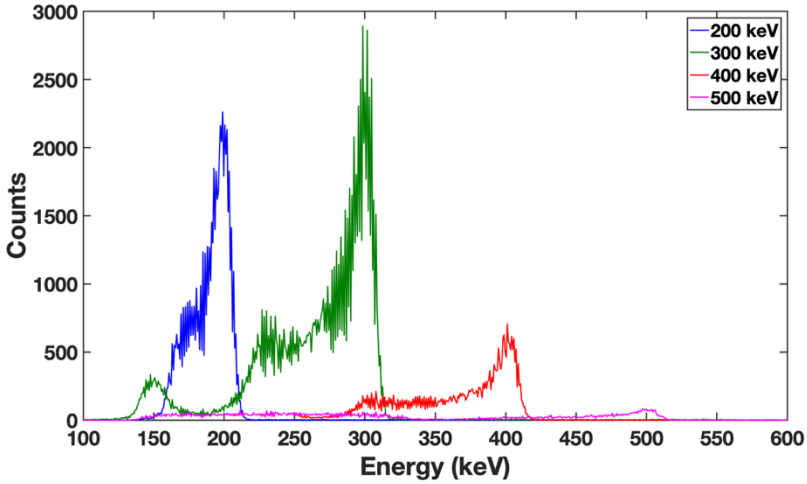

Figure 4.30: Energy spectrum in keV obtained for a 200 keV, 300 keV, 400 keV and 500 keV beam, measured with pixel 27.

4.4.3 Event efficiencies

Afterwards, we analysed the relative efficiency of single, double events and multiple events. The relative efficiency is defined as the ratio between the number of selected events (single, double or multiple) and the total number of detected events (sum of the previous). The experimental set-up did not allow a precise determination of the photon beam flux irradiating the detector surface, therefore absolute efficiencies were not calculated.

Figure 4.31 presents the relative efficiency obtained for single, double and multiple events as a function of the photon energy. These results were obtained for an inter-plane distance of 8 mm. As can be seen the double events efficiency has its maximum for photon energies around 300 keV. This is explained by the Compton scattering cross section for CdTe that stars to be dominant over the photoelectric effect interaction at about 300 keV. This is also evident on the single events efficiency that has its maximum at 200 keV and then it exponentially decreases. Regarding the multiple events efficiency, as expected, it smoothly increases with the energy because for higher energies the photons have enough energy to make multiple Compton scatterings. As a consequence, the double event efficiency also decreases. In our system the only events that can provide polarimetric information are the double events, thus we expect that the higher double event efficiency ~300 keV will maximize the polarimetric performance of the instrument.

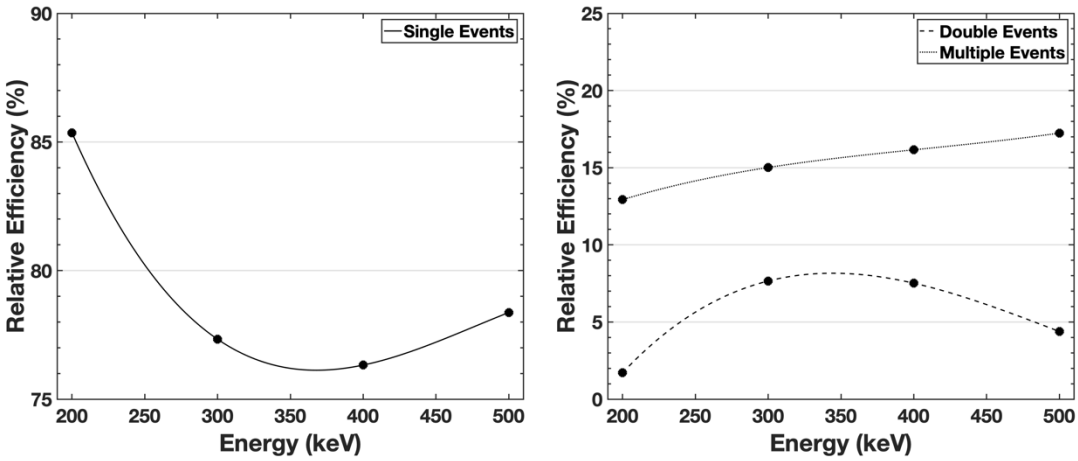

Figure 4.31: Relative efficiency of single, double and multiple events as function of the photon energy.

As we are mainly interested in evaluating the events in a dual plane configuration mode, we also evaluate the relative efficiency of these events. Figure 4.32 shows the results as function of the distance between planes for different energies. It is evident that the relative efficiency of these events decreases with the increase of the distance between planes. There are two main effects that occur when the distance between planes increase: the allowed scattering angles decreases, thus there is an increase of events that are scattered in the top plane and escape from detector; and the energy of the second event becomes very low and unable to be detected by the system. Is expected that both these

effects reduce the modulation factor as well. The second effect explained is also the responsible for the lower relative efficiency for lower energies obtained. As the energy increases the system is able to detect all the events in the top detector because the energy of these events surpasses the minimum energy threshold of the system.

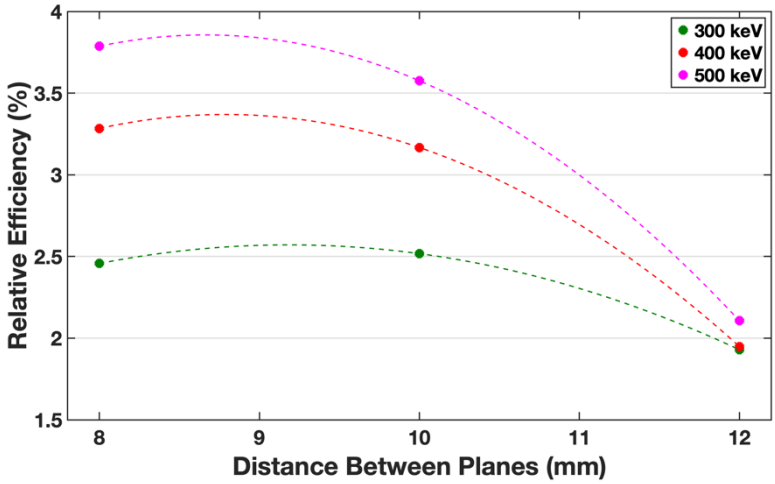

Figure 4.32: Relative efficiency of the double events in dual layer configuration, i.e., double events that are scattered in the top plane and absorbed in the bottom plane, for inter-plane distances of 8, 10 and 12 mm, and energies of 300, 400 and 500 keV.

4.4.4 Polarimetric Performance Evaluation

The polarimetric analysis in this chapter will be divided in two irradiation configurations: the centre pixel measurements and the corner pixel measurements. The main objective is to analyse the performance of the dual plane detector by selecting double events with different scattering angles and distances between events.

4.4.4.1 Centre Pixel Analyses

The first set of polarimetric measurements was dedicated to analyse the modulation factor as function of inter-plane distance by irradiating one the four central pixels of the detectors. Pixel 27 was irradiated while 4 distances between planes (6, 8, 10 and 12 mm) where set and 4 energies (200, 300, 400 and 500 keV) were tuned. By irradiating pixel 27 we are able to obtain double event distributions throughout the crystal volume until

third order pixels. These measurements will be used to evaluate the polarimetric performance of Compton-POLCA detector in the different operation modes: single plane; dual plane; and full detector.

4.4.4.1.1 Single Plane Operation Mode

These tests have the aim to evaluate the polarimetric performance of each of the detector plane in a dual plane detector configuration. In particular, the aim of these measurements is to determine the modulation factor of both detectors as a function of the beam energy. We preformed several data selection procedures:

1. *By Double Events* – Selection of the double events triggered by the system and exclusion of the single and multiple events.

2. *By Single Plane Double Events* – Selection of the double events that have both interactions in the same plane (single plane interactions): double events generated only in the top plane and double events generated only in the bottom.

3. *By Position* – Exclusion of the double events that do not have at least one interaction in the target pixel for each detector, as we know that the first interaction is coincident with the position of the pixel irradiated by the collimated beam.

4. *By Energy* – Selection of the double events whose energy of each interaction is within a window centred in an energy given by the Compton kinematics for scattering angles ~90° (single plane interactions), and the sum of the two energies is within a window centred at the selected beam energy.

As an example of the selection performed, figure 4.33 presents the energy spectrum of the first and second interaction, after the described corrections, for a 300 keV and 400 keV beam, obtained with the top plane detector. The first interaction is coincident with the position of the pixel irradiated by the collimated beam, pixel 27. The second interaction spectrum is obtained from pixel 11. Despite the high FWHM, the peaks are measured at the expected energies presented in table 4.5.

Table 4.5: Expected energies for Compton events with 90° scattering angles, for the four energies used in the experiment.

Beam Energy (keV)	E1 (keV)	E2 (keV)
200	56	144
300	111	189
400	176	224
500	248	252

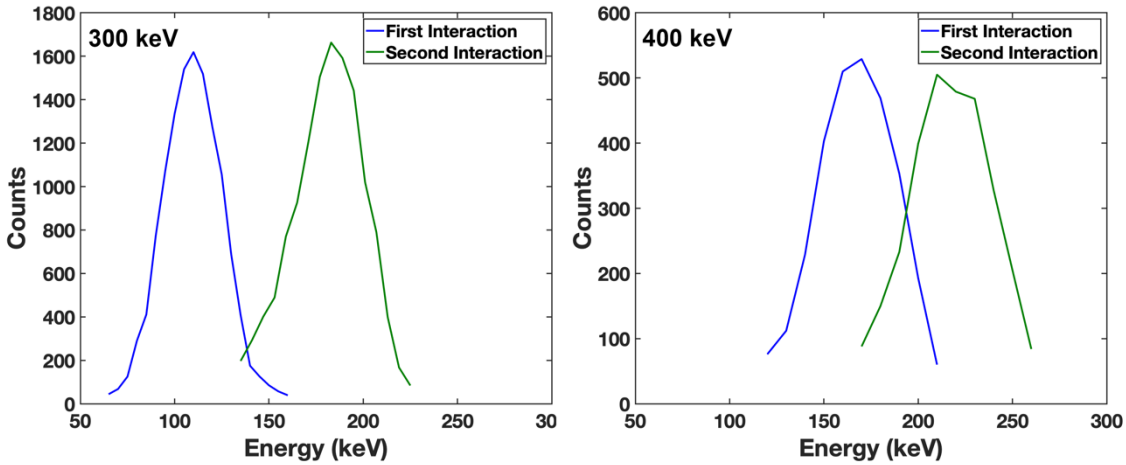

Figure 4.33: Energy spectrum of the first and second interaction of the top plane detector double events after the corrections. The left is the result for a 300 keV beam and the right for a 400 keV beam. The first interaction spectrum is obtained from the irradiated pixel, pixel 27, and the second interaction spectrum from pixel 11.

The modulation factor was calculated by averaging the values obtained from each central pixel measurements at the same energy. Each measurement was performed for a different inter-plane distance; however, we know from simulations that the modulation factor for single plane interactions does not change for neither detector. Figure 4.34 shows the polarimetric factors calculated for the two planes as a function of the polarized photon beam energy. For comparison, the Monte Carlo derived factor values for a single plane are also presented. The results are in good agreement with the results obtained through the Monte Carlo simulation except for the 500 keV case where the modulation factor of the top detector is considerably lower than the simulation. The reason for this deviation is the slit size for the 500 keV case has the same dimensions of the pixel, 1.8×1.8 mm^2, and a slightly misalignment between both detectors are revealed: in the bottom detector the beam is centred in the incident pixel, but in the top plane, a neighbour pixel of the

incident reveals some photo-electric abortion. We preferred to centre in the bottom detector due to the dual plane interaction analyses, where the position precision of the bottom plane interaction is much important than in the top plane. Besides all correction done to eliminate the effects of this misalignment it decreased significatively the modulation factor of the top detector as shown. The slightly lower modulation factor for the 200 keV case could be explained by a different minimum energy threshold between the simulation and the experiment. Due to the low energy of the first interaction for 200 keV case, the minimum energy threshold can affect heavily the efficiency of the double events acquisition. This lower modulation factor can indicate a slightly higher minimum threshold in the experiment in comparation to the simulation.

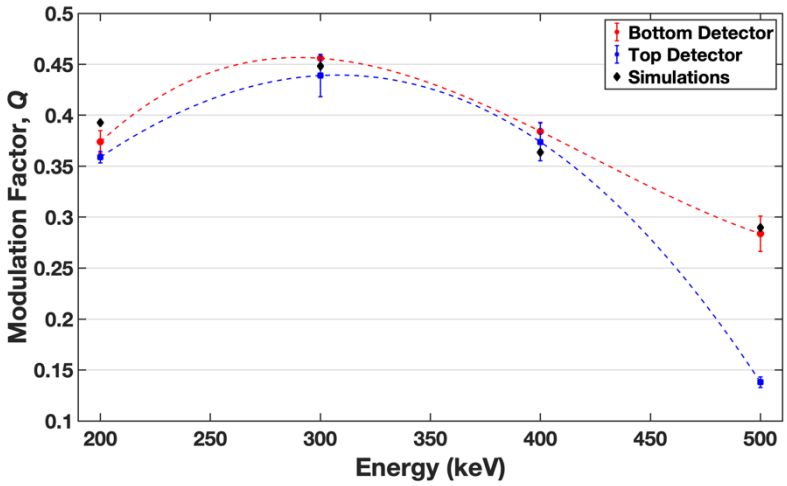

Figure 4.34: Modulation factor as function of the photon energy obtained for both detector planes using Compton-POLCA in single plane operation mode. The black markers are the simulation results.

4.4.4.1.2 Dual Plane Operation Mode

Subsequently, we evaluated the modulation factor as function of the distance between planes by selecting the dual plane interactions, i.e. photons that are scattered in the top plane and absorbed in the bottom plane. The scattering angles for these Compton events can be as low as ~9.5° corresponding to energies for the first interactions as low as ~2.4 keV. This value is much lower than the minimum energy threshold of the system thus, most of the double events will appear as single events on the absorber detector leaving there the remaining energy of the initial photon. In order to increase the efficiency of the

events collected we used a different approach for this analysis. We performed the selection by energy, calculating the expected energy for the second interaction and select the events within a window centred in it. The selection procedures were:

1. *By Bottom Plane Events* – Selection of the bottom plane events and exclusion of the events from the incident pixel, pixel 27.

2. *By Energy* – Selection of the events whose energy of each interaction is within a window centred in an energy given by the Compton kinematics for a given pixel order.

As an example, figure 4.35 shows the spectrum of the neighbour pixels relative to the irradiated pixel (pixel 27) for a 300 keV beam. It presents the spectrums for three order of pixels, corresponding to pixel 24, 25, and 26. The expected energies for these interactions are: first order (pixel 26), ~295 keV; second order (pixel 25), ~282 keV; and third order (pixel 24), ~268 keV. These energies correspond to the events that hit on the centres of the scattering and absorber pixel, but in fact, there is a range of allowed scattering angles due to the size of the pixels explaineng the large FWHM of the peaks.

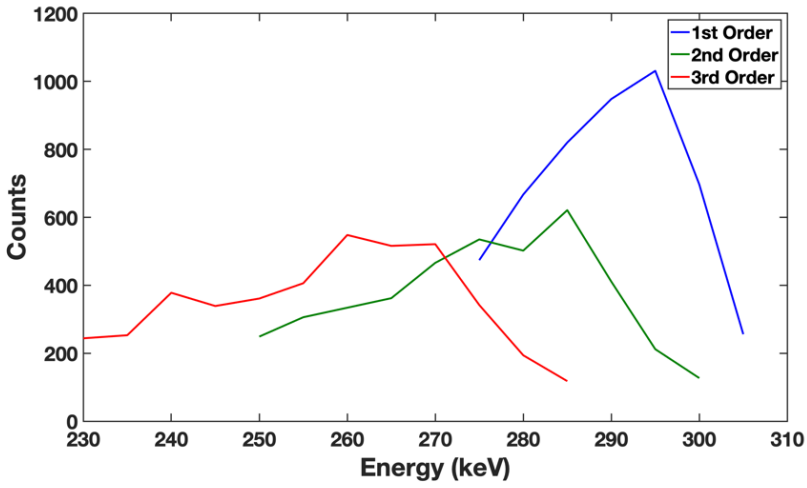

Figure 4.35: Energy spectrum of obtained from pixels 24, 25, and 26 for a 300keV beam irradiating in pixel 27.

In figure 4.36 is shown the modulation factor as a function of the distance between planes for the four energies evaluated. Is also represented the results obtained from simulations for the same beam conditions and distances between planes from 2-14 mm. The results, as expected, show a decrease of the modulation factor when the distance between

planes increase and good agreement of the trends of both experimental and simulated results.

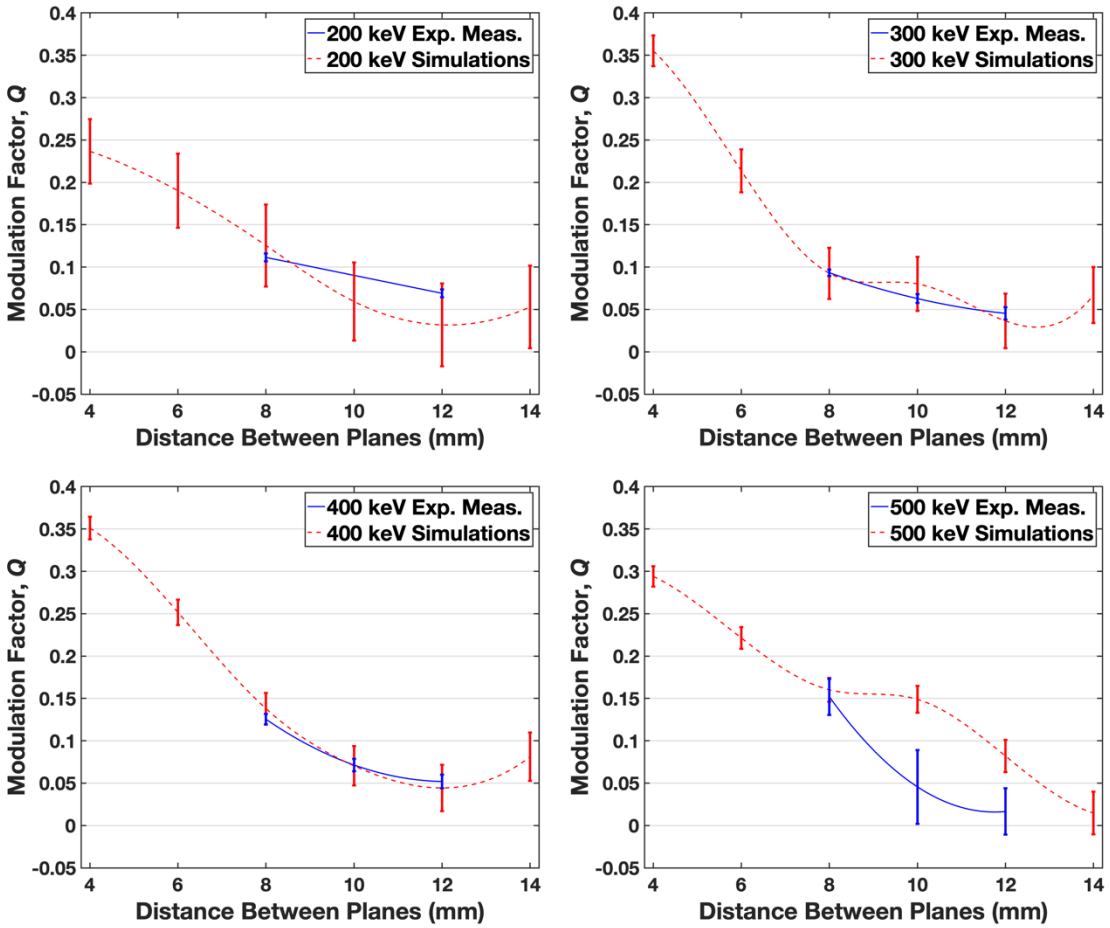

Figure 4.36: The modulation factor measured for ~200 keV, ~300 keV, ~400 keV and ~500 keV photons at three different distances between planes obtained by Compton-POLCA in dual plane operation mode, compared with the simulations for distances between planes from 2-14 mm.

4.4.4.1.3 Full Detector Operation Mode

As next, we analyse the polarimetric performance of the Compton-POLCA in full detector operation mode. Figure 4.37 presents the modulation factor as function of the detector plane distance and the simulations for distances between planes between 2-12 mm. Results show a good agreement of the trends of both experimental and simulated results, both presenting a smooth increase of the modulation factor for detector plane distance

from 8-12 mm, due to the efficiency decrease of the dual plane mode and therefore of its less weight on combined modulation, as explained in the previous chapter.

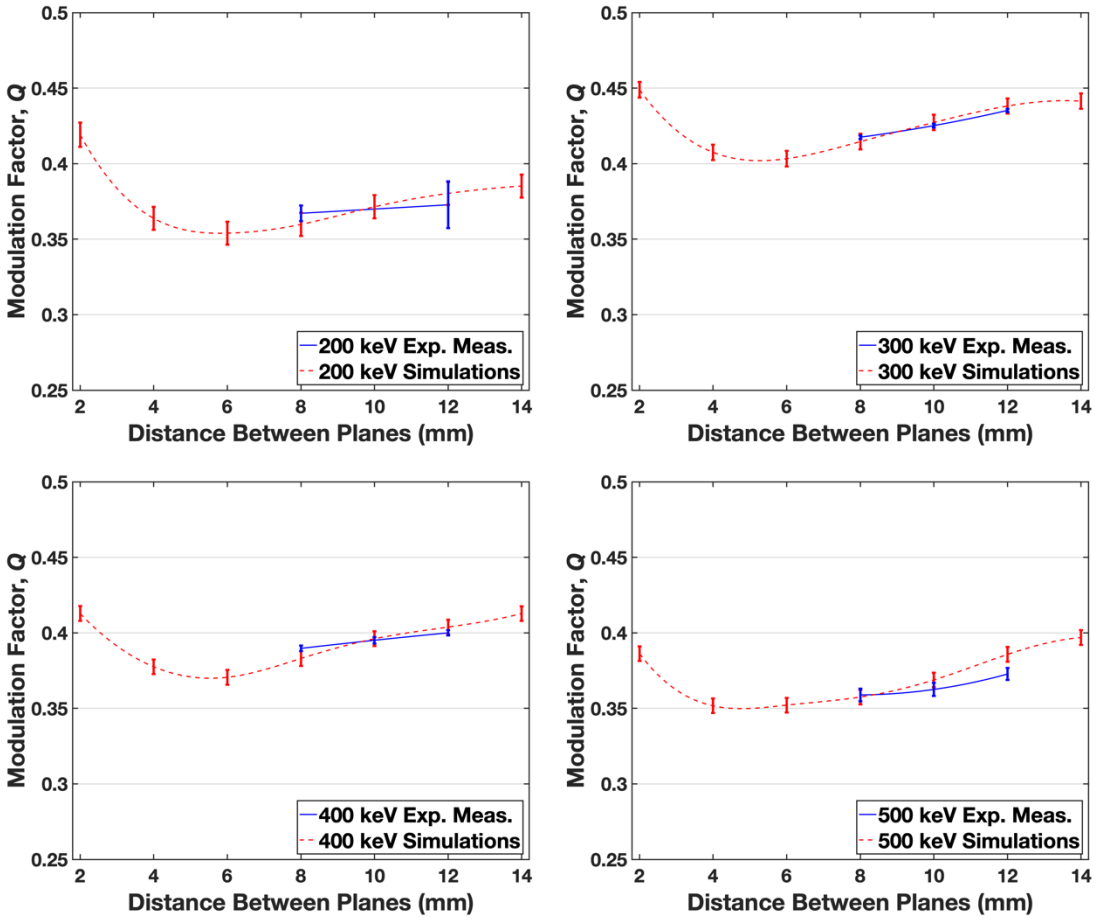

Figure 4.37: The modulation factor measured for ~200 keV, ~300 keV, ~400 keV and ~500 keV photons at three different distances between planes obtained by Compton-POLCA in full detector operation mode, compared with the simulations for distances between planes from 2-14 mm.

The modulation curves are essential to calculate the direction of the polarization vector of the source. In order to evaluate the potential of the dual plane detector to measure the polarization angle we traced the modulation curves from the performed event selection. In order to optimize the double-event histogram readout we applied the radial bin technique (RBT) [9], by dividing the matrix into 36 radial bins of 10º each. Pixels partially crossed by angular bin lines contribute only with a fraction of the number of events equal to the fraction of its area that is in the sector. As we know from simulations (section 3.2) and from the unpolarized beam measurements performed in the LARIX facility (further

described in section 4.5) that the geometric systemic errors has a period of π/2, we performed a further correction to the modulation curves by fitting the measured modulation curve with a function of the form:

$$N(\phi) = a_0(1+a_1 \cos(2\phi - a_2) + a_3 \cos(4\phi - a_4)) \quad (4.2)$$

The fit parameters a_1 and a_2 provide the information on the signal polarization: a_1 the amplitude and a_2 the angle perpendicular to the polarization direction ($a_2 = P + \pi/2$). The parameters a_3 and a_4 provide the information on the 0% polarization response of the detector due to its geometry: a_3 the amplitude of the non-polarized component of the signal and a_4 is its phase. a_0 is the curve offset. By removing the geometric component of the modulation curve, we were able to correct the signal polarization component. This correction method is also presented in reference [28]. Figure 4.38 present the results obtained for a 300 keV energy beam and an inter-plane distance of 8 mm. These present the modulation curves before and after the correction. As expected from theory, for a polarization angle of 0° a maximum number of Compton photons were detected in the perpendicular direction with respect to the polarization direction. Inside the experimental hutch it corresponds to the vertical direction. This matches with the fact that the beam polarization is horizontal inside the hutch since the polarization is always perpendicular to the maximum intensity direction. The measured angles for each energy and inter-plane distance are presented in table 4.6.

Table 4.6: Measured polarization direction obtained for the energies 200, 300, 400 and 500 keV and inter-plane distances of 8, 10 and 12 mm.

Energy (keV)	Measured Polarization Direction (°)		
	d = 8 mm	d = 10 mm	d = 12 mm
200	0.0 ± 3.9		– 1.7 ± 8.5
300	– 0.1 ± 3.0	0.0 ± 3.1	0.0 ± 3.2
400	0.1 ± 3.3	– 0.3 ± 3.7	– 0.3 ± 3.4
500	– 0.2 ± 4.7	– 0.2 ± 5.6	– 0.2 ± 4.5

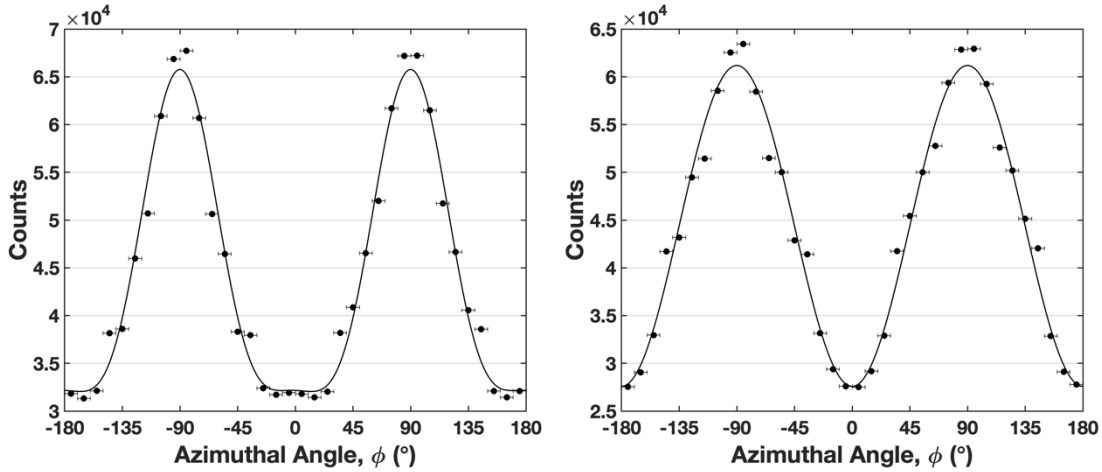

Figure 4.38: Modulation curves obtained for a 300 keV energy beam and an inter-plane distance of 8 mm. The left mage is the modulation curve obtained directly from the selected double events. The right image is the modulation curve obtained after the geometrical correction relative to the detector response to a 0% polarization beam.

4.4.4.2 Corner Pixel Analyses

The corner pixel measurements allowed double events with higher scattering angles. Since the polarimetric Compton azimuthal angle distribution is 90° symmetric, we can obtain the polarimetric parameters using double events with azimuthal angles between 0° to 90°. By irradiating pixel 0 and pixel 63 we were able to perform polarimetric analysis till the 7th order of pixels. We focused on the analyses in dual plane operation mode and the influence of the modulation factor with the distance between planes. The data selection procedure was the following:

3. *By Double Events* – Selection of the double events triggered by the system and exclusion of the single and multiple events.

4. *By Dual Plane Double Events* – Selection of the double events that have one interaction on the top plane and one on the bottom plane.

5. *By Position* – Exclusion of the double events that do not have at least one interaction in the target pixel of the top plane and one the bottom plane.

6. *By Energy* – Selection of the events whose energy of each interaction is within a window defined by the Compton kinematics for a given pixel order.

The first set of measurement was performed by irradiating pixel 63 for inter-plane distances between 8 to 16 mm in steps of 2 mm. By irradiating this pixel, we were able to analyse the bottom plane events for pixel orders between 4 to 7. The selection of these events forms a hollow cone of Compton events limited by θ_{min} and θ_{max}. Expected values for inter-plane distances from 8-16 mm are presented in table 4.7, considering pixel orders from 4-7. The modulation factor as function of the distance between planes for a 300 keV beam is presented in figure 4.39. Identical to the centre pixel measurements the modulation factor shows a decrease as distance between planes increase.

Table 4.7: Expected values of θ_{min} and θ_{max} for the various inter-plane distances used, when selecting events from pixel orders between 4 to 7.

Distance Between Planes (mm)	θ_{min} (°)	θ_{max} (°)
8	41	62
10	35	56
12	30	51
14	27	47
16	24	43

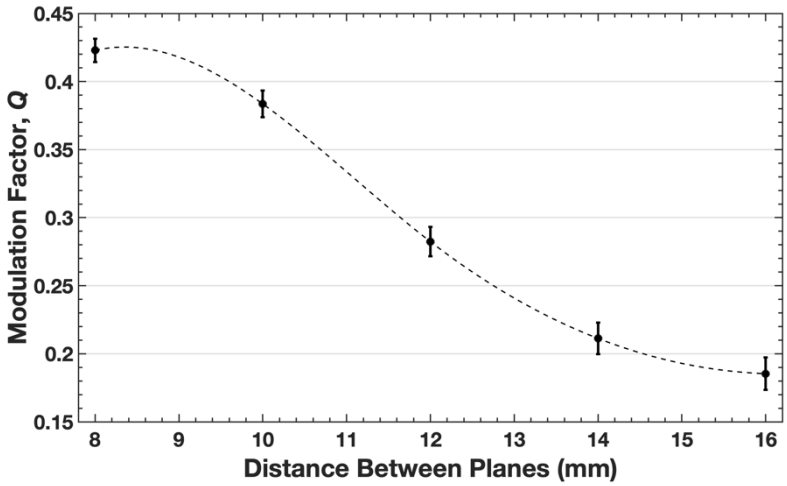

Figure 4.39: Modulation factor for distances between planes obtained by irradiating pixel 63 of the Compton-POLCA in dual plane operation mode by a 300 keV beam.

In order to analyse the dual plane modulation factor as a function of the scattering angle, we implemented a different approach. We irradiated the pixel 0 for two inter-plane distances: 8 and 12 mm. Hereby, we were able to make polarimetric analysis between the 3rd and the 7th order of pixels. The selection of the events by scattering angle made was the same as in the simulations presented in section 3.3.2. In figure 4.40 is presented the modulation factor as function of the scattering angle. The error on the *x* axis represents the range of scattering angles allowed in that analyses (θ_{min} and θ_{max}). The results of both distances align perfectly with each other showing the increase of the modulation factor with the increase of the scattering angle. The values obtained for the highest scattering angle are higher as the ones in the single plane detector. This suggest that a higher pixel order can lead to best polarimetric performances. The main cause for this could be the higher distance between the double events. Higher distance between the double events lead to higher precision on the azimuthal angle measurement increasing the modulation factor. This result is in accordance with the simulations performed in section 3.3.2.

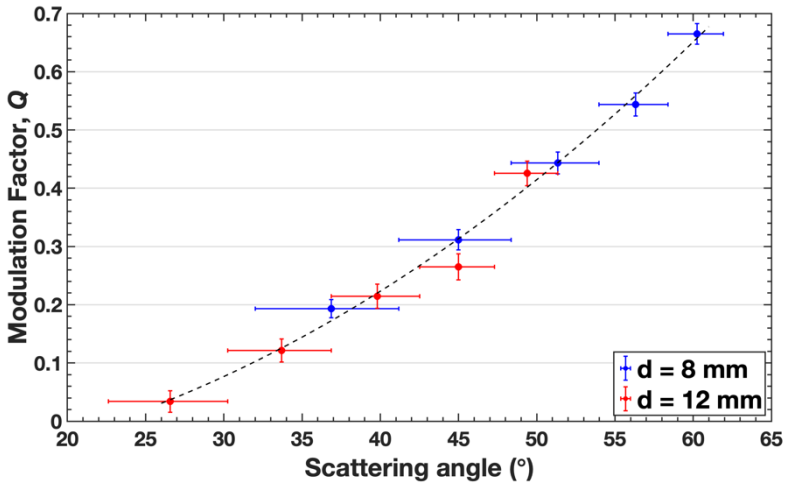

Figure 4.40: Modulation factor as function of the scattering angle obtained by irradiating pixel 0 of the Compton-POLCA detector in dual plane operation mode by a 300 keV beam.

4.4.5 Discussion

The results obtained in this campaign reinforce the fine polarimetric potential of the multi-layer configuration CdTe focal planes. By analysing the polarimetric performance of the different Compton interactions we conclude that high polarimetric performances can be achieved when combined single and dual plane operation modes, with the advantage of the high detection efficiency provided by the multi-layer solution. We were able to test the dual plane detector for energies between 200 keV to 500 keV and detector plane distances from 8 to 16 mm. A modulation factor of Q ~0.46 was achieved for a 300 keV beam in the single plane operation mode; Q ~0.09 in dual plane operation mode (inter-plane distance: 8 mm); and Q ~0.42 in full detector operation mode. However, as seen in the simulations, the trends of the modulation as a function of the distance between the two interactions show a slight increase. This is observed in the corner pixel irradiation measurements, where is observer a modulation factor Q up to ~0,67 for scattering angles between 58.4° and 62.0°, and when combining all the interactions in a dual-layer mode, where we observe a marginal increase of the modulation factor with the increase of the detector plane distance, from ~0.42 to ~0.44 for detector plane distances of 8 mm and 12 mm respectively, as anticipated in the Monte Carlo simulation chapter.

Furthermore, the combined experimental and simulated results provide as well a valuable estimation of the great polarimetric potential of 3D position detection solutions, as

the ones being developed by our team for ASTENA mission. Since 3D will be able to probe in greater detail the double event photons' trajectories as well as adding the capability to reconstruct the respective electron path, that is also modulated by the polarization [9], it will increase the polarization sensitivity to the celestial sources' emissions. Additionally, it will provide a better reconstruction of the Compton events and therefore better source position and spectroscopic resolution.

4.5 LARIX Unpolarized Beam Measurements

In order to characterize a polarimeter it is important to describe its response not only to polarized, but also to unpolarized signals. For a perfectly uniform and symmetric instrument the modulation curve from a 0% polarized signal should be totally flat. However, the discretization produced in double event distributions inherent to the polarimeter voxels' geometry is a source of systematic effects on polarization measurements. In fact, the square shape geometry of this prototype introduces an asymmetry, since there is more material thickness in the diagonal directions than along the x and y axis, leading to a modulation curve with four peaks. For a polarized beam, this effect becomes especially important for square pixels when the polarization direction does not align with either the two main axis of the pixelized matrix and when the double event distribution around a central pixel spreads over a few pixels from the central pixel. For this propose we tested the prototype in the unpolarized gamma-ray beam of LARIX facility.

4.5.1 LARIX Facility

The LARIX laboratory is located in the Scientific-Technological Pole of the University of Ferrara in an underground building that includes a 100 m long tunnel. This facility was implemented to develop a Laue lens system advanced technology, with broad energy band (70/100-600 keV) and long focal length (up to 100 m), for space astrophysics. A diagram of the beam-line is shown in figure 4.42. It carries two x/gamma-ray sources able to meet the experiment requirements: a portable Betatron source that emits in the energy pass-band from few tens of keV up to 2 MeV (practically its flux makes it available up to 1 MeV); and the a hard X-ray generator with an energy pass-band from a few keV to about 300 keV. The emissions of both sources are unpolarized. The expected photon

spectrum from the hard X-ray generator and for the current Betatron are shown in figure 4.41.

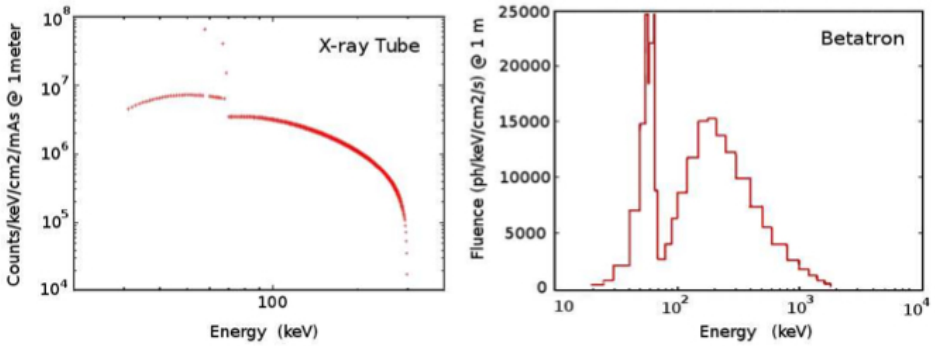

Figure 4.41: Expected photon spectrum (in photons $keV^{-1}\,cm^{-2}\,s^{1}$) at 1 m distance of the X-ray tube (left) and from the Betatron (right).

In a preliminary meeting before the experiments. we decided to use the Betatron since its energy range spans over the energy range of the previous ESRF experiments. Unfortunately, after we mount our detector setup for this propose we notice that the Betatron had technical problems that we could not resolve in the available time frame. For that reason, we moved the detector setup for the hard X-ray generator.

The hard X-ray source consists on a Tungsten rotating anode (fine focus of 0.3 mm diameter) operating at a maximum voltage of the X-ray source at 320 keV. A 20 mm thick Tungsten plate with a 3 mm diameter hole and a 50 mm thick Lead shield with a 1 mm diameter hole are placed just after the source to limit the beam divergence. After the collimator, the photons cross a 21 m long stainless steel beam-line with an internal diameter of 60 cm. A set of vacuum pumps guarantees a vacuum of at least 1 mbar inside the tubes in order to minimise photon absorption and scattering.

The beam-line outcoming gamma-ray beam enters in a clean-room which is composed by a collimator and a hexapod. The collimator is equipped with a slit with variable aperture; four Tungsten blades (20 mm thick) can be independently adjusted in order to provide a beam from 0 to 30×30 mm^2 size. The hexapod is used to adjust the position of a Laue lens sample and was not used in this experiment.

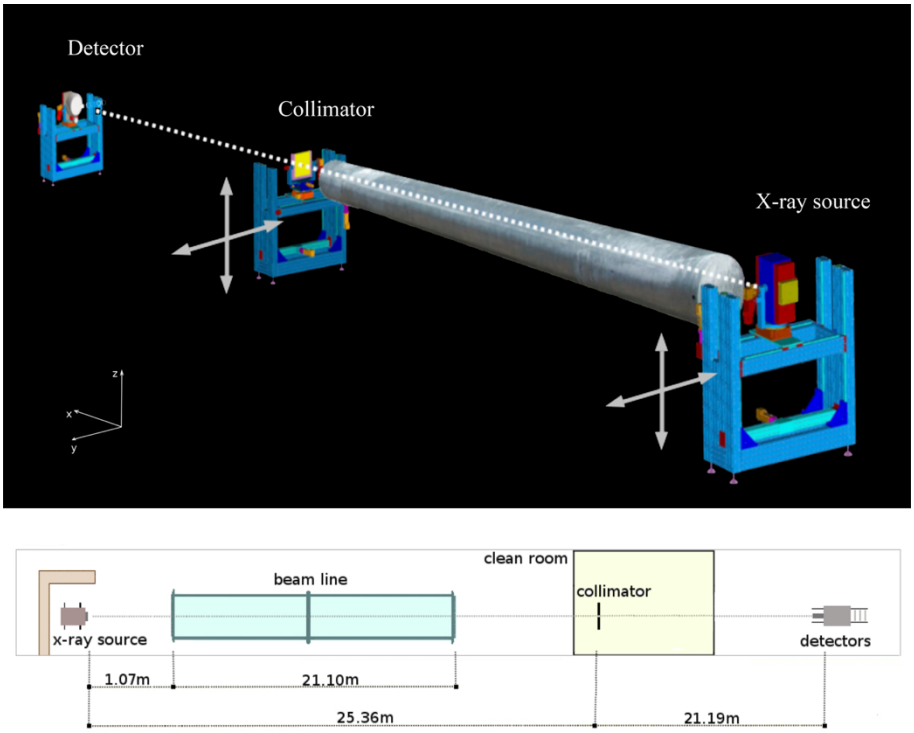

Figure 4.42: Layout and sketch of the tunnel with the relative distances between the sub-systems of the LAUE apparatus at the University of Ferrara. Adapted from [197].

Finally, the beam exits the clean-room, and interacts with the detection system. Two auxiliary detectors were operated: a gamma-ray imaging detector (20×20 cm^2 sensitive area, spatial resolution 200 μm) and a HPGe detector (2.5 cm diameter, energy resolution of 500 eV @ 122 keV). The Compton-POLCA is mounted next to these two detectors as shown in figure 4.43. The detectors are placed on carriage that can move back and forth on a 15 m long rail along the beam axis and a 2-axis motorized stage allow the translation of the detectors in the plane perpendicular to the beam. A manual rotation stage is also mounted to rotate the Compton-POLCA in the plane perpendicular to the beam (*y*-*z* plane). In figure 4.42 is schematized the LARIX facility and its sub-systems. It also presents the relative distances between the sub-systems used in the experiments.

In order to analyse the detector performance under an unpolarized beam we made four long measurements of four azimuthal angles: 0°, 15°, 30° and 45°. In each azimuthal angle measurement, the double event distribution was analysed and the correspondent modulation curve was obtained.

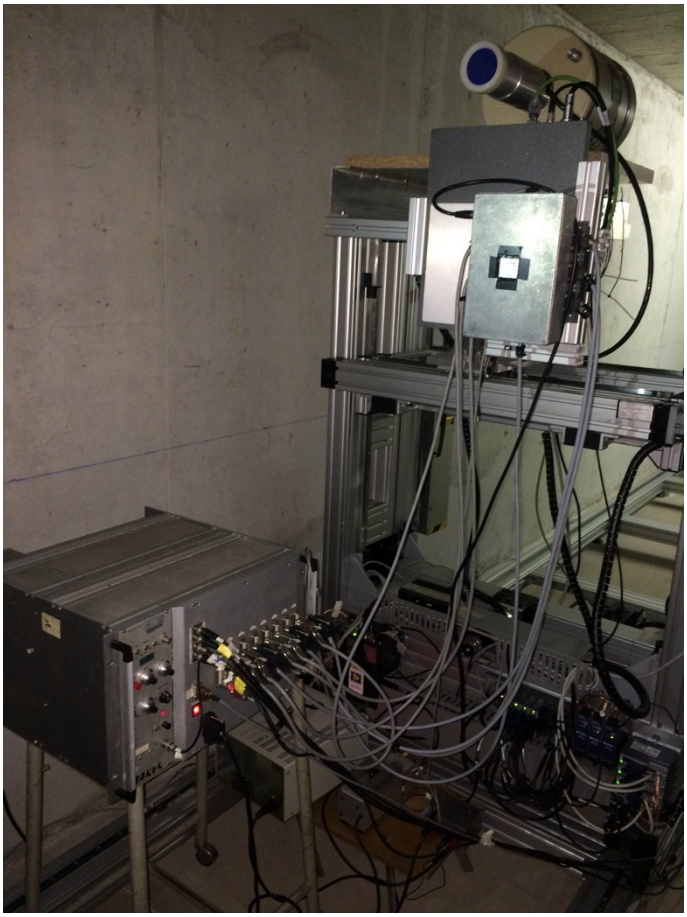

Figure 4.43: The dual plane detector mounted on the carriage. On the side of the dual plane detector is the gamma-ray imaging detector and on top the HPGe detector. Is possible to see also the TAKES read out system.

4.5.2 Spectral measurements

In figure 4.44 is shown the spectrum for each plane, registered in the beam incident pixel. The spectrum obtained is a continuum, with a higher flux at the lower energies, decreasing until ~300 keV, becoming the count rate very low up to 500 keV. The differences between the bottom and the top detector spectra are due to the photoelectric efficiency that is very high for energies ~100 keV. For these energies most of the photon will interact in the top plane detector, decreasing drastically the number of events recorded in the bottom detector.

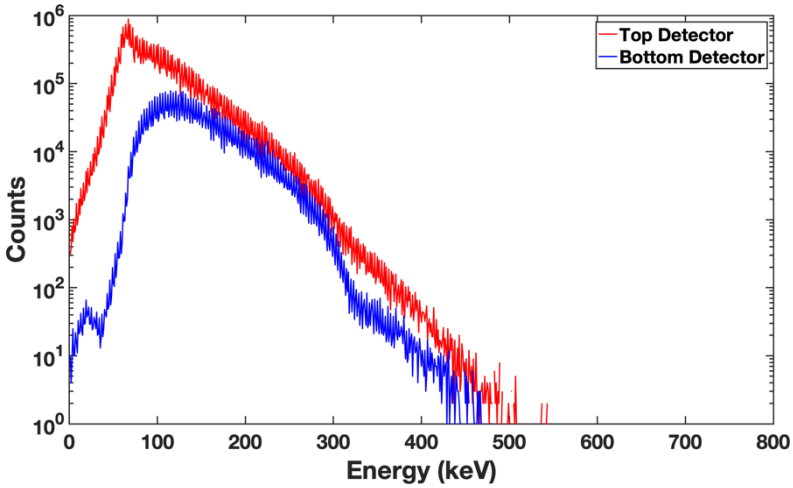

Figure 4.44: Energy spectrum obtained at the LARIX-A facility for both top plane and bottom plane detectors.

4.5.3 Modulation Curves

To evaluate the modulation curves obtained under an unpolarized beam, we selected the double events of each measurement. We considered only the top plane events since the geometry is the same for both planes. We exclude the multiple events since we cannot determine the order of each hit. For double events, we know were occurred the first interaction because it is the position of the pixel irradiated by the collimated beam and therefore during the analyses, we exclude double events that do not have at least one interaction in the target pixel. As the beam generate a continuum spectrum, we selected the double events only those in which the sum of the two interactions is within a window centred at the selected beam energy in order to reduce the range of the photon energies. Furthermore, taking into account the Compton kinematics and the detector geometry we also calculated the approximate energy of each hit. Since we are looking for single layer double events, we considered a scattering angle of ~90°. The modulation curve, $N(\phi)$, giving the number of double-events as a function of the azimuthal angle, was then obtained. In order to optimize the double-event histogram readout, we applied the radial bin technique (RBT) [9], dividing the matrix into 36 radial bins of 10º each.

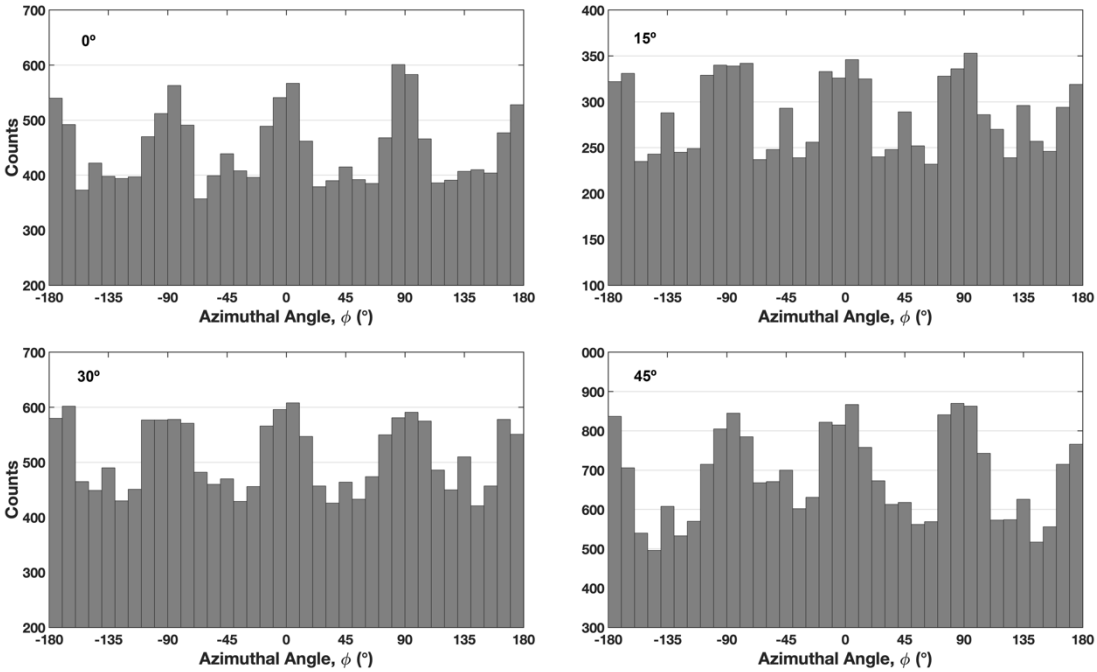

Figure 4.45: Modulation curves obtained at the LARIX facility.

The modulation curves obtained for the 4 azimuthal angles are presented in figure 4.45. As expected, the modulation curves are similar for the 4 azimuthal angles since the beam is nonpolarized. The modulation curves follow a of $\pi/2$ periodicity. This is due to the square geometry of the pixels and detector. The peaks in -180°, -90°, 0°, 90° and 180° are correlated with the neighbour pixels around the irradiated pixel. Since the pixels are squared, most of the second interactions will occur in the neighbour pixels generating a systemic effect on the results. The smaller peaks for -135°, -45º, 45º and 135° are related to the square shape of the detector. These angles correspond to the diagonal double events which have the highest probability since there is a longer detector thickness for photons to cross.

The primary objective for this experiment was to correct the ESRF results, however the conditions were quite different, namely the continuum spectrum of the beam and its size that makes it difficult to correct the data. Therefore, we performed a qualitative approach on the results. Starting from the unpolarized pattern obtained by the simulations of the experiment (section 3.2), we integrated the $\pi/2$ periodicity pattern component herein obtained on the modulation curves correction. This method was performed on the results from the ESRF 2018 campaign reported in section 4.4. This correction method was successfully previously implemented in the analysis of reference [28].

4.6 Minimum Detectable Polarization

Based on the values of the modulation factor obtained with the Compton-POLCA in full detector operation mode we can evaluate the MDP achievable for a broadband Laue lens telescope with the characteristics of the ASTENA NFT in the 90–600 keV band in a Low Earth Orbit (LEO). For such type of instrument, the MDP expression defined by equation 1.17, the term giving the source counts ($A \cdot S_F$) is the product of the source flux (photons/s/cm^2) integrated over a defined energy band (ΔE) by the Laue lens collecting area in the same energy band. The coefficient B is the background in counts/s integrated over ΔE and on a surface (cm^2) described by the radius (FWHM) of the point spread function (PSF), i.e., $\pi \cdot 32$ mm2 (~0.3 cm2). Using a source with a Crab spectrum [198], focal plane detector double events efficiencies, as evaluated by Monte Carlo over the Laue lens pass band, and backgrounds level, as reported in [199], we could estimate the achievable MDP for different observation time and various source intensities. In the figure 4.46 we used two values of the modulation factor Q_{100} derived from measurements with Compton-POLCA detector using ~100% polarized beam. These values are compatible with the assumed focal plane 3D spatial resolution of 0.35 mm in each direction projected for the NFT.

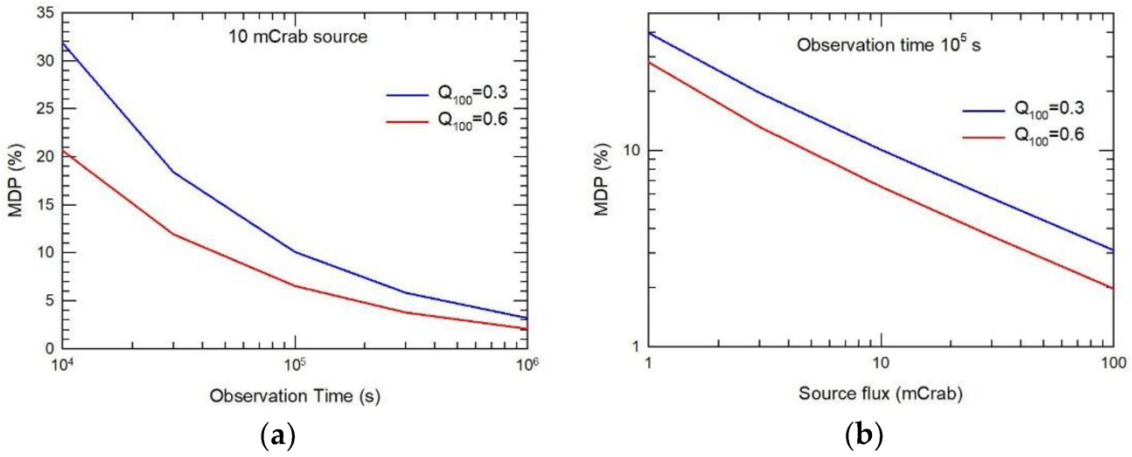

Figure 4.46: Polarimetric performance achievable by a 20 m focal length broadband (90–600 keV) Laue lens telescope in a LEO orbit: (a) MDP vs observation time for a 10 mCrab source and two representative modulation factors and, (b) MDP vs source intensity (100% polarized) for a 105 s observation time.

5 Proton Radiation Analyses on CdTe Detectors

Analysis of potential effects of the orbital radiation environment on space instrumentation is essential to project and design a high-energy astrophysics space mission [139], [200]–[203]. Inline, it is crucial to study instrument materials' radiation damage and its effects on their operational performances under conditions that are as similar as possible to the orbital radiation environment conditions. To foresee the operational performances and the expected lifetime of a detection device in a particular orbit, it is critical to know the environment radiation type and its profile. Semiconductor based instruments, particularly CdTe planes, require further space equivalent radiation environment tests in order to guarantee the required sensitivity in orbit. Among the specific instruments that require further orbital radiation environment testing are 3-D CZT/CdTe detection planes and Laue lens CZT/CdTe focal planes, for gamma-ray astrophysics applications.

In order to improve future missions' instrument inflight operational performances, we have studied and analysed the proton radiation damage effects and the nuclear activation of several CdTe detector prototypes when irradiated by a proton beam with energies up to ~ 14 MeV and at the ICNAS cyclotron facility in Coimbra. These experiments were carried out by two master students in 2015 [204] and 2018 [205], and as a complement of my PhD project, I participated on most of the activities within the context of this work. My participation on the first work, [204], was mainly on the activities at the ICNAS facility and in the evaluation of the detectors' performance one year after the experiments.

In the second work, [205], I took part in most of the preparatory phase at LIP laboratory and during the irradiations at the ICNAS facility, by helping on the detector setup development, spectral and mobility measurements and irradiations setup. Herein we summarize the methods and the results of these experiments.

The detector prototypes tested during the first proton irradiation experiment were from the same batch of the ACRORAD detectors used in the Compton-POLCA design and described in section 2.3. The CdTe detectors were mounted at the ICNAS cyclotron proton setup and were then irradiated from cathode layer side by an 18 mm diameter uniform proton beam with ~14 MeV. Prototype external and internal (figure 5.1 a)) measurements show low activation background level (<1.3×10−5 counts/cm^2.s.keV scaled for 1 day LEO protons and short-lived radioisotopes) compared with the emission level of main gamma-ray sources such as the Crab Nebula, when irradiated by proton fluences equivalent to scientific mission time-frames up to ~22 years. Furthermore, a CdTe based high-energy space telescope equipped with passive and active (anti-coincidence) shielding will reduce one or more orders of magnitude proton nuclear activation component. Therefore, we can fairly estimate that the contribution of CdTe activation background should have a minimal impact in instruments' performance deterioration. Furthermore, CdTe presents good radiation hardness for typical LEO proton fluences. The measured energy resolution shows a small degradation up to 9 years orbital proton fluence equivalent, but for lower energies (122 keV) and 22 years equivalent proton fluence the energy resolution deteriorates by 60%, however it is still suitable for most of the mission scientific requirements (figure 5.1 b)). For 511 keV the energy resolution degradation is about 14%, becoming lower for higher gamma-ray energies. Furthermore, CdTe show a very good level of spectroscopic properties' recovery, actually one year after the irradiation the energy resolution recovered almost totally for higher energies (e.g. 511 and 1275 keV) and recovered down to an energy resolution level only ~15% worse before proton irradiation for the 122 keV line, figure 5.1 b) [192].

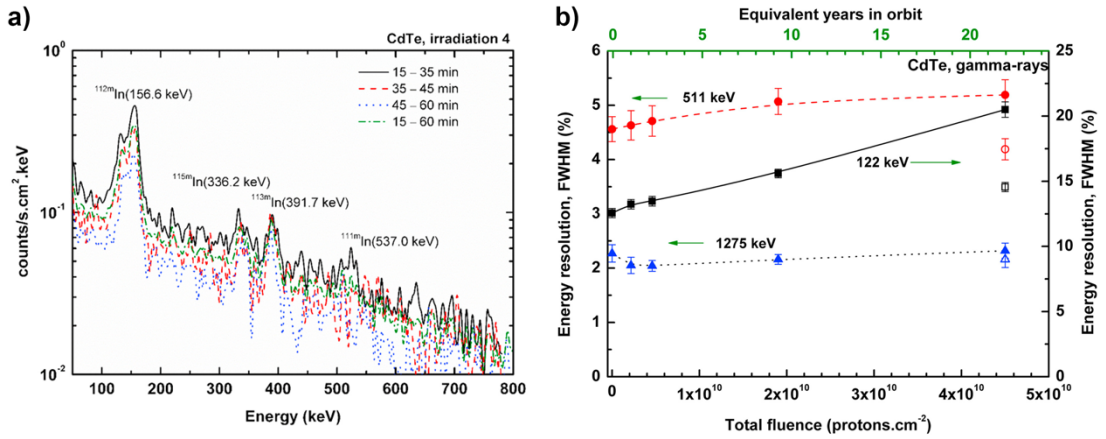

Figure 5.1: b) CdTe detector internal activation emission spectra after irradiation (total fluence: 4.50×10^{10} protons/cm^2). The spectra were measured ~15 to 35 min, ~35 to 45 min, ~45 to 60 min and ~15 to 60 min. b) Prototype energy resolution degradation for ^{57}Co 122 keV (right vertical axis) and for ^{22}Na 511 keV and 1274 keV peaks (left vertical axis), after its irradiation. Open symbols correspond to measurements performed one year later for the same emission lines.

During the second proton irradiation experiment, we tested several 1.0-mm-thick EURORAD ohmic CdTe monolithic detectors. The CdTe detectors were exposed to several irradiation sets with four proton beam energies at the Coimbra University ICNAS cyclotron: 13.8, 9.7, 5.7, and 3.3 MeV, for cumulative fluences from ~2×10^9 up to ~5×10^{10} protons.cm^{-2}. With this proton irradiation sequence, we aimed to simulate the typical LEO proton almost-flat energy spectrum profile in the low-energy band, 3-14 MeV [206]. The total fluence was set to generate a total proton fluence of ~1, ~2, ~10, and ~20 years in a LEO. The impact of the proton radiation field was analysed through; its charge transport properties; mobility-lifetime product for electrons, ($\mu\tau_e$), and holes, ($\mu\tau_h$); and spectroscopic properties (energy resolution and peak-to-valley ratio, for gamma-ray lines within 60-662 keV). The measured ($\mu\tau_{e,h}$) products exhibit values very close to the initial ones, prior to proton irradiation, with small variation (<10%) which was uncorrelated with the proton dose as presented in figure 5.2 b) The small overall changes in ($\mu\tau_{e,h}$) generate small changes in the energy resolution (figure 5.2 a) and the peak-to-valley ratio, beyond an initially sharp response up to ~5×10^9 protons cm^{-2}. From the obtained results, we can infer that the proton dose applied (significantly lower than in the first experiment due to a greater component of lower energy protons stopped near the surface of the detector) was not enough to modify significantly the charge transport properties and the

spectroscopic properties of the detectors, due to the low perturbation of the steady-state of trap concentration [207], [208].

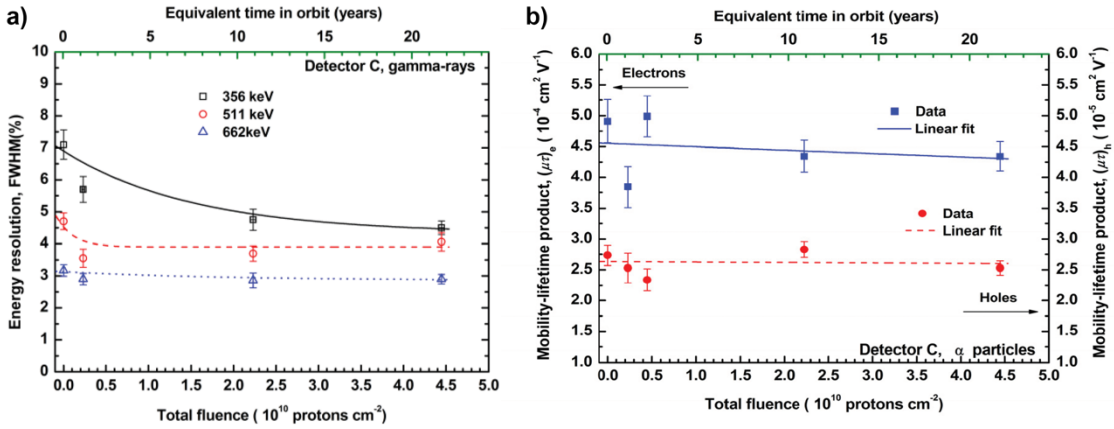

Figure 5.2: a) Energy resolution versus the total proton fluence for several gamma-ray lines with a CdTe detector. b) Estimated values for electron and hole mobility-lifetime products versus the total proton fluence.

6 Laue Lens

With the advent of the NASA NuSTAR mission [41] carrying on board two focusing telescopes operating in the 3-79 keV band, higher sensitivity observations on the hard X-ray sky are finally becoming possible. Despite the techniques developed for gamma-ray astronomy, sensitivity in the 0.1-100 MeV band is still a critical parameter due to the low signal-to-noise relation. A Laue lens telescope, which is based on diffraction from crystals in a transmission configuration, offers a very interesting technical solution to the implementation of a focusing telescope that can extend the energy band beyond 80 keV. Using this technology, it is expected a big leap in sensitivity, by a factor 10-100 with respect to one of the most sensitive instruments of the current generation, and a significant increase in angular resolution (from ∼10 arcmin of the mask telescopes like the INTEGRAL IBIS to less than 1 arcmin) [209], [210].

One of the Laue lens instruments being proposed is the ASTENA telescope, based in a multi-layer CdTe based detector on its focal plane, the NFT. The LARIX facility provides the best conditions to evaluate this mission concept. In fact, the LARIX laboratory was developed and built within the context of the LAUE project, supported by the Italian Space Agency (ASI) devoted to create a reliable technology and process to build a Laue lens with long focal length (100 m) able to focus photons in the 80-600 keV energy range [210]–[214]. The Laue lens prototype assembled so far is composed by bent crystals of Gallium Arsenide (GaAs, 220) and Germanium (Ge, 111). Past experiments using an X-ray imager and an HPG spectrometer were performed to evaluate the focusing properties of bent crystals. Herein, we present a preliminary study of the response of a sample of

GaAs bent crystals obtained using the Compton-POLCA as focal plane detector. In particular, we report on the capability of the detector to sample the focused image, i.e. the PSF, of GaAs bent crystals, determine its energy pass band and evaluate its uniformity. The series of experiments were performed between December 2018 to February 2019 at the LARIX facility and were partially founded by the AHEAD project.

6.1 The Laue lens concept

Laue lenses principle exploit the interference between the periodic nature of the electro-magnetic radiation and the periodic configuration of the atoms in a crystal. In a Laue lens, photons pass through the full crystal, using its entire volume to interact coherently. In order to be diffracted, an incoming gamma-ray must satisfy the Bragg-condition, relating the spacing of lattice planes, d_{hkl}, with the energy of incident photons E and with the angle of incidence θ_B with respect to the chosen set of planes (hkl) (the indices h, k, l, known as Miller indices, are defined as the reciprocals of the fractional intercepts which the lattice plane makes with the crystallographic axis),

$$2d_{hkl} \sin \theta_B = n \frac{hc}{E} \tag{6.1}$$

where d_{hkl} (in Å) is the spacing of the lattice planes (hkl), n is the diffraction order, hc = 12.4 keVÅ and E is the energy (in keV) of the gamma-ray photon.

A Laue lens is made of a large number of crystals, in transmission configuration (Laue geometry), that are disposed in such a configuration that they will concentrate the incident radiation onto a common focal spot (figure 6.1 a)). The Laue lens under development in the LARIX facility is requested to have a spherical shape with radius R and focal length $f = R/2$ (figure 6.1 b)). Any Laue lens will diffract photons over a certain energy passband (E_{min}, E_{max}), that is dependent on the radius, r_{max}, of the outer ring of crystals, and on the radius, r_{min}, of the innermost ring of crystals, respectively, figure 6.1 b). Ideally, for astronomical applications, the Laue lens passband should provide the highest effective area, with the better uniformity as possible as a function of energy.

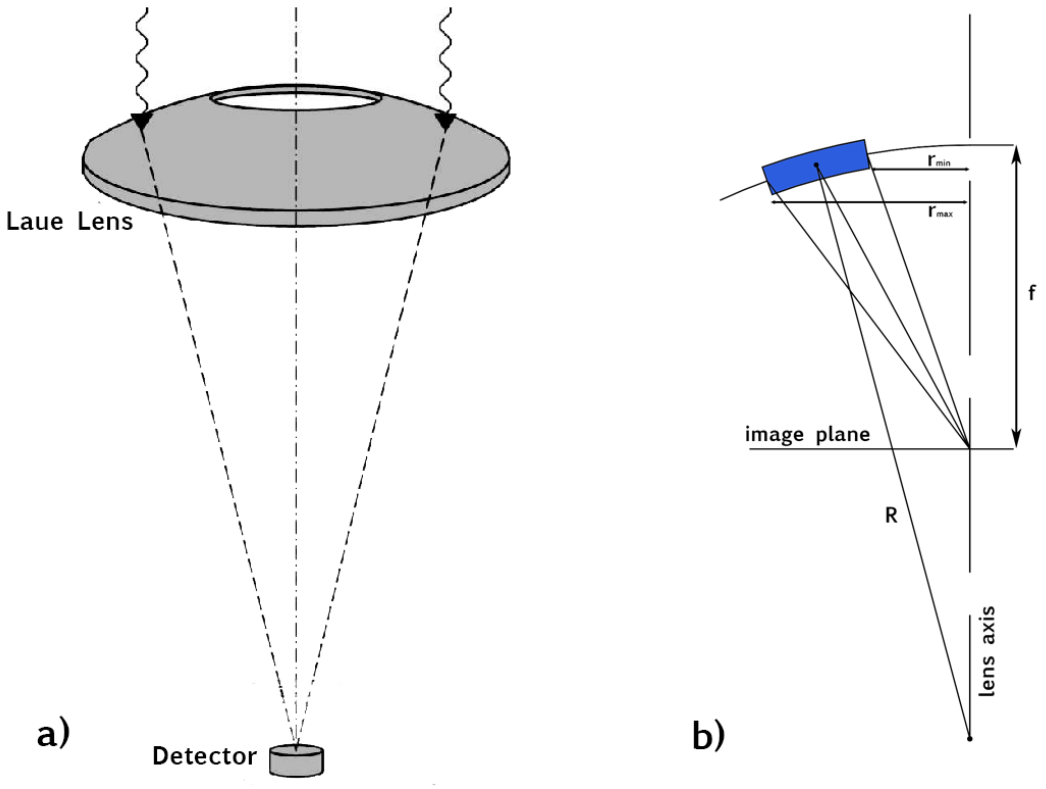

Figure 6.1: a) Principle of Laue lens. The gamma-rays from a source at the infinity are diffracted, to the focal point of the lens b) Basic principle of a Laue lens in which the crystals are placed on a spherical surface.

6.2 Experimental Setup

The LARIX laboratory facility is described in section 4.5 and in several thesis and papers [197], [210], [213], [215], [216]. The main elements of the LARIX project are summarised in figure 6.2, where are also shown the reference axes to clarify the description of each component and its possible motion. A set of nine (220) GaAs crystals were placed after the collimator in the clean room, figure 6.3. The crystals were glued on a petal attached to a frame which is controlled by an *y-z* translation stage, used for coarse translations, and a 6-axis hexapod, for fine translations and rotations. The crystals used are GaAs planes (220), size of 30×10 mm^2, 2 mm thickness and a curvature radius of 40 m, resulting in focal length of 20 m. Their nominal curvature value can differ by 5-10 %. The detector was placed at ~11.4 m where the crystals provide the best focusing, when irradiated by diverging radiation, as in LARIX, where the setup has a source-crystals distance = 26.5 m and presents a divergence after the fine collimator ~1.5' [217].

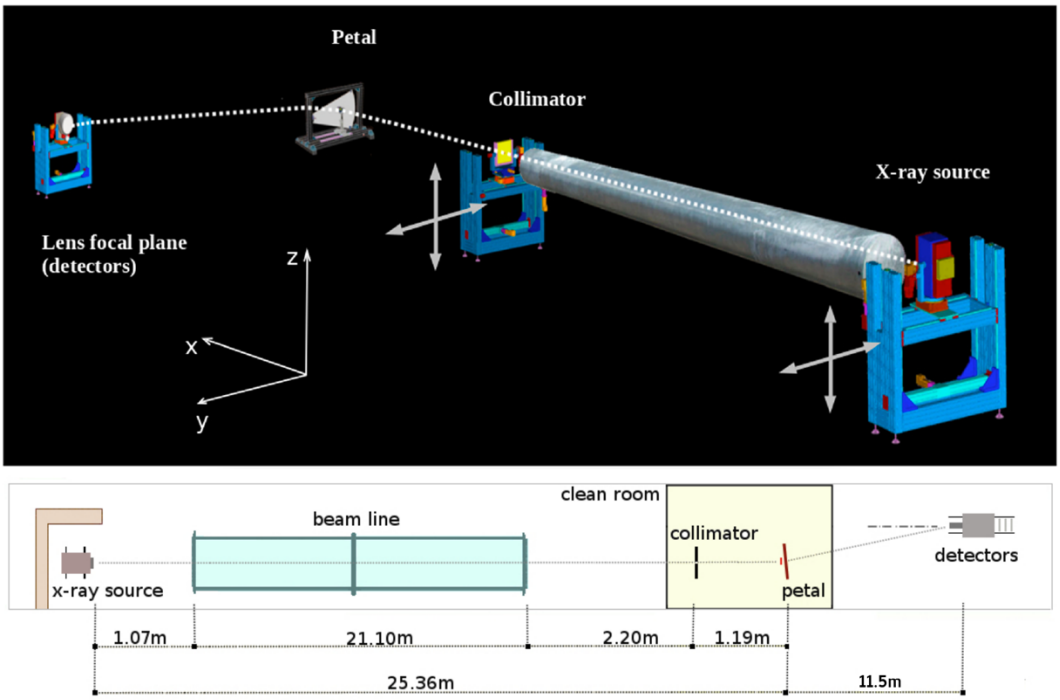

Figure 6.2: Top: Layout of the LAUE apparatus in the facility of the University of Ferrara. Bottom: Sketch of the tunnel with the relative distances between the sub-systems.

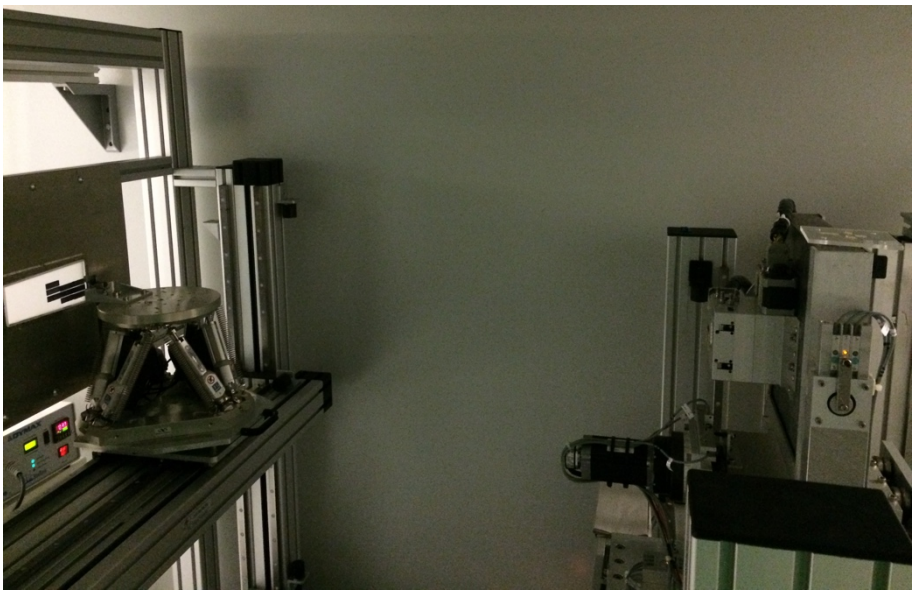

Figure 6.3: Picture inside the clean room. The system on the right is the square aperture remotely adjustable collimator. On the left is the petal with the GaAs crystals bonded on a quartz glass substrate, through a hexapod and a *y*-*z* translation stage.

In figure 6.4 is presented the image obtained with the X-ray imager (200 μm spatial resolution) of the diffracted beam by a GaAs (220) crystal, at a crystal-detector distance

of ~11.4 m. Along the *y* direction, where the focusing effect is expected, the diffracted image is ~1.5 mm wide. Along the *z* direction, no focusing effect is expected and the diffracted beam is 12-13 mm wide, mainly due to the divergence of the beam.

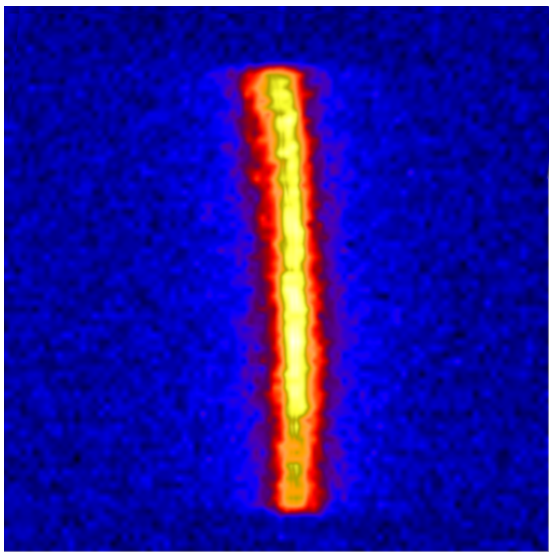

Figure 6.4: Diffracted image generated by a GaAs bent crystal with a beam size of 20×10 mm^2, observed at 11.5 m from the crystal. The image was obtained with the X-ray imager (200 μm spatial resolution).

6.3 PSF Scan Tests

The first set of measurements were performed in December 2018 with the objective to evaluate the capability of the Compton-POLCA detector to perform PSF analyses for the Laue lens crystals. For these measurements we irradiate the centre of a GaAs (220) 30×10 mm^2 crystal with an 8×8 mm^2 beam. The resulting diffracted beam was measured with the Compton-POLCA detector. As expected, the beam profile was identical to the one presented in figure 6.4, thus, we perform a set of scan test along the *y* direction, where the focussing effect occur. We centred the beam along the Compton-POLCA *z* direction and we performed a scan along the *y* direction in steps of 1 mm (9 measurements, integration time 180 s each). Our objective was to evaluate the spatial resolution of the Compton-POLCA and analyse if it is capable to detect these shifts. To do this, for each measurement, we reconstructed the beam position along the *y* direction by integrating the events in each detector column (detector *z* direction) and performing a gaussian fit of the

distribution (number of events in each detector column). The position of the gaussian peak will correspond to the detector reconstructed position in pixel units.

In figure 6.5 is presented the reconstructed position as function of beam position, both in pixel units (1 pixel = 2mm). From the figure we see that each measurement step is perfectly resolved by the detector, since the reconstructed position match the real beam position. This means that with a scanning procedure is possible to simulate a virtual pixel with a considerably smaller size. Therefore, a second scan was performed by moving the detector in the *y* direction in steps of 0.2 mm. The results are presented in figure 6.6 and it shows that even in this case the position is well resolved. From the residuals' distribution we estimated a resolution of 0.130 pixels (= 0.260 mm) (FWHM).

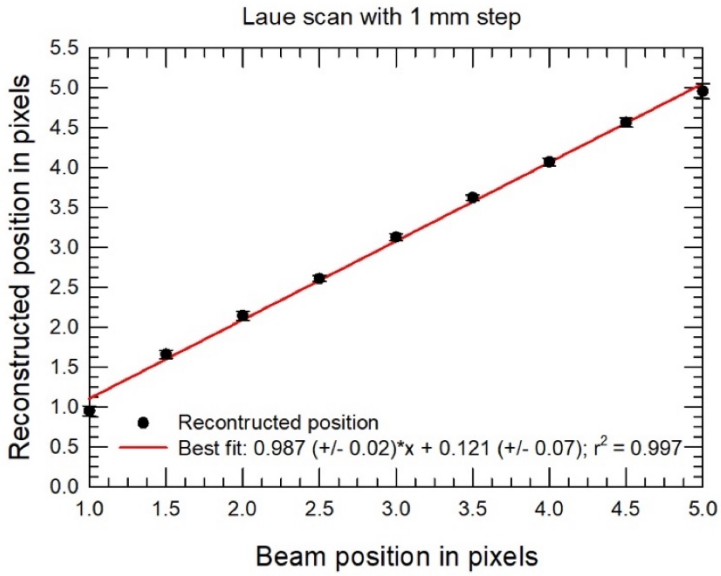

Figure 6.5: Reconstructed position as function of the beam position for the PSF 1 mm scans.

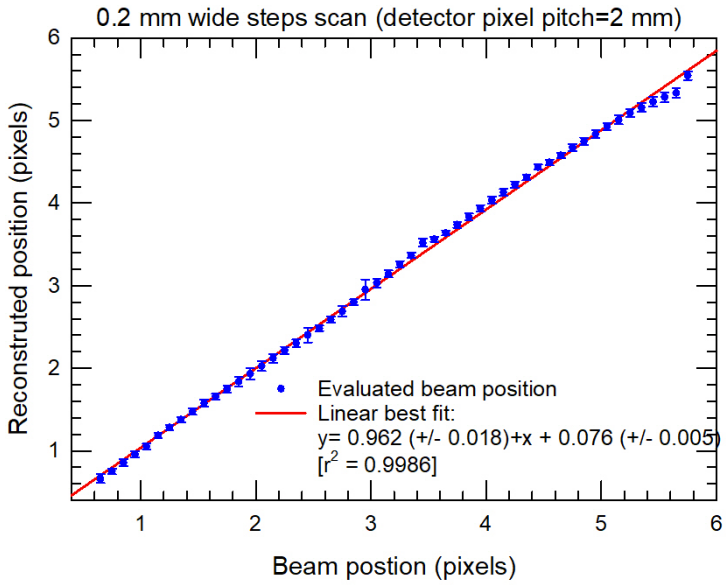

Figure 6.6: Reconstructed position as function of the beam position for the 0.2 mm PSF scans.

6.4 Laue Crystals' PSF

From the previous results we know that the system is capable to evaluate the PSF of a single Laue crystal tile thus, a new set of measurements was performed with a GaAs (220) crystal. As we want to cover the total are of the tile, for these measurements we collimated the beam to have a square shape of 10×10 mm^2 and we performed a scan covering the total area of crystal by progressively moving the collimator in steps of 5 mm. A schematic of the measurements positions along the crystal is illustrated in figure 6.7. The tile position was also changed: we placed the crystal in 4 four positions along the *y* direction which pretends to simulate the position of 4 crystals tiles next to each other in different Laue ring positions, positions *I*, *L*, *M* and *N* from figure 6.8. A total number of 20 measurements were performed (4 tile position × 5 beam positions) with an integration time of 600 s for each.

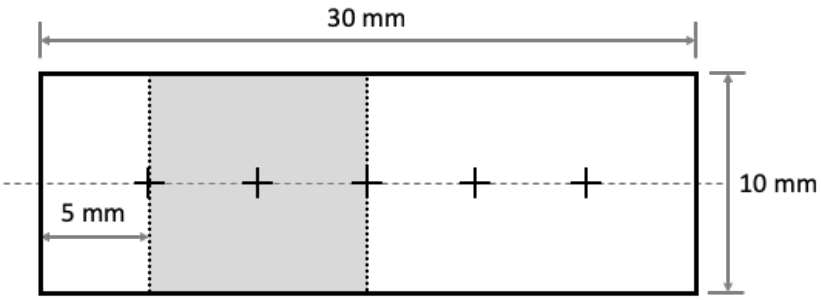

Figure 6.7: Schematic of the beam position along the crystal. 5 measurements were performed to cover the all crystal area. The crosses correspond to the centre of the beam. As an example, the grey area corresponds to the beam cross section on the second measurement.

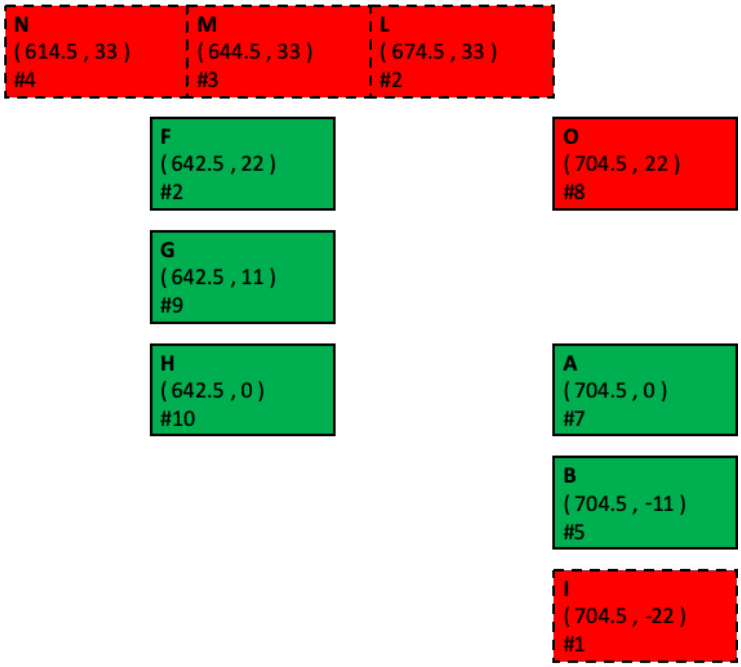

Figure 6.8: Schematic of the GaAs crystals position for the PSF and energy passband measurements. The crystals in green boxes were used for the passband measurements and the red for both passband and PSF measurements. The red boxes always refer to crystal *O* placed in different positions, being the solid edge its real position and the dotted edge the virtual positions. The coordinates shown are the *y* and *z* position of the crystals, being *y* the distance from the lens axis. The number below corresponds to the measurement order.

In figure 6.9 is presented the intensity maps obtained for the 5 steps when the crystal is in position *I*. It is visible that the rectangular shape of the diffracted focused beam hits the detector in different locations from one measurement to another, moving through

three detector columns. In order to evaluate this shift and analyse the crystal' PSF we proceed to the same position reconstruction as we did in the scan measurements. The results of the reconstructed position as function of the absolute beam position are presented in figure 6.10. The 4 humps that correspond to each tile position are clearly identified. It is also clear that the 4 humps have the same shape, since the same crystal was used for the different positions. Therefore, in order to obtain the average response of crystal *O* we present in figure 6.11 the average of each measurement for the 4 tile positions. The hump reflects the fact that the crystal is not perfectly uniform along its length, as it would present a flat response. The width (PSF) of the displacement is ~0.7 detector pixel, i.e. 1,4 mm, in excellent agreement with the value measured with the X-ray flat panel.

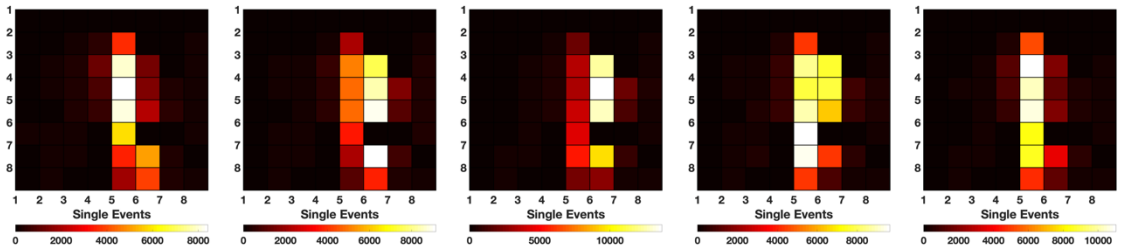

Figure 6.9: Intensity maps obtained by irradiating crystal *O* (position *I*) in the 5 positions represented in figure 6.7.

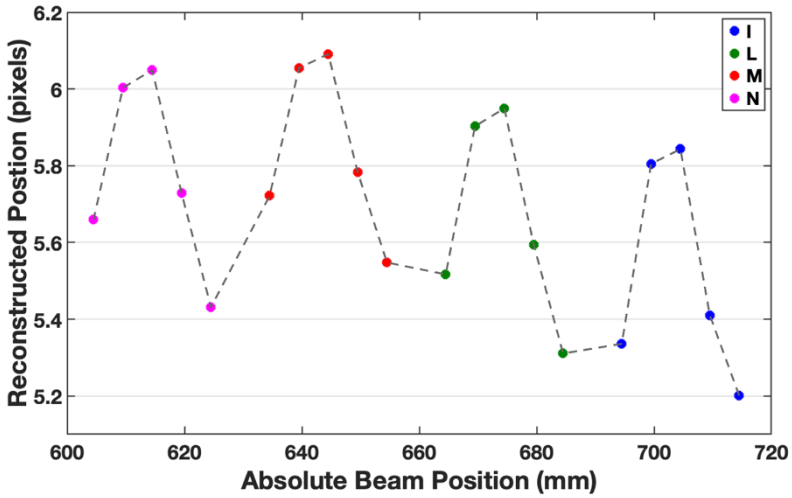

Figure 6.10: Reconstructed position as function of the absolute beam position obtained by irradiating crystal *O* in 4 tile position along the radius of the lens (*I, L M, N*), each point representing one of the 5 beam positions represented in figure 6.7.

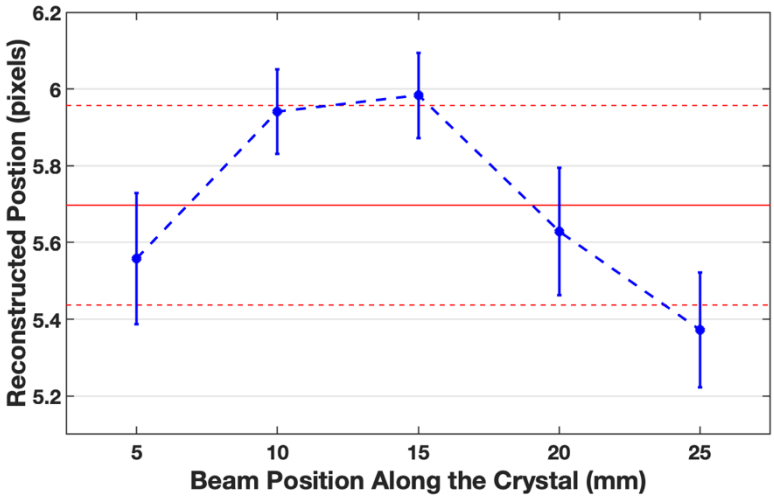

Figure 6.11: Average response of the *O* crystal in different ring positions.

6.5 Energy Passband

The final step consisted in a set of measurements with the objective to evaluate the energy passband of the crystals in different ring positions. Each ring position will diffract photons in a specific energy passband and each crystal tile belonging to a given ring (same distance from the lens axis) will diffract photons within the same energy passband. For these measurements we analyse all the crystal positions represented in figure 6.8. Note that the crystals represented with solid line edges in figure 6.8 correspond to real positions of crystals. These crystals were glued to a petal with gap between them to avoid contact during the assembling phase. The measurements were performed by irradiating the crystal tiles with a 10×10 mm^2 square shape beam in the same positions represented in figure 6.7. However, here, the source and collimator move together to the desired position in order to ensure that the X-ray beam is always parallel to the lens axis. The acquisition time was 600 s for each measurement.

In figure 6.12 is presented the energy passband obtained for crystal *O* in the different ring positions. For each measurement we selected the single events from the pixel with higher count rate and fitted the spectrum to a sum of gaussian functions to obtain the peak centroid energy. As expected, there is a decrease of the energy when the ring distance from the lens axis is increased. The energy passband obtained is from ~140 keV to ~170 keV.

The same procedure was applied for the measurements of the reimaging crystals. Figure 6.13 presents the energy bandwidth obtained. It is evident the difference between the energy passband of both lens rings. For the ring closer to the lens axis (crystals *F*, *G* and *H*) we obtained an energy passband of 162-170 keV and for the further ring (crystals *A*, *B* and *O*) a passband of 138-146 keV.

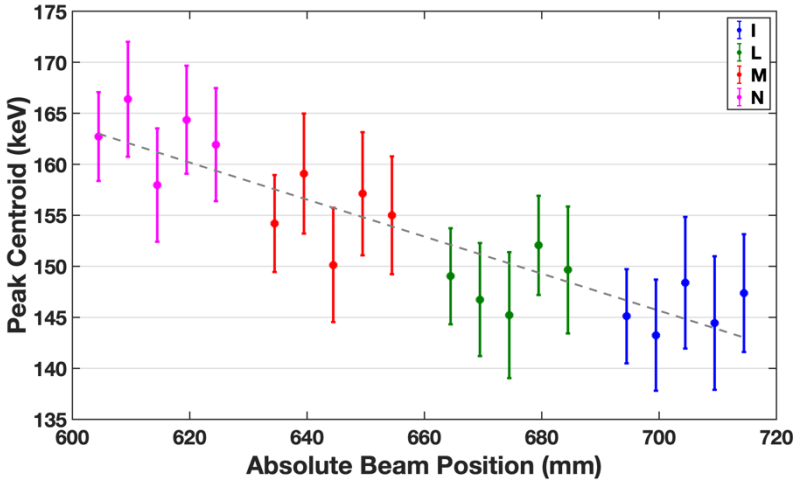

Figure 6.12: Energy passband using of the crystal *O* placed in positions *I*, *L*, *M* and *N*.

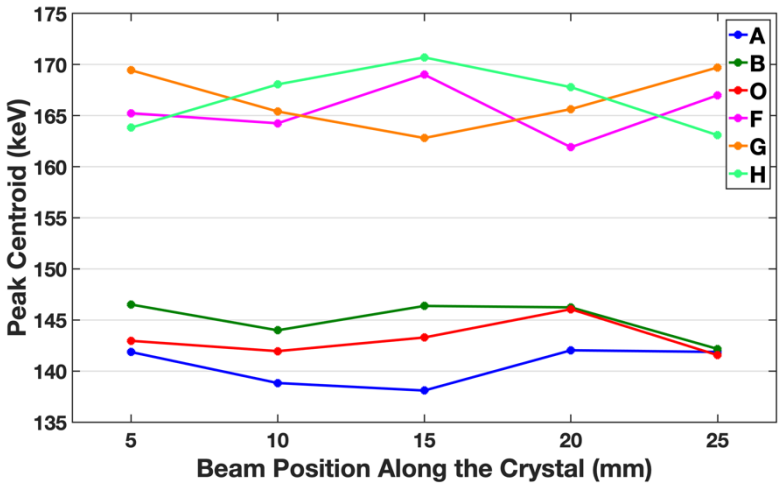

Figure 6.13: Energy passband for the 6 crystal tiles of two different Laue rings.

6.6 Discussion

A big leap in the sensitivity and angular resolution with respect to that of the current hard X-/soft g-ray instrumentation based on direct-viewing of the sky (with or without a coded mask) has long been recognized as key issue to address still open hot scientific topics in high/energy astrophysics for the next decade. The development of broadband Laue lens appears one of most promising technique to solve these instrumental issues. In perspective, we are developing since several years broad band Laue lens based on bent crystals. We are assembling a Laue lens prototype for 90-300 keV, and in the near future, we would face the problem of reliable evaluation of its performance. The X-ray beam facility, we currently use to mount the bent crystals on the lens support, make use of a detection system based on two different devices: an HPGe spectrometer and an X-ray flat panel imager. Instead, to perform this performance evaluation, the use of a spectro-imager detector with fine spatial resolution (<0.5 mm) and fine spectroscopy (few % at 150 keV) is mandatory. In fact, only the use of such a device as focal plane detector can give a reliable measurement of the Laue lens PSF characteristics providing simultaneously both imaging and spectroscopy. Herein we present a preliminary study of the response of a sample of GaAs bent crystals obtained using the Compton-POLCA as focal plane. This system is far from the required performance for the NFT instrument aboard ASTENA nevertheless, we were interested in study which kind of information on the bent crystal focusing response we can achieve with this detector prototype. In particular, we report on the capability of the Compton-POLCA to sample the focused image, i.e. the point spread function, of GaAs bent crystals, determine its energy pass band and evaluate its uniformity. The results proved that the Compton-POLCA can be used to perform this analysis and remain available at the LARIX laboratory for further measurements with more crystals.

7 Conclusions

In the context of future high-energy astrophysics' mission development, this Ph.D. thesis presents and validates new solutions regarding the polarimetric potential of future space observatories based on CdTe detectors' multi-layer/tracker solutions. High-energy polarimetry is today recognised as a main scientific topic, therefore future space missions will certainly provide polarimetric observations, contemporaneously with spectroscopy and imaging, providing new parameters to understand gamma-ray astronomical sources' physical models. CdTe planar detectors have already proven the capability to perform polarimetry in the soft gamma-ray domain [88]–[96]. Herein, we designed and assembled a 2-layers Compton spectro-imager based on 2 CdTe matrices of 8×8 pixels, each with 2×2 mm^2 size and 2 mm thickness, the Compton-POLCA. We tested this prototype under polarized beams in order to access its polarimetric performance. While changing the prototype configuration, by varying the detector inter-plane distance, the polarimetric response was analysed under different beam and detector operational conditions: beam energy, beam size, energy threshold, polarization direction and polarization degree.

Firstly, a simulation code based on MEGAlib software simulation tool was implemented with the objective to evaluate the polarimetric potential of the dual plane geometry. The simulation results were used as input for the prototype final geometry design and to set an adequate experimental test plan.

For a 300 keV beam irradiating the centre of the top matrix, we obtained a modulation factor *Q* of 0.405 selecting single plane interactions; a *Q* factor of 0.34 for a detector plane distance of 4 mm selecting exclusively dual plane interactions; and a *Q* of 0.362 for the same 4 mm distance, combining all double interactions and therefore operating in the maximum detection efficiency mode. Therefore, for such detector thickness, the polarization performance is dominated by the single detector double events. When varying the distance between the two detector planes, the results show that the modulation factor *Q* decreases with the detector plane distance when operating in the dual plane mode, since better modulation is obtained for scattering angles ~90º, when the two planes are closer. The shorter inter-plane distance configuration is also the best option in the full detector mode since the best polarimetric sensitivity (MDP) is obtained for higher detection double-event efficiency when the modulation varies marginally with the distance.

Simulating the irradiation of the full top active surface by a 300 keV 100% polarized beam, in the full detection mode, a modulation factor *Q* as high as 0.483 is obtained for a detector plane distance of 12 mm due to the higher number of double events scattered near 90º generated between opposite peripheral pixels of top and bottom planes.

The prototype was then tested at the high-energy beamline ID15A at the ESRF under an 100% polarized beam in the 200 keV up to 500 keV energy band and for detector inter-plane distances from 8 to 16 mm. The registered energy resolution (FWHM) of the Compton-POLCA was ~7.3% @200 keV and ~4.3% @500 keV. The measured modulation polarimetric factor in the full detector operation mode for a 300 keV beam was a *Q* factor of ~0.46 when selecting single plane interactions; a *Q* of ~0.09 when selecting dual plane interactions (detector plane distance 8 mm); and *Q* ~0.42 when combining both interactions (detector plane distance 8 mm). When increasing the distance between the prototypes' detector planes, we observed that the *Q* factor decreases, since the value of both minimum and maximum scattering angles also decreases. Finally, measurements were also performed for a beam polarization angle oriented at three distinct polarization angles: 0°, 20° and 45°. The prototype measured polarization angles were: 2.0°, 25.0° and 46.3°, respectively, providing a polarization angle resolution lower than ~7°. These results are in fine agreement with the conclusions draw from the simulation analysis.

The analysis of potential effects of the orbital radiation environment on a CdTe by proton beam irradiation (up to ~14 MeV) at the ICNAS cyclotron facility in Coimbra. The results showed that the contribution of CdTe activation background should have a minimal impact in instruments' performance deterioration. Furthermore, CdTe presented

good radiation hardness for typical LEO proton fluences. The measured energy resolution shows a small degradation up to 9 years orbital proton fluence equivalent, but for lower energies (122 keV) and 22 years equivalent proton fluence the energy resolution deteriorates by 60%, however it is still suitable for most of the mission scientific requirements. For 511 keV the energy resolution degradation is about 14%, becoming lower for higher gamma- ray energies. Furthermore, CdTe show a very good level of spectroscopic properties' recovery, actually one year after the irradiation the energy resolution recovered almost totally for higher energies (511 and 1275 keV) and recovered down to an energy resolution level only ∼15% worse before proton irradiation for the 122 keV line.

Both, the simulated and the experimental dual-plane prototype analysis confirm the fine polarimetric potential of the multi-layer configuration CdTe focal planes. However, the present work provides as well a valuable estimation of the great polarimetric potential of 3D position detection solutions, as the ones being developed by our team for ASTENA mission. Since 3D detectors will be able to probe in greater detail the double event photons' and Compton electron trajectories, these will provide a more accurate polarization modulation curve as well as a better reconstruction of the Compton events and therefore better source position and spectroscopic resolution.

Within the ASTENA consortium we are presently participating in the development of such 3D CZT/CdTe detectors both by Monte Carlo [199], [218] and experimental testing [219]. These studies will lead to a new generation of high performance spectro-imagers equipped with both all-sky capability and Laue lens focusing technology capable of: high detection efficiency (>80% at 500 keV); fine spectroscopy (1% FWHM at 511 keV); fine spatial resolution (<0.5 mm); high-energy dynamics (10-1000 keV) response; good scattering polarimetry capability in parallel to spectroscopy, imaging and timing. Furthermore, the greater double event efficiency provided by such kind of large volume multi-layer/3D detectors, will offer fine sensitivity observations (MDP < 5% for a 10 mCrab source, 1 Ms observation time and 3σ significance) contributing to open a new knowledge window integrating the new polarimetric dimension in hard X/gamma-rays astrophysics. A prototype will be developed for a balloon borne test flights in order to set a solid proposal for a future ESA mission selection call.

List of Acronyms

AGILE	Astro-Rivelatore Gamma a Immagini Leggero
AGN	Active Galactic Nuclei
AHEAD	Activities in the High Energy Astrophysics Domain
ASIC	Application Specific Integrated Circuits
ASTENA	Advanced Surveyor of Transient Events and Nuclear Astrophysics
BBH	Binary Black Holes
CCE	Charge Collection Efficiency
CdTe	Cadmium Telluride
CGRO	Compton Gamma-Ray Observatory
COMPTEL	Imaging Compton Telescope
COSI	Compton Spectrometer and Imager
CsI	Cesium Iodide
CZT	Cadmium Zinc Telluride
CZTI	Cadmium Zinc Telluride Imager
DSSD	Double-Sided Strip Detector
ESA	European Space Agency
ESRF	European Synchrotron Radiation Facility
FM	Flight Model
FPGA	Field Programmable Gate Array
GAP	Gamma-ray bursts Polarimeter
Ge	Germanium
GRAPE	Gamma Ray Polarimeter Experiment
GRB	Gamma Ray Burst
HPGe	High Precision Germanium
IBIS	INTEGRAL Soft Gamma-Ray Imager
ICNAS	Instituto de Ciências Nucleares Aplicadas à Saúde
INAF	Istituto di Astrofisica

INTEGRAL	International Gamma-Ray Astrophysics Laboratory
JAXA	Japan Aerospace Exploration
LAT	Large Area Telescope
LARIX	LARge Italian X-ray
LEO	Low Earth Orbit
LIP	Laboratory of Instrumentation and Experimental Particle Physics
MAPMT	Multi-Anode Photomultiplier Tube
MEGAlib	Medium-Energy Gamma-ray Astronomy library
NFT	Narrow Field Telescope
PCB	Printed Circuit Board
PFM	Proto-Flight Model
PoGO	Polarized Gamma Ray Observer
QM	Qualification Model
RHESSI	Ramaty High-Energy Solar Spectroscopic Imager
SDD	Silicon Drift Detectors
SGD	Soft Gamma-ray Detector
Si	Silicon Drift Detectors
SPI	Spectrometer on INTEGRAL
WFM-IS	Wide Field Monitor-Imaging Spectrometer

List of Figures

List of Tables

Bibliography

[1] N. A. Gehrels and C. Winkler, *International Gamma-Ray Astrophysics Laboratory (INTEGRAL): a future ESA mission for gamma-ray astronomy*, in *Proceedings of SPIE 2806* (1996).

[2] A. A. Moiseev, *Gamma-ray Large Area Space Telescope: Mission overview*, *Nucl. Instruments Methods Phys. Res. Sect. A* 588 (2008) 41.

[3] C. Kopper and E. Blaufuss, *IceCube-170922A - IceCube observation of a high-energy neutrino candidate event.*, *GRB Coord. Network, Circ. Serv. No. 21916, #1* (2017).

[4] A. Keivani *et al.*, *A Multimessenger Picture of the Flaring Blazar TXS 0506+056: Implications for High-energy Neutrino Emission and Cosmic-Ray Acceleration*, *Astrophys. J.* 864 (2018) 84.

[5] Y. T. Tanaka, S. Buson, and D. Kocevski, *Fermi-LAT detection of increased gamma-ray activity of TXS 0506+056, located inside the IceCube-170922A error region*, *Astron. Telegr.* 10791 (2017).

[6] R. Mirzoyan, *First-time detection of VHE gamma rays by MAGIC from a direction consistent with the recent EHE neutrino event IceCube-170922A*, *Astron. Telegr.* 10817 (2017).

[7] E. N. Alexeyev, L. N. Alexeyeva, I. V. Krivosheina, and V. I. Volchenko, *Detection of the neutrino signal from SN 1987A in the LMC using the INR Baksan underground scintillation telescope*, *Phys. Lett. B* 205 (1988) 209.

[8] B. P. Abbott *et al.*, *Multi-messenger Observations of a Binary Neutron Star Merger**, *Astrophys. J. Lett.* 848 (2017).

[9] F. Lei, A. J. Dean, and G. L. Hills, *Compton Polarimetry in Gamma-Ray Astronomy*, *Space Sci. Rev.* 82 (1997) 309.

[10] R. Bellazzini and F. Muleri, *X-ray polarimetry: A new window on the high energy sky*, *Nucl. Instruments Methods Phys. Res. Sect. A* 623 (2010) 766.

[11] M. McConnell, *X-Ray and Gamma-Ray Polarimetry*, *Astro2010 White Pap. Submiss.* (2009).

[12] S. McGlynn *et al.*, *High energy emission and polarisation limits for the* INTEGRAL *burst GRB 061122*, *Astron. Astrophys.* 499 (2009) 465.

[13] D. Gotz *et al.*, *Variable polarization measured in the prompt emission of GRB 041219A using IBIS on board INTEGRAL*, *Astrophys. J.* 695 (2009) 208.

[14] P. Laurent, D. Götz, P. Binétruy, S. Covino, and A. Fernandez-Soto, *Constraints on Lorentz invariance violation using integral/IBIS observations of GRB041219A*, *Phys. Rev. D* 83 (2011).

[15] D. Gotz, S. Covino, A. Fernandez-Soto, P. Laurent, Z. . Bosnjak, and D. Götz, *The polarized gamma-ray burst GRB 061122*, *Mon. Not. R. Astron. Soc.* 431 (2013) 3550.

[16] D. Gotz *et al.*, *GRB 140206A: the most distant polarized Gamma-Ray Burst*, 8 (2014) 1.

[17] E. Kalemci, S. E. Boggs, C. Kouveliotou, M. Finger, and M. G. Baring, *Search for*

polarization from the prompt gamma-ray emission of GRB 041219a with SPI on INTEGRAL, *Astrophys. J. Suppl. Ser.* 169 (2007) 8.

[18] E. Jourdain, J. P. Roques, M. Chauvin, and D. J. Clark, *Separation of two contributions to the high energy emission of Cygnus X-1: Polarization measurements with integral SPI*, *Astrophys. J.* 761 (2012) 1.

[19] M. Forot, P. Laurent, I. A. Grenier, C. Gouiffès, and F. Lebrun, *Polarization of the Crab pulsar and nebula as observed by the INTEGRAL/IBIS telescope*, *Astrophys. J.* 688 (2008) 29.

[20] A. J. Dean *et al.*, *Polarized Gamma-Ray Emission from the Crab*, *Science* 321 (2008) 1183.

[21] P. Moran *et al.*, *A recent change in the optical and gamma-ray polarization of the Crab nebula and pulsar*, *Mon. Not. R. Astron. Soc.* 456 (2016) 2974.

[22] P. Moran, A. Shearer, C. Gouiffes, and P. Laurent, *INTEGRAL/IBIS and optical observations of the Crab nebula/pulsar polarisation*, in *Proceedings of 9th INTEGRAL Workshop* (2013).

[23] C. Gouiffès *et al.*, *New hard X-rays and optical polarimetric observations of the Crab nebula and pulsar*, in *Proceedings of 11th INTEGRAL Conference* (2017).

[24] P. Laurent *et al.*, *Integral observations of polarization: From the Crab pulsar to Cygnus X-1*, in *Proceedings of 9th INTEGRAL Workshop* (2013).

[25] V. G. P. Laurent, J. Rodriguez, J. Wilms, M. Cadolle Bel, K. Pottschmidt, *Polarized Gamma-Ray Emission from the Galactic Black Hole Cygnus X-1*, 332 (2011) 438.

[26] S. V Vadawale *et al.*, *Phase-resolved X-ray polarimetry of the Crab pulsar with the AstroSat CZT Imager*, *Nat. Astron.* 2 (2018) 1.

[27] S.-N. Zhang *et al.*, *Detailed polarization measurements of the prompt emission of five Gamma-Ray Bursts*, (2019).

[28] E. S. GARCIA, *X-Ray Polarization : RHESSI Results and POLAR Prospects*, Thèse de doctorat, Université Genève, 2010.

[29] D. Rapin *et al.*, *Response of the Compton polarimeter POLAR to polarized hard X-rays*, *Nucl. Instruments Methods Phys. Res. Sect. A* 648 (2011) 139.

[30] M. Kole *et al.*, *Instrument performance and simulation verification of the POLAR detector*, *Nucl. Instruments Methods Phys. Res. Sect. A* 872 (2017) 28.

[31] T. Chattopadhyay, S. V. Vadawale, A. R. Rao, S. Sreekumar, and D. Bhattacharya, *Prospects of hard X-ray polarimetry with Astrosat-CZTI*, *Exp. Astron.* 37 (2014) 555.

[32] S. V. Vadawale *et al.*, *Hard X-ray polarimetry with Astrosat-CZTI*, *Astron. Astrophys.* 578 (2015) A73.

[33] J. Knödlseder *et al.*, *GRI: Focusing on the evolving violent universe*, *Exp. Astron.* 23 (2009) 121.

[34] P. von Ballmoos, T. Takahashi, and S. E. Boggs, *A DUAL mission for nuclear astrophysics*, *Nucl. Instruments Methods Phys. Res. Sect. A* 623 (2010) 431.

[35] M. Tavani, *ASTROGRAM - Summary of a proposal submitted for the ESA M4 Mission Programme*, (2015).

[36] A. De Angelis *et al.*, *The e-ASTROGAM mission: Exploring the extreme Universe with gamma rays in the MeV – GeV range*, *Exp. Astron.* 44 (2017) 25.

[37] V. Tatischeff *et al.*, *All-Sky-ASTROGAM: The MeV Gamma-Ray Companion to Multimessenger Astronomy*, in *Proceedings of the 12th INTEGRAL Conference* (2019).

[38] J. McEnery *et al.*, *All-sky Medium Energy Gamma-ray Observatory: Exploring the Extreme Multimessenger Universe*, *Astro2020 White Pap. Submiss.* (2019).

[39] N. Gehrels, E. Chipman, and D. Kniffen, *The Compton Gamma Ray Observatory*, *Astrophys. J. Suppl. Ser.* 92 (1994) 351.

[40] G. G. Stokes, *On the composition and resolution of streams of polarized light from different sources*, *Trans. Cambridge Philos. Soc.* 9 (1852) 399.

[41] M. Matsumiya and K. Ioka, *Circular Polarization from Gamma-Ray Burst Afterglows*, *Astrophys. J.* 595 (2003) 25.

[42] S. Tashenov, *Circular polarimetry with gamma-ray tracking detectors*, *Nucl. Instruments Methods Phys. Res. Sect. A* 640 (2011) 164.

[43] O. Klein and Y. Nishina, *Über die Streuung von Strahlung durch freie Elektronen nach der neuen relativistischen Quantendynamik von Dirac*, *Zeitschrift für Phys.* 52 (1929) 853.

[44] W. S. Paciesas *et al.*, *The Fourth BATSE Gamma-Ray Burst Catalog (Revised)*, *Astrophys. J. Suppl. Ser.* 122 (1999) 465.

[45] S. E. Woosley, *Gamma-ray bursts from stellar mass accretion disks around black holes*, *Astrophys. J.* 405 (1993) 273.

[46] K. Iwamoto *et al.*, *A hypernova model for the supernova associated with the γ-ray burst of 25 April 1998*, *Nature* 395 (1998) 672.

[47] A. I. MacFadyen and S. E. Woosley, *Collapsars: Gamma-Ray Bursts and Explosions in 'Failed Supernovae'*, *Astrophys. J.* 524 (1999) 262.

[48] N. Gehrels and S. Razzaque, *Gamma-ray bursts in the swift-Fermi era*, *Front. Phys.* 8 (2013) 661.

[49] A. Goldstein *et al.*, *An Ordinary Short Gamma-Ray Burst with Extraordinary Implications:* Fermi -*GBM Detection of GRB 170817A*, *Astrophys. J.* 848 (2017) L14.

[50] P. Kumar and B. Zhang, *The physics of gamma-ray bursts & relativistic jets*, *Phys. Rep.* 561 (2015) 1.

[51] P. Mészáros, *Gamma-Ray Bursts*, *Reports Prog. Phys.* 69 (2006) 2259.

[52] T. Piran, *The physics of gamma-ray bursts*, *Reviews of Modern Physics* 76. American Physical Society 1143 28-Jan-2004.

[53] B. Zhang, *Gamma-Ray Bursts in the Swift Era*, *Chinese J. Astron. Astrophys.* 7 (2007) 329.

[54] W. Coburn and S. E. Boggs, *Polarization of the prompt γ-ray emission from the γ-ray burst of 6 December 2002*, *Nature* 423 (2003) 415.

[55] S. McGlynn *et al.*, *Polarisation studies of the prompt gamma-ray emission from GRB 041219a using the spectrometer aboard* INTEGRAL, *Astron. Astrophys.* 466 (2007) 895.

[56] R. E. Rutledge and D. B. Fox, *Re-analysis of polarization in the γ-ray flux of GRB 021206*, *Mon. Not. R. Astron. Soc.* 350 (2004) 1288.

[57] C. Wigger, W. Hajdas, K. Arzner, M. Gudel, and A. Zehnder, *Gamma-Ray Burst Polarization: Limits from RHESSI Measurements*, *Astrophys. J.* 613 (2004) 1088.

[58] D. R. Willis *et al.*, *Evidence of polarisation in the prompt gamma-ray emission from GRB 930131 and GRB 960924*, *Astron. Astrophys.* 439 (2005) 245.

[59] D. Yonetoku *et al.*, *Magnetic structures in gamma-ray burst jets probed by gamma-ray polarization*, *Astrophys. J. Lett.* 758 (2012).

[60] D. Yonetoku *et al.*, *Detection of Gamma-Ray Polarization in Prompt Emission of GRB*

100826A, *Astrophys. J.* 743 (2011) 30.

[61] T. Chattopadhyay *et al.*, *Prompt emission polarimetry of Gamma Ray Bursts with ASTROSAT CZT-Imager*, *Astrophys. J.* 884 (2017) 123.

[62] V. Chand *et al.*, *AstroSat-CZTI Detection of Variable Prompt Emission Polarization in GRB 171010A*, *Astrophys. J.* 874 (2019) 70.

[63] S.-N. Zhang *et al.*, *Detailed polarization measurements of the prompt emission of five gamma-ray bursts*, *Nat. Astron.* 3 (2019) 258.

[64] M. L. McConnell, *High Energy Polarimetry of Prompt GRB Emission*, *New Astron. Rev.* 76 (2016) 1.

[65] J. M. Burgess *et al.*, *Time-resolved GRB polarization with POLAR and GBM*, *Astron. Astrophys.* 627 (2019) 105.

[66] A. Lyne and F. Graham-Smith, *Pulsar Astronomy*. Cambridge University Press, 2012.

[67] H. Krawczynski *et al.*, *Scientific prospects for hard X-ray polarimetry*, *Astropart. Phys.* 34 (2011) 550.

[68] J. Dyks, A. K. Harding, and B. Rudak, *Relativistic Effects and Polarization in Three High-Energy Pulsar Models*, *Astrophys. J.* 606 (2004) 1125.

[69] J. Pétri, *Phase-resolved polarization properties of the pulsar striped wind synchrotron emission*, *Mon. Not. R. Astron. Soc.* 434 (2013) 2636.

[70] M. C. Weisskopf, E. H. Silver, H. L. Kestenbaum, K. S. Long, and R. Novick, *A precision measurement of the X-ray polarization of the Crab Nebula without pulsar contamination*, *Astrophys. J.* 220 (1978) 117.

[71] M. Chauvin *et al.*, *Observation of polarized hard X-ray emission from the Crab by the PoGOLite Pathfinder*, *Mon. Not. R. Astron. Soc.* 456 (2016) L84.

[72] M. Chauvin *et al.*, *Accretion geometry of the black-hole binary Cygnus X-1 from X-ray polarimetry*, *Nat. Astron.* 2 (2018) 652.

[73] K. Salgado, *Accretion Disk Spectra of Black Hole X-ray Binaries*, *Undergrad. Honor. Theses* (2015).

[74] W. Hajdas *et al.*, *X-Ray Polarization of Solar Flares Measured with Rhessi*, *Sol. Phys.* 239 (2006) 149.

[75] S. E. Boggs, W. Coburn, and E. Kalemci, *Gamma-Ray Polarimetry of Two X-Class Solar Flares*, *Astrophys. J.* 638 (2006) 1129.

[76] *RHESSI Web Site*,. [Online]. Available: https://hesperia.gsfc.nasa.gov/rhessi3/. [Accessed: 25-Jul-2019].

[77] T. I. IceCube Collaboration *et al.*, *Multimessenger observations of a flaring blazar coincident with high-energy neutrino IceCube-170922A.*, *Science* 361 (2018).

[78] R. Ojha *et al.*, *Neutrinos, Cosmic Rays and the MeV Band*, *Astro2020 White Pap. Submiss.* (2019).

[79] *Active Galactic Nuclei (AGNs)*,. [Online]. Available: https://heasarc.gsfc.nasa.gov/docs/cgro/images/epo/gallery/agns/index.html. [Accessed: 25-Jul-2019].

[80] G. F. Knoll, *Radiation Detection and Measurement, 4th Edition*. Wiley, 2010.

[81] W. R. Leo, *Techniques for Nuclear and Particle Physics Experiments*. Springer, 1994.

[82] B. S. Ishkhanov, *The atomic nucleus*, *Moscow Univ. Phys. Bull.* 67 (2012) 1.

[83] M. Suffert, P. M. Endt, and A. M. Hoogenboom, *Polarization measurements of proton*

capture gamma rays, *Physica* 25 (1959) 659.

[84] E. Caroli *et al.*, *Hard X-ray and Soft Gamma Ray Polarimetry with CdTe/CZT Spectro-Imager*, *Galaxies* 6 (2018) 69.

[85] M. C. Weisskopf, R. F. Elsner, V. M. Kaspi, S. L. O'Dell, G. G. Pavlov, and B. D. Ramsey, *X-Ray Polarimetry and Its Potential Use for Understanding Neutron Stars*, in *Neutron Stars and Pulsars*, Springer, 2009, 589.

[86] R. A. Kroeger *et al.*, *Gamma-ray instrument for polarimetry, spectroscopy, and imaging (GIPSI)*, in *Proceedings of SPIE 2806* (1996).

[87] S. E. E. Inderhees *et al.*, *Spectroscopy, imaging and compton-scatter polarimetry with a germanium strip detector*, *IEEE Trans. Nucl. Sci.* 43 (1996) 1467.

[88] M. Pinto, *CdTe Matrix Polarimetric Analysis with a Crystal Polarizer*, Dissertação de Mestrado, Universidade de Coimbra, 2014.

[89] E. Caroli *et al.*, *A CdTe position sensitive spectrometer for hard X- and soft gamma-ray polarimetry*, *Nucl. Instruments Methods Phys. Res. Sect. A* 477 (2002) 567.

[90] E. Caroli *et al.*, *A study of prototype CdTe hard X- and gamma-ray detectors*, *Nucl. Instruments Methods Phys. Res. Sect. A* 513 (2003) 350.

[91] R. M. C. da Silva *et al.*, *Hard X- And Soft Gamma-ray Polarimetry with CdTe Array Prototypes*, *IEEE Trans. Nucl. Sci.* 51 (2004) 2478.

[92] R. M. Curado da Silva *et al.*, *Polarimetric performance of a Laue lens gamma-ray CdZnTe focal plane prototype*, *J. Appl. Phys.* 104 (2008) 1.

[93] E. Caroli *et al.*, *A polarimetric experiment with a laue lens and CZT pixel detector*, *IEEE Trans. Nucl. Sci.* 56 (2009) 1848.

[94] S. Antier, O. Limousin, and P. Ferrando, *Fine pitch CdTe-based Hard-X-ray polarimeter performance for space science in the 70-300 keV energy range*, *Nucl. Instruments Methods Phys. Res. Sect. A* 787 (2011) 297.

[95] R. M. C. da Silva *et al.*, *Polarimetry study with a CdZnTe focal plane detector*, *IEEE Trans. Nucl. Sci.* 58 (2011) 2118.

[96] R. M. Curado Da Silva and E. Caroli, *Polarization degree and direction angle effects on a CdZnTe focal plane performance*, *IEEE Trans. Nucl. Sci.* 59 (2012) 1628.

[97] H. L. Xiao *et al.*, *Calibration of gamma-ray burst polarimeter POLAR*, in *Proceedings of 2015 IEEE NSS/MIC Conference* (2015).

[98] J.-L. Chiu *et al.*, *The Compton Spectrometer and Imager (COSI)*, in *Proceedings of 35th International Cosmic Ray Conference* (2017).

[99] C. A. Kierans *et al.*, *Calibration of the Compton Spectrometer and Imager in preparation for the 2014 balloon campaign*, in *Proceedings of 2015 IEEE NSS/MIC Conference* (2015).

[100] C. Sleator *et al.*, *Benchmarking COSI's detector effects engine*, in *Proceedings of 11th INTEGRAL Conference* (2017).

[101] C.-Y. Yang *et al.*, *The polarimetric performance of the Compton spectrometer and imager (COSI)*, in *Proceedings of SPIE 10699* (2018).

[102] A. W. Lowell *et al.*, *Maximum Likelihood Compton Polarimetry with the Compton Spectrometer and Imager*, *Astrophys. J.* 848 (2017) 120.

[103] A. W. Lowell *et al.*, *Polarimetric Analysis of the Long Duration Gamma-Ray Burst GRB 160530A With the Balloon Borne Compton Spectrometer and Imager*, *Astrophys. J.* 848 (2017) 119.

[104] M. Chauvin *et al.*, *The design and flight performance of the PoGOLite Pathfinder balloon-borne hard X-ray polarimeter*, *Exp. Astron.* 41 (2016) 17.

[105] M. Kiss and M. Pearce, *PoGOLite: Opening a new window on the universe with polarized gamma-rays*, *Nucl. Instruments Methods Phys. Res. Sect. A* 580 (2007) 876.

[106] M. Kiss *et al.*, *The PoGOLite balloon-borne soft gamma-ray polarimeter*, in *AIP Conference Proceedings* (2008) 1054 225.

[107] M. Chauvin *et al.*, *Shedding new light on the Crab with polarized X-rays*, *Sci. Reports 7* 7816 (2017).

[108] G. J. Fishman, C. A. Meegan, T. A. Parnell, and R. B. Wilson, *The burst and transient source experiment for the gamma-ray observatory*, in *AIP Conference Proceedings* (1982) 77 443.

[109] M. L. McConnell, J. M. Ryan, D. M. Smith, R. P. Lin, and A. G. Emslie, *RHESSI as a hard x-ray polarimeter*, *Sol. Phys.* 210 (2002) 125.

[110] P. Ubertini *et al.*, *IBIS: The Imager on-board INTEGRAL*, *Astron. Astrophys.* 411 (2003) L131.

[111] C. Winkler *et al.*, *The INTEGRAL mission*, *Astron. Astrophys.* 411 (2003) L1.

[112] G. Vedrenne *et al.*, *SPI: The spectrometer aboard INTEGRAL*, *Astron. Astrophys.* 411 (2003) 63.

[113] M. Chauvin, J. P. Roques, D. J. Clark, and E. Jourdain, *Polarimetry in the hard X-ray domain with integral SPI*, *Astrophys. J.* 769 (2013) 2.

[114] F. Tokanai *et al.*, *Development of polarimeter for gamma-ray bursts onboard the solar-powered sail mission*, in *Proceedings of SPIE 6266* (2006).

[115] H. SAKAMOTO *et al.*, *Development of Deployment System for Small Size Solar Sail Mission*, *Trans. Japan Soc. Aeronaut. Sp. Sci. Sp. Technol. Japan* 7 (2009) 87.

[116] D. Yonetoku, *Study of emission mechanism of Gamma-Ray Bursts by the gamma-ray polarization with IKAROS-GAP*, in *Proceedings of Gamma-Ray Bursts 2012 Conference* (2012).

[117] N. Produit *et al.*, *POLAR, a compact detector for gamma-ray bursts photon polarization measurements*, *Nucl. Instruments Methods Phys. Res. Sect. A* 550 (2005) 616.

[118] T. Takahashi *et al.*, *Hitomi (ASTRO-H) X-ray Astronomy Satellite*, *J. Astron. Telesc. Instruments, Syst.* 4 (2018).

[119] H. Tajima *et al.*, *Design and performance of Soft Gamma-ray Detector onboard the Hitomi (ASTRO-H) satellite*, *J. Astron. Telesc. Instruments, Syst.* 4 (2018).

[120] F. Aharonian *et al.*, *Detection of polarized gamma-ray emission from the Crab nebula with the Hitomi Soft Gamma-ray Detector†*, *Publ. Astron. Soc. Japan* 70 (2018) 113.

[121] A. R. Rao *et al.*, *Cadmium Zinc Telluride Imager onboard AstroSat : a multi-faceted hard X-ray instrument*, *Curr. Sci.* 113 (2017) 595.

[122] V. Bhalerao *et al.*, *The Cadmium Zinc Telluride Imager on AstroSat*, *J. Astrophys. Astron.* 38 (2017) 31.

[123] O. Mori *et al.*, *First Solar Power Sail Demonstration by IKAROS*, *Trans. Japan Soc. Aeronaut. Sp. Sci. Aerosp. Technol. Japan* 8 (2010) 25.

[124] D. Yonetoku *et al.*, *Gamma-Ray Burst Polarimeter (GAP) aboard the small solar power sail demonstrator IKAROS*, *Publ. Astron. Soc. Japan* 63 (2011) 625.

[125] M. Kole *et al.*, *POLAR: Final calibration and in-flight performance of a dedicated GRB polarimeter*, in *Proceedings of 2016 IEEE NSS/MIC/RTSD Conference* (2017) 2017-

Janua.

[126] I. Britvich *et al.*, *Design and construction of the POLAR detector*, *Nucl. Instruments Methods Phys. Res. Sect. A Accel. Spectrometers, Detect. Assoc. Equip.* 877 (2017) 259.

[127] H. Tajima *et al.*, *Soft Gamma-ray Detector for the ASTRO-H Mission*, in *Proceedings of SPIE 7732* (2010).

[128] T. Takahashi *et al.*, *High resolution CdTe detectors for the next-generation multi-Compton gamma-ray telescope*, in *Proceedings of SPIE 4851* (2003).

[129] T. Takahashi *et al.*, *Hard X-ray and γ-ray detectors for the NeXT mission*, *New Astron. Rev.* 48 (2004) 269.

[130] T. Takahashi *et al.*, *Wide band X-ray Imager (WXI) and Soft Gamma-ray Detector (SGD) for the NeXT Mission*, in *Proceedings of SPIE 5488* (2004).

[131] H. Tajima *et al.*, *Design and performance of the soft gamma-ray detector for the NeXT mission*, *IEEE Trans. Nucl. Sci.* 52 (2005) 2749.

[132] S. Watanabe *et al.*, *Soft gamma-ray detector for the ASTRO-H Mission*, in *Proceedings of SPIE 8443* (2012).

[133] S. Takeda *et al.*, *Polarimetric performance of Si/CdTe semiconductor Compton camera*, *Nucl. Instruments Methods Phys. Res. Sect. A* 622 (2010) 619.

[134] J. Katsuta *et al.*, *Study of the polarimetric performance of a Si/CdTe semiconductor Compton camera for the Hitomi satellite*, *Nucl. Instruments Methods Phys. Res. Sect. A* 840 (2016) 51.

[135] P. C. Agrawal, *A broad spectral band Indian Astronomy satellite 'Astrosat'*, *Adv. Sp. Res.* 38 (2006) 2989.

[136] W. H. Zachariasen and IUCr, *A general theory of X-ray diffraction in crystals*, *Acta Crystallogr.* 23 (1967) 558.

[137] K. P. Singh *et al.*, *ASTROSAT mission*, in *Space Telescopes and Instrumentation 2014: Ultraviolet to Gamma Ray* (2014) 9144 91441S.

[138] S. V. Vadawale *et al.*, *In-orbit performance of AstroSat CZTI*, in *Proceedings SPIE 9905* (2016).

[139] F. A. Harrison *et al.*, *THE* NUCLEAR SPECTROSCOPIC TELESCOPE ARRAY *(* NuSTAR *) HIGH-ENERGY X-RAY MISSION*, *Astrophys. J.* 770 (2013) 103.

[140] F. Acero *et al.*, *FERMI LARGE AREA TELESCOPE THIRD SOURCE CATALOG*, *Astrophys. J. Suppl. Ser.* 218 (2015) 23.

[141] V. Schonfelder *et al.*, *The Imaging Compton Telescope Comptel on the Gamma Ray Observatory*, *IEEE Trans. Nucl. Sci.* 31 (1984) 766.

[142] A. Moiseev and on behalf of the AMEGO Team, *All-Sky Medium Energy Gamma-ray Observatory (AMEGO)*, in *Proceedings of 35th International Cosmic Ray Conference* (2017).

[143] E. Burns *et al.*, *Opportunities for Multimessenger Astronomy in the 2020s*, *Astro2020 White Pap. Submiss.* (2019).

[144] E. Burns *et al.*, *Gamma Rays and Gravitational Waves*, *Astro2020 White Pap. Submiss.* (2019).

[145] E. Burns *et al.*, *A Summary of Multimessenger Science with Neutron Star Mergers*, *Astro2020 White Pap. Submiss.* (2019).

[146] E. Orlando *et al.*, *Cosmic Rays and Interstellar Medium with Gamma-Ray Observations at MeV Energies*, *Astro2020 White Pap. Submiss.* (2019).

[147] B. Rani *et al.*, *High-Energy Polarimetry - a new window to probe extreme physics in AGN jets*, *Astro2020 White Pap. Submiss.* (2019).

[148] T. M. Venters *et al.*, *Energetic Particles of Cosmic Accelerators II: Active Galactic Nuclei and Gamma-ray Bursts*, *Astro2020 White Pap. Submiss.* (2019).

[149] M. L. McConnell *et al.*, *Prompt Emission Polarimetry of Gamma-Ray Bursts*, *Astro2020 White Pap. Submiss.* (2019) 1.

[150] V. S. Paliya *et al.*, *Supermassive black holes at high redshifts*, *Astro2020 White Pap. Submiss.* (2019).

[151] E. Meyer *et al.*, *Prospects for AGN Studies at Hard X-ray through MeV Energies*, *Astro2020 White Pap. Submiss.* (2019).

[152] Z. Wadiasingh *et al.*, *Magnetars as Astrophysical Laboratories of Extreme Quantum Electrodynamics: The Case for a Compton Telescope*, *Astro2020 White Pap. Submiss.* (2019).

[153] M. Di Mauro, S. Manconi, and F. Donato, *Prospects for the detection of synchrotron halos around middle-age pulsars*, *Astro2020 White Pap. Submiss.* (2019).

[154] R. Caputo *et al.*, *Looking Under a Better Lamppost: MeV-scale Dark Matter Candidates*, *Astro2020 White Pap. Submiss.* (2019).

[155] C. L. Fryer *et al.*, *Catching Element Formation In The Act*, *Astro2020 White Pap. Submiss.* (2019).

[156] C. A. Kierans *et al.*, *Positron Annihilation in the Galaxy*, *Astro2020 White Pap. Submiss.* (2019).

[157] P. Von Ballmoos, *Focusing telescopes in nuclear astrophysics*. Springer, 2006.

[158] I. Kuvvetli, C. Budtz-Jørgensen, E. Caroli, and N. Auricchio, *CZT drift strip detectors for high energy astrophysics*, *Nucl. Instruments Methods Phys. Res. Sect. A* 624 (2010) 486.

[159] E. Caroli *et al.*, *A Small 3D CZT Payload for Hard X-Ray Polarimetry and Spectroscopic Imaging*, in *Proceedings of 2014 IEEE NSS/MIC Conference* (2014).

[160] E. Caroli *et al.*, *Development of a 3D CZT detector prototype for Laue Lens telescope*, in *Proceedings of SPIE 7742* (2010).

[161] A. F. V. Cortez *et al.*, *Future gamma-ray missions' polarimetric prospects*, *Exp. Astron.* 48 (2019) 65.

[162] *Polar*,. [Online]. Available: https://www.astro.unige.ch/polar/. [Accessed: 29-Jul-2019].

[163] T.E.Schlesinger and R.B.James, *Chapter 1 - Introduction and Overview*, in *Semiconductors and Semimetals*, 43, Elsevier, 1995, 1.

[164] M. Hage-Ali and P. Siffert, *Chapter 8 - CdTe Nuclear Detectors and Applications*, in *Semiconductors and Semimetals*, 43, Elsevier, 1995, 291.

[165] L. Abbene and S. Del Sordo, *CdTe Detectors*, in *Comprehensive Biomedical Physics*, 8, Elsevier, 2014, 285.

[166] L. Strüder, *High-resolution imaging X-ray spectrometers*, *Nucl. Instruments Methods Phys. Res. Sect. A* 454 (2000) 73.

[167] C. Guazzoni, *The first 25 years of silicon drift detectors: A personal view*, *Nucl. Instruments Methods Phys. Res. Sect. A* 624 (2010) 247.

[168] Y. K. Akimov, *Silicon radiation detectors (Review)*, *Instruments Exp. Tech.* 50 (2007) 1.

[169] A. Sokolov, V. Gostilo, A. Loupilov, and V. Zalinkevich, *Performance improvement of Si(Li) peltier cooled detectors*, *IEEE Trans. Nucl. Sci.* 49 (2002) 2427.

[170] F. Hartmann, *Evolution of silicon sensor technology in particle physics*. Springer, 2017.

[171] D. Alexiev, M. I. Reinhard, L. Mo, A. R. Rosenfeld, and M. L. Smith, *Review of Ge detectors for gamma spectroscopy*, *Australas. Phys. Eng. Sci. Med.* 25 (2002) 102.

[172] J. Eberth and J. Simpson, *From Ge(Li) detectors to gamma-ray tracking arrays-50 years of gamma spectroscopy with germanium detectors*, *Prog. Part. Nucl. Phys.* 60 (2008) 283.

[173] D. S. McGregor and H. Hermon, *Room-temperature compound semiconductor radiation detectors*, *Nucl. Instruments Methods Phys. Res. Sect. A* 395 (1997) 101.

[174] T. Takahashi and S. Watanabe, *Recent progress in CdTe and CdZnTe detectors*, *IEEE Trans. Nucl. Sci.* 48 (2001) 950.

[175] S. del Sordo, L. Abbene, E. Caroli, A. M. Mancini, A. Zappettini, and P. Ubertini, *Progress in the development of CdTe and CdZnTe semiconductor radiation detectors for astrophysical and medical applications*, *Sensors* 9 (2009) 3491.

[176] A. Owens and IUCr, *Semiconductor materials and radiation detection*, *J. Synchrotron Radiat.* 13 (2006) 143.

[177] H. H. Barrett, J. D. Eskin, and H. B. Barber, *Charge Transport in Arrays of Semiconductor Gamma-Ray Detectors*, *Phys. Rev. Lett.* 75 (1995) 156.

[178] J. E. Toney, T. E. Schlesinger, and R. B. James, *Optimal bandgap variants of Cd1-xZnxTe for high-resolution X-ray and gamma-ray spectroscopy*, *Nucl. Instruments Methods Phys. Res. Sect. A* 428 (1999) 14.

[179] A. Owens and A. Peacock, *Compound semiconductor radiation detectors*, *Nucl. Instruments Methods Phys. Res. Sect. A* 531 (2004) 18.

[180] S. M. Sze and K. K. Ng, *Physics of Semiconductor Devices 3rd Ed.* Wiley, 2006.

[181] T. Tanaka *et al.*, *Recent achievements of the high resolution Schottky CdTe diode for γ-ray detectors*, *New Astron. Rev.* 48 (2004) 309.

[182] K. Nakazawa *et al.*, *Improvement of the CdTe diode detectors using a guard-ring electrode*, *IEEE Trans. Nucl. Sci.* 51 (2004) 1881.

[183] T. Takahashi *et al.*, *High-resolution Schottky CdTe diode for hard X-ray and gamma-ray astronomy*, *Nucl. Instruments Methods Phys. Res. Sect. A* 436 (1999) 111.

[184] A. Meuris, O. Limousin, and C. Blondel, *Characterization of polarization phenomenon in Al-Schottky CdTe detectors using a spectroscopic analysis method*, *Nucl. Instruments Methods Phys. Res. Sect. A* 654 (2011) 293.

[185] H. Toyama *et al.*, *Formation of Aluminum Schottky Contact on Plasma-Treated Cadmium Telluride Surface*, *Jpn. J. Appl. Phys.* 43 (2004) 6371.

[186] L. Abbene, G. Gerardi, F. Principato, A. A. Turturici, S. Del Sordo, and G. Raso, *Characterization of Al-Schottky CdTe detectors*, in *Proceedings of 2011 IEEE NSS Conference* (2011) 4636.

[187] I. Farella, G. Montagna, A. M. Mancini, and A. Cola, *Study on Instability Phenomena in CdTe Diode-Like Detectors*, *IEEE Trans. Nucl. Sci.* 56 (2009) 1736.

[188] H. L. Malm and M. Martini, *Polarization Phenomena in CdTe Nuclear Radiation Detectors*, *IEEE Trans. Nucl. Sci.* 21 (1974) 322.

[189] F. Principato, G. Gerardi, A. A. Turturici, and L. Abbene, *Time-dependent current-voltage characteristics of Al/p-CdTe/Pt x-ray detectors*, *J. Appl. Phys.* 112 (2012) 094506.

[190] P. De Chiara and F. Frontera, *Bragg diffraction technique for the concentration of hard x-rays for space astronomy*, *Appl. Opt.* 31 (1992) 1361.

[191] R. M. Curado Da Silva, E. Caroli, J. B. Stephen, and F. Frontera, *The POLCA*

Experiments, in *Proceedings of Polarimetry days in Rome: Crab status, theory and prospects* (2008).

[192] N. Simões *et al.*, *Inflight proton activation and damage on a CdTe detection plane*, *Nucl. Instruments Methods Phys. Res. Sect. A* 877 (2018) 183.

[193] *MEGAlib - The Medium-Energy Gamma-ray Astronomy library*,. [Online]. Available: http://megalibtoolkit.com/. [Accessed: 10-Apr-2019].

[194] R. M. C. Da Silva, E. Caroli, J. B. Stephen, and P. Siffert, *Cipher, a polarimeter telescope concept for hard X-ray astronomy*, *Exp. Astron.* 15 (2003) 45.

[195] S. Antier *et al.*, *Hard X-ray polarimetry with Caliste, a high performance CdTe based imaging spectrometer*, *Exp. Astron.* 39 (2015) 233.

[196] *ID15A - Materials Chemistry and Materials Engineering*,. [Online]. Available: https://www.esrf.eu/home/UsersAndScience/Experiments/StructMaterials/ID15A.html. [Accessed: 20-Aug-2016].

[197] V. Liccardo, *Gamma-ray Lens : Development and Test*, PhD Thesis, Università degli Studi di Ferrara, 2013.

[198] M. G. Kirsch *et al.*, *Crab: the standard x-ray candle with all (modern) x-ray satellites*, in *Proceedings of SPIE 5898* (2005).

[199] E. Caroli *et al.*, *Monte Carlo evaluation of a CZT 3D spectrometer suitable for a Hard X- and soft-γ rays polarimetry balloon borne experiment*, in *Proceedings of 2015 IEEE NSS/MIC Conference* (2016) 1.

[200] J. M. Lavigne *et al.*, *The INTEGRAL experiment*, *Nucl. Phys. B - Proc. Suppl.* 60 (1998) 69.

[201] P. Leleux *et al.*, *Neutron-induced nuclear reactions and degradation in germanium detectors*, *Astron. Astrophys.* 411 (2003) L85.

[202] R. Terrier *et al.*, *In-flight calibration of the ISGRI camera*, *Astron. Astrophys.* 411 (2003) L167.

[203] M. Ajello *et al.*, *Cosmic X-Ray Background and Earth Albedo Spectra with Swift BAT*, *Astrophys. J.* 689 (2008) 666.

[204] N. Simões, *Ativação e degradação da resposta de um instrumento de CdTe em condições de voo para um telescópio espacial de raios gama*, Dissertação de Mestrado, Universidade de Coimbra, 2015.

[205] M. Pelica, *Análise dos Danos da Radiação de Protões Orbitais em Detectores de CdTe*, Dissertação de Mestrado, Universidade de Coimbra, 2018.

[206] M. P. Pascoa *et al.*, *Orbit-Like Proton Radiation Sensitivity of CdTe Detectors: Evaluation of Mobility-Lifetime Products and Spectroscopic Properties*, *IEEE Trans. Nucl. Sci.* 66 (2019) 1.

[207] M. Zanarini *et al.*, *Radiation damage induced by 2 MeV protons in CdTe and CdZnTe semiconductor detectors*, *Nucl. Instruments Methods Phys. Res. Sect. B Beam Interact. with Mater. Atoms* 213 (2004) 315.

[208] B. Fraboni, A. Cavallini, N. Auricchio, and M. Bianconi, *Deep Traps Induced by 700 keV Protons in CdTe and CdZnTe Detectors*, *IEEE Trans. Nucl. Sci.* 54 (2007) 828.

[209] A. Pisa *et al.*, *Feasibility study of a Laue lens for hard X–rays for space astronomy*, *Adv. Comput. Methods X-Ray Neutron Opt.* 5536 (2004) 39.

[210] F. Frontera *et al.*, *Development status of a Laue lens project for gamma-ray astronomy*, *Opt. EUV, X-Ray, Gamma-Ray Astron. III* 6688 (2007) 66880N.

[211] F. Frontera *et al.*, *Scientific prospects in soft gamma-ray astronomy enabled by the LAUE project*, in *Proceedings of SPIE 8861* (2013).

[212] V. Liccardo, E. Virgilli, F. Frontera, and P. Rosati, *The LAUE project: latest developments*, *J. Phys. Conf. Ser.* 706 (2016) 052037.

[213] E. Virgilli *et al.*, *The LAUE project and its main results*, in *Proceedings of SPIE 8861* (2013).

[214] E. VIRGILLI *et al.*, *THE LAUE PROJECT FOR BROADBAND GAMMA-RAY FOCUSING LENSES*, *Int. J. Mod. Phys. Conf. Ser.* 23 (2013) 43.

[215] V. Valsan, *Extending the band of focusing X-ray telescopes beyond 100 keV: motivations and proposed solutions*, PhD Thesis, Università degli Studi di Ferrara, 2013.

[216] G. Loffredo *et al.*, *X–ray facility for the ground calibration of the X–ray monitor JEM-X on board INTEGRAL*, *Astron. Astrophys.* 411 (2003) L239.

[217] E. Virgilli *et al.*, *Focusing effect of bent GaAs crystals for γ-ray Laue lenses: Monte Carlo and experimental results*, *Exp. Astron.* 41 (2016) 307.

[218] E. Caroli *et al.*, *A 3D CZT hard x-ray polarimeter for a balloon-borne payload*, in *Proceedings of SPIE 8443* (2012).

[219] I. Kuvvetli *et al.*, *A 3D CZT high resolution detector for x- and gamma-ray astronomy*, in *Proceedings of SPIE 9154* (2014) 9154.